



---

seit 1558

# Structure-property relationships of polymer-based multi-phase systems

## **Dissertation**

(Kumulative Disseration)

zur Erlangung des akademischen Grades  
Doktor-Ingenieur (Dr.-Ing.)

vorgelegt dem Rat der Chemisch-Geowissenschaftlichen Fakultät der  
Friedrich-Schiller-Universität Jena

von

Diplom-Ingenieur **Stefan Hölzer**,  
geboren am 01.03.1984 in Saalfeld (Saale)

Gutachter:

1. Prof. Dr. habil. Ulrich S. Schubert, Friedrich-Schiller-Universität Jena
2. Prof. Dr. habil. Mario Beiner, Martin-Luther-Universität Halle-Wittenberg

Tag der öffentlichen Verteidigung: 22.04.2015

*Für meine Familie*



## Table of contents

Documentation of authorship	V
1 Introduction	1
2 Deformation mechanisms of styrene-diene-based block copolymers	3
3 Tailoring morphology and mechanical behavior by blending of olefin copolymers	11
4 Controlling semi-crystalline statistical and block copolymers by annealing	17
5 Summary	29
6 Zusammenfassung	32
References	XI
List of abbreviations	XV
Curriculum vitae	XIX
List of publications & presentations	XX
Acknowledgments / Danksagung	XXII
Declaration of Authorship / Selbstständigkeitserklärung	XXV
Publications [P1–P7]	XXVII



## **Erklärung zu den Eigenanteilen des Promovenden sowie der weiteren Doktoranden/Doktorandinnen als Co-Autoren an den Publikationen und Zweitpublikationsrechten bei einer kumulativen Dissertation**

**Für alle in dieser kumulativen Dissertation verwendeten Manuskripte liegen die notwendigen Genehmigungen der Verlage ("Reprint permissions") für die Zweitpublikation vor.**

Die Co-Autoren der in dieser kumulativen Dissertation verwendeten Manuskripte sind sowohl über die Nutzung, als auch über die oben angegebenen Eigenanteile informiert und stimmen dem zu (es wird empfohlen, diese grundsätzliche Zustimmung bereits mit Einreichung der Veröffentlichung einzuholen bzw. die Gewichtung der Anteile parallel zur Einreichung zu klären). Die Anteile der Co- Autoren an den Publikationen sind in der Anlage aufgeführt.

**Ich bin mit der Abfassung der Dissertation als publikationsbasiert, d.h. kumulativ, einverstanden und bestätige die vorstehenden Angaben. Eine entsprechend begründete Befürwortung mit Angabe des wissenschaftlichen Anteils des Doktoranden/der Doktorandin an den verwendeten Publikationen werde ich parallel an den Rat der Fakultät der Chemisch-Geowissenschaftlichen Fakultät richten.**

Prof. Dr. Ulrich S. Schubert, Jena, 08.01.2015, .....

Stefan Hölzer, Jena, 08.01.2015, .....





Publication [P1]	High-strain-induced deformation mechanism in block-graft and multigraft copolymers, <i>Macromolecules</i> 2011, 44, 9374–9383.									
Author	R. Schlegel	Y. X. Duan	R. Weidisch <sup>*,†</sup>	S. Hölzer	K. Schneider	M. Stamm	D. Uhrig	J. W. Mays	G. Heinrich	N. Hadjichristidis
Development of concept			X							
Mechanics	X									
Modelling	X									
FTIR-Analysis & interpretation		X								
SAXS investigation & interpretation	X			X	X		X	X		
Synthesis										
Supervision			X							
Preparation of the manuscript	X									
Corrections of the manuscript	X	X	X	X	X	X	X	X	X	X
Proposed publication equivalent	0.5									

\* ... corresponding author, † ... deceased

Publication [P2]	Deformation mechanism in lamellar S-S/B-S triblock copolymers, <i>Eur. Polym. J.</i> 2013, 49, 261–269					
Author	S. Hölzer	M. Ganß	K. Schneider	K. Knoll	R. Weidisch <sup>*,†</sup>	
Development of concept				X	X	
Planning of the investigations	X	X				
Mechanics	X	X	X			
Synthesis				X		
SAXS measurements & interpretation	X		X			
Supervision						
Preparation of the manuscript	X				X	
Corrections of the manuscript	X	X	X	X	X	
Proposed publication equivalent	1.0					

\* ... corresponding author, † ... deceased

Publication [P3]	Blends of ethylene–octene copolymers with different chain architectures – Morphology, thermal and mechanical behavior, <i>Polymer</i> <b>2013</b> , 54, 5207–5213.						
Author	S. Hölzer	M. Menzel	Q. Zia	U.S. Schubert	M. Beiner*	R. Weidisch†	
Development of concept	X					X	
Planning of the investigations	X						
Polymer processing, Mechanics	X						
AFM		X			X		
DSC			X		X		
DMA, WAXS, Ultramicrotomy	X						
Data analysis & interpretation	X		X		X		
Supervision					X		
Preparation of the manuscript	X						
Corrections of the manuscript	X	X	X	X	X	X	
Proposed publication equivalent	1.0						

\* ... corresponding author, † ... deceased

Publication [P4]	Combinatorial screening of inkjet printed ternary blends for organic photovoltaics: Absorption behavior and morphology, <i>ACS Comb. Sci.</i> <b>2013</b> , 15, 410–418								
Author	A. Teichler	S. Hölzer	J. Nowotny	F. Kretschmar	C. Bader	J. Perelaer	M. D. Hager	S. Hoeppeener	U. S. Schubert*
Development of Concept	X					X			
Sample preparation & interferometry	X								
AFM		X							
Optical Characterization			X		X				
Synthesis				X					
Supervision						X	X		X
Preparation of the manuscript	X						X		
Corrections of the manuscript	X	X	X	X	X	X	X	X	X
Proposed publication equivalent	1.0	0.5							0.5

\* ... corresponding author

Publication [P5]	Inkjet printed micropump actuator based on piezoelectric polymers: Device performance and morphology studies, <i>Organ. Electron.</i> <b>2014</b> , <i>15</i> , 3306–3315.						
Author	O. Pabst*	S. Hölzer†	E. Beckert*	J. Perelaer	U. S. Schubert	R. Eberhardt	A. Tümmermann
Development of concept	X	X	X				
Planning of the Investigations	X	X					
Sample Preparation	X						
Electro-mechanical studies	X						
Structure & morphology studies		X					
Data analysis & interpretation	X	X					
Supervision			X		X	X	X
Preparation of the manuscript	X	X					
Corrections of the manuscript	X	X	X	X	X	X	X
Proposed publication equivalent	1.0	1.0					

†... contributed equally, \*... corresponding author

Publication [P6]	Mechanisms and kinetics of the crystal thickening of poly(butadiene)- <i>block</i> -poly(ethylene oxide) during annealing within the melting range, <i>Eur. Polym. J.</i> , <i>in press</i> . DOI:10.1016/j.eurpolymj.2015.04.010						
Author	S. Hölzer	T. N. Bittner	R. Schulze	M. M. L. Arras	F. H. Schacher	U. S. Schubert*	K. D. Jandt*
Development of concept	X		X				X
Planning of the investigations	X		X				
DSC		X					
SAXS, WAXS	X						
Model development	X	X		X			
Data analysis & interpretation	X	X	X	X	X		
Supervision			X			X	X
Preparation of the manuscript	X						
Corrections of the manuscript	X	X	X	X	X	X	X
Proposed publication equivalent	1.0						

\*... corresponding author

Publication [P7] How the calorimetric properties of a crystalline copolymer correlate to its surface nanostructures, *Macromolecules* 2014, 47, 1705–1714

Author	R. Schulze†	M. M. L. Arras†	C. Helbing	S. Hölzer	U. S. Schubert	T. F. Keller	K. D. Jandt*
Development of concept	X	X				X	X
Planning of the investigations	X	X	X	X			
Datenerhebung	X	X	X				
Data analysis & interpretation	X	X	X	X	X	X	X
Supervision							
Preparation of the manuscript	X	X					
Corrections of the manuscript	X	X	X	X	X	X	X
Proposed publication equivalent				0.5			

†...contributed equally, \*...corresponding author

# 1 Introduction

Polymeric materials offer a wide range of properties that are relevant for applications and, hence, these materials can be found in various fields of every day life. Prominent examples are, for instance, packaging materials or consumables, where the suitability of the polymer is mainly determined by its mechanical properties. Other polymers offer the possibility to solve nowadays problems in the fields of life science,<sup>[1]</sup> energy harvesting<sup>[2]</sup> or energy storage.<sup>[3]</sup> Due to the very broad range of possible applications, it is useful to categorize polymers into different groups.<sup>[4]</sup> In the field of *functional polymers*, the polymer has to fulfill one specific function, e.g., high absorption in a defined spectral range for organic photovoltaics or stealth behavior in drug delivery systems.<sup>[1]</sup> These polymers are generally well-defined and more advanced synthesis strategies are necessary, which often makes these polymers very expensive. *Commodity plastics* are produced in large amounts and are very cost-effective.<sup>a</sup> This makes them interesting for applications where special mechanical properties and service environments are not required. Between these two classes is the field of *technical* and *high performance* polymers, which are characterized by a superior mechanical behavior or offer a special property-profile, i.e. a suitable combination of material properties.<sup>[4]</sup>

The overall behavior of a polymer depends on various parameters. Generally, this connection is referred to as *structure-property relationship*, where *structure* can be interpreted either as chemical or physical structure. The chemical structure includes (i) constitutional unit(s), which are the (different) monomers, (ii) their arrangement, which is in particular the macromolecular architecture and (iii) parameters that describe the distribution of their chain length, in particular the molar masses,  $M_w$  and  $M_n$  as well as the polydispersity index  $PDI = M_w / M_n$ . Most of these parameters can only be adjusted during polymer synthesis. The advances in this field during the last decades provides flexibility in the macromolecular design.<sup>[6,7]</sup> However, the transfer from pure academic interest to a commercial application is determined by the ratio of the benefit of the materials properties and the costs of the often more elaborate synthesis technique. Therefore, usually only a limited selection of polymers with different macromolecular architectures is available on an industrial scale.

The physical structure of a polymeric system describes the arrangement of the chains inside a polymer crystal (*crystal structure*) and the overall morphology of the system on multiple length scales. For clarity, the term *structure* will, in the following, only be used in the context of the *crystalline structure*, which describes the lattice parameters of the polymer crystal and the arrangement of chains within these crystals. *Morphology* will be used for the general arrangement of the polymer chains (in a crystalline or amorphous state), in microphase-separated

---

<sup>a</sup>  $\approx 1.24$  k€/t for general purpose low density polyethylene.<sup>[5]</sup>

(like in block copolymers)<sup>[8]</sup> and macrophase-separated states (like in polymers blends)<sup>[9]</sup> as well as orientations, due to polymer processing.

Since the need for high performance polymers is increasing, different approaches are developed to fulfill the desired property-profiles. Some of them have been investigated in this work, with emphasis on understanding the relationship between macromolecular architecture, structure and morphology as well as macroscopic properties of polymers that exhibit more than one phase. The chapters of this thesis are divided according to the different approaches that are used to improve the material behavior of the polymer systems.

- In Chapter 2, the influence of the **macromolecular architecture** and the morphology on the deformation mechanism in a styrene-butadiene-based block copolymer system will be presented.
- The impact of **blending** two linear-low density polyethylenes, having similar densities but different macromolecular architectures, was investigated regarding the crystallization and phase behavior as well as the consequences on the mechanical properties. The results of these investigations will be discussed in Chapter 3.
- Exemplary for the **processing conditions**, annealing close to the melting point and its influence on structure and morphology as well as the macroscopic properties will be briefly discussed in Chapter 4. The first study was carried out on a ferro- and piezoelectric poly(vinylidene fluoride-co-trifluoroethylene) in order to improve its electro-mechanical behavior. In a second investigation, annealing close to the melting point was used to adjust the morphology of an amorphous-crystalline block copolymer. It was found that the surface and bulk morphology can be efficiently adjusted by the annealing conditions.

Although the investigated materials differ in their composition, the underlying processes carry obvious similarities, which underline the importance of structure and morphology as the linking unit between the macromolecular architecture and the macroscopic properties. The main methods that were used to describe structure and morphology of the investigated polymers are: (i) Differential scanning calorimetry (DSC), which provides important insights about the melting behavior in semi-crystalline systems,<sup>[10]</sup> (ii) dynamic-mechanical analysis (DMA),<sup>[10]</sup> to describe the dynamic glass transition of the systems, (iii) microscopic methods, like atomic force microscopy (AFM)<sup>[11]</sup> or transmission electron microscopy (TEM)<sup>[12]</sup> as well as (iv) small and wide angle X-Ray scattering,<sup>[13]</sup> to study the morphology (SAXS) and the crystal structure (WAXS), respectively. Since each of these techniques have their own advantages and disadvantages, it becomes obvious that only the combination of different techniques enables an understanding of the role of structure and morphology on the macroscopic properties of the investigated materials and to fulfill the future challenges in the field of polymer engineering.

## 2 Influence of macromolecular architecture on the deformation mechanism of styrene-diene-based block copolymers

Parts of this chapter have been published: [P1] R. Schlegel, Y. X. Duan, R. Weidisch, S. Hölzer, K. Schneider, M. Stamm, D. Uhrig, J. W. Mays, G. Heinrich, N. Hadjichristidis, *Macromolecules* **2011**, *44*, 9374–9383; [P2] S. Hölzer, M. Ganß, K. Schneider, K. Knoll, R. Weidisch, *Eur. Polym. J.* **2013**, *49*, 261–269.

Block copolymers, which base on blocks of polystyrene (PS) and polybutadiene (PB) or polyisoprene (PI), are of high practical significance and scientific interest due to their ability to self-assemble into microphase-separated morphologies, which can be used to tune their mechanical behavior. Classically, these polystyrene-*block*-polydiene (S-D) diblock or (S-D-S) triblock copolymers can be effectively tailored by the fraction of the styrenic hard-phase (S) and the polydiene based soft-phase (D), which typically consists of PB or PI. The volume fraction  $\phi$  of these individual components influences the microphase separated morphology (typically 10 to 50 nm) and, as a consequence, a significantly different mechanical behavior can be achieved, which reaches from brittle failure up to highly elastomeric behavior.<sup>[14]</sup> For instance, sphere and cylinder-forming SD-block copolymers, with styrene being the minor phase, typically show an elastomeric property-profile, having high strain at break, low tensile strength and high recoverability, whereas lamellar morphologies generally show distinct yielding, lower strain at break as well as a high toughness.<sup>[15]</sup> The glassy styrene domains act thereby as physical cross-links that soften upon heating, which allows a cost-effective thermoplastic processing.

Two major trends can be observed in the material development concerning the macromolecular architecture of styrene-diene based block copolymers in the last years. The first one is the development of new, complex architectures that can further improve the mechanical behavior, *e.g.*, the recoverability of thermoplastic elastomers. In this field multigraft copolymers yielded very promising results. Partially, the observed mechanical behavior exceeded that of commercial thermoplastic elastomers by far.<sup>[16–22]</sup> For instance, one major advantage of these *superelastic* multigraft copolymers is their high elastic recovery, even after deformations >1000%.<sup>[21]</sup> Detailed information on the deformation mechanism of these multigraft copolymers were obtained by synchrotron SAXS and FTIR spectroscopy during stretching in the group of Weidisch and can be found in Ref.<sup>[20]</sup> and [P1].

The second trend is the use of poly(styrene-*stat*-diene) as the soft phase in SD-based thermoplastics, which offers the possibility to improve stiffness and strength of the polymer, without sacrificing its toughness.<sup>[17,23–27]</sup> Thereby, the macromolecular architecture and mor-

phology were found to significantly influence the mechanical behavior. A detailed study on this topic is given in [P2] and will be concisely presented here.

The co-polymerization of butadiene and styrene to create the soft S/B middle block of S-S/B-S block copolymers provides an elegant tool (i) to tune the glass transition temperature of the soft S/B phase  $T_{g, S/B}$  and (ii) to control the phase behavior by adjusting the segregation strength  $\chi N$ .<sup>[23,24]</sup> Here, the Flory interaction parameter  $\chi$  describes mainly enthalpic interactions between the inner and outer blocks, and  $N$  denotes the degree of polymerization. Higher styrene-contents in the middle block reduce the interaction between the blocks and, thus, decrease  $\chi$ . The independent control of  $\chi$  and  $N$  enables the possibility to investigate their influence on the morphology and their corresponding (micro-)mechanics in differently segregated systems. Earlier works by the groups of Michler<sup>[23]</sup> and Weidisch<sup>[17,24–26,28]</sup> describe the impact of different macromolecular architectures, like stars, or asymmetric triblock copolymers as well as the influence of the S/B ratio on the phase behavior, morphology and mechanical behavior. Most of these studies deal with differently segregated systems and focus on the influence of the initial morphology on the macroscopic properties. Detailed investigations on the deformation mechanism, which describes the development of the morphology during deformation in systems with soft S/B blocks were carried out by Michler *et al.* using TEM investigations during deformation, which is reviewed in Ref.<sup>[23]</sup>. Although TEM during stretching represents a suitable technique to investigate the deformation mechanism, it has some limitations:

- (i) The probed volume by TEM is very little and, hence, the question arises, if the observed features are representative for the whole sample.
- (ii) For the TEM measurements, the samples have to be very thin, typically 10 to 100 nm. This is in the range of the microphase-separated block copolymer morphology and, thus, it is questionable if similar effects can be observed in the bulk material.
- (iii) Due to the small contrast of the electron-density between the hard and soft phase, staining with OsO<sub>4</sub> is required, which might influence the deformation behavior.

A complementary method to investigate the deformation mechanism of microphase separated polymers is small angle X-ray scattering (SAXS). The probed volume is defined by the size of the beam ( $\approx 1 \text{ mm}^3$ ) and no staining is necessary.

In the presented study, the impact of the S/B ratio on the morphology and the deformation mechanisms at similar segregation strengths  $\chi N$  was investigated. Two symmetric S-S/B-S, LN50 and LN70, were provided by the BASF SE. The polymers consisted of two PS outer blocks (each 20 wt.%) and a S/B copolymer middle block (60 wt.%). The styrene contents in the S/B middle block were 50 wt.% and 70 wt.% styrene in the case of LN50 and LN70, respectively. In order to reach similar segregation strengths of  $\chi_{\text{eff}} N \approx 30$ , the degree of polymerization  $N$  was adjusted. The following methods were used to investigate LN50 and LN70. Transmission electron microscopy (TEM) of stained ultra-thin sections



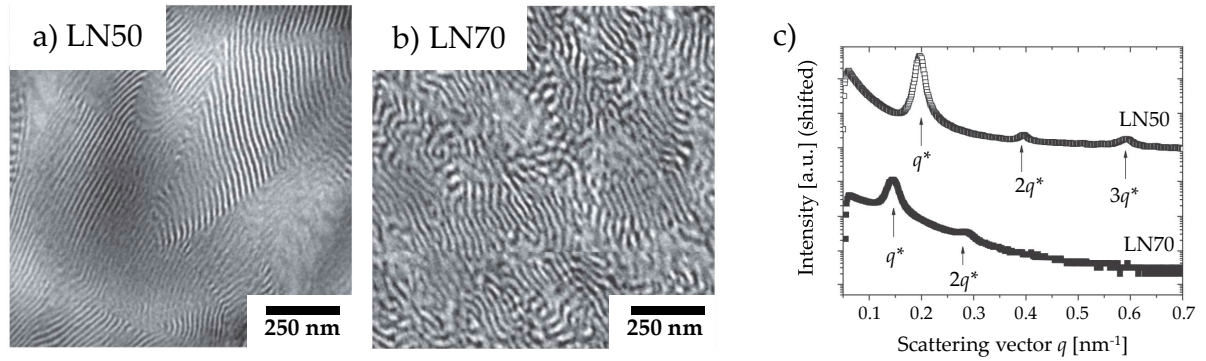


**Figure 1:** TEM micrographs of a) LN50 and b) LN70, stained with  $\text{OsO}_4$ . c) SAXS curves of the unstretched polymers, shifted for better visibility. TEM and SAXS indicate lamellar morphologies with different degrees of long-range order. Reprinted from Ref.<sup>[27]</sup>, by permission of Elsevier.

and small-angle X-ray scattering (SAXS) were used to investigate the initial morphology of LN50 and LN70. The tensile tests were performed, in order to study their mechanical behavior. Moreover, the morphological development under tension, which provides information on the deformation mechanism of these polymers, was investigated by synchrotron SAXS during online-deformation. This was carried out at the synchrotron beamline BW4 at HASYLAB (DE-SY, Hamburg) with a wavelength of  $\lambda = 0.138$  nm, an exposure time of 120 s and a sample to detector distance of 4024 mm. Online deformation was realized with a home-made stretching apparatus. To ensure that the beam exposes the actually deformed volume, waisted tensile bars were used. Image processing, including background correction and exposure time normalization was performed, using ImageJ.<sup>[29]</sup> The long periods  $l_{p,0} = 2\pi/q^*$  were calculated from the first order reflex  $q^*$ . The respective deviations were estimated from the full width at half maximum value (FWHM) of the reflex.

Figure 1 shows the results of the morphological investigations of the unstretched polymers. Lamellar morphologies were found for LN50 and LN70 by TEM measurements and could be confirmed by SAXS, as indicated by the occurrence of higher order reflexes at integer ratios of  $q^*$ .<sup>[7]</sup> LN70 obtains a significantly higher long period of  $l_{p,0} = 43 \pm 3.5$  nm compared to LN50 ( $l_{p,0} = 32 \pm 1.0$  nm), due to its higher molar mass.

Significant differences were found in the mechanical behavior, as can be seen in the stress-strain diagram in Figure 2. The curve of the plot can be divided for both polymers into three regimes:

- (i) **Linear visco-elastic regime** (small deformations,  $\epsilon \lesssim 5\%$ ): Here the deformation is mainly reversible.
- (ii) **Necking and cold drawing** ( $\epsilon \gtrsim 10\%$ ): Leads to irreversible deformations. Necking of the material is characterized by a drop of the stress-strain curve. This is followed by cold drawing, which is indicated by a stress-plateau.
- (iii) **Strain hardening**: After cold drawing, the stress increases again until the material breaks.

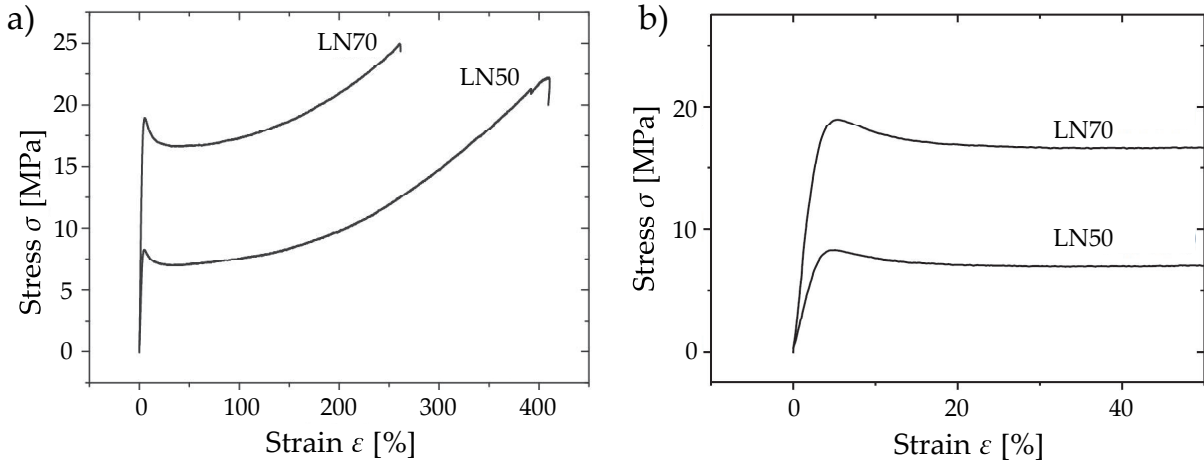


**Figure 2:** Stress-strain diagrams of LN50 and LN70. a) Complete curve. b) Magnification of the curves at low strains. Higher styrene-content in the middle block leads to increasing yield stress, a higher  $E$ -Modulus as well as decreasing strain at break. Adapted from Ref.<sup>[27]</sup>, by permission of Elsevier.

With higher styrene contents in the S/B middle block, the  $E$ -Modulus and yield stress were significantly increasing, while the strain at break was decreasing from 400 to 250%. The overall tensile strength, however, remains on a similar level.

Exemplary 2D-SAXS patterns are given in Figure 3 of (i) the initial state, (ii) in the cold drawing region, (iii) during strain hardening and (iv) before the break. It is obvious that the pattern look dissimilar, which points to different deformation mechanisms.

In Figure 3 (a–d), LN50 shows a four-point scattering pattern upon stretching, which is commonly accepted to result from the formation of chevrons.<sup>[23,30–32]</sup> This can be described by lamellae undulating during stretching into a zick-zack pattern. Further deformation is carried out by tilting of the undulated lamellae, which is described by:<sup>[27,31,32]</sup>

$$1 / \cos(\alpha) = a \cdot (1 + \epsilon_{M,x}) \quad (1)$$

Here,  $\alpha$  is the inclination angle between the undulated lamellae that was extracted from the 2D-SAXS pattern and  $\epsilon_{M,x}$  is the macroscopic strain in stretching direction. The factor  $a$  can be interpreted as a parameter that describes the influence of lamellae tilting on the overall deformation process; in the case of affine tilting, it can be roughly estimated to be  $\sqrt{2}$  for initially unoriented samples.<sup>[27]</sup> However, a detailed investigation of the morphological development of LN50 during stretching leads to (i) significantly lower values of  $a$  and (ii) to the finding that  $a$  is a function of the actual strain. The influence of lamellae tilting is systematically decreasing with increasing strain and the corresponding values for the parameter  $a$  are  $a_1 = 0.42$  during cold drawing ( $30\% \leq \epsilon_{M,x} \leq 80\%$ ),  $a_2 = 0.22$  at  $80\% \leq \epsilon_{M,x} \leq 180\%$  and  $a_3 = 0$  in the strain hardening regime ( $\epsilon_{M,x} \geq 180\%$ ). It could be found that the contribution of lamellae tilting on the overall microscopic deformation is only  $\epsilon_{\text{tilt}} \approx 45\%$ . Thus, the microscopic deformation behavior of LN50 cannot only be described by chevron formation and lamellae tilting.

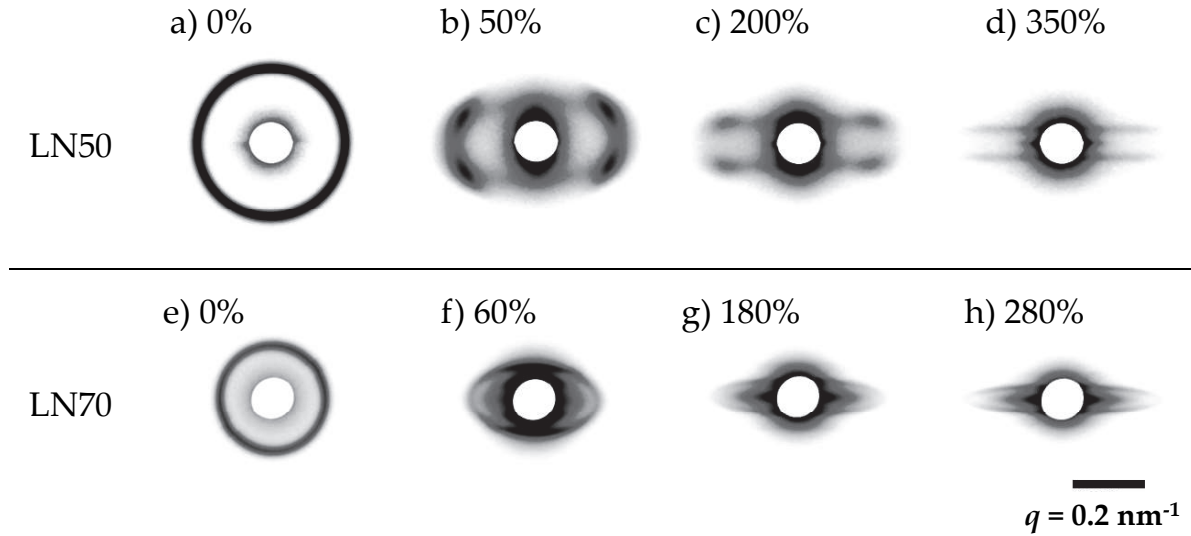


**Figure 3:** 2D-SAXS pattern of LN50 (a–d) and LN70 (e–h). The numbers denote the actual strain and the scale bar represents  $q = 0.2 \text{ nm}^{-1}$ . The intensity is plotted in linear scale and is increasing from white to black. The stretching direction is vertical. Adapted from Ref.<sup>[27]</sup>, by permission of Elsevier.

A second proposed deformation mechanism is the triaxial deformation of the domains, in the ideal case leading to affine deformation, where the microscopic strain  $\epsilon_{\mu,x}$  equals the macroscopic strain  $\epsilon_{M,x}$ . The dependence of  $\epsilon_{\mu,x}$  on  $\epsilon_{M,x}$  is plotted for LN50 in Figure 4a. The meridional streaks, that were exemplary given in the Figures 3 (b–d), were used to estimate the long-period in stretching direction during deformation ( $l_{p,i}$ ). From that, the microstrain  $\epsilon_{\mu,x} = (l_{p,i} - l_{p,0})/l_{p,0}$  could be calculated. It was found that the microstrain in stretching direction is higher than the measured macroscopic strain. This was interpreted as the influence of lamellae tilting, because the above-average increase of the strain is in particular pronounced at lower deformations and the offset between pure triaxial deformation (black dotted line) to the data points is close to the overall contribution of lamellae tilting (45%).

Moreover, it was tested if the obtained microstrain behavior in stretching direction can be described by triaxial deformation and the additional contribution of lamellae tilting. For this purpose, the prefactor of  $\epsilon_{M,x}$ , which is 1 for affine deformation, was modified by adding the parameter  $a_i$  of the relating deformation regime, which describes the additional contribution of lamellae tilting. Furthermore, microstrain-offsets were appended, to obtain a continuous function. This leads to Equation 2 (displayed in Figure 4a as red line).

$$\epsilon_{\mu,x}(\epsilon_{M,x}) = \begin{cases} (1 + a_1) \cdot \epsilon_{M,x} & \text{for } 0\% \leq \epsilon_{M,x} \leq 80\% \\ (1 + a_2) \cdot \epsilon_{M,x} + \epsilon_{\mu,x}(80\%) & \text{for } 80\% \leq \epsilon_{M,x} \leq 180\% \\ (1 + a_3) \cdot \epsilon_{M,x} + \epsilon_{\mu,x}(180\%) & \text{for } \epsilon_{M,x} \geq 180\% \end{cases} \quad (2)$$

Equation 2 describes the measured data points in a very good manner. Hence, it can be concluded that lamellae undulation and tilting is especially pronounced at low deformations; at higher strains, triaxial deformation is dominating for LN50.

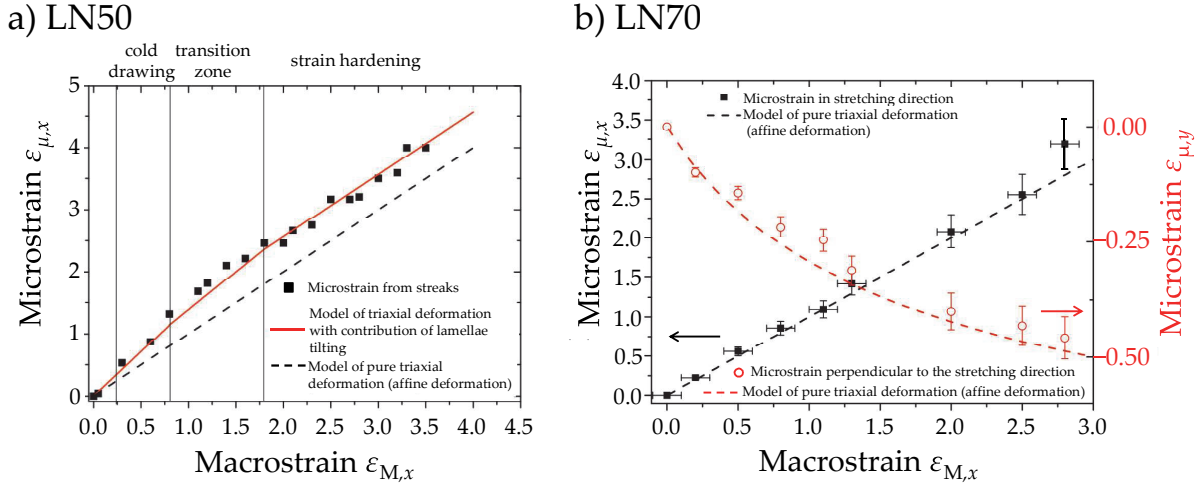


**Figure 4:** Microscopic strain *versus* macroscopic strain. LN50 (a) shows distinct contributions of triaxial deformation; at strains above 180%, the slope is 1, indicating affine deformation. Adapted from Ref.<sup>[27]</sup>, by permission of Elsevier.

A different deformation mechanism was observed for LN70, which has a significantly higher styrene-content in the S/B middle block. Selected 2D-SAXS pattern of LN70 during deformation are given in Figure 3 (e–h). The initial ring transforms upon loading into an ellipse, where the minor semi-axis is located in stretching direction. The decreasing scattering vector  $q^*$  in stretching direction points to increasing long-periods during elongation from initially  $l_{p,0} = 43$  nm to  $l_{p,20\%} = 52$  nm at a strain of  $\epsilon_{M,x} = 20\%$ . The elliptical shape of the 2D-SAXS pattern remains until the specimen broke, which indicates an affine deformation behavior. In order to prove this, the  $q^*$  ellipses in the 2D-SAXS pattern were fitted and extracted values of the semi-axes were used to calculate the microstrain in stretching direction ( $\epsilon_{\mu,x}$ ) and perpendicular to it ( $\epsilon_{\mu,y}$ ). The values were then plotted against the macroscopic strain  $\epsilon_{M,x}$ , which is displayed in Figure 4b. The curves for ideal affine deformation parallel ( $\epsilon_{\mu,x} = \epsilon_{M,x}$ ; black, dotted line) and perpendicular (red, dotted line) to the stretching direction are also given in this plot. The latter can be described by:

$$\epsilon_{\mu,y} = \sqrt{\frac{1}{(\epsilon_{M,x} + 1)}} - 1 \quad (3)$$

under the assumption of incompressibility.<sup>[27]</sup> Both curves approximate the measured data points in a very good manner, which is a clear indication for an affine deformation behavior within this sample. Thus, the triaxial deformation is dominating the micro-mechanical behavior of LN70. The four-point pattern, which was observed in LN50 and is typical for lamellae-forming block copolymers, was absent.

The different micro-mechanical behavior might be explained by theoretical considerations of Rachela and co-workers.<sup>[33]</sup> Undulation and lamellae tilting are expected to require less energy to deform upon stretching than the triaxial deformation.<sup>[33]</sup> Hence, the absence of this low-energy deformation mechanism in LN70 provides one explanation for the higher stress-strain curve, compared to LN50.

The absence of chevron formation in LN70 is expected to result from the higher styrene-content in the soft S/B middle block. The most important reasons are:

- (i) Smaller grain sizes: As shown in Figure 1, LN70 obtains a reduced long-range order compared to LN50, which hinders the cooperative lamellae undulation that is necessary to form chevrons.<sup>[32]</sup> In other words, lamellae tilting is expected to be easier in long-range ordered systems.
- (ii) The stiffness contrast between the soft S/B-phase and the styrenic outer blocks is decreasing with higher styrene fractions in the middle block. As predicted by Castañeda *et al.*,<sup>[33]</sup> there is a transition from »shear-along the layers« (*i.e.* lamellae tilting in the presented study) to triaxial deformation, when the stiffness contrast between the hard and soft phase reaches a critical value.

From these observations it can be concluded that the styrene content in the middle block not only enhances the ability of the material to carry higher stresses during stretching. It also directly influences the deformation mechanism of the polymer, which is crucial for the mechanical behavior and, thus, the possible applications.



### 3 Tailoring morphology and mechanical behavior by blending of olefin copolymers

Parts of this chapter have been published: [P3] S. Hölzer, M. Menzel, Q. Zia, U.S. Schubert, M. Beiner, R. Weidisch, *Polymer* **2013**, *54*, 5207–5213; [P4] A. Teichler, S. Hölzer, J. Nowotny, J. Perelaer, S. Hoeppe-ner, F. Kretschmar, C. Bader, M. D. Hager, U. S. Schubert, *ACS Comb. Sci.* **2013**, *15*, 410–418.

As presented in Chapter 2, the variation of the macromolecular architecture offers an effective tool to adjust the mechanical behavior of polymers. However, many polymers, in particular those with more sophisticated macromolecular architectures, are not easily accessible in the large scales that are necessary for commercial usage because the improved properties do often not justify the higher costs of an advanced synthesis method. Thus, there is only a limited range of polymers available which can fulfill the demanding material properties in future. Common practical solutions to satisfy these requirements are compounding and blending, *i.e.* the addition of additives, fillers or other polymers. Understanding the interplay between the different components is of high interest, but, due to the nature of a multi-phase system, often not easily accessible. This counts not only for the here-in focused mechanical behavior; a prominent example of actual research are polymer-based bulk-heterojunction solar cells, where the distribution of active polymer as electron donor and PC<sub>61</sub>BM<sup>b</sup> as acceptor material strongly defines the overall efficiency of the organic photovoltaics.<sup>[34,35]</sup> More details on this topic are provided in [P4].

In the present study, blends of two poly(ethylene-*co*-octene) copolymers (EOCs), differing in their macromolecular architecture, have been investigated. These polymers belong to the class of linear-low density polyethylenes (LLD-PEs), where the co-polymerization with 1-octene is used to adjust the optical and mechanical properties.<sup>[36–38]</sup> Typical applications are foils in the packaging sector, tubings or geomembranes.

The production of olefin copolymers on an industrial scale has long been limited to olefin random copolymers (ORC). However, recently, the new chain shuttling synthesis<sup>[39]</sup> allows the production of olefin block copolymers (OBC) in an application-relevant scale. Two catalysts with different octene selectivities are used to synthesize blocks with either a low octene content and, thus, a high crystallinity or blocks with a high octene content and very low crystallinities. Moreover, a chain shuttling agent enables to exchange the blocks from one catalyst to the other and *vice versa*, leading to a multiblock architecture. The macroscopic properties of these olefin block copolymers can be adjusted by (i) the selected catalysts, which influence

---

<sup>b</sup> Phenyl-C61-butyric acid methyl ester

**Table 1:** Molecular information of the investigated olefin copolymers.

Material	$M_w$ [kg/mol]	PDI -	Octene content [mol%]
Olefin Block Copolymer (OBC)	124	2.1	12
Olefin Random Copolymer (ORC)	111	2.1	12

the octene level in the blocks and (ii) the chain shuttling level, which controls the block length distribution within the multiblock copolymer.<sup>[39–43]</sup>

In this chapter, the thermal, mechanical and morphological behavior of blends composed of (i) an olefin random copolymer (ORC) and (ii) an olefin block copolymer (OBC), having similar overall octene contents are presented.

Both polymers were provided by The DOW Chemical Company. Molecular data of the components is given in Table 1, as received from the supplier. The names that were given to the ORC:OBC blends ( $Rxx$ ) reflect the fraction of ORC in wt.%, *e.g.* R25 consists of 25 wt.% ORC and 75 wt.% OBC. The blends were prepared by melt-mixing in a miniextruder and compression molding at 200 °C. During molding, the blends were subjected to a pressure of 30 N/cm<sup>2</sup> and cooled to room temperature with a rate of 40 °C/min. Prior to the investigations, the samples were stored at room temperature for at least 2 weeks. Calorimetric measurements were performed at temperatures between  $-50\text{ °C} \leq T \leq 150\text{ °C}$  with heating and cooling rates of 10 °C/min. The crystallinity of the samples was calculated from the ratio of the measured melting enthalpies  $\Delta H_m$  to melting enthalpy of a perfect PE crystal ( $\Delta H_{m,PE} = 290\text{ J/g}$ ).<sup>[41]</sup> Dynamic mechanical analysis (DMA) was carried out in tension mode between  $-100$  and  $50\text{ °C}$  with a heating rate of 2 °C/min, a strain amplitude of 0.5% and a measurement frequency of 1 Hz. Tensile tests were performed according to DIN EN ISO 527 on at least five dog-bone specimens. The initial gauge length was 28 mm and the crosshead speed was held constant at 28 mm/min. For atomic force microscopy (AFM), small areas of the compression molded plates were trimmed with a cryo-ultramicrotome at a temperature of  $-100\text{ °C}$  to minimize the irreversible deformation of the morphology. AFM was performed in tapping mode, using super sharp silicon tips with tip radii  $\leq 2\text{ nm}$ . Wide-angle X-ray Scattering (WAXS) experiments were carried out, using  $\text{CuK}\alpha$  radiation ( $\lambda = 1.54\text{ \AA}$ ) and a sample to detector distance of 124 mm.

The thermal and calorimetric properties were investigated by DSC measurements. The first DSC heating runs of ORC and OBC and their blends are given in Figure 5. The first endotherm can be found at temperatures between 30 and 80 °C and has been attributed to the melting of ORC rich crystals. This peak has a bimodal shape, which originates from different thicknesses of crystalline lamellae (Gibbs-Thomson effect). The second melting peak is found at a temperature of about 120 °C and is ascribed to the melting of OBC crystals. The dotted line plots the PE lamellae thickness *versus* the respective melting point according to the Broadhurst equation.<sup>[44]</sup> Based on that, the PE lamellae thickness within the blends was estimated, being 2 to 4 nm for the ORC and 10 to 20 nm for the OBC crystals. A detailed analysis in (Figure 5b)



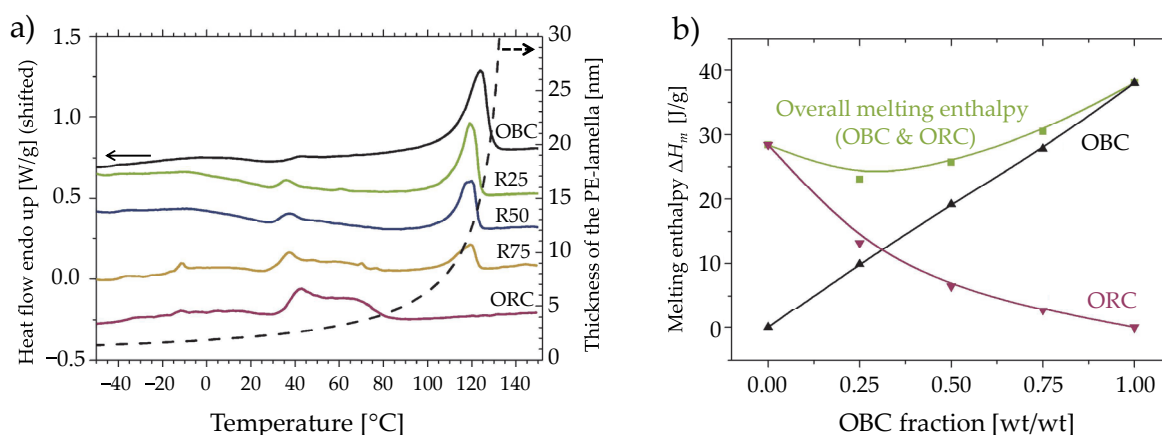


**Figure 5:** Thermal behavior of ORC, OBC and their blends: a) First heating curves together with dependence of the melting point and the PE-lamella thickness according to the Broadhurst equation.<sup>[44]</sup> The DSC curves are shifted for better visibility. b) Enthalpy of the low ( $\blacktriangledown$ ) and high ( $\blacktriangle$ ) melting temperature peaks *versus* the OBC fraction. Adapted from Ref.<sup>[45]</sup>, by permission of Elsevier.

reveals that the melting enthalpy of the high-temperature endotherm is linearly increasing with the OBC fraction. For the low temperature peak, however, the melting enthalpy is nonlinearly decreasing. This effect can be explained by constrained crystallization of ORC chains in an already semi-crystalline matrix during cooling. Moreover, this points to a homogeneous amorphous matrix, since the crystallization can only be hindered if the OBC and ORC chains are mixed. The occurrence of a homogeneous matrix was approved a single dynamic glass transition temperature in dynamic-mechanical measurements within the blends.<sup>[45]</sup>

In order to describe the mechanical behavior of ORC, OBC and their blends, tensile tests were performed. Representative stress-strain curves are given in Figure 6a. At small strains,  $\epsilon \leq 50\%$ , the mechanical behavior of the blends differs only slightly. However, distinct differences become observable at higher strains. It turns out that the mechanical properties can be systematically changed by the blend composition. Higher OBC contents lead to a more elastomeric material behavior, marked by decreasing 300% secant moduli, a higher onset for strain hardening and increasing strain at break, as shown in Figure 6b. Interestingly, the tensile strength is only slightly affected by the blend composition, which indicates synergistic effects due the bimodal crystalline network that is formed from the individual ORC and OBC crystals.<sup>[46,47]</sup> Thereby, the blocky architecture of OBC results in (i) thick but rare crystals and (ii) long, flexible chain segments that can be easily stretched upon deformation. In contrast, ORC crystallizes in thinner, but well distributed crystals between shorter flexible chain segments.

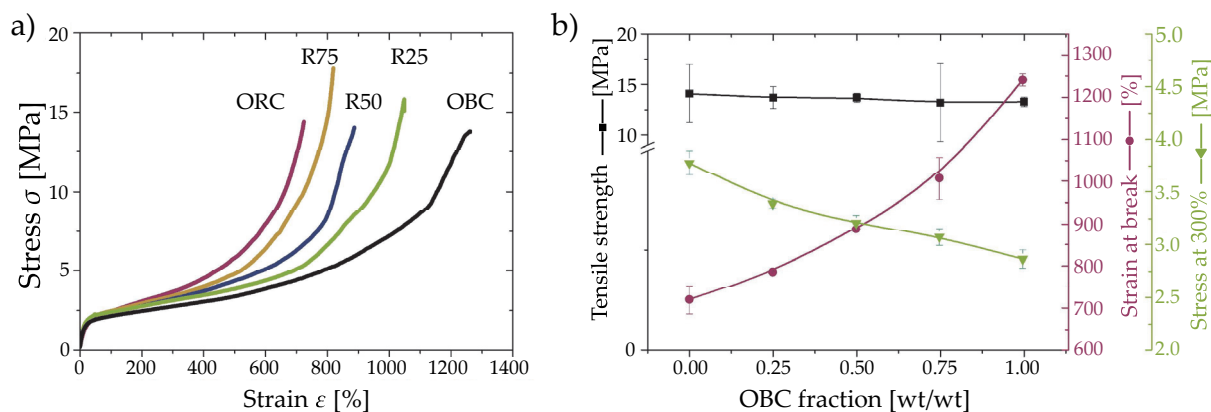


**Figure 6:** Mechanical behavior of ORC, OBC and their blends. a) Typical engineering stress-strain curves. b) Important mechanical properties in dependence of the OBC content. Adapted from Ref.<sup>[45]</sup>, by permission of Elsevier.

Morphological studies of the olefin copolymers and their blends were carried out by AFM and WAXS. Figure 7 shows AFM phase contrast images of the investigated materials. OBC and blends with high OBC fractions reveal needle-like features. The observed average thickness of these crystals ( $14 \pm 4$  nm)<sup>c</sup> is in a fair agreement with the estimated PE-lamellae thickness of the OBC crystals, based on the DSC melting temperatures (Figure 5). As a consequence, these *needles* are attributed to the crystals formed by OBC chains. In R25, the concentration of the thicker crystals is decreasing — a trend that systematically propagates with increasing ORC contents until the thicker crystals are not observed anymore (Figure 7e). A detailed study of the ORC crystals in these AFM images is hard, because the size of the ORC crystals (2 to 4 nm) is close to the radius of the AFM tip ( $\leq 2$  nm) and, hence, they cannot be clearly resolved by this technique. However, a network-like morphology can be observed in ORC. The micrographs of the blends basically obtain features of the single polymers, which is in agreement with the results from DSC.

WAXS measurements were carried out to study the crystal structure of the samples. Bragg reflexes were found at  $2\theta \approx 20.6^\circ$  and  $23.0^\circ$ . These were attributed to the (110) and (200) reflections of orthorhombic PE. Moreover, it is obvious that the sharpness of the peaks differs, *i.e.* the full width at half maximum value (FWHM) is significantly smaller for the olefin block copolymer OBC. According to the Scherrer equation, this value is inverse proportional to the size of the crystal.<sup>[48]</sup> Therefore, an orthorhombic lattice is expected for ORC, OBC and their blends, whereas the crystals formed by ORC are significantly thinner. Note that hexagonal reflections were not observed, as reported elsewhere<sup>[42,49]</sup> for a random EOC.

Summarizing the results of DSC as well as morphological and mechanical investigations, it can be concluded that the ORC:OBC blends exhibit three distinct phases:

- (i) *Thicker crystals*, originating from the long methylene sequences of the OBC chain segments with a very low octene content. These are packed in an orthorhombic lattice with a lamellae thickness of 10 to 20 nm and a peak melting temperature of about  $T_m \approx 120^\circ\text{C}$ .

<sup>c</sup> as estimated from at least 50 individual crystals.

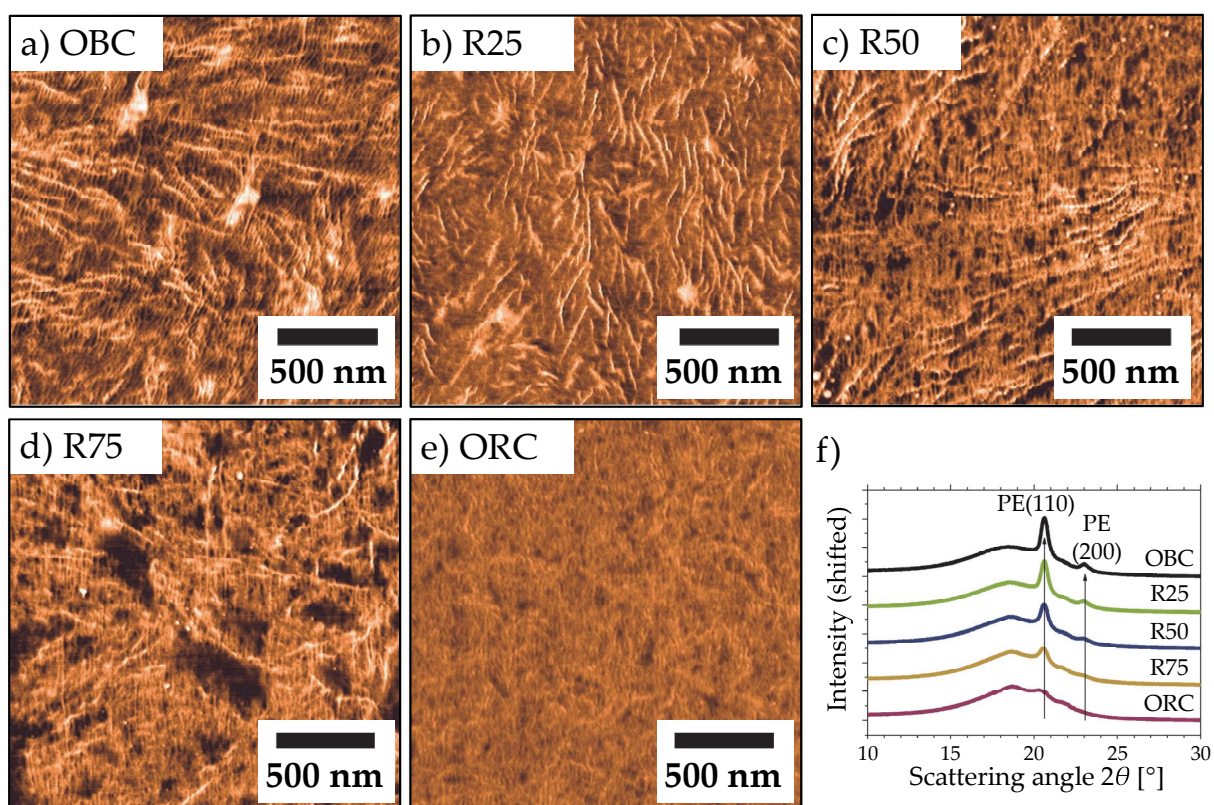


**Figure 7:** AFM tapping mode phase images of a) OBC, e) ORC and their blends (b–d). The scale bar represents 500 nm. f) WAXS curves of the same samples, which are shifted for better visibility. The observed peaks are attributed to the (110) and (200) reflections of orthorhombic PE. Adapted from Ref.<sup>[45]</sup>, by permission of Elsevier.

- (ii) *Thinner crystals*, with a thickness of 2 to 4 nm ( $30\text{ }^{\circ}\text{C} \leq T_m \leq 80\text{ }^{\circ}\text{C}$ ) that can be attributed to the crystallization of ORC chain segments. In the blends, the crystallization of these crystals seems to be constraint by the already formed *thicker crystals*.
- (iii) *Homogeneous amorphous phase*, which is indicated by (i) the hindered ORC crystallization, as expected from the low melting enthalpies and (ii) a single dynamic glass transition that was observed by dynamic-mechanical analysis (data not shown, c.f. [P3].)

The proposed deformation mechanism of this morphology can be imagined as follows. Firstly, upon stretching, the thinner ORC crystals were plastically deformed, due to the finite chain extensibility of the short flexible ORC chain segments. This results in higher repulsive forces due to entropy elasticity. This theory is also supported by *in situ* synchrotron SAXS investigations by the group of Hsiao.<sup>[42]</sup> Although the composition of their olefin random and block copolymers differs slightly from the materials investigated here, it is assumed that their findings are generally transferable. In their study, the increasing FWHM of the (110) reflection during stretching indicated decreasing crystal sizes. Hsiao and co-workers explained this by a fragmentation of the ORC crystals. This process was more pronounced for ORC at small strains ( $\epsilon \leq 100\%$ ), as indicated by a relative increase of FWHM of  $\approx 30\%$ , compared to less than 10% in the case of OBC.<sup>[42]</sup> Since this fragmentation process requires energy, this is accompanied with an increase of stress in Figure 6a. In the case of OBC, the fragmentation process starts at higher deformations, due to its longer, flexible chain segments. This directly results in a shift of the strain hardening onset to higher elongations. Moreover, the longer flexible chain segments obtain a higher chain extensibility, which is an explanation for the increasing strain at break in OBC.

The results show that the mechanical behavior of ORC:OBC blends can be systematically controlled by the composition, without changing the overall octene content of the system. Moreover, this underlines the influence of the crystallinity and morphology on the macroscopic properties of polymeric systems.

## 4 Controlling structure and morphology of semi-crystalline copolymers by annealing

Parts of this chapter have been or will be published: [P5] O. Pabst,<sup>d</sup> S. Hölzer,<sup>d</sup> E. Beckert, J. Perelaer, U. S. Schubert, R. Eberhardt A. Tünnermann, *Org. Electron.* **2014**, 15(11), 3306–3315; [P6], S. Hölzer, T. N. Büttner, R. Schulze, M. M. L. Arras, F. H. Schacher, K. D. Jandt, U. S. Schubert, *Eur. Polym. J.*, *in press*. DOI:10.1016/j.eurpolymj.2015.04.010; [P7] R. Schulze, M. M. L. Arras, C. Helbing, S. Hölzer, U. S. Schubert, T. F. Keller, K. D. Jandt, *Macromolecules* **2014**, 47, 1705–1714.

The previous chapters dealt with the tuning of the mechanical behavior by (i) improving the macromolecular architecture and (ii) blending of different polymers. It was discussed that the morphology plays a crucial role in order to understand the relationship between structure and the macroscopic property-profile. Other possibilities to the well-directed modification of the morphology are the selected processing conditions of the material. Prominent examples in this field are:

- Changing of the block copolymer morphology, using different solvents.<sup>[50,51]</sup>
- Crystallization<sup>[52]</sup> or orientation<sup>[53]</sup> induced by shearing, due to extrusion, injection molding or fiber spinning.
- Crystallization effects due to different cooling rates.<sup>[8,54,55]</sup>
- Annealing the semi-crystalline<sup>[56]</sup> or block copolymer morphologies.<sup>[57,58]</sup>

In the following two sections, studies related to the last mentioned point are introduced. Annealing treatments near the melting point have been carried out on (i) a piezoelectric poly(vinylidene fluoride-*co*-trifluoroethylene) (P(VDF-*co*-TrFE)) and (ii) a semi-crystalline polybutadiene-*block*-poly(ethylene oxide) (PB-*b*-PEO). Annealing changed in both cases the semi-crystalline morphology. In case of the P(VDF-*co*-TrFE) this coincides with an improved electro-mechanical behavior and, in the case of PB-*b*-PEO, the defect healing of the PEO crystals systematically increased the long-period, which offers an elegant tool to tune its self-assembled block copolymer morphology, which might be interesting for, *e.g.* block copolymer-based photonic crystals.<sup>[59,60]</sup>

---

<sup>d</sup> O. Pabst and S. Hölzer contributed equally to this manuscript.

#### 4.1 Improving the electro-mechanical behavior of inkjet-printed Poly(vinylidene fluoride-*co*-trifluoroethylene)

Poly(vinylidene fluoride-*co*-trifluoroethylene) (PVDF-TrFE) belongs to the class of semi-crystalline, piezoelectric polymers that induce an electrical field due to a mechanical stress, or *vice versa*.<sup>[61]</sup> In contrast to their inorganic counterparts, they offer several advantages, such as low processing temperatures or mechanical flexibility. Moreover, it is possible to process them with solution-based techniques, like inkjet-printing.<sup>[62]</sup> However, the electro-mechanical properties, expressed by the piezoelectric coefficient  $d_{31}^e$  are relatively low, which currently limits the application range of P(VDF-*co*-TrFE) as material for sensor and actuator applications.<sup>[63]</sup>

In the presented study, an inkjet-printed P(VDF-*co*-TrFE) film should be used as an actuator material in a micropump for microfluidic chips.<sup>[64]</sup> In order to increase the pump rate, the electro-mechanical behavior of P(VDF-*co*-TrFE) had to be improved. Fortunately, this material system has been studied in great detail during the last decades, due to its fascinating properties as well as high commercial interest. A recently published article<sup>[63]</sup> reviews the advances in this material system.

Four crystalline modifications are known for P(VDF-*co*-TrFE). The  $\beta$ -phase, where the chains arrange in an all-*trans* configuration, obtains the best piezoelectric performance.<sup>[65]</sup> Its stability depends strongly on the trifluoroethylene content within the polymer; an optimum was found between 25 wt% and 30 wt% trifluoroethylene.<sup>[66]</sup> Moreover, it is known that there is a strong influence of the thermal,<sup>[67]</sup> mechanical,<sup>[68]</sup> and electrical<sup>[69]</sup> history of the polymer on its electro-mechanical performance. However, the studies are basically limited to bulk material or thin films produced by spin coating or drop casting. There is little information about the structure and morphology of inkjet-printed P(VDF-*co*-TrFE) films, which are known to show different morphological features than the other, mentioned solution processing techniques<sup>[70]</sup> and, hence, are supposed to obtain different electro-mechanical properties. Therefore, the influence of annealing on the printed P(VDF-*co*-TrFE) films on the morphology and the resulting device performance was investigated.

Commercial P(VDF-*co*-TrFE) was supplied by Solvay Specialty Polymers and has a VDF:TrFE ratio of 70:30 wt.%. To use this material as an actuator, the  $\approx 9 \mu\text{m}$  thick, inkjet-printed polymer film was sandwiched between two metal electrodes, which were printed from commercial silver nanoparticle inks. The substrate was a PET sheet with an upper working temperature of approximately 140 °C. The specimens for electro-mechanical deflection and ferroelectric hysteresis tests were prepared in a similar manner. A detailed description of the printing process can be found in Ref.<sup>[64]</sup>. After manufacturing, the films were annealed in a convection oven for 24 h at temperatures between 95 to 145 °C with heating and cooling rates of 0.8 °C/min. Moreover, the influence of an additional plasma treatment was investigated, which was carried out to improve the conductivity of the printed metal electrodes. The piezoelectric coefficient

<sup>e</sup> The piezoelectric tensor  $d_{i,j}$  is a  $(3 \times 6)$  tensor that is defined as the electric polarization generated in direction  $i$  per unit mechanical stress in the area  $J$ . The most important coefficient,  $d_{31}$ , describes the electrical polarization generated perpendicular to the direction of the mechanical stress.<sup>[61]</sup>

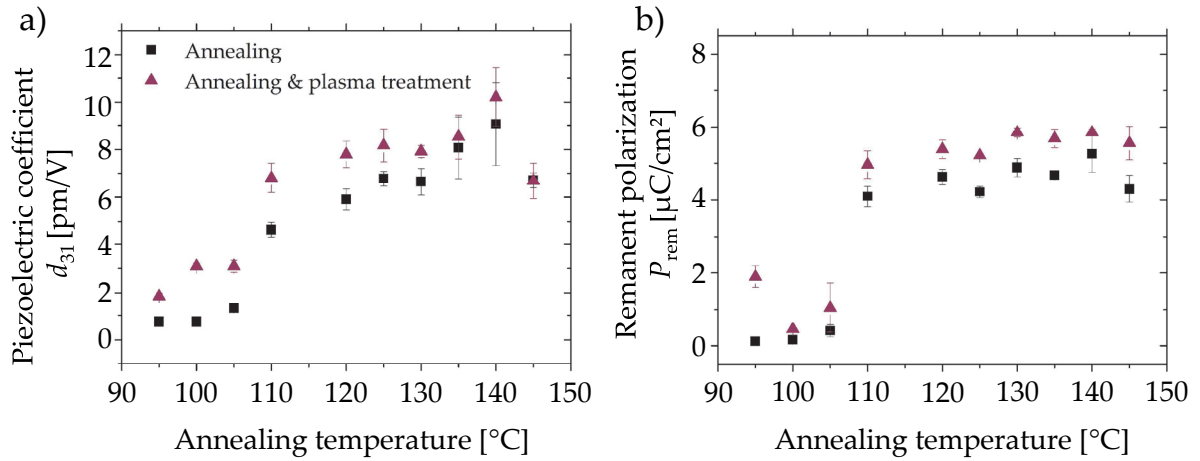


**Figure 8:** Electro-mechanical properties after different *post*-printing treatments (■...annealing; ▲...annealing and subsequent plasma treatment). a) Piezoelectric coefficient  $d_{31}$ . b) Remanent polarization  $P_{rem}$ . Adapted from Ref.<sup>[71]</sup>, by permission of Elsevier.

$d_{31}$  was derived from static deflection tests, using a laser triangulation sensor, while driving voltages of 400 V were applied.<sup>[64]</sup> The values of the remanent ( $P_{rem}$ ) and the maximum polarization ( $P_{max}$ ) were calculated from the deflection tests, where maximum voltages of 600 V and a frequency of 0.05 Hz were applied. Further details are provided in [P5].

Structural and morphological investigations have been carried out at selected annealing temperatures  $T_a$  of 95, 135 and 145 °C, after printing the film on a metalized glass slide (soda-lime glass, sputtered with Ti/Pt/Au). X-ray diffraction was performed on a Bruker D5005 diffractometer using  $\text{CuK}\alpha$  radiation ( $\lambda = 1.54 \text{ \AA}$ ). The morphology of the inkjet-printed samples was studied by AFM in tapping mode, using tips with a radius  $< 10 \text{ nm}$ . DSC was carried out in a temperature range between  $-20$  and  $200 \text{ }^\circ\text{C}$  with heating and cooling rates of  $10 \text{ }^\circ\text{C}/\text{min}$ . For these measurements, the film was carefully removed from the metalized glass slide with a razor blade.

The dependence of the annealing temperature  $T_a$  on the piezoelectric parameters  $d_{31}$  and  $P_{rem}$  are given in Figure 8. One can see that there is a step-wise increase of  $d_{31}$  by a factor of 10 at  $T_a = 110 \text{ }^\circ\text{C}$ . Moreover, increasing  $P_{rem}$  and  $P_{max}$  values were found at this  $T_a$ . The dependence of  $P_{rem}$  is given in Figure 8b and for  $P_{max}$  it is provided in the supplementary content of [P5]. The slightly higher values of the samples with an additional plasma treatment are expected to result from the heat, which is generated during plasma sintering.

In order to understand the reasons for the increasing piezoelectric properties, additional calorimetric, structural and morphological investigations have been carried out to elaborate the structure-property relationships of this system.

The first DSC heating runs of the as-printed and annealed P(VDF-co-TrFE) films are given in Figure 9. The curves show two distinct endothermic peaks with maxima at  $\approx 105$  and  $\approx 150 \text{ }^\circ\text{C}$ . The peak at  $105 \text{ }^\circ\text{C}$  originates from the phase transition of the ferroelectric  $\beta$ -phase into the paraelectric  $\alpha$ -phase, also known as the Curie transformation temperature and the endotherm at  $150 \text{ }^\circ\text{C}$  corresponds to the melting point of the P(VDF-co-TrFE) crystals.<sup>[72]</sup> The

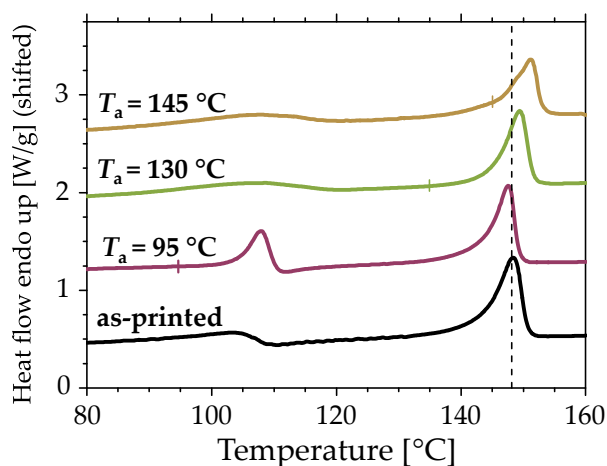


**Figure 9:** First DSC heating runs of the inkjet-printed P(VDF-co-TrFE) films after different thermal treatments. The dashed line represents the peak melting temperature of the as-printed reference sample and the tick point to the maxima of the first endothermic peak. The curves are shifted for better visibility. Adapted from Ref.<sup>[71]</sup>, by permission of Elsevier.

105 °C endotherm is relatively broad in the as-printed reference sample and sharpens after an additional annealing at 95 °C, which is slightly below the observed peak phase transition temperature (Figure 9). This is interpreted as the transformation of chain segments in the crystalline parts of the polymer from *gauche* defects in the all-*trans* configuration during annealing at 95 °C, which is also reported elsewhere for solvent-cast films.<sup>[67]</sup> The results indicate a similar behavior for inkjet printed films. Annealing at higher temperatures of 130 and 145 °C lead to three observations::

- (i) A much broader Curie transition peak is observed compared to the sample annealed at 95 °C. This is somewhat expected, since the applied annealing temperature lies outside of the stability range of the  $\beta$ -phase.<sup>[65]</sup> Instead, the  $\alpha$ -phase is stable, which is known to obtain a *gauche-trans* chain configuration. Thus, the transformation of *gauche*-defects into an all-*trans* configuration is not favorable.
- (ii) The Curie transition temperature slightly shifted to higher temperatures (108 compared to 104 °C in the as-printed reference). That behavior might result from the different crystallization conditions of the samples. In the as-printed films, the crystallization of the polymer is determined by the drying of the inkjet-printed film and, thus, depends on parameters like ink-formulation and printing temperatures. In contrast, the crystallization and phase transition of the samples, which were annealed at 130 and 145 °C is determined by the cooling rate of the system that is applied after annealing. Since that parameter was kept constant at 0.8 °C/min, the observed endothermic Curie transition peaks look similar for, both, the 130 and the 145 °C sample.
- (iii) The second endothermic peak at 150 °C shifted to higher temperatures upon annealing at 130 or 145 °C. Peak melting temperatures of 148.3, 149.4 and 151.1 °C were observed for the as-printed reference, the 130 and the 145 °C sample, respectively. Similar peak



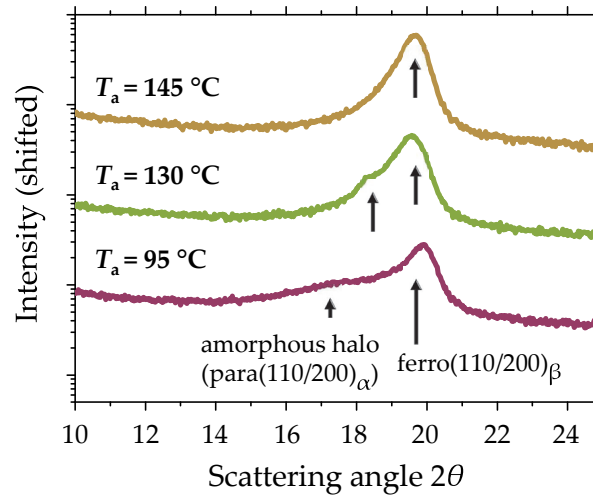


**Figure 10:** XRD curves of the inkjet-printed P(VDF-co-TrFE) films after different annealing temperatures. Adapted from Ref.<sup>[71]</sup>, by permission of Elsevier.

melting temperatures of  $151.8 \text{ }^\circ\text{C} \pm 0.2 \text{ }^\circ\text{C}$  were observed in the second DSC heating run, after erasing the thermal history. Hence, it is assumed that the shift of the melting temperature results from the thermal annealing and is not an error of measurement. Higher melting temperatures point to the formation of larger crystals, commonly described as Gibbs-Thomson effect.<sup>[44]</sup> Moreover, a morphological rearrangement during annealing in the partly molten state might occur, which is also described for other semi-crystalline systems.<sup>[56]</sup>

Figure 10 depicts the results from the XRD measurements. All samples exhibit a distinct Bragg peak at  $2\theta = 19.9^\circ$ , where  $2\theta$  is the scattering angle. This corresponds to spacings of 0.45 nm. The observed peak is attributed to the (110) and (200) reflections of the ferroelectric  $\beta$ -phase, denoted as  $(110/200)_\beta$ .<sup>[73]</sup> A broad halo was observed for the  $95 \text{ }^\circ\text{C}$  sample at  $2\theta \approx 17.1^\circ$ , which is interpreted as scattering from the amorphous phase of the polymer. However, it should be noted that this value is close to scattering angles reported for reflexes of the paraelectric  $\alpha$ -phase,  $(110/200)_\alpha$ ,<sup>[73,74]</sup> which might point to different polymorphic forms of P(VDF-co-TrFE) crystals after annealing at  $95 \text{ }^\circ\text{C}$ .

At higher  $T_a$  (130 and  $145 \text{ }^\circ\text{C}$ ), the intensity of the amorphous halo is significantly decreasing and the  $(110/200)_\beta$  reflex becomes more pronounced. This indicates that the crystals grow during annealing, which leads to the formation of  $\beta$ -crystals after cooling to room temperature. The small shoulder, which is observed at  $130 \text{ }^\circ\text{C}$ , can be explained by the incorporation of the co-monomer trifluoroethylene in the crystal, which causes slight changes in the lattice parameters.<sup>[75]</sup> However, this shoulder was not observed after annealing at  $145 \text{ }^\circ\text{C}$ , while the peak area of the  $(110/200)_\beta$  reflection further increases. The latter is a clear indication for a higher crystallinity after the annealing at this temperature.<sup>[13]</sup>

AFM tapping mode images of the films are given in Figure 11 of the as-printed sample (a) and the films after the annealing treatments (b–d). The as-printed sample obtains rod-like structures with a thickness of  $(21.0 \pm 6.9) \text{ nm}$ , that are frequently reported for P(VDF-co-

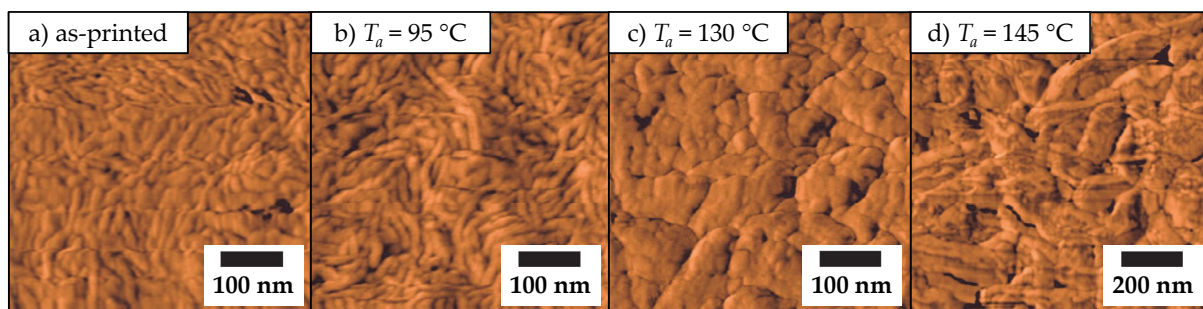


**Figure 11:** AFM phase images for a) the as-printed reference sample and the films after thermal treatment at b) 95 °C, c) 130 °C and d) 145 °C. The scale bar represents 100 nm for the images a) to c) and 200 nm for d), which was taken after annealing at  $T_a = 145$  °C. Adapted from Ref.<sup>[71]</sup>, by permission of Elsevier.

TrFE).<sup>[76,77]</sup> After annealing at 95 °C, similar features were observed, with rod-like domains, having comparable dimension ( $(21.2 \pm 6.9)$  nm).<sup>f</sup> Distinct changes are observed after annealing at 130 and 145 °C, as shown in the Figures 11c and 11d, respectively. Both samples show crystal thickening and the average domain size increases to 63 nm for the 130 °C sample and 138 nm for the 145 °C sample. Moreover, the morphology changes from rod-like to a more globular shape. Hence, it is expected that annealing at this temperature provides sufficient thermal energy to generate far-reaching changes in the overall morphology. The fact that the crystal thickening becomes more pronounced at 145 °C might originate from two circumstances. Firstly, the higher  $T_a$  increase the chain mobility of the polymer and, hence, the defect healing within the crystals is expected to be accelerated. Secondly, the polymer is partly molten at 145 °C (c.f. Figure 9), because smaller P(VDF-co-TrFE) crystals are instable at this temperature. Thus, these either have to melt and crystallize upon cooling or the chains attach to the larger P(VDF-co-TrFE) crystals that obtain a higher melting temperature; a process that is denoted as thermal fractionation.<sup>[56]</sup> Moreover, the presence of partly molten chain segments might further promote an accelerated defect healing, since the system is less constraint and the chains are more flexible. Thermal fractionation and defect healing will be discussed more detailed in Section 4.2.

The presented DSC, XRD and AFM data provide consistent information about the morphological development of the inkjet-printed P(VDF-co-TrFE) films after annealing. Below the Curie transition temperature ( $T_a = 95$  °C), the *gauche*-defects were healed in the already present  $\beta$ -crystals. The topology, however, was unaffected, since the typical rod-like domains are similar to those of the as-printed reference. Annealing between the Curie transition and the onset melting temperature changes the shape of the crystalline domains from rod-like to globular. Furthermore, the peak and the offset melting temperatures increase, which indicates that thicker crystals are formed during annealing (Gibbs-Thomson effect). Unfortunately, only qualitative statements can be given here, since the electrostatic nature of the samples causes interactions with the DSC pan due to their high polarity. Thus, complete thermal contact between sample and pan cannot be assured and, hence, the obtained melting enthalpies that are

<sup>f</sup> as estimated from at least 30 individual objects.

**Table 2:** Electro-mechanical and morphological properties of P(VDF-co-TrFE), after annealing at different annealing temperatures  $T_a$ .

$T_a$ [ °C]	$d_{31}$ [pm/V]	$P_{rem}$ [ $\mu\text{C}/\text{cm}^2$ ]	Morphology	Domain size [nm]
95	$0.8 \pm 0.04$	$0.1 \pm 0.01$	rod-like	$21 \pm 7$
130	$8.0 \pm 0.2$	$5.8 \pm 0.1$	globular	$63 \pm 24$
145	$6.6 \pm 0.4$	$4.3 \pm 0.4$	globular	$138 \pm 62$

necessary to calculate the crystallinity, might be flawed. The estimation from XRD is also difficult, since the amorphous and crystalline scattering contributions can hardly be separated, which hinders the calculation of the absolute crystallinity.<sup>[13]</sup> Higher  $T_a = 145$  °C lead to further crystal thickening, as observed by DSC and larger domains (AFM). Moreover, the XRD measurements point to an increased crystallinity.

The observed morphological changes coincide with significantly higher  $d_{31}$  and  $P_{rem}$ , as summarized in Table 2. The lower piezoelectric properties of the 145 °C sample compared to the 130 °C sample are expected to result from deformations, due to the softening of the PET substrate at temperatures above the upper working temperature of the PET (140 °C), rather than from intrinsic changes within P(VDF-co-TrFE) structure and morphology. For the application as micropump actuator, an annealing temperature of 130 °C was therefore selected, which represents a good compromise between the improved electro-mechanical behavior and the thermal stability of the substrate. A micropump was manufactured, using P(VDF-co-TrFE) annealed at  $T_a = 130$  °C as actuator material. Thereby, pump rates of up to 130  $\mu\text{L}/\text{min}$  were realized, using isopropyl alcohol as test liquid. Further information on the manufactured micropump are given in [P5] and its supplementary information as well as Ref.<sup>[78]</sup>.

From a materials science point of view, the results show that the electro-mechanical properties of P(VDF-co-TrFE) can be effectively tuned by a *post*-printing annealing step above the Curie transition temperature of approximately 110 °C. The importance of understanding the influence of the crystalline structure and morphology of the system on these properties has been emphasized. Further improvement of the system is expected by optimizing the annealing duration. As known for other semi-crystalline polymers, the perfection of crystal rearrangement depends strongly on this parameter, which will be discussed in detail within the next section. Another important parameter is the cooling rate. Recently, Singh *et al.*<sup>[75]</sup> showed that this parameter strongly affects the crystallinity and the morphology of spin-coated P(VDF-co-TrFE) films. High cooling rates were found to increase the crystallinity (as observed by XRD) and remanent polarization as well as to decrease coercivity. An open question is, however, if this effect is only pronounced in thin films ( $\approx 60$  nm in Ref.<sup>[75]</sup>) or if this can be also applied for more bulky films, as employed here for the micropump actuator.

## 4.2 Controlling the Morphology of Semi-crystalline

### Poly(butadiene)-*block*-poly(ethylene oxide) by crystal thickening

In Section 4.1, it was shown how the structure and morphology of a semi-crystalline copolymer and, with that, its electro-mechanical behavior can be improved by annealing close to the melting point. This annealing step increased the degree of crystallinity and the thickness of the crystals.

The polymer, which will be discussed in this section, PB-*b*-PEO, belongs to the class of amorphous-crystalline block copolymers and comprises of an amorphous polybutadiene (PB) and a semi-crystalline poly(ethylene oxide) block (PEO). In contrast to the previously discussed P(VDF-*co*-TrFE), PB-*b*-PEO is able to form a microphase-separated morphology, which depends on the interaction parameter  $\chi$  between the blocks, the degree of polymerization  $N$  as well as the volume fractions of PB and PEO. Moreover, the crystallization process of the PEO block is another influencing parameter. The PB block imposes a soft confinement on the PEO crystallization, since the PB phase is well-above the glass transition temperature  $T_{g,PB} \approx -100 \text{ }^\circ\text{C}$ <sup>[79]</sup> during the PEO crystallization ( $T_{c,PEO} \geq -40 \text{ }^\circ\text{C}$ ).<sup>[80]</sup> As a consequence, break-out crystallization is possible, *i.e.* the morphology that is present in the melt can be transformed during the crystallization process.<sup>[81]</sup> Understanding the mutual relation of the morphology and the crystallization in block copolymers is of great interest, because it provides insights into the crystallization process under variable confinements.<sup>[81–84]</sup>

The crystallizable block offers the possibility to tune the microphase-separated morphology either by a defined isothermal crystallization<sup>[85–88]</sup> or an additional annealing procedure.<sup>[58,89]</sup> A tuneable block copolymer morphology is interesting for potential applications as photonic crystals. Furthermore, due to its amphiphilic nature, the microphase-separated morphology of PB-*b*-PEO is of interest for biomaterials and -analytics, since it can be used to investigate the protein absorption on biomaterials, which represents a key factor for the development of the next generation of implants and sensors.<sup>[58]</sup>

In order to control the morphological development, it is necessary to understand the underlying mechanisms and kinetics. Whereas isothermal crystallization has been widely studied in PB-*b*-PEO,<sup>[85–88]</sup> only little information is known about morphological development during an annealing treatment. Moreover, these studies are currently limited to thin films.<sup>[58,89]</sup> Hence, the mechanisms and kinetics of the morphological development of bulk PB-*b*-PEO, was investigated by time and temperature dependent DSC, SAXS and WAXS.

The molar masses of the PB and the PEO blocks were  $M_{n,PB} = 5200 \text{ g/mol}$  and  $M_{n,PEO} = 3960 \text{ g/mol}$ , respectively. This corresponds to degrees of polymerization of  $N_{PB} = 96$  for the PB block and the  $N_{PEO} = 90$  for the PEO block. In the following, the polymer will be named as B<sub>96</sub>E<sub>90</sub>. In order to create comparable sample conditions, B<sub>96</sub>E<sub>90</sub> was heated to 90 °C, which is well-above the melting temperature and erases the thermal history of the sample. After that, B<sub>96</sub>E<sub>90</sub> was cooled down to 0 °C, with a cooling rate of 10 °C/min. This initial state is referred to as crystalline standard (CS). For the DSC measurements, the investigated

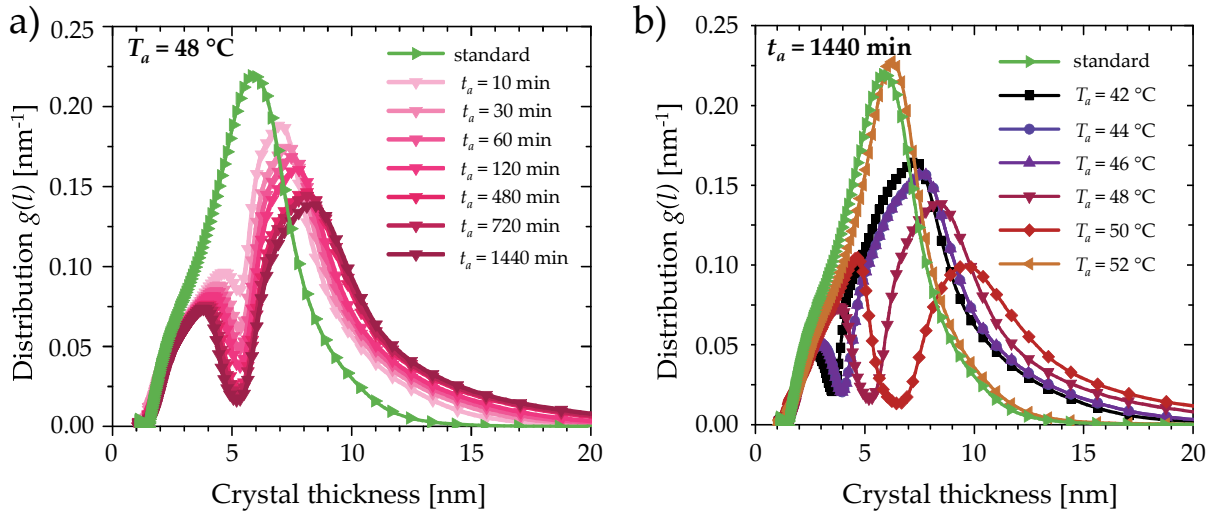


**Figure 12:** a) Crystal thickness distributions after different annealing durations  $t_a$  at annealing temperatures  $T_a = 48^\circ\text{C}$ . b) Crystal thickness distributions after 24 h at different  $T_a$ . Adapted from [P6].

range of annealing temperatures  $T_a$  was between 42 and 52 °C and the annealing durations  $t_a$  were between 10 min and 24 h. After annealing,  $\text{B}_{96}\text{EO}_{90}$  was cooled to 0 °C to crystallize the already molten PEO fractions. Subsequently,  $\text{B}_{96}\text{EO}_{90}$  was heated to 90 °C to gain information about the thermal properties after the annealing treatment. Heating and cooling rates were 10 °C/min for all measurements. In order to relate the observed melting temperatures to the PEO crystal thickness values, a modified approach of Crist and Mirabella<sup>[90]</sup> was applied, which bases on Gibbs-Thomson.<sup>[44]</sup> With that, the crystal thickness dependence was calculated by:

$$g(l_{\text{PEO},c}) = K \cdot P_c(T) \cdot (T_{m,\text{corr}}^\infty - T)^2 \quad (4)$$

In Equation 4,  $g$  is the distribution function of the PEO crystal thickness  $l_{\text{PEO},c}$  and  $P_c(T)$  is the measured heat flow of the DSC that can be ascribed to the melting of PEO crystals, as a function of the temperature  $T$ .  $T_{m,\text{corr}}^\infty$  originates from  $T_m^\infty$  of the Gibbs-Thomson equation,<sup>[44]</sup> but takes into account the low molar mass of the PEO block.<sup>[91]</sup> The factor  $K$  normalizes  $g(l_{\text{PEO},c})$  so that the area under the function becomes unity. Details on the derivation of Equation 4 are provided in the supplementary content of [P6].

The SAXS annealing experiments were performed at annealing temperatures  $T_a$  between 42 and 54 °C for annealing durations  $t_a$  of 1 min to 10 000 min. The average long-periods  $l_p$  were calculated by:

$$l_p = \frac{2\pi}{q^*} \quad (5)$$

Here,  $q^*$  is the maximum of the corresponding reflex in the SAXS patterns. The deviations from  $l_p$  were estimated from 90% of the intensity of  $q^*$ . Further details on the utilized equipment and methods as well as the temperature dependent WAXS investigations are provided in [P6].

In order to estimate the crystal thickness distributions from the DSC results, Equation 4 was applied on the heating scans of each series. Exemplary crystal thickness distributions are shown in the Figures 12 (a and b). For comparison, the distribution of the CS is also provided within these plots. Figure 12a shows the crystal thickness distribution at  $T_a = 48$  °C after different  $t_a$ . Two distinct crystal thickness maxima can be observed for the annealed samples: The lower thickness values (1 to 4 nm) correspond to crystals that are formed during the DSC cooling scan and originates from the molten PEO crystals during annealing. The higher crystal thickness values are attributed to crystal thickening, due to the annealing treatment. With longer  $t_a$ , the average crystal thickness of the thicker crystals increases and the thickness as well as the respective fraction of the thinner crystals decreases. This points to a thermal fractionation during annealing.<sup>[92]</sup> The crystal thickness distribution after annealing for 24 h at different  $T_a$  is given in Figure 12b. It is obvious that the thermal fractionation process becomes more pronounced with increasing  $T_a$ . At relatively low  $T_a$  of 42 to 46 °C, the peak which corresponds to the thinner crystals possesses area fractions of less than 10%. Therefore, it is assumed that thermal fractionation is not dominating within this annealing temperature regime. Instead, classical crystal thickening due to defect healing and transformation of the PEO chains into less folded states inside the PEO crystals is assumed, which has been previously discussed in hydrated PB-*b*-PEO by Reiter and co-workers.<sup>[93]</sup> At annealing temperatures between 46 and 50 °C, the area fractions of the thinner crystals increased from 9% (46 °C) to 17% (48 °C) and 33% (50 °C). Obviously, thermal fractionation was dominating in this annealing regime. At  $T_a = 52$  °C, only a single crystal thickness distribution peak, having a maximum of 6.23 nm, was observed, which is close to the average crystal thickness of the CS (5.90 nm). Thus, melting and self-nucleation effects<sup>[94]</sup> are expected to prevail in this annealing regime.

The crystal thickness distributions based on the DSC heating scans offer a powerful tool to investigate the mechanism of crystal thickening during annealing within the melting range. It should, however, be mentioned that the basis of Equation 4 has some limitations. Possible deviations from  $T_m^\infty$ , due to constraints on the PEO crystal that originate from the presence of the PB block, could not be incorporated, because a suitable model, which describes the relation between melting temperature and crystal thickness under these constraints, is not reported. Thus, the variation that is carried out with  $T_{m,corr}^\infty$  in Equation 4 corrects only the low molar mass of the PEO block. Therefore, great care should to be taken if the absolute values of the crystal thickness distribution shall be discussed.

In order to receive information about the absolute values of the morphological development, time and temperature dependent SAXS investigations were carried out. The average long-periods  $l_p$  and its deviations according to 90% of the intensity of  $q^*$  are provided in Figure 13. The CS of B<sub>96</sub>EO<sub>90</sub> shows an average long-period of  $l_p \approx 22$  nm and is given at  $t_a = 0$  min in Figure 13. Three distinct reflexes were observed in the CS at  $q^*$ ,  $2q^*$  and  $3q^*$ , which points to a lamellar morphology.<sup>[7]</sup> The last data point of each curve corresponds to the long-period after cooling to room temperature. The various  $T_a$  were classified according to

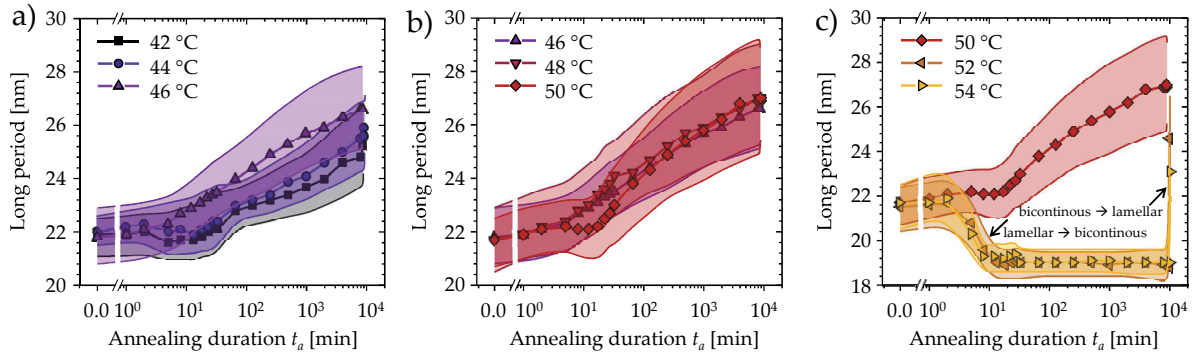


**Figure 13:** Kinetics of the morphological evolution at different annealing temperatures  $T_a$ . a) Regime (i), steady long-period growth, due to defect healing. b) Regime (ii), approximately similar growth rates, due to thermal fractionation. c) Regime (iii), melting and self-nucleation, which coincides with break-out crystallization. Adapted from [P6].

the different annealing regimes that were deduced from the results of the DSC based crystal thickness distributions:

- (i) **Regime of defect healing** ( $42\text{ °C} \leq T_a \leq 46\text{ °C}$ , Figure 13a): The long-period growth is increasing with higher  $T_a$ , being 25.2 nm for  $T_a = 42\text{ °C}$ , 25.6 nm for  $T_a = 44\text{ °C}$  and 26.6 nm for  $T_a = 46\text{ °C}$  after 140 h. The deviations within this annealing temperature regime are similar ( $\pm 1.4\text{ nm}$ ), which points to a steady domain growth and controlled crystal thickening.
- (ii) **Regime of thermal fractionation** ( $46\text{ °C} \leq T_a \leq 50\text{ °C}$ , Figure 13b): Approximately similar spacings of  $l_p \approx 27\text{ nm}$  were observed after  $t_a = 140\text{ h}$  in this annealing regime. However the deviations are continuously increasing with higher  $T_a$ , being  $\pm 1.4\text{ nm}$ ,  $\pm 2.0\text{ nm}$  and  $\pm 2.3\text{ nm}$  for 46 °C, 48 °C and 50 °C respectively. Apparently, the exclusion of the PEO chains from the crystals points to an increase of the observable long-periods. On the one hand, thicker crystals can be formed, due to this PEO chain exclusion, which leads to a domain growth. On the other hand, the PEO chains, that are not included, form smaller PEO domains. Thus, also smaller long-periods can be found within  $B_{96}EO_{90}$  after annealing in this regime.
- (iii) **Regime of melting and self-nucleation** ( $T_a \geq 52\text{ °C}$ , Figure 13c): Annealing at  $T_a \geq 52\text{ °C}$  showed a decrease of  $l_p$  after the sample is completely heated through. Further, the reflex ratios of  $q^*$  changed from 1:2:3 to 1:2: $\sqrt{7}$ , which indicates a phase transition during annealing at these temperatures. Since the volume fraction the PEO (35 vol.%) is close to the phase boundary between a lamellar and a gyroid / perforated lamellar morphology, it can be assumed that such a gyroid morphology or perforated lamellae exists within the molten  $B_{96}EO_{90}$ .<sup>[95]</sup> This leads to a break-out crystallization during cooling  $B_{96}EO_{90}$  from this temperature regime, which also explains the increase of  $l_p$  from 19 nm at  $T_a$  to 24 nm ( $T_a = 52\text{ °C}$ ) and 23 nm ( $T_a = 54\text{ °C}$ ) after cooling to room temperature.

Based on these observations, it can be concluded that the annealing regimes (i) and partially (ii) are suitable to obtain controlled PEO crystal thickening and, thus, a defined morphological development. In the presented case, breakout-crystallization after cooling from annealing regime (iii) impedes such a defined morphology development.

It was observed that DSC based crystal thickness distributions as well as time and temperature dependent SAXS investigations provide a suitable combination to study, both, the mechanisms and kinetics of the morphological development. The crystal thickness distributions obtain qualitative information about the underlying crystal thickening mechanism, *i.e.* defect healing and thermal fractionation. However, to study the kinetics of such a system, which is important to predict the morphological development in a quantitative manner, time and temperature dependent SAXS measurements are mandatory. Moreover, the SAXS investigations provide information about the self-assembled block copolymer morphology. This is also important in order to understand the mechanisms of the morphological development. Thus, it is obvious that only the combination of these techniques allows to understand and predict the ordering processes of crystallizable block copolymers during crystal thickening by annealing within the melting range.



## 5 Summary

The aim of the presented work was to elaborate the relationship between the macromolecular architecture, the morphology and the macroscopic properties of polymers that exhibit more than one phase and, thus, to contribute to the elucidation of structure-property relationships of different polymer systems. Moreover, the obtained knowledge should be used to tailor these polymers with respect to their typical applications. The investigated polymers range from *commodity plastics*, like olefin ethylene-*co*-octene copolymers (EOCs), *technical polymers*, like the styrene-butadiene block copolymers, up to *functional polymers*, like the piezoelectric P(VDF-*co*-TrFE) or the semi-crystalline block copolymer PB-*b*-PEO. The presented results will be summarized in the following; a graphical summary is provided in Figure 14.

The influence of the macromolecular architecture in styrene-butadiene and styrene-isoprene-based block copolymers on the morphology and the mechanical behavior was presented in Chapter 2. By variation of the S/B middle block ratio in S-S/B-S triblock copolymers, different deformation mechanisms were found, based on 2D-SAXS studies with online deformation. Chevron formation and lamellae tilting was observed at a styrene content of 50 wt.% in the S/B block, whereas at higher styrene contents (70 wt.%) affine deformation behavior was found to describe the morphological evolution during deformation in a very good manner. Chevron formation and lamellae tilting requires less energy to deform the sample than the affine deformation. Thus, the deviating deformation mechanisms provide a possible explanation for the very different mechanical behavior of the investigated S-S/B-S triblock copolymers. The results contribute to the understanding of the macromolecular architecture, the deformation mechanism and the resulting mechanical behavior in styrene-diene based block copolymers.

The effect of blending of different ethylene-octene copolymers (EOC) and its consequence on the relationship between morphology and mechanical properties were discussed in Chapter 3. By changing the blend composition, consisting of a blocky (OBC) and a statistical EOC (ORC), the mechanical behavior of the thermoplastic elastomers could be systematically tailored over a wide range. DSC, DMA, AFM and WAXS investigations gained insight into the structure and morphology of these blends. It was found that these exhibit three phases, consisting of (i) thick OBC crystals, (ii) thin ORC crystals and (iii) a matrix, where both polymers are miscible. In other words, this results into a bimodal network of differently thick PE-like crystals, which are connected by a homogenous matrix. This is known to positively affect the mechanical properties of thermoplastic elastomers and, hence, increasing strain at break was observed with higher OBC weight fractions without sacrificing the tensile strength of

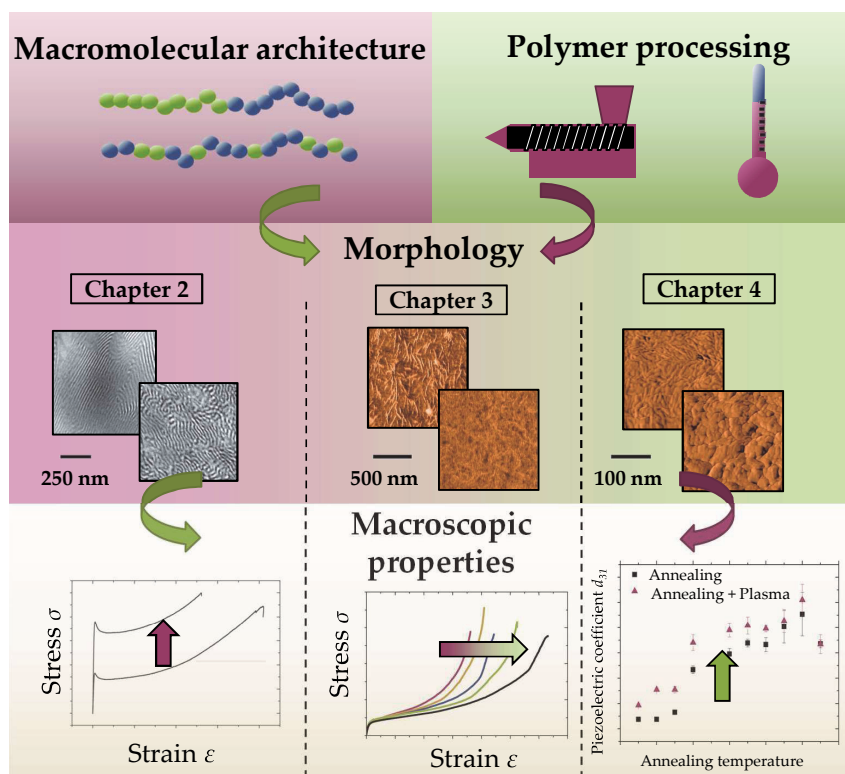


**Figure 14:** Graphical summary of the presented investigations. The colors violet and green refer to the focus points *macromolecular architecture* and *polymer processing* in the respective study. Significant improvements of the macroscopic behavior could be observed in the respective polymer systems.

these blends. The results show that blending represents an effective strategy to control the morphology and, thus, to optimize the mechanical properties of semi-crystalline polymers.

The impact of annealing semi-crystalline copolymers on the structure and morphology of the crystallites as well as the resulting (i) electro-mechanical properties of P(VDF-*co*-TrFE) and (ii) the development of the microphase-separated nanostructure of PB-*b*-PEO were discussed in Chapter 4.

For inkjet-printed P(VDF-*co*-TrFE) it was shown that the electro-mechanical behavior can be improved by an annealing treatment near the melting point. Thereby, annealing temperatures  $T_a$  between 110 and 145 °C were found to be beneficial for the electro-mechanical properties, like the piezoelectric coefficient  $d_{31}$ , which increases one order of magnitude due to annealing. It was observed that the degree of crystallinity as well as the size of the crystals increases, employing DSC, XRD and AFM investigations. The results point to an interrelation between the electro-mechanical behavior and the morphological properties as a direct consequence of the annealing treatment.

Moreover, annealing within the melting range of PB-*b*-PEO was applied to adjust the long-period of the block copolymer morphology by controlled PEO crystal thickening. The focus of the presented results was to investigate the underlying thickening mechanism and kinetics in bulk by a combination of time and temperature dependent DSC and SAXS measurements. It was found that the crystal thickening can be basically described by defect healing,

which is dominating at relatively low temperatures  $T_a \leq 46$  °C and thermal fractionation, which prevails at intermediate annealing temperatures ( $46$  °C  $\leq T_a < 52$  °C). Furthermore, a crystallization under a soft confinement is present in the investigated PB-*b*-PEO, which lead to a break-out crystallization during cooling if the annealing temperatures were too close or above the peak melting temperature ( $T_a \geq 52$  °C). This impeded a controlled morphology development at such high temperatures. The presented results contribute to the understanding of crystallization under confinement and the applied methodology provides a powerful tool to further investigate the mechanism and kinetics of crystal thickening as well as the morphological development in crystallizable block copolymers. However, to predict the long-period prior to an annealing treatment, additional molecular as well as processing parameters have to be varied over a wide range.

This thesis provides an overview of different methods to adjust macroscopic properties of polymers on a molecular level (Chapters 2 and 3), by the blend composition (Chapter 3) as well as fine-tuning of the processing parameters (Chapter 4). The obtained results underline the impact of the morphology in polymeric multi-phase system on the achievable mechanical and electro-mechanical properties. Within this work, various analysis techniques were employed. Only by a combination of the applied techniques, essential information about the structure-property relationship can be achieved.

## 6 Zusammenfassung

Zielstellung der vorliegenden Arbeit war es, Zusammenhänge zwischen der makromolekularen Architektur, der Morphologie und den makroskopischen Eigenschaften von mehrphasigen, polymer-basierten Materialien herauszuarbeiten und damit Beiträge für das Verständnis der Beziehungen zwischen Struktur und Eigenschaften zu leisten, um diese im Hinblick auf eine mögliche, spätere Anwendung gezielt zu beeinflussen. Das Spektrum der hierbei verwendeten Materialien reichte von den weit verbreiteten Polyolefinen sowie Styrol-Butadien- und Styrol-Isopren-basierten Polymeren, mit Einsatzbereichen in denen die mechanischen Eigenschaften von übergeordneter Bedeutung sind, bis hin zu Spezial-Kunststoffen, wie dem semikristallinen P(VDF-co-TrFE), welches Anwendung als Sensor- und Aktuator-Material findet oder dem Blockcopolymer PB-*b*-PEO, welches aktuell vorwiegend von akademischem Interesse ist, aufgrund seiner amphiphilen und einstellbaren mikrophasenseparierten Nanostruktur allerdings als Überzug für Implantatmaterialien interessant sein könnte. Es folgt eine Zusammenfassung der Ergebnisse; eine Kurzübersicht der Ergebnisse ist in Abbildung 15 zu finden.

Der Einfluss der makromolekularen Architektur in Styrol-Butadien und Styrol-Isopren-basierten Blockcopolymeren auf die Morphologie und mechanischen Eigenschaften wurde in Kapitel 2 vorgestellt. Hier wurden durch Variation der S/B Mittelblockverhältnisse unterschiedliche Deformationsmechanismen in S-S/B-S Triblockcopolymeren, mittels Röntgenstreuung unter gleichzeitiger Zugbelastung der Probe, festgestellt. Während bei einem Styrol-Gehalt von 50 Gew.% im Mittelblock noch eine klassische Chevron-Bildung in den mikrophasenseparierten Lamellen festgestellt werden konnte, war dies bei einem Styrol-Gehalt von 70 Gew.% nicht mehr zu beobachten. Stattdessen konnte der Deformationsmechanismus sehr gut durch affines Materialverhalten beschrieben werden. Da diese verschiedenen Mechanismen unterschiedliche Energien benötigen um aktiv zu werden, beschreiben die hier präsentierten Ergebnisse eine wesentliche Ursache für die stark unterschiedlichen mechanischen Eigenschaften der untersuchten Proben und tragen daher zum Verständnis des Zusammenhangs zwischen makromolekularer Architektur, Deformationsmechanismus und den makroskopischen, mechanischen Eigenschaften in diesem Materialsystem bei.

Der Effekt von Polymermischungen aus Ethylene-Octene-Copolymeren (EOC) wurde in Kapitel 3 präsentiert. Wiederum stand hierbei der Zusammenhang zwischen Morphologie und den mechanischen Eigenschaften im Fokus. Über die Blend-Zusammensetzung, bestehend aus einem blockartigen (OBC) und einem statistischen EOC (ORC), konnten die mechanischen Eigenschaften der thermoplastischen Elastomere systematisch variiert werden. Strukturell wurde dabei mittels DSC, DMA, AFM und WAXS-Untersuchungen festgestellt, dass die Blends eine Dreiphasen-Morphologie aufzeigen, bestehend aus dicken OBC-Kristalliten, dün-

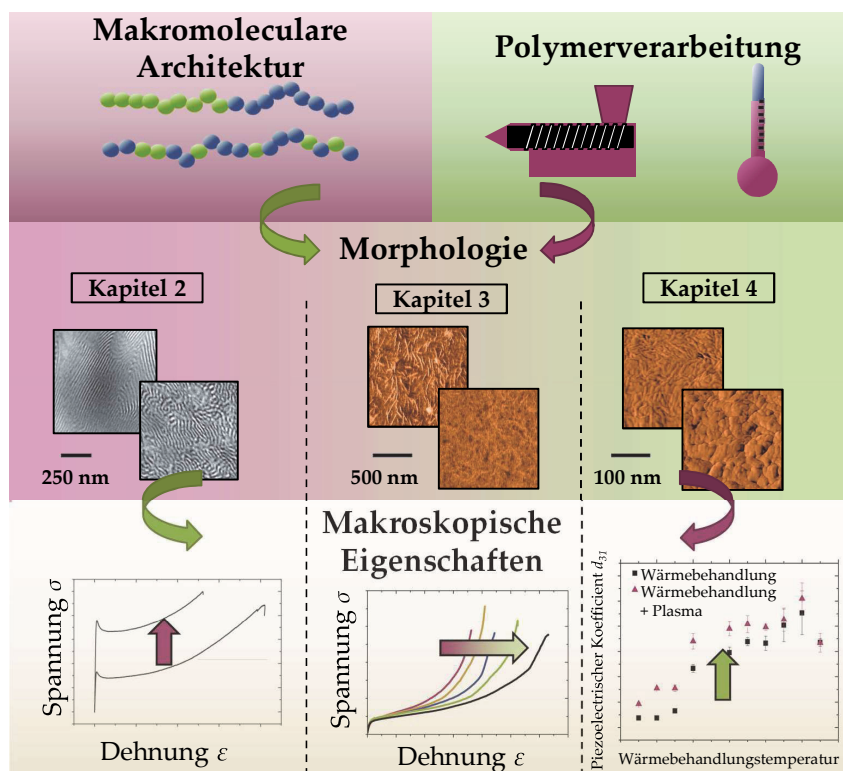


**Abbildung 15:** Kurzübersicht der vorgestellten Ergebnisse. Die Farben violett und grün spiegeln die jeweiligen Schwerpunkte *Makromolekulare Architektur* und *Polymerverarbeitung* in den entsprechenden Untersuchungen dar. In den untersuchten Polymersystemen konnten signifikante Eigenschaftsverbesserungen verzeichnet werden.

nen ORC-Kristalliten sowie einer amorphen Phase, in welcher die beiden Polymere mischbar sind. Dadurch ergibt sich innerhalb der Blends ein bimodales Netzwerk aus orthorhombischen PE-Kristalliten unterschiedlicher Dicke, welche verbunden sind über eine gemeinsame amorphe Matrix. Dies wirkte sich positiv auf die erreichten mechanischen Eigenschaften aus. So konnte, trotz teilweise sinkender Kristallinitäten, eine Erhöhung der Bruchdehnung erreicht werden, ohne Einbußen in der Zugfestigkeit des Materials zu erhalten. Die Ergebnisse zeigen, dass Blenden eine effektive Strategie darstellt, um die Morphologie dieser semi-kristallinen Polymere zu kontrollieren und deren mechanische Eigenschaften zu optimieren. Die Wirkung einer gezielten Wärmebehandlung nahe des Schmelzpunktes auf die Struktur und Morphologie der Kristallite sowie der Einfluss auf (i) die piezoelektrischen Eigenschaften von P(VDF-co-TrFE) und (ii) die Entwicklung der mikrophasenseparierten Nanostruktur in PB-*b*-PEO wurde in Kapitel 4 diskutiert.

Im Fall des tintenstrahlgedruckten P(VDF-co-TrFE) wurde gezeigt, dass dessen elektro-mechanischen Eigenschaften gezielt, durch eine Wärmebehandlung nahe dem Schmelzpunkt, verbessert werden können. Als Wärmebehandlungstemperatur eignen sich hierbei Temperaturen zwischen 110 und 145 °C, wodurch beispielsweise der piezoelektrische Koeffizient  $d_{31}$  um den Faktor 10 erhöht werden konnte. Über eine Kombination aus DSC, XRD und AFM-Studien wurde zudem herausgefunden, dass sowohl Kristallinität als auch die Kristallitdicke durch den Wärmebehandlungsprozess ansteigen. Die Ergebnisse zwischen den elektro-

mechanischen Tests sowie den strukturellen und morphologischen Betrachtungen, einen eindeutigen Zusammenhang zwischen der Struktur, der Morphologie und den piezoelektrischen Eigenschaften des gedruckten Films, als direkte Konsequenz der durchgeführten Wärmebehandlung.

Weiterhin wurde, über die Wärmebehandlung innerhalb des Schmelzbereiches von PEO, die Kristallverdickung von PEO in einem PB-*b*-PEO Blockcopolymer genutzt, um eine gezielte Verbreiterung der Periodizität der mikrophasenseparierten Nanostruktur des Blockcopolymer hervorzurufen. Schwerpunkt der hier präsentierten Ergebnisse waren die zugrundeliegenden Verdickungsmechanismen und die Verdickungskinetik in thermisch vereinheitlichtem PB-*b*-PEO, über eine Kombination aus zeit- und temperatur-abhängiger DSC und SAXS. Es stellte sich dabei heraus, dass sich die Verdickung weitestgehend durch zwei Prozesse beschreiben lässt: Während bei relativ niedrigeren Temperaturen ( $T_a \leq 46 \text{ °C}$ ) die Kristallverdickung hauptsächlich über Defektheilung innerhalb der PEO-Kristallite stattfindet, überwiegt die thermische Fraktionierung bei mittleren Wärmebehandlungstemperaturen ( $46 \text{ °C} \leq T_a \leq 50 \text{ °C}$ ). Bei höheren Temperaturen konnte keine kontrollierte Kristallverdickung mehr erreicht werden. Die gewonnenen Ergebnisse tragen zum Verständnis der Kristallisation unter Zwangsbedingungen bei und liefern methodisch eine interessante Möglichkeit, um die Mechanismen und die Kinetik der Kristallverdickung von kristallisierbaren Blockcopolymeren zu untersuchen. Um Vorhersagen hinsichtlich einer einstellbaren Periodizität zu gewährleisten, müssen jedoch noch weitere molekulare Parameter und Wärmebehandlungsbedingungen in größerer Breite variiert werden, als dies im Rahmen dieser Arbeit möglich war.

Die Arbeit bietet einen Überblick über verschiedene Methoden, um die makroskopischen Eigenschaften von Kunststoffen über die molekulare Architektur (Kapitel 2 und 3), die Zusammensetzung (Kapitel 3) sowie Prozessparameter (Kapitel 4) maßgeblich zu beeinflussen. Die gewonnenen Erkenntnisse unterstreichen den Einfluss der *Morphologie* der betrachteten Multiphasensysteme auf die erzielbaren mechanischen und elektro-mechanischen Eigenschaften. In diesem Zusammenhang kamen verschiedenste Charakterisierungstechniken zum Einsatz, wobei oftmals nur durch eine Kombination der angewandten Techniken wesentliche Informationen über die Beziehung zwischen Struktur und Eigenschaften ermittelt werden konnte.

## References

- [1] R. Duncan, *Nat. Rev. Drug. Discov.* **2003**, *2*, 347–360.
- [2] G. Dennler, M. C. Scharber, C. J. Brabec, *Adv. Mater.* **2009**, *21*, 1323–1338.
- [3] T. Janoschka, M. D. Hager, U. S. Schubert, *Adv. Mater.* **2012**, *24*, 6397–6409.
- [4] H.-G. Elias in *Makromoleküle: Band 4, Anwendung von Polymeren*, Wiley-VCH Verlag GmbH & Co. KGaA, **2003**, Chapter Einteilung von Kunststoffen, pp. 296–299.
- [5] Website accessed 05.01.2015, [http://plasticker.de/preise/preise\\_ecebd\\_en.php](http://plasticker.de/preise/preise_ecebd_en.php).
- [6] H.-G. Elias in *Makromoleküle, Band 1: Chemische Struktur*, Wiley-VCH Verlag GmbH & Co. KGaA, **1999**, Chapter Molekülarchitektur, pp. 47–62.
- [7] N. Hadjichristidis, S. Pispas, G. Floudas, *Block Copolymers: Synthetic Strategies, Physical Properties, and Applications*, John Wiley & Sons, **2003**.
- [8] S. Darling, *Prog. Polym. Sci.* **2007**, *32*, 1152–1204.
- [9] R. M. Lloyd in *Polymer Blends*, Carl Hanser Verlag GmbH & Co. KG, **2007**, pp. 11–64.
- [10] B. Wunderlich, *Thermal Analysis of Polymeric Materials*, Springer, **2005**.
- [11] M. Stamm in *Polymer Surfaces and Interfaces — Characterization, Modification and Applications*, (Ed.: M. Stamm), Springer, **2008**, Chapter Polymer Surface and Interface Characterization Techniques, pp. 1–16.
- [12] P. J. Goodhew, J. Humphreys, R. Beanland, *Electron microscopy and analysis*, Taylor & Francis Inc., **2001**.
- [13] N. Stribeck, *X-ray-scattering of Soft Matter*, Springer, **2007**.
- [14] U. Staudinger, B. K. Satapathy, M. Thunga, R. Lach, R. Weidisch, K. Knoll, *Acta Mater.* **2007**, *55*, 5844–5858.
- [15] H.-G. Elias in *Makromoleküle: Band 4, Anwendung von Polymeren*, Wiley-VCH Verlag GmbH & Co. KGaA, **2003**, Chapter Kautschuke und Elastomere, pp. 244–290.
- [16] R. Weidisch, S. P. Gido, D. Uhrig, H. Iatrou, J. Mays, N. Hadjichristidis, *Macromolecules* **2001**, *34*, 6333–6337.
- [17] U. Staudinger, B. K. Satapathy, R. Weidisch, *Eur. Polym. J.* **2008**, *44*, 1822–1833.
- [18] U. Staudinger, R. Schlegel, R. Weidisch, J. Fritzsche, M. Klüppel, G. Heinrich, J. W. Mays, D. Uhrig, N. Hadjichristidis, *Eur. Polym. J.* **2008**, *44*, 3790–3796.
- [19] K. Schneider, A. Schöne, T.-S. Jun, A. M. Korsunsky, *Procedia Eng.* **2009**, *1*, 159–162.
- [20] Y. Duan, M. Thunga, R. Schlegel, K. Schneider, E. Rettler, R. Weidisch, H. W. Siesler, M. Stamm, J. W. Mays, N. Hadjichristidis, *Macromolecules* **2009**, *42*, 4155–4164.
- [21] D. Uhrig, J. Mays, *Polym. Chem.* **2011**, *2*, 69–76.
- [22] R. Schlegel, Y. X. Duan, R. Weidisch, S. Hölzer, K. Schneider, M. Stamm, D. Uhrig, J. W. Mays, G. Heinrich, N. Hadjichristidis, *Macromolecules* **2011**, *44*, 9374–9383.
- [23] R. Adhikari, G. H. Michler, *Prog. Polym. Sci.* **2004**, *29*, 949–986.
- [24] U. Staudinger, PhD thesis, TU Dresden, **2007**.

- [25] M. Ganß, B. K. Satapathy, M. Thunga, R. Weidisch, K. Knoll, *Macromol. Mater. Eng.* **2010**, *295*, 178–188.
- [26] M. Ganß, U. Staudinger, M. Thunga, K. Knoll, K. Schneider, M. Stamm, R. Weidisch, *Polymer* **2012**, *53*, 2085–2098.
- [27] S. Hölzer, M. Ganß, K. Schneider, K. Knoll, R. Weidisch, *Eur. Polym. J.* **2013**, *49*, 261–269.
- [28] M. Thunga, PhD thesis, TU Dresden, **2009**.
- [29] C. A. Schneider, W. S. Rasband, K. W. Eliceiri, *Nat. Meth.* **2012**, *9*, 671–675.
- [30] C. C. Honeker, E. L. Thomas, *Chem. Mat.* **1996**, *8*, 1702–1714.
- [31] Y. Cohen, R. J. Albalak, B. J. Dair, M. S. Capel, E. L. Thomas, *Macromolecules* **2000**, *33*, 6502–6516.
- [32] Y. Cohen, M. Brinkmann, E. L. Thomas, *J. Chem. Phys.* **2001**, *114*, 984–992.
- [33] V. Racherla, O. Lopez-Pamies, P. P. Castaneda, *Mech. Mater* **2010**, *42*, 451–468.
- [34] R. A. J. Janssen, J. Nelson, *Adv. Mater.* **2013**, *25*, 1847–1858.
- [35] A. Teichler, S. Hölzer, J. Nowotny, F. Kretschmer, C. Bader, J. Perelaer, M. D. Hager, S. Hoepfener, U. S. Schubert, *ACS. Comb. Sci.* **2013**, *15*, 410–418.
- [36] M. Kim, P. Phillips, *J. Appl. Polym. Sci.* **1998**, *70*, 1893–1905.
- [37] A. G. Simanke, G. B. Galland, R. Baumhardt Neto, R. Quijada, R. S. Mauler, *J. Appl. Polym. Sci.* **1999**, *74*, 1194–1200.
- [38] S. Bensason, J. Minick, A. Moet, S. Chum, A. Hiltner, E. Baer, *J. Polym. Sci. Part B: Polym. Phys.* **1996**, *34*, 1301–1315.
- [39] D. J. Arriola, E. M. Carnahan, P. D. Hustad, R. L. Kuhlman, T. T. Wenzel, *Science* **2006**, *312*, 714–719.
- [40] H. P. Wang, D. U. Khariwala, W. Cheung, S. P. Chum, A. Hiltner, E. Baer, *Macromolecules* **2007**, *40*, 2852–2862.
- [41] H. P. Wang, S. P. Chum, A. Hiltner, E. Baer, *J. Appl. Polym. Sci.* **2009**, *113*, 3236–3244.
- [42] F. Zuo, C. Burger, X. Chen, Y. Mao, B. S. Hsiao, H. Chen, G. R. Marchand, S.-Y. Lai, D. Chiu, *Macromolecules* **2010**, *43*, 1922–1929.
- [43] F. Zuo, Y. Mao, X. Li, C. Burger, B. S. Hsiao, H. Chen, G. R. Marchand, *Macromolecules* **2011**, *44*, 3670–3673.
- [44] G. Höhne, *Polymer* **2002**, *43*, 4689–4698.
- [45] S. Hölzer, M. Menzel, Q. Zia, U. S. Schubert, M. Beiner, R. Weidisch, *Polymer* **2013**, *54*, 5207–5213.
- [46] J. E. Mark, M.-Y. Tang, *J. Polym. Sci. Part B: Polym. Phys.* **1984**, *22*, 1849–1855.
- [47] Y. Termonia, *Macromolecules* **1990**, *23*, 1481–1483.
- [48] P. Scherrer, *Gött. Nachr. Math.-Physik. Kl.* **1918**, *1918*, 98–100.
- [49] R. Androsch, J. Blackwell, S. N. Chvalun, B. Wunderlich, *Macromolecules* **1999**, *32*, 3735–3740.
- [50] H. Elbs, C. Drummer, V. Abetz, G. Krausch, *Macromolecules* **2002**, *35*, 5570–5577.
- [51] Y. S. Jung, C. A. Ross, *Adv. Mater.* **2009**, *21*, 2540–2545.



- [52] G. Portale, D. Cavallo, G. C. Alfonso, D. Hermida-Merino, M. van Drongelen, L. Balzano, G. W. M. Peters, J. G. P. Goossens, W. Bras, *J. Appl. Crystallogr.* **2013**, *46*, 1681–1689.
- [53] M. Langela, U. Wiesner, H. W. Spiess, M. Wilhelm, *Macromolecules* **2002**, *35*, 3198–3204.
- [54] R. Morgan, M. Hill, P. Barham, *Polymer* **1999**, *40*, 337–348.
- [55] D. Mileva, Q. Zia, R. Androsch, *Polym. Bull.* **2010**, *65*, 623–634.
- [56] B. Fillon, J. C. Wittmann, B. Lotz, A. Thierry, *J. Polym. Sci. Part B: Polym. Phys.* **1993**, *31*, 1383–1393.
- [57] G Kim, M Libera, *Macromolecules* **1998**, *31*, 2569–2577.
- [58] R. Schulze, M. M. L. Arras, C. Helbing, S. Hölzer, U. S. Schubert, T. F. Keller, K. D. Jandt, *Macromolecules* **2014**, *47*, 1705–1714.
- [59] A. Urbas, R. Sharp, Y. Fink, E. L. Thomas, M. Xenidou, L. J. Fetters, *Adv. Mater.* **2000**, *12*, 812–814.
- [60] J.-H. Lee, C. Y. Koh, J. P. Singer, S.-J. Jeon, M. Maldovan, O. Stein, E. L. Thomas, *Adv. Mater.* **2014**, *26*, 532–569.
- [61] K. S. Ramadan, D Sameoto, S Evoy, *Smart Mater. Struct.* **2014**, *23*, 033001 (1–26).
- [62] M. Singh, H. M. Haverinen, P. Dhagat, G. E. Jabbour, *Adv. Mater.* **2010**, *22*, 673–685.
- [63] P. Martins, A. Lopes, S. Lanceros-Mendez, *Prog. Polym. Sci.* **2014**, *39*, Topical issue on Electroactive Polymers, 683–706.
- [64] O. Pabst, J. Perelaer, E. Beckert, U. S. Schubert, R. Eberhardt, A. Tünnermann, *Org. Electron.* **2013**, *14*, 3423–3429.
- [65] A. J. Lovinger, *Science* **1983**, *220*, 1115–1121.
- [66] F. Baltá-Calleja, A. Arche, T. Ezquerra, C. Cruz, F. Batallán, B. Frick, E. Cabarcos, *Adv. Polym. Sci.* **1993**, *108*, 1–48.
- [67] M. Barique, H. Ohigashi, *Polymer* **2001**, *42*, 4981–4987.
- [68] V. Sencadas, R. Gregorio, Jr., S. Lanceros-Mendez, *J. Macromol. Sci. Phys.* **2009**, *48*, 514–525.
- [69] D. Mao, M. Quevedo-Lopez, H. Stiegler, B. Gnade, H. Alshareef, *Org. Electron.* **2010**, *11*, 925–932.
- [70] A. Teichler, J. Perelaer, U. S. Schubert, *J. Mater. Chem. C* **2013**, *1*, 1910–1925.
- [71] O. Pabst, S. Hölzer, E. Beckert, J. Perelaer, U. S. Schubert, R. Eberhardt, A. Tünnermann, *Org. Electron.* **2014**, *15*, 3306–3315.
- [72] K. J. Kim, G. B. Kim, C. L. Vanlencia, J. F. Rabolt, *J. Polym. Sci. Part B: Polym. Phys.* **1994**, *32*, 2435–2444.
- [73] M.-C. Garcia-Gutierrez, A. Linares, I. Martin-Fabiani, J. J. Hernandez, M. Soccio, D. R. Rueda, T. A. Ezquerra, M. Reynolds, *Nanoscale* **2013**, *5*, 6006–6012.
- [74] E. Bellet-Amalric, J. Legrand, *EPJ B* **1998**, *3*, 225–236.
- [75] D. Singh, A. Garg, Deepak, *Org. Electron.* **2014**, *15*, 82–90.
- [76] W. Li, Y. Zhu, D. Hua, P. Wang, X. Chen, J. Shen, *Appl. Surf. Sci.* **2008**, *254*, 7321–7325.
- [77] D. Mao, B. E. Gnade, M. A. Quevedo-Lopez in *Ferroelectrics – Physical Effects*, (Ed.: M. Lallart), InTech, **2011**, Chapter Ferroelectric Properties and Polarization Switching Kinetic of Poly (vinylidene fluoride-trifluoroethylene) Copolymer, pp. 77–100.

- [78] O. Pabst, PhD thesis, Friedrich-Schiller-Universität Jena, **2014**.
- [79] G. Holden, N. Legge in, (Eds.: G. Holden, N. Legge), Carl Hanser Verlag München Wien, **1996**, Chapter Styrenic Thermoplastic Elastomers, pp. 47–70.
- [80] M. L. Arnal, V. Balsamo, F. López-Carrasquero, J. Contreras, M. Carrillo, H. Schmalz, V. Abetz, E. Laredo, A. J. Müller, *Macromolecules* **2001**, *34*, 7973–7982.
- [81] W.-N. He, J.-T. Xu, *Prog. Polym. Sci.* **2012**, *37*, 1350–1400.
- [82] M. Beiner, H. Huth, *Nat. Mater.* **2003**, *2*, 595–599.
- [83] M. Beiner, *J. Polym. Sci. Part B: Polym. Phys.* **2008**, *46*, 1556–1561.
- [84] A. Boschetti-de Fierro, A. T. Lorenzo, A. J. Müller, H. Schmalz, V. Abetz, *Macromol. Chem. Phys.* **2008**, *209*, 476–487.
- [85] H.-L. Chen, S.-C. Hsiao, T.-L. Lin, K. Yamauchi, H. Hasegawa, T. Hashimoto, *Macromolecules* **2001**, *34*, 671–674.
- [86] S. Hong, L. Yang, W. J. MacKnight, S. P. Gido, *Macromolecules* **2001**, *34*, 7009–7016.
- [87] D. M. Lambrea, R. Opitz, G. Reiter, P. M. Frederik, W. H. de Jeu, *Polymer* **2005**, *46*, 4868–4875.
- [88] R. V. Castillo, M. L. Arnal, A. J. Müller, I. W. Hamley, V. Castelletto, H. Schmalz, V. Abetz, *Macromolecules* **2008**, *41*, 879–889.
- [89] R. Schulze, M. M. L. Arras, G. Li Destri, M. Gottschaldt, J. Bossert, U. S. Schubert, G. Marletta, K. D. Jandt, T. F. Keller, *Macromolecules* **2012**, *45*, 4740–4748.
- [90] B. Crist, F. M. Mirabella, *J. Polym. Sci. Part B: Polym. Phys.* **1999**, *37*, 3131–3140.
- [91] C. Buckley, A. Kovacs, *Colloid Polym. Sci.* **1976**, *254*, 695–715.
- [92] A. J. Müller, M. L. Arnal, *Prog. Polym. Sci.* **2005**, *30*, 559–603.
- [93] G. Reiter, G. Castelein, P. Hoerner, G. Riess, J.-U. Sommer, G. Floudas, *Eur. Phys. J. E Soft Matter* **2000**, *2*, 319–334.
- [94] G. Reiter, *Chem. Soc. Rev.* **2014**, *43*, 2055–2065.
- [95] M. W. Matsen, F. S. Bates, *Macromolecules* **1996**, *29*, 1091–1098.

## List of abbreviations

$2\theta$	scattering angle
$\alpha$	inclination angle between adjacent domains in a chevron pattern
$a_i$	parameter describing the influence of lamellae tilting
AFM	atomic force microscopy
B <sub>96</sub> EO <sub>90</sub>	polybutadiene- <i>block</i> -poly(ethylene oxide), where the blocks consist of 96 and 90 monomer units, respectively
CS	crystalline standard
CuK $_{\alpha}$	K $_{\alpha}$ radiation of copper
$\Delta H_{m,i}$	melting enthalpy of substance $i$
$d_{i,j}$	tensor of piezoelectric coefficients
$d_{31}$	piezoelectric coefficient that describes the electrical polarization generated perpendicular to the direction of the applied mechanical stress
D	diene
DSC	differential scanning calorimetry
DMA	dynamic-mechanical analysis
$\epsilon$	strain
$\epsilon_{M,x}$	macroscopic strain in stretching direction, $x$
$\epsilon_{\mu,x}$	microscopic strain in stretching direction, $x$
$\epsilon_{\mu,y}$	microscopic strain perpendicular to the stretching direction, $y$
$E$	modulus of elasticity
EOC(s)	poly(ethylene- <i>co</i> -octene) copolymer(s)
FWHM	full width at half maximum value
$g$	crystal thickness distribution
Gew.%	Gewichtsprözent
$K$	normalizing constant for the crystal thickness distribution
$\lambda$	wavelength
LLD-PE	linear, low density polyethylene

---

LN50	polystyrene- <i>block</i> -poly(styrene- <i>co</i> -butadiene)- <i>block</i> -poly(styrene) with 50 wt.% styrene in the middle block
LN70	polystyrene- <i>block</i> -poly(styrene- <i>co</i> -butadiene)- <i>block</i> -poly(styrene) with 70 wt.% styrene in the middle block
$l_{\text{PEO},c}$	crystal thickness of PEO
$l_p$	long period
$l_{p,i}$	long period in the $i^{\text{th}}$ state
$l_{p,0}$	initial long period
$M_{w,i}$	weight-average molar mass of substance $i$
$M_{n,i}$	number-average molar mass of substance $i$
$N$	degree of polymerization
OBC	olefin block copolymer
ORC	olefin random copolymer
PB	polybutadiene
PB- <i>b</i> -PEO	polybutadiene- <i>block</i> -poly(ethylene oxide)
$P_c$	heat flow of the DSC which can be attributed to the melting of crystals
PC <sub>61</sub> BM	phenyl-C61-butyric acid methyl ester
PDI	index of polydispersity
PE	polyethylene
PEO	poly(ethylene oxide)
PI	polyisoprene
PS	polystyrene
$P_{\text{rem}}$	remanent polarization
$P_{\text{max}}$	maximum polarization
P(VDF- <i>co</i> -TrFE)	poly(vinylidene fluoride- <i>co</i> -trifluoroethylene)
$q$	scattering vector
$q^*$	scattering vector of the first reflex
Rxx	olefin copolymer blend with a fraction of $xx$ wt.% ORC
Ref.	reference
$\sigma$	stress
S/B	poly(styrene- <i>co</i> -butadiene)

---

SAXS	small angle X-ray scattering
S-D	polystyrene- <i>block</i> -polydiene
S-D-S	polystyrene- <i>block</i> -polydiene- <i>block</i> -polystyrene
S-S/B-S	polystyrene- <i>block</i> -poly(styrene- <i>co</i> -butadiene)- <i>block</i> -polystyrene
$T$	temperature
$t_a$	annealing duration
$T_a$	annealing temperature
$T_c$	crystallization temperature
TEM	transmission electron microscopy
$T_{g,i}$	glass transition temperature of substance $i$
$T_m$	melting temperature
$T_m^\infty$	equilibrium melting temperature
$T_{m,\text{corr}}^\infty$	equilibrium melting temperature, corrected for low molar mass.
$\chi$	Flory interaction parameter
$\chi_{\text{eff}}$	effective Flory interaction parameter
WAXS	wide angle X-ray scattering
wt.%	weight percentage
XRD	X-ray diffraction



# Curriculum vitae

## Personal Information

Name: Hölzer, Stefan  
Birthday: 01.03.1984  
Place of birth: Saalfeld (Saale)

## Professional Career

- 06/2012–present PhD student & scientific co-worker at the Friedrich-Schiller-Universität Jena, Laboratory of Organic and Macromolecular Chemistry (IOMC).  
PhD thesis: “Structure-property relationships of polymer-based multi-phase systems” under the supervision of Prof. Ulrich S. Schubert.
- 03/2010–05/2012 Scientific co-worker at the Fraunhofer Institute for Mechanics of Materials IWM and PhD student at the Martin-Luther-Universität Halle-Wittenberg.  
Topic: “Structure-property relationships of polymer-based multi-phase systems” under the supervision of Prof. Roland Weidisch & Prof. Mario Beiner.
- 10/2009–02/2010 Research fellowship of the Carl-Zeiss-Stiftung at the Friedrich-Schiller-Universität Jena under supervision of Prof. Roland Weidisch.  
Topic: “Deformation behavior and dynamical properties of superelastic polymers”.
- 03/2009–08/2009 Guest researcher at the Leibnitz Institute for Polymer Research Dresden in the group of Prof. Manfred Stamm / Dr. Konrad Schneider.  
Topic: Small-angle X-ray scattering of styrene/butadiene based block copolymers under deformation.

## Education

- 10/2003–12/2008 Study of Material Science at the Friedrich-Schiller-Universität Jena  
Degree: Diplom-Ingenieur (equivalent to M.Sc.)
- 01/2008–12/2008 Execution of Diploma Thesis: “Morphologie und mechanische Eigenschaften von Blockcopolymeren mit komplexen Architekturen” under the supervision of Prof. Roland Weidisch and Prof. Ulrich S. Schubert.
- 08/1994–07/2002 Gymnasium & Abitur (german university entrance qualification), Heinrich-Böll-Gymnasium Saalfeld.

Jena, 08.01.2015

.....  
Stefan Hölzer

## List of publications & presentations

### Refereed publications in scientific journals

- R. Schlegel, Y. X. Duan, R. Weidisch, **S. Hölzer**, K. Schneider, M. Stamm, D. Uhrig, J. W. Mays, G. Heinrich, N. Hadjichristidis: "High-strain-induced deformation mechanism in block-graft and multigraft copolymers" *Macromolecules* **2011**, *44*, 9374–9383.
- **S. Hölzer**, M. Ganß, K. Schneider, K. Knoll, R. Weidisch: "Deformation mechanisms in S–S/B–S triblock copolymers" *Eur. Polym. J.* **2013**, *49*, 261–269.
- **S. Hölzer**, M. Menzel, Q. Zia, U. S. Schubert, M. Beiner, R. Weidisch: "Blends of ethylene–octene copolymers with different chain architectures – Morphology, thermal and mechanical behavior" *Polymer* **2013**, *54*, 5207–5213.
- A. Teichler, **S. Hölzer**, J. Nowotny, J. Perelaer, S. Hoepfener, F. Kretschmar, C. Bader, M. D. Hager, U. S. Schubert "Combinatorial screening of inkjet printed ternary blends for organic photovoltaics: Absorption behavior and morphology", *ACS Comb. Sci.* **2013**, *15*, 410–418.
- O. Pabst, **S. Hölzer**, E. Beckert, J. Perelaer, U. S. Schubert, R. Eberhardt, A. Tünnermann: "Inkjet printed micropump actuator based on piezoelectric polymers: Device performance and morphology studies" *Org. Electron.* **2014**, *15*, 3306–3315.
- R. Schulze, M. M. L. Arras, C. Helbing, **S. Hölzer**, U. S. Schubert, T. F. Keller, K. D. Jandt: "How the calorimetric properties of a crystalline copolymer correlate to its surface nanostructures" *Macromolecules* **2014**, *47*, 1705–1714.
- **S. Hölzer**, T. N. Büttner, R. Schulze, M. M. L. Arras, F. H. Schacher, U. S. Schubert, K. D. Jandt: "Mechanisms and kinetics of the crystal thickening of poly(butadiene)-block-poly(ethylene oxide) during annealing within the melting range", *Eur. Polym. J.*, *in press*. DOI:10.1016/j.eurpolymj.2015.04.010

### Other publications

- Student research thesis: "Herstellung und Charakterisierung von Einstoff-Verbunden auf Basis von Polypropylen", Rudolstadt/Jena, **2007**.
- Diploma thesis: "Morphologie und mechanische Eigenschaften von Blockcopolymeren mit komplexen Architekturen", Jena, **2008**.



### Oral presentations

- “Beeinflussung des dynamisch-mechanischen Verhaltens von thermoplastischen Elastomeren für tribologische Untersuchungen” *Annual PhD meeting of the Fraunhofer IWM*, Obertrubach, Germany, February **2012**.
- “In-situ crystal thickening in semi-crystalline diblock copolymer under soft confinement” *DPG-Frühjahrstagung*, Dresden, Germany, March **2014**.
- “Controlling the mechanical and thermal behavior by blending of olefin random and block copolymers” *PolymerTec*, Merseburg, Germany, June **2014**.

### Poster presentations

- “Deformation behavior of lamellae-forming styrene/butadiene-based triblock copolymers with statistical copolymer middle blocks” *Polymeric Materials 2010*, Halle (Saale), Germany, September **2010**.
- “Influence of PS-modified layered silicates on the morphology and mechanical response of a styrene-butadiene based star block copolymer” *Asia-Europe Symposium on Processing and Properties of Reinforced Polymers*, Dresden, Germany, May/June, **2011**.

## Acknowledgments / Danksagung

Auf diesen letzten Seiten soll all jenen Menschen gedankt werden, die zum Gelingen dieser Arbeit beigetragen haben.

Zuerst möchte ich mich aufrichtig bei den wissenschaftlichen Betreuern meiner Dissertationsarbeit bedanken: Prof. Roland Weidisch, Prof. Mario Beiner und Prof. Ulrich S. Schubert. Die schwere Krankheit und der frühe Tod von Prof. Weidisch haben alle in unserer damaligen Gruppe im Fraunhofer IWM schwer erschüttert. Vielen Dank für das entgegengebrachtes Vertrauen und die Unterstützung seit Beginn meiner Diplomarbeitsphase, den Forschungsaufenthalts am IPF Dresden und die Möglichkeit, die Gruppe am Fraunhofer IWM mit aufzubauen. Vielen Dank, für das Verständnis und letztlich auch die Motivation zu dem sich damals anbahnenden Wechsel nach Jena. Ihre äußerst menschliche Art der Führung wird mir für immer ein Beispiel sein. Ihnen, Herr Prof. Beiner, danke ich für Ihre Hingabe mit der Sie sich, trotz diverser Leitungsfunktionen im Fraunhofer IWM sowie an der Uni, immer die Zeit genommen haben für wissenschaftliche Diskussionen — nicht nur mit Ihnen — sondern auch mit den Doktoranden von Prof. Weidisch, der aufgrund seiner Erkrankung dazu nicht mehr in der Lage war. Für diese zahl- und lehrreichen Diskussionen sowie die wissenschaftliche Betreuung der Arbeit, möchte ich mich herzlich bei Ihnen bedanken. Prof. Schubert danke ich für die Möglichkeit, meine Dissertation in seiner Arbeitsgruppe fertig stellen zu können. Danke, für ihr entgegengebrachtes Vertrauen sowie den Freiraum für eigene Ideen und Kooperationen. Außerdem, vielen Dank für die schnelle Korrektur der Arbeit.

Zudem bedanke ich mich bei den finanziellen Unterstützern der Arbeit. Erwähnen möchte ich hier die Carl-Zeiss-Stiftung, sowie die Fraunhofer-Gemeinschaft für das Stipendium sowie der Möglichkeit zur kooperativen Dissertation.

Weiterhin sei folgenden Partnern aus anderen Arbeitsgruppen herzlich gedankt:

- Prof. Stamm, Dr. Konrad Schneider und Uta Reuter vom IPF Dresden sowie den Mitarbeitern am DESY für die Möglichkeit der Synchrotron-SAXS unter Zugbelastung sowie die TEM-Untersuchungen an den S-S/B-S Blockcopolymeren.
- I thank Prof. Uhrig and Prof. Mays, (Oak Ridge National Laboratory, Tennessee), Dr. Knoll (BASF SE) as well as Dr. Henschke (The DOW Chemical Company) for providing me with these interesting polymers, which are the basis of this thesis (Multigraft copolymers, S-S/B-S triblock copolymers and the olefine copolymers, respectively.)
- Michael Gutmann und Christof Koplín vom Fraunhofer IWM in Freiburg (Breisgau) für die tribologischen Untersuchungen an den olefinen Blends.

- Matthias Menzel und Dr. Qamer Zia for the AFM and DSC measurements at Fraunhofer IWM.
- Dr.-Ing. Oliver Pabst für die exzellente Zusammenarbeit im Rahmen des P(VDF-co-TrFE)-Projektes. Im Speziellen für die Bestimmung der elektromechanischen Kennwerte und die Herstellung des Demonstrators.
- Prof. Felix Schacher für die Möglichkeit der SAXS/WAXS Untersuchungen am Nanostar sowie die aufschlussreichen Diskussionen.
- Dr. Robert Schulze, Tobias N. Büttner, Matthias M. L. Arras und Prof. K. D. Jandt für die sehr gute Kooperation im Rahmen des PB-*b*-PEO-Projektes und die vielen, interessanten Diskussionen.

Weiterhin sei meinen aktuellen und ehemaligen Kollegen ein herzliches Dankeschön ausgesprochen. Besonders verdient gemacht haben sich hierbei durch bereichernde Beiträge, seien diese fachlicher oder fach-fremder Natur: Ulli & Maria, Sven und Rothi; Katharina, Martin und Ralf; (Dr.) Ulli & (Dr.) Franzi, Claudia Stehr, Lutz Berthold sowie Thomas & Ivonne Wagner. Within the group of Prof. Schubert, I acknowledge all the members of the inkjet- as well as the nano-group for the fruitful cooperations & discussions. I thank Renzo for the technical support with the computers as well as introducing me to the DSC. Dr. Jürgen Vitz danke ich für Hilfestellungen bei all den kleinen und großen technischen Problemen sowie für die Korrekturlesung der Arbeit.

Vielen Dank meinen Freunden für die schöne, gemeinsame Zeit und die zahlreichen, interessanten Gespräche, Diskussionen und Aktivitäten.

Die letzten Worte dieser Arbeit gelten meiner Familie. Meinen Eltern und meinem Bruder danke ich für die jahrzehntelange Unterstützung, sei es finanzieller oder beratender Natur; eine helfende Hand oder zwei. Was immer sei — ich weiß ihr seid für mich da; vielen Dank dafür und *dito*. Meiner Oma Helga danke ich ebenfalls von Herzen; ich hoffe Du siehst darüber hinweg, dass Du nicht die Arbeit auf Deiner Reiseschreibmaschine in Reinform schreiben durftest. Dir, liebe Dörte, danke ich besonders dafür, dass Du bist, wie Du bist; Deine unendliche Geduld mit mir; Dein sonniges Gemüt; Dein ehrliches, freundliches Lachen. Ohne Eure Unterstützung wäre diese Arbeit nicht zustande gekommen.



## Declaration of Authorship / Selbstständigkeitserklärung

Ich erkläre, dass ich die vorliegende Arbeit selbstständig und unter Verwendung der angegebenen Hilfsmittel, persönlichen Mitteilungen und Quellen angefertigt habe.

I certify that the work here disclosed is, to the best of my knowledge, original and are the results of my own investigations, except as acknowledged, and has not been submitted, either in part or whole, for a degree at this or any other university.

Stefan Hölzer,

Jena, 08.01.2015,

.....



## Publications [P1–P7]

- Publication [P1]: Reprinted from “High-strain-induced deformation mechanism in block-graft and multigraft copolymers”, *Macromolecules* **2011**, *44*, 9374–9383. Copyright 2011 American Chemical Society.
- Publication [P2]: Reprinted with permission from “Deformation mechanism in lamellar S–S/B–S triblock copolymers”, *European Polymer Journal* **2013**, *49*, 261–269 Copyright 2013 Elsevier B.V. All rights reserved.
- Publication [P3]: Reprinted with permission from “Blends of ethylene–octene copolymers with different chain architectures – Morphology, thermal and mechanical behavior”, *Polymer* **2013**, *54*, 5207–5213. Copyright 2013 Elsevier B.V. All rights reserved..
- Publication [P4]: Reprinted with permission from “Combinatorial screening of inkjet printed ternary blends for organic photovoltaics: Absorption behavior and morphology”, *ACS Combinatorial Science* **2013**, *15*, 410–418. Copyright 2013 American Chemical Society.
- Publication [P5]: Reprinted with permission from “Inkjet printed micropump actuator based on piezoelectric polymers: Device performance and morphology studies”, *Organic Electronics* **2014**, *15*, 3306–3315. Copyright 2014 Elsevier B.V. All rights reserved.
- Publication [P6]: Reprinted from “Mechanisms and kinetics of the crystal thickening of poly-(butadiene)-*block*-poly(ethylene oxide) during annealing within the melting range”, *Eur. Polym. J.*, *in press*. DOI:10.1016/j.eurpolymj.2015.04.010
- Publication [P7]: Reprinted with permission from “How the calorimetric properties of a crystalline copolymer correlate to its surface nanostructures”, *Macromolecules* **2014**, *47*, 1705–1714. Copyright 2014 American Chemical Society.

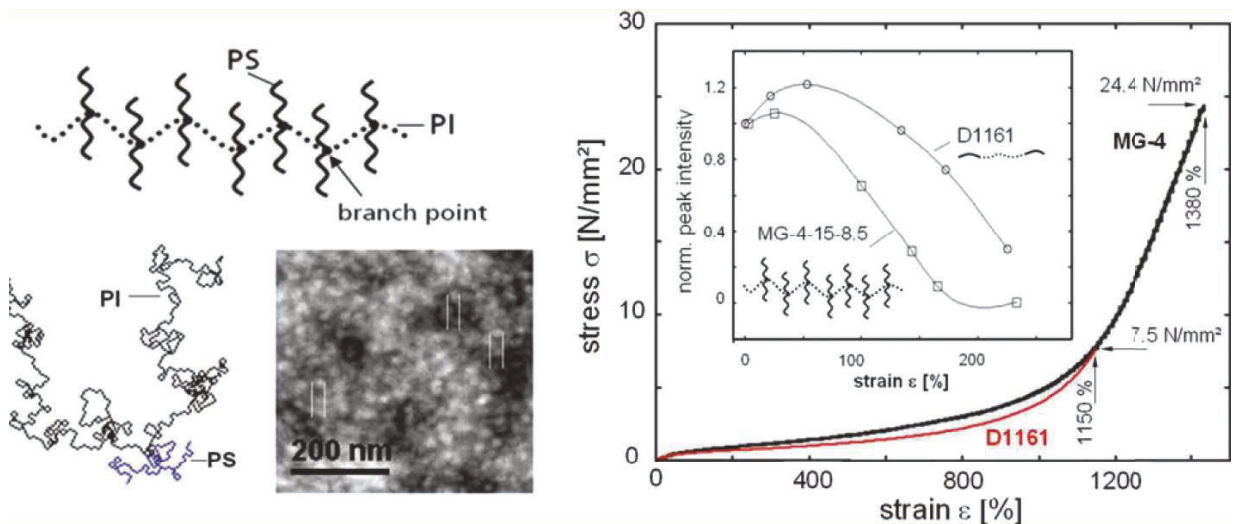




## Publication [P1]

# High-strain-induced deformation mechanism in block-graft and multigraft copolymers

Ralf Schlegel, Youngxin Duan, Roland Weidisch, Stefan Hölzer, Konrad Schneider, Manfred Stamm, David Uhrig, Jimmy W. Mays, Gert Heinrich, Nikos Hadjichristidis



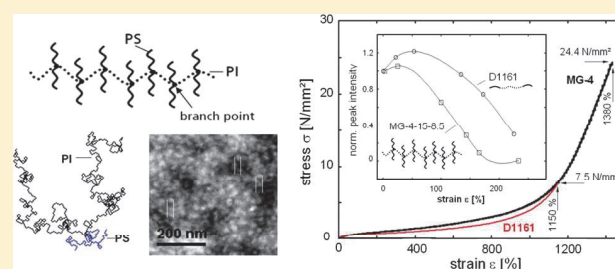
*Macromolecules* **2011**, *44*, 9374–9383



## High-Strain-Induced Deformation Mechanisms in Block–Graft and Multigraft Copolymers

R. Schlegel,<sup>†</sup> Y. X. Duan,<sup>‡</sup> R. Weidisch,<sup>\*,†,§</sup> S. Hölzer,<sup>†</sup> K. Schneider,<sup>||</sup> M. Stamm,<sup>||</sup> D. Uhrig,<sup>⊥</sup> J. W. Mays,<sup>⊥,¶</sup> G. Heinrich,<sup>||</sup> and N. Hadjichristidis<sup>||</sup><sup>†</sup>Fraunhofer Institute for Mechanics of Materials IWM, D-06120 Halle, Germany<sup>‡</sup>Key Laboratory of Rubber-Plastics (QUST), Ministry of Education, Qingdao University of Science and Technology, Zhenzhou Road, Qingdao 266042, China<sup>§</sup>Institute of Chemistry, University of Halle, D-06099 Halle, Germany<sup>||</sup>Leibniz-Institut für Polymerforschung Dresden e.V., Hohe Strasse 6, D-01069 Dresden, Germany<sup>⊥</sup>Center for Nanophase Materials Sciences, Oak Ridge National Laboratory, Oak Ridge, Tennessee 37831, United States<sup>¶</sup>Department of Chemistry, University of Tennessee, Knoxville, Tennessee 37996, United States<sup>\*</sup>Department of Chemistry, University of Athens, Athens 157 71 Greece, and Life Sciences & Engineering Division, King Abdullah University of Science and Technology (KAUST), Thuwal 23955-6900, Kingdom of Saudi Arabia

**ABSTRACT:** The molecular orientation behavior and structural changes of morphology at high strains for multigraft and block–graft copolymers based on polystyrene (PS) and polyisoprene (PI) were investigated during uniaxial monotonic loading via FT-IR and synchrotron SAXS. Results from FT-IR revealed specific orientations of PS and PI segments depending on molecular architecture and on the morphology, while structural investigations revealed a typical decrease in long-range order with increasing strain. This decrease was interpreted as strain-induced dissolution of the glassy blocks in the soft matrix, which is assumed to affect an additional enthalpic contribution (strain-induced mixing of polymer chains) and stronger retracting forces of the network chains during elongation. Our interpretation is supported by FT-IR measurements showing similar orientation of rubbery and glassy segments up to high strains. It also points to highly deformable PS domains. By synchrotron SAXS, we observed in the neo-Hookean region an approach of glassy domains, while at higher elongations the intensity of the primary reflection peak was significantly decreasing. The latter clearly verifies the assumption that the glassy chains are pulled out from the domains and are partly mixed in the PI matrix. Results obtained by applying models of rubber elasticity to stress–strain and hysteresis data revealed similar correlations between the softening behavior and molecular and morphological parameters. Further, an influence of the network modality was observed (random grafted branches). For sphere forming multigraft copolymers the domain functionality was found to be less important to achieve improved mechanical properties but rather size and distribution of the domains.



## 1. INTRODUCTION

Understanding the correlations between new molecular architectures of thermoplastic elastomers and their mechanical properties is of significant importance in polymer science. During the past decades the synthesis techniques of graft copolymer architectures have been successively improved where macromonomers of polystyrene and polyisoprene serve as building blocks from which to create complex model architectures.<sup>1–4</sup> Multigraft and block–graft copolymers are novel types of such macromolecules demonstrating the wide freedom to construct, modify, and tailor such systems. Until now an understanding of how modification of molecular architecture can be used to specifically adjust a certain mechanical property profile has not been achieved. The superelastic nature of these polymers requires further detailed and reasonable explanation. It is important to

note that the modification of molecular architecture is not the only means of adjusting the behavior of block copolymer materials. Blending triblock copolymers with a certain amount of diblocks is a common method of reducing the hardness and increasing the strain at break. However, this method strongly reduces the stress at break of these polymers. For triblock–diblock and triblock–diblock–resin blends, investigations on mechanical behavior combined with models of rubber elasticity were carried out by Roos and Creton, showing that the amount of diblocks controls the ratio between entanglements and cross-links.<sup>5</sup> This finding was demonstrated by the observation that for

Received: June 16, 2011

Revised: October 20, 2011

Published: November 10, 2011

the triblocks blended with 60 wt % of a tackifying resin (small molecule with high  $T_g$ ) the residual strain was similar to that of the pure triblock. For multigraft copolymers the increase of strain at break can be controlled by the molecular architecture, while the preservation of tensile strength is significantly better than triblock–diblock blends. Studies have been carried out considering the cyclic deformation behavior. Additionally, models of rubber elasticity have been applied to softening effects in multigraft copolymers, taking into account filler particles.<sup>6,7</sup> Furthermore, the deformation-dependent molecular orientation of tri- and tetrafunctional multigraft copolymers was studied by in situ FT-IR measurements.<sup>8,9</sup> The aim of the present paper is to investigate the large-scale deformation behavior of block–graft and multigraft copolymers and, by combining the findings from mechanical tests and modeling with information obtained from in situ FT-IR and synchrotron SAXS measurements, to deduce a reasonable explanation for their superelasticity and efficiency of physical cross-linking.

## 2. EXPERIMENTAL SECTION

**2.1. Materials.** The molecular architectures of the investigated polymers are shown in Figure 1. Tri- and tetrafunctional multigraft

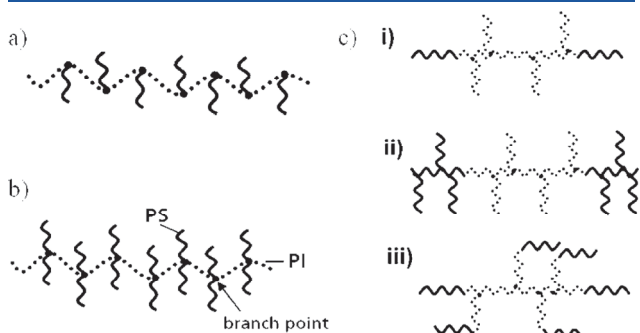


**Figure 1.** Molecular architecture of (a) trifunctional, (b) tetrafunctional multigraft copolymers,<sup>11</sup> and (c) block–graft copolymers: (i) BDG 1, (ii) BDG 4, (iii) BDG 6.

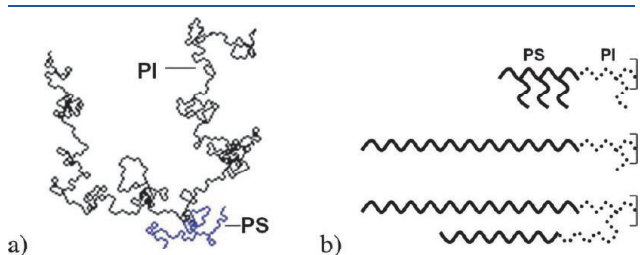


**Figure 2.** (a) Two-dimensional random walk showing a repeating unit of a tetrafunctional multigraft copolymer. (b) Outer blocks of block–graft copolymers (Figure 1c) drawn to scale.

copolymers (Figure 1a,b) consist of a rubbery polyisoprene backbone chain (dotted lines) with grafted PS branches, which are regularly spaced along the backbone. For multigraft copolymers (MG) the nomenclature MG- $n$ - $\phi$ - $\beta$  was introduced, where  $n$  is the functionality,  $\phi$  is the volume content of PS phase, and  $\beta$  is the number of PS-grafting points. To illustrate the molecular architecture, Figure 2a shows a two-dimensional random walk of a tetrafunctional branch point. Detailed molecular simulations of multigraft copolymers were carried out by Sumpster.<sup>10</sup> Details regarding the anionic synthesis techniques of these graft- and multigraft copolymers can be found elsewhere.<sup>3,4,11</sup> Block–double-graft copolymers (BDG) as shown in Figure 1c are in principle composed of an SIS triblock backbone with PI and PS arms or SI diblocks grafted to the middle or end blocks. In contrast to multigraft copolymers these blocks are grafted randomly. Three types of block–grafts were investigated: (a) PS–PI(I)<sub>10</sub>–PS termed BDG 1. (b) PS(S)<sub>5</sub>–PI(I)<sub>10</sub>–PS(S)<sub>5</sub> termed BDG 4, and (c) PS–PI(SI)<sub>4</sub>–PS termed BDG 6. Figure 2c shows the outer blocks of the BDG types drawn to scale.

The molecular weight of the graft copolymers was measured by size exclusion chromatography with multiangle light scattering detection (SEC-MALLS).<sup>3,4</sup> Relevant molecular characteristics are summarized in Table 1, where  $M_{w,spacer}$  is the molecular weight between two adjacent PS grafts,  $M_{w,graft}$  is the molecular weight of the arms, and  $M_{w,block}$  refers to the outer blocks. The overall molecular weight of multigraft chain is obtained by multiplying  $M_w$  of a repeating unit with the number of branch points resulting in values between 400 and 980 kg/mol. As a reference material, the commercially available TPE Kraton D1161 was chosen, which is a SIS–SI triblock–diblock copolymer with about 15 wt % PS and similar to the MG 4 multigrafts. The amount of diblock copolymer is 19 vol %.

**2.2. Experimental Methods.** Samples were prepared by solution casting. The polymers were dissolved in toluene, and the solutions were poured into glass forms, allowing the solvent to evaporate over 7 days. To remove residual toluene, the polymer films were annealed at 70 °C under vacuum for 3 days. For mechanical testing, dog-bone samples according ISO 527-2 of type 5B (overall length 20 mm, parallel length 6 mm) were stamped from the films. Mechanical characterization was performed with a Zwick/Roell universal testing machine Z020 equipped with a 500 N load cell. The samples were deformed at a constant strain rate of 0.025 s<sup>-1</sup> cross-head displacement, resulting in a true strain rate of  $0.0204 \pm 1.3 \times 10^{-3}$  s<sup>-1</sup>. The strain was measured by an optical method using an imaging system (GOM, Aramis). Images were taken at a constant time interval, and the positions of the markers were automatically detected based on the gray scale value profile (Figure 3). The obtained optical true strain was further correlated to the stress data at equal time intervals and plotted in  $\sigma$  vs  $\epsilon$  diagrams to apply the rubber elasticity models.

The morphology was characterized by synchrotron SAXS at DESY Hamburg (BW4 at DORIS III storage ring). Scattering patterns were obtained at a sample to detector distance of typically 6049 mm. The wavelength of characteristic radiation was 0.138 nm. The samples were mounted in a modified mechanical testing device (Kamrath and Weiss) which was additionally used to measure strain-dependent scattering patterns.<sup>12</sup> The average domain distance  $d_{av}$  was calculated according to

**Table 1.** Molecular Data of Multigraft and Block–Graft Copolymers

	$\Phi_{PS}$ [vol %]	$M_{w,PI-spacer}$ [kg/mol]	$M_{w,PS-graft}$ [kg/mol]	$M_{w,PI-graft}$ [kg/mol]	$M_{w,PS-block}$ [kg/mol]	$M_w$ [kg/mol]
MG-3-17- $\beta$	17	86	32			$\beta \cdot 117$
MG-4-15- $\beta$	15	97	11			$\beta \cdot 104$
BDG 1	28	73		2.4	21.5	145
BDG 4	28	68	2.7	3.3	7.7	143
BDG 6	30	163 (backbone) 41 (average)	12 (PI–PS grafts)		21.5	287

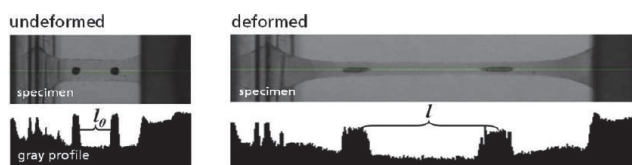


**Figure 3.** Undeformed and deformed elastomer samples with optical markers and corresponding gray profile ( $l_0$ : distance at  $t = 0$ ;  $l$ : marker distance during deformation).

the relation  $d_{av} = 2\pi/q^*$ , where  $q^*$  is the position of the primary reflection peak.

FT-IR measurements were carried out in the group of Prof. H. W. Siesler at University Essen using a Bruker IFS88FT-IR spectrometer with a spectral resolution of  $4\text{ cm}^{-1}$ . The samples were stretched with an electromechanical film stretching device mounted in the sample compartment of the spectrometer. About  $30\text{--}40\ \mu\text{m}$  thick films were deformed at a constant rate of  $3.2\text{ mm/min}$ . The polarization direction of the IR radiation was adjusted by a pneumatically rotatable wire-grid polarizer (SPECAC) to obtain the spectra parallel and perpendicular to the stretching direction by a rapid  $90^\circ$  rotation.<sup>9</sup>

**2.3. Applied Models.** Stress–strain data were analyzed by applying the slip-tube model of Rubinstein and Panuykov.<sup>13</sup> The stress response is described by eq 1, where  $G_{c,ST}$  and  $G_{e,ST}$  are the chemical and the physical cross-link modulus and  $\lambda$  is the elongation ratio  $l/l_0$ .

$$\sigma^{\text{load}} = \left( \lambda - \frac{1}{\lambda^2} \right) \left( G_{c,ST} + \frac{G_{e,ST}}{0.74\lambda + 0.61\lambda^{-0.5} - 0.34} \right) \quad (1)$$

In contrast to more complex models including strain hardening effects, the parameters of the slip tube model are easy to obtain by plotting the reduced stress  $\sigma_R = \sigma^{\text{load}}/(\lambda - \lambda^{-2})$  vs the expression  $(0.74\lambda + 0.61\lambda^{-0.5} - 0.34)^{-1}$ . By this procedure, eq 1 reduces to an equation of the type  $y(x) = a + bx$ , where  $a$  and  $b$  are the two moduli. In contrast, in the case of the nonaffine tube model taking into account finite chain extensibility, a nonlinear least-squares algorithm with several iteration cycles is required to fit the data. However, the advantage of the latter model is that it covers all experimental data and therefore offers a better accuracy in the obtained model parameters. This model yields additionally a parameter representing the portion of elastically active entanglements ( $n$ ), which is defined by  $n_e/T_e$ , where  $T_e$  is the Langley trapping factor. This parameter can be understood as the probability that a certain entanglement becomes a permanently trapped one and  $n_e$  as the number of statistical chain segments between two successively trapped entanglements.<sup>14</sup>  $T_e$  was assumed as unity for all investigated polymers. However, based on sol extraction measurements, the value can be calculated for chemical cross-linked networks.<sup>15</sup> The stress response during uniaxial loading is obtained by deriving the strain energy function of the model with respect to the elongation  $\lambda$ , resulting in eq 2.

$$\sigma_0^{\text{load}} = G_c \left( \lambda - \frac{1}{\lambda^2} \right) \left( \frac{1 - \frac{1}{n}}{\left( 1 - \frac{1}{n} \left( \lambda^2 + \frac{2}{\lambda} - 3 \right) \right)^2} - \frac{1}{n} \right) + 2G_e \left( \frac{1}{\sqrt{\lambda}} - \frac{1}{\lambda^2} \right) \quad (2)$$

Load cycles of hysteresis curves were evaluated using this extended nonaffine tube model of rubber elasticity with finite chain extensibility according to eq 2.<sup>16,17</sup> The parameters  $G_c$  and  $G_e$  of the slip tube are comparable with nonaffine tube if the model fit is performed below the inflection point of the stress–strain curve. Finite chain extensibility results the up turn of the stress–strain curve at high strains. This was

**Table 2.** Morphology and Average Domain Distance  $d_{av}$

material	morphology	$d_{av}$ [nm]
MG-3-17-3.7	spherical	40
MG-4-15-5.1	spherical	25
MG-4-15-8.5	spherical	23
BDG 1	cylindrical	37
BDG 4	cylindrical	39
BDG 6	lamellae (weakly ordered)	29

especially observed for predeformed samples where in contrast to undeformed samples the inflection point is shifted to lower values.

Further, the hysteresis unload curve was characterized by applying an energy-based softening model in eq 3, where  $W(\lambda)$  and  $W_{\text{max}}$  are the strain energy functions of the nonaffine tube model during deformation and at maximum elongation, respectively,  $b$  is a softening parameter, and  $\sigma_0^{\text{load}}$  is the stress response of the initial load curve.<sup>18</sup>

$$\sigma^{\text{unload}} = \sigma_0^{\text{load}} \exp(-b\sqrt{W_{\text{max}} - W(\lambda)}) \quad (3)$$

## 3. RESULTS AND DISCUSSION

**3.1. Molecular Deformation Behavior and Morphological Aspects.** Morphology and average domain distance  $d_{av}$  of the undeformed polymers are shown in Table 2. The tri- and tetrafunctional multigrafts form spherical PS domains. It is known from other block copolymer morphology work that these domains can be arranged in a face-centered cubic (fcc), body-centered cubic (bcc), and hexagonal close-packed (hcp) lattice structure.<sup>19,20</sup> In the presents studies no long-range order was observed for sphere forming multigrafts. The average domain distance  $d_{av}$  is clearly decreasing with increasing functionality and slightly decreasing with the number of branch points. Multigraft copolymer morphology can be predicted by combined use of the Milner phase diagram and the constitutive block copolymer concept, which is in fair agreement with the observed morphologies.<sup>21–23</sup>

For the block–graft copolymers BDG 1 and BDG 4,  $d_{av}$  was observed to be governed by  $M_{w,PI\text{-spacer}}$  and further by the number and lengths of the PI arms grafted to the middle block. The former aspect is reasonable because the end-to-end distance  $r$  is increasing by higher  $M_w$ . Further the same effect is obtained by increasing  $M_w$  of the grafted side chains, which can be expected to expand the polymer coil of the backbone. BDG 6 exhibited a weakly ordered lamellar morphology, as supported both by a peak at  $2q^*$  in the scattering diagram and by a slight yield point during tensile testing; however, TEM micrographs could not clearly verify this order.

To correlate molecular data with the results of microstructural investigations, the number of PS arms necessary to form one domain (functionality of domains) should be obtained, which is of importance to discuss the efficiency of physical cross-linking. As a first approximation the average PS domain size should be calculated from the known value of the PS content and the average domain distance. The assumption of densely filled phases (PS and PI) is strictly not true; however, results are in fair agreement with experimental data as shown later. The volume of the spherical PS domains can be estimated by eq 4, where  $d_{av,PS}$  is the diameter of the PS sphere,  $d_{av,PI-PS}$  is the average PI–PS domain distance, and  $\Phi_{PS}$  is the volume fraction of PS. Assuming

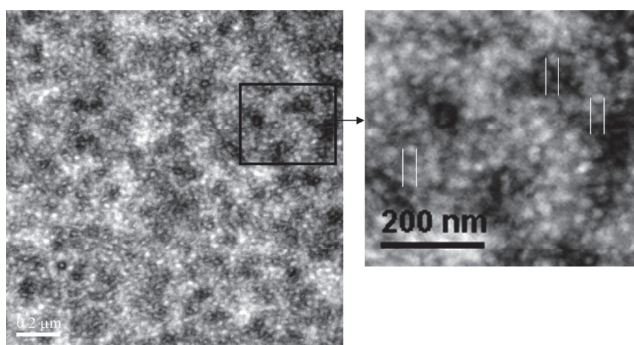


**Figure 4.** TEM micrograph of the morphology of MG-3-17-3.7.

a bcc order,  $d_{av,PS,sph}$  can be obtained with the relation given in eq 5. The number of PS monomers per sphere is obtained by eq 6, where  $V_{s,seg}$  is the segmental volume of styrene ( $0.176 \text{ nm}^3$ ).<sup>23</sup> This value is slightly different from that calculated by the relation  $V_{PS,seg} = M_{w,PS-mon}/(\rho N_{Av})$ , with  $M_{w,PS-mon}$  the molecular weight of PS monomer,  $\rho$  the density of PS, and  $N_{Av}$  the Avogadro number, which equals  $0.19 \text{ nm}^3$ . Finally, the number of PS grafts forming one domain is obtained by eq 7, where  $N_{PS,arm}$  is the degree of polymerization of one graft.

$$V_{PS,sph} = \frac{1}{6} \pi d_{av,PS}^3 \quad (4)$$

$$V_{bcc} = \Phi_{PS} = \frac{2V_{sph}}{V_{lattice}} = \frac{\frac{1}{6} \pi d_{av,PS,sph}^3}{d_{av,PI-PS}^3};$$

$$d_{av,PS,sph} = d_{av,PI-PS} \sqrt[3]{\frac{3}{\pi} \Phi_{PS}} \quad (5)$$

$$N_{PS,sph} = V_{PS,sph}/V_{PS,seg} \quad (6)$$

$$n_{PS,grafts} = N_{PS,sph}/N_{PS,arm} \quad (7)$$

Thus, with MG-3-17 showing a  $d_{av,PI-PS}$  of  $\sim 40 \text{ nm}$  and MG-4-15 of about  $25 \text{ nm}$ , we can calculate the average values for  $d_{av,PS,sph}$  of  $24$  and  $14.5 \text{ nm}$ , respectively. For the trifunctional multigraft this is in accordance with TEM micrographs shown in Figure 4, where the average diameter of the PS domains is in between  $23$  and  $27 \text{ nm}$ . Further, the functionalities of the PS spheres (number of branch points connected to the domains) according eq 7 are  $128$  and  $40$  for tri- and tetrafunctional MGs, respectively.

On the basis of computer simulations, Sumpter has shown that the PS arms of tetrafunctional branch points form pseudospherical domains with several intradomain interactions of the PS grafts.<sup>11</sup> These small domains were further suggested to interact (interdomain interactions) with other domains forming larger clusters.

Now these findings should be correlated to the orientation of PI and PS monomers during deformation by results from FTIR, which can be used to obtain information on the efficiency of physical cross-linking in dependence of the number of grafting points. The orientation functions of both PS and PI monomers

are plotted in Figure 5 vs the applied strain. In Figure 5,  $f$  is the orientation function perpendicular to the stretching direction (SD) calculated by the relation  $f = -2(R - 1)/(R + 2)$ .  $R$  represents the dichroic ratio given by  $R = A_{||}/A_{\perp}$ , with  $A_{||}$  and  $A_{\perp}$  being the absorbencies of the selected IR band parallel and perpendicular to SD, respectively. The method of data analysis can be found in our former publications.<sup>8,9</sup>

The orientation function was observed to show an increasing trend with higher strain for tetrafunctional multigraft copolymers and also for trifunctional MGs (not shown). This increase indicates that the domains are deformable up to high external strains.  $\Delta f_{PI,PS}$  represents the difference in the orientation functions of PI and PS. Between  $1300$  and  $1400\%$  strain, this value was found to be about  $0.05$  for a trifunctional architecture with  $2.6$  branch points (larger domains as compared to MG-4-15), while it was  $\sim 0.01$  for the MG-4-15-5.1 (Figure 5a). The difference appears reasonable when comparing the average diameter of the PS spheres. These findings suggest lower interfacial area and a larger amount of unoriented PS monomers in the cores of the domains for the MG-3-17 type. The ratio of orientable to unorientable PS monomers can be assumed to be higher for the tetrafunctional MG, which is reflected in the reduced value of  $\Delta f_{PI,PS}$ . For the tetrafunctional MG with lower number of branch points (Figure 5b) larger differences between the orientation functions were observed, although the average domain distances ( $23$ – $25 \text{ nm}$ ) are similar to MG-4-15-5.1.<sup>24</sup> In the case of MG-4-15-3.3 (Figure 5b)  $\Delta f_{PI,PS}$  first becomes obvious at about  $600\%$ , where  $f_{PS}$  reaches a plateau. However, such a plateau was not observed for the MG-3-17 material.<sup>8</sup> This effect may be attributed to the physical cross-linking density expressed by the number of  $I_2S_2$  repeating units ( $\beta$ ). Obviously, multigrafts with high  $\beta$  and small domains can keep the cohesion of the domains at high strains because the internal stress is distributed to a larger number of grafting points and therefore spherical domains. This assumption is reasonable because for spherical morphologies it was shown that domain–domain bridging is the most probable configuration of the PI spacer.<sup>8,25</sup> For the appearance of the plateau, two explanations may be given: (a) PS grafts are pulled out of the domains if a critical stress is achieved, and they return to its original coiled configuration; (b) a fracture of PS domains without further orientation of the monomers.

Because of the confinement by neighboring PI chains which prevent a return of the PS grafts to their coiled shape, point (a) appears to be unreasonable. Therefore, it must be concluded that the continuous orientation of PS covers both effects chain pull out and orientation of PS monomers in the interface. The partial or complete pullout of PS grafts we term stress-induced mixing of polymer chains. The fact that in case of the MG-3-17 material no plateau was observed (obviously no fracture of the domains) may be attributed to the larger  $M_w$  of the grafts, which on the one hand results in a stronger PS–PS interaction; on the other hand, this distributes the stress to a reduced number of domains. The decrease of  $T_g$  by reduction of graft  $M_w$  is less important because this would only reduce the glass transition temperature of PS to about  $360 \text{ K}$ .<sup>26</sup> Additionally, less attention must be paid to the entanglement  $M_w$  of PS<sup>26,27</sup> because testing temperature is far below the  $T_{g,PS}$ .

**3.2. Deformation Characteristics.** The tensile and hysteresis behavior of multigraft and block–graft copolymers are now discussed. The mechanical data were analyzed by the slip tube

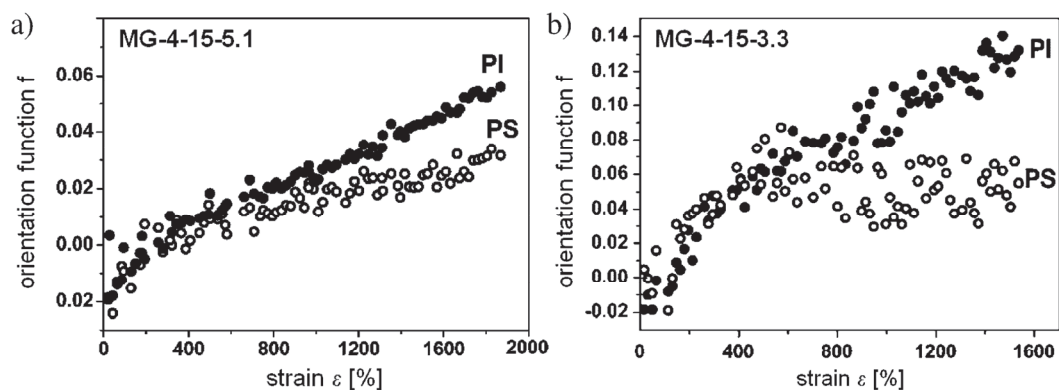


Figure 5. Strain-dependent orientation function of tetrafunctional multigraft copolymers.<sup>9</sup>

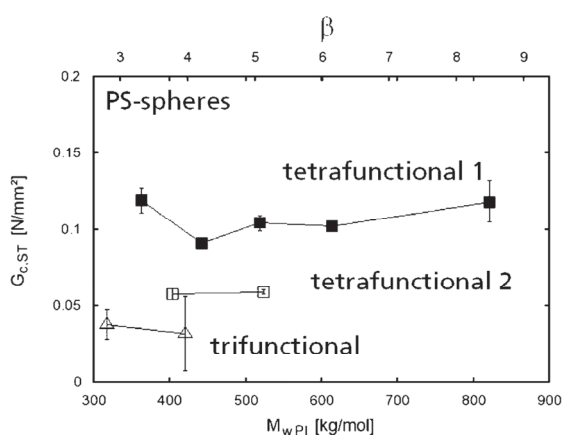


Figure 6. Chemical cross-link modulus obtained from the slip tube model for tri- and tetrafunctional multigraft copolymers with 15–17 vol % PS (tetrafunctional 1 and 2 are multigrafts of type MG-4-15 originating from different batches).

and the nonaffine tube model. Investigations on the fractured morphology of block-graft copolymers are also presented.

**3.2.1. Tensile Behavior of Sphere Forming Multigraft Copolymers.** The deformation behavior of multigrafts with spherical morphology was characterized through medium elongations below the inflection point of the stress-strain curve by applying the slip tube model to the tensile data, and the chemical  $G_{c,ST}$  and physical  $G_{e,ST}$  cross-link modulus were obtained.  $G_{c,ST}$  is plotted vs the molecular weight of the PI backbone and the number of branch points  $\beta$  in Figure 6. In contrast to the  $G_e$ , which was found to increase slightly with  $\beta$ ,<sup>28</sup>  $G_{c,ST}$  is independent of the overall molecular weight. This observation is reasonable because the investigated multigrafts are regularly spaced. The slight increase of  $G_{c,ST}$  above 4 branch points (tetrafunctional 1) may be attributed to the improved distribution of the PS domains in the matrix.  $G_c$  is nearly branch point independent for tetrafunctional multigrafts. Such constancy may be understood because this value is obtained at medium elongations below 500% where the stress acting on each branch point is low (see section 3.1).

The in situ deformation characteristics were studied by synchrotron SAXS. Figure 7 shows the in situ deformation scattering pattern of the tetrafunctional multigraft copolymer MG-4-15-8.5 and Kraton D1161. Because the average

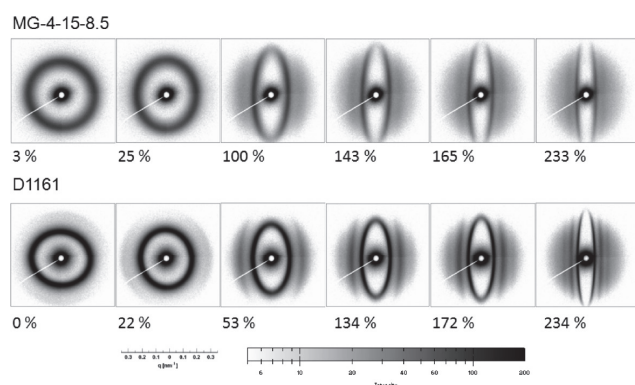
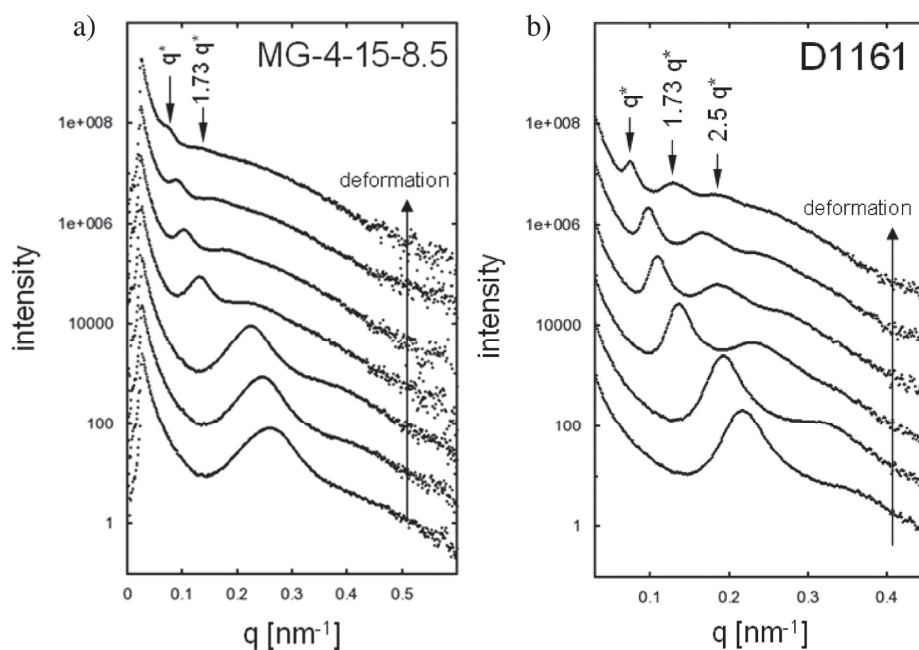


Figure 7. Scattering pattern of the sphere forming tetrafunctional multigraft copolymer and Kraton D1161, stretching direction horizontally.

domain distance decreases with increasing ring radius of the primary reflection peak, D1161 shows a lower value for  $d_{av}$  (29 nm) in comparison to MG-4-15-8.5 (22.4 nm). The patterns become elliptical by increasing the deformation.  $d_{av}$  increases in the stretching direction while it decreases perpendicular to it.

For Kraton D1161 a secondary and ternary reflection peak can be observed. The ratio between the position of the secondary and primary peak reflection is at about  $1.73q^*$  at medium to high elongations. This value was also observed for the tetrafunctional multigraft copolymer, while the intensity of the secondary reflection peak is obviously less. The formation of an ordered structure may be caused by finite extensibility of the PI chains. Short chains can be assumed to reach their finite extensibility earlier than long chains, and the stress is forcing the spherical domains into an ordered structure. This tendency is more pronounced for the D1161 in comparison to MG-4-15 architecture. From literature three types of densely packed structures are known (fcc, bcc, hcp).<sup>20</sup> The scattering positions at  $1.74q^*$  is correlating to the (110) reflection in the hcp structure. Further, for the stretched Kraton D1161 a peak at about  $2.5q^*$  appears, which may correspond to the (203) diffraction plane of hcp (Figure 8). Other peaks cannot be found. It can be assumed that by stretching these polymers the domains are forced into a hcp lattice structure. These domains are at about 11.7 nm in diameter for MG-4-15-8.5, while for D1161  $d_{av,PS,sph}$  is 16.5 nm. The fact that nearly no secondary reflection peak is observed illustrates



**Figure 8.** Intensity vs  $q$  plot of the scattering pattern in Figure 7 obtained in the stretching direction for (a) MG-4-15-8.5 and (b) Kraton D1161.

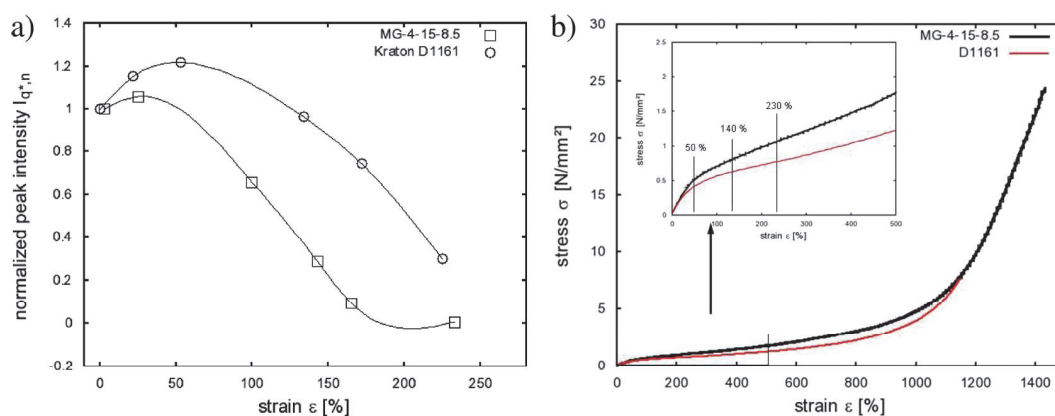


**Figure 9.** (a) Normalized intensity of the primary reflection peak vs elongation (in stretching direction). (b) Corresponding stress–strain curve of MG-4-15-8.5 and Kraton D1161 (elongation measurement with a Zwick/Roell multiXtens system).

that these domains are highly deformable and that their shape is more maintained in the case of Kraton D1161 (larger domains).

Comparing the undeformed state of the tetrafunctional multi-graft copolymer in Figure 7, it becomes obvious that (a) the peak width appears broader and (b) the intensity of the primary reflection peak is less in comparison to Kraton D1161. From this observation it can be concluded that the matrix of the latter contains more effective scattering centers and that the MG-4 copolymer reveals a broader domain size distribution. In Figure 9a, the peak intensity of the primary reflection peak is related to the unstretched state and plotted vs the applied elongation. The peak intensity was obtained by subtracting the intensity at the right bottom of the peak from the intensity at  $q^*$ . The scattering intensity of both materials was found to differ clearly.  $I_{q^*}$  is about 2–3 times higher for Kraton D1161 in comparison to MG-4. It shows a maximum at about 140% and decreases to round 2 at about 233% strain.

In Figure 8, up to about 50% strain an increase of  $I_{q^*,n}$  can be observed, which correlates to the formation of a strain-induced domain ordering. The domains are initially well separated in the undeformed state, and the increase of domain order let assume that the domains approach each other. The inflection point of both curves corresponds to the end of the neo-Hookean region (Figure 9b). For Kraton D1161 the transition to the linear stress–strain region is observed at higher strains in comparison to the MG-4 type (Figure 9b), and the inflection point is shifted in the same direction. Further, elongation results in a reduction of the normalized peak intensity.

This reduction indicates to a decrease of scattering centers in the matrix while the domain order is still increasing. This can be clearly observed by the presents of secondary and primary reflection peaks in Figures 7 and 8. During elongation the embedded PS domains (coiled PS branches) are dissolved in the PI matrix (elongated) by deformation, which was also found



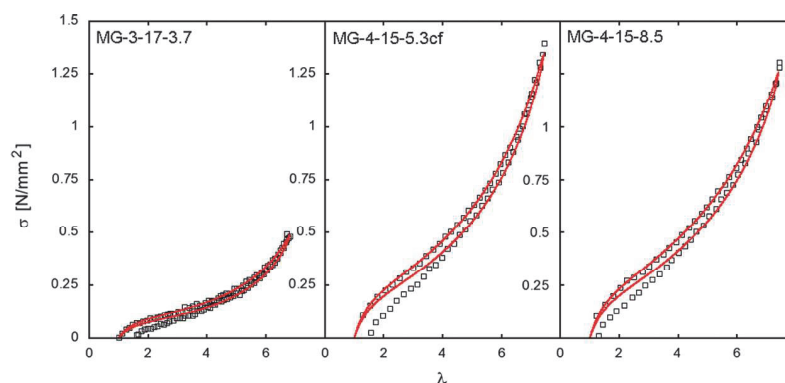


**Figure 10.** Hysteresis data (squares) and model curves according eqs 2 and 3 (red lines) for tri- and tetrafunctional multigraft copolymers.

**Table 3. Model Parameters of the Nonaffine Tube Model with Finite Chain Extensibility and the Softening Model**

	nonaffine tube model			softening model $b$ (N m) <sup>-1/2</sup>
	$G_c$ [kPa]	$G_e$ [kPa]	$n$	
MG-3-17-3.7	26	48	114	0.177
MG-4-15-5.3cf	84	86	171	0.086
MG-4-15-8.5	90	80	197	0.083
BDG 4	48	95	113	0.13
BDG 1	68	125	109	0.094
BDG 6	296	447	74	0.078

by FT-IR. We assume that this behavior corresponds to a strain induced mixing of the copolymer chains. The polymer chains are assumed to slide along each other, yielding a reduction of the  $T_g$  which may promote further sliding.

**3.2.2. Cyclic Deformation of Sphere Forming Multigraft Copolymers.** Mechanical characterization at high strains was done by performing hysteresis tests of pre-deformed samples and applying the nonaffine tube model to the stress–strain data. The samples were stretched in a first cycle to 900% to pre-deform the morphology and in the second cycle to 700% only to avoid further stress softening. The rubber elasticity model was applied to the second hysteresis cycle because in this cycle softening effects originating from the virgin morphology are less. Hysteresis data and corresponding model curves are shown in Figure 10. The experimental error of the strain measurement method is about 0.5 px, which corresponds here to  $\sim 50$   $\mu\text{m}$ . However, this error is less significant because of the high strains. In further work theoretical accuracy of the strain measurement procedure was improved to typically 0.0045 px. A detailed discussion of this development will be part of a future publication. To determine analytical errors, three hysteresis tests of Kraton D1161 samples were performed. The data were evaluated by the nonaffine tube and the softening model. We obtained model parameters and errors for the second cycle at 700% as follows:  $G_c = 0.136$  ( $\pm 4.2\%$ ) MPa;  $G_e = 0.218$  ( $\pm 1\%$ ) MPa,  $n = 240$  ( $\pm 9.5\%$ ), and  $b = 0.0303$  ( $\pm 15\%$ ) (N m)<sup>-1/2</sup>. Because of the limited amount of multigraft and block–graft copolymers, each molecular architecture of these polymers was characterized using only one sample.

In Figure 10, it can be observed that the model curve approaches the point of zero deformation while the experimental

data do not. An explanation may be given by the fact that viscoelastic material effects are neglected in the softening model.<sup>18</sup> However, the advantage of this combined model is that it offers a minimum set of parameters which are easily correlated to the material behavior. A closing of the hysteresis curve can be observed if the samples shape enables a tensile and compressive deformation (dumbbells). The presently used dog-bone-shaped samples were exclusively deformed in tensile mode (positive forces).

Pronounced low stress values can be observed for the trifunctional multigraft copolymer with an average domain distance of about 40 nm. The tetrafunctional types with 8.5 and 5.3 (cf = coarsely fractionated) are showing a steeper slope in the middle part, which corresponds to an increase in  $G_c$ . All model parameters are summarized in Table 3. The increase of  $G_c$  directly correlates with a reduction of the softening parameter. The decrease of  $b$  indicates that the unload cycle approaches the load cycle. This correlates with an increase of the PS-domain distribution. By comparing  $G_c$  and  $b$  for the MG-3 and MG-4 type, it can be concluded that high deformable PS domains are more important to achieve improved mechanical properties than a high functionality of these domains. The model parameter  $n$  directly correlates to the molecular weight of the PI spacer. The lower  $n$  value of MG-3-17 in comparison to MG-4-15 is in agreement with the molecular weight of the PI backbone chain, which are 86 and 97 kg/mol, respectively. However, it can be observed that the magnitude of the change in  $n$  is less reasonable. This parameter almost doubles but  $M_{w,PI\text{-}spacer}$  increases by about 13% only. By comparing  $G_c$  of the nonaffine tube and the slip tube model, slightly improved values can be observed for the latter model since in case of slip tube the PS domains were considered as filler particles using the Einstein/Guth relation as a prefactor:

$$G_{c,ST} = G_{c,ST}^0 (1 + 2.5\Phi_{PS} + 14.1\Phi_{PS}^2) \quad (8)$$

However, multiplying the  $G_c$  value of the nonaffine tube with the term in parentheses of eq 8 leads to slightly higher values as obtained by the slip tube model (Figure 6). This difference may be attributed to softening effects from the first to the second cycle.  $G_c$  was observed to decrease by about 17–22% between these two cycles. These softening effects can be attributed to two mechanisms: the breakdown of aggregated clusters of spherical domains and also to domain chain pullout (resolving of “physical” cross-links) and fracture of domains. Because of the breakdown of filler cluster aggregates, the estimated modulus  $G_{c,ST}$  is expected to be lower for virgin undeformed samples in

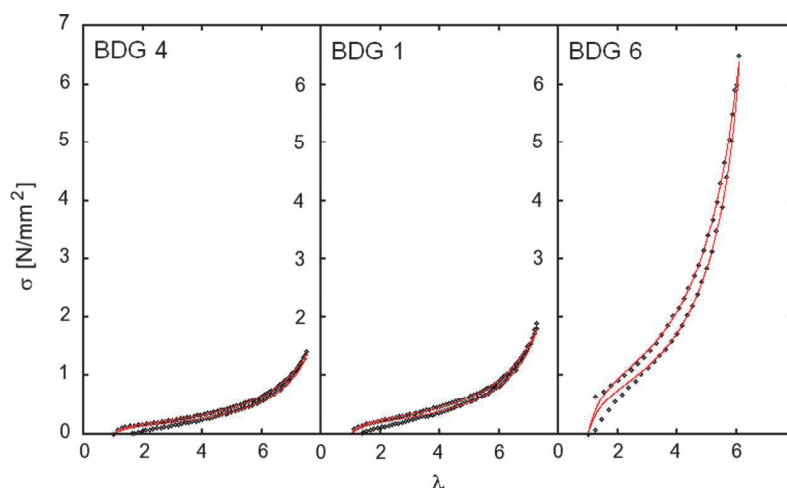


Figure 11. Hysteresis data and model curves for block–double-graft copolymers.

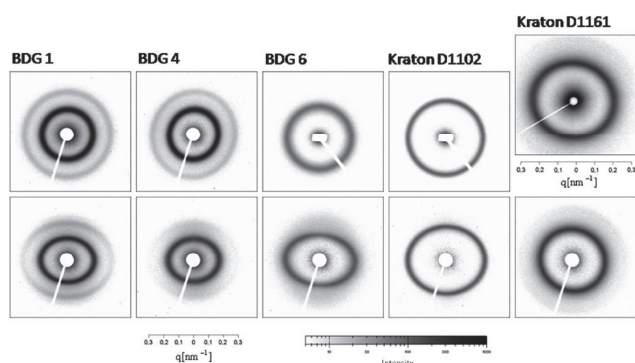


Figure 12. Scattering pattern of block–double-graft and commercially available triblock copolymers: top, undeformed; bottom, after deformation and relaxation (previous stretching direction vertically).

comparison to the modulus  $G_c$  from the nonaffine tube model in the second cycle. This assumption is verified when considering  $G_{c,ST}$  for MG-3-17-3.7 and MG-4-15-8.5 divided by the Einstein/Guth prefactor.

**3.2.3. Cyclic Deformation of Block–Graft Copolymers.** Hysteresis and model curves for block–graft copolymers are shown in Figure 11. At similar hysteresis strain the stress response is different for the investigated materials. It is increasing with decreasing  $d_{av}$ . In comparison to BDG 1 and 4, a reduced maximum true hysteresis strain can be observed for BDG 6, but the maximum hysteresis stress is exceeding that of BDG 1 and 4 by about a factor of 3.5. The parameters of the nonaffine tube model and the softening model are summarized in Table 3. On the basis of the information from molecular architecture, it can be expected that  $G_c$  is decreasing with increasing molecular weight of PS backbone, which is not verified by the comparison between BDG 4 and BDG 1 (Tables 1 and 3). In contrast, BDG 6 reveals an improved  $G_c$ , which indicates that not the molecular weight of the PS backbone is important but rather the average  $M_{w,PI}$  between neighboring PS blocks, which is about 41 kg/mol. Additionally, significant differences in the mechanical behavior of block–grafts were observed when comparing the model parameters between first and second hysteresis cycle, where  $G_c$  reduces by about 72 and 80% for BDG 1 and 4 and by about

30% for BDG 6 only. Aspects contributing to the increase of  $G_c$  from BDG 1 to BDG 6 are (i) the reduced  $d_{av}$  resulting in a well-dispersed filler structure, (ii) the long PS outer blocks providing an effective connection to the PS domains, and (iii) the small  $M_{w,PI-spacer}$  which increases the chemical cross-link modulus. Contributing further to improved  $G_c$  values is the fact that in case of BDG 6 the PS blocks are grafted randomly to the PI backbone, resulting in a multimodal PI network, which is in contrast to MG-3 and MG-4 where PS blocks are in equal distance. Mark has shown that for end-linked PDMS networks strain at break and tensile strength increases by combining small and long network chains.<sup>29</sup> The expectation that strain at break is reduced by small chains (weakest link theory) was not observed because the deformation is highly nonaffine. However, detailed investigations are available only for bimodal networks due to the large molecular combinations for three and more chain lengths. In the case of BDG 4 the PS outer blocks can be considered as branched, and about 10 kg/mol is an estimated value for the average block length. For BDG 1 the  $M_w$  of the outer block length is 23.5 kg/mol and for BDG 6 two values 12 kg/mol for the diblock and 21.5 for the triblock have to be taken into account. Under these considerations BDG 6 fulfills the three aspects mentioned before to achieve small well-distributed domains and effective physical cross-linking. The number of statistical segments  $n$  as a model parameter most reasonably explains the correlation to  $M_{w,PI-spacer}$ . In the case of BDG 6, this value is the lowest among the block–double grafts. The differences between BDG 1 and 4 should be statistically verified by further investigations.

**3.2.4. Microstructure of Undeformed and Deformed BDG Types.** Deformation characteristics of fractured morphologies of the block–graft types were studied by synchrotron SAXS. Scattering patterns are shown in Figure 12. The patterns reveal at least one primary peak and in the cases of BDG 4 and 1 a secondary reflection peak. The position corresponds to a morphology composed of hexagonally packed cylinders with reflection peaks at  $3^{1/2} q^*$  and  $7^{1/2} q^*$ . In the case of BDG 6 a slight secondary peak was found at  $2q^*$ , indicating a lamellar morphology with weak long-range order.

Further, samples of the investigated polymer films were deformed to 800% cross-head displacement and subsequently unloaded to zero force. The samples were removed from the

**Table 4.** Average Domain Distance of Deformed Samples after about 2 weeks of Relaxation

	BDG 1	BDG 4	BDG 6	D1102	D1161
$d_{av,res  }$ [nm]	41.6	42.7	36.3	27.8	30.1
$\lambda_{res  }$	1.09	1.1	1.23	1.1	1.01

clamps, relaxed for about 14 days at room temperature, and again investigated by SAXS. The obtained scattering patterns are shown at the bottom of Figure 12. The elliptical shape of the pattern becomes more pronounced from BDG 4 to BDG 1 to BDG 6. The secondary peak at  $(3q)^{1/2}$  was still observed for the two BDG 4 and BDG 1 architectures. The position of the primary reflection peak is decreasing in the direction in which the sample was originally elongated, and it is increasing perpendicular to it, which corresponds to the average domain distance.  $d_{av}$  increases in the stretching direction, and it decreases perpendicular to it.  $d_{av}$  was obtained for undeformed and deformed/relaxed samples parallel to the previous stretching direction. These values are summarized in Table 4. Additionally, the triblock copolymer Kraton D1102 (SBS type, 28 wt % PS, 17 wt % diblock) with a cylindrical morphology was investigated for comparison. The residual deformation  $\lambda_{res||}$  was calculated based on the average domain distance of the undeformed samples.

When considering the values of  $\lambda_{res||}$  for the copolymers with cylindrical morphology BDG 1, BDG 4, and Kraton D1102, we can observe similar values. For the disordered morphology of BDG 6 with a weak lamellar long-range order, a clearly higher value of  $\lambda_{res||}$  can be found. In contrast, for Kraton D1161 (spherical PS domains)  $\lambda_{res||}$  is almost identical to the undeformed samples. It is assumed that these parameters are specific for the type of morphology.

Furthermore, when calculating the residual elongation perpendicular to the stretching direction, it was found that the incompressibility condition was not fulfilled. The highest deviation was observed for BDG 6 (+16.5%) while BDG 4 (+14.1%) and D1102 (+15.7%) are similar but slightly below BDG 6. BDG 1 and D1161 were found to show a deviation from incompressibility of +5.3 and +7.2%. It was originally assumed that rigid domain fragments of formally continuous morphologies (BDG 6) are acting as steric hindrances in the back cycle, which do not allow the polymer matrix to return to its original constitution resulting in cavities on nanoscale. However, this assumption could not be verified because the expected additional scattering was not observed. We rather suspect that the polymer matrix keeps a strain induced orientation, which can be interpreted as partial mixing of the polymer chains.

To verify this assumption, the invariant  $Q$  was calculated using eq 9 where  $I(q_x, q_y)$  represents the scattering intensity and  $I_b(q_x, q_y)$  the scattering intensity of the background.  $q_x$  and  $q_y$  are  $q$  components perpendicular and parallel to the stretching direction. The patterns were first harmonized. In a next step every intensity value was multiplied by its distance to the meridian, and finally integration between  $90^\circ$  and  $180^\circ$  was carried out. By a second integration over all available data points of the so-received  $Iq^2$  vs  $q$  plot the invariant  $Q$  was obtained. This value corresponds to the phase ratio  $\nu$  and the density contrast  $\rho_1 - \rho_2$  in eq 10.

$$Q = \int_0^\infty \int_0^\infty (I(q_x, q_y) - I_b(q_x, q_y)) q_x dq_y dq_x \quad (9)$$

$$Q = (\rho_1 - \rho_2)\nu(1 - \nu) \quad (10)$$

For BDG 1  $Q$  was observed to reduce from about 0.0366 to 0.0216 and for BDG 4 from 0.0301 to 0.0181, which is a decrease of about 40–41%. Because the phase ratio  $\nu$  in eq 10 can be considered as constant, the reduction of  $Q$  is originating from a change in density contrast and therefore points to a strain induced mixing of the block copolymer phases.<sup>30</sup>

In contrast to homopolymers, this mixing results in an additional enthalpic contribution and in a retracting force because the mixed phases tend to phase separate again. By this mechanism the  $T_g$  of the hard phase can be expected to decrease, which supports further sliding of the different polymer chain types. The strain induced mixing of both PI and PS blocks would explain at least two aspects: (i) the reduction of the peak intensity and constant scattering at small  $q$  values and (ii) the reduced contrast in TEM as observed in our other publications.<sup>9</sup> A final conclusion if the deviation from incompressibility condition reflects a strain-induced volume increase on molecular scale or not requires further studies. Thereby, strain calorimetry and positron annihilation lifetime spectroscopy could serve as useful techniques.<sup>31,32</sup>

#### 4. CONCLUSIONS

This work has focused on the molecular and morphological processes taking place during uniaxial monotonic loading of multigraft and block-graft copolymers based on polystyrene and polyisoprene. For sphere forming multigrfts the nearly identical orientation of PS and PI up to high strains and the simultaneous decrease of scattering intensity reveal elongation and partial chain pull out of glassy blocks, which we interpreted as strain-induced mixing of polymer chains. We assumed further that this affects an additional enthalpic contribution (the mixed polymer chains tend to phase separate again) which increases the restoring forces of the chains. Similar results were observed for block-graft copolymers with cylindrical and disordered lamella-like morphologies after high strains and long time relaxation, where a residual orientation of either elongated chains or domain fragments was found. At low strain in the neo-Hookean region, a simple approach of spherical domains without a decrease in long-range order was observed. We identified four essential features to improve the mechanical behavior of these thermoplastic elastomers: (i) the distribution of the applied stress to several branches along the PI backbone chain, (ii) an appropriate high  $M_w$  of the PI spacer to enable high extension ratios, (iii) an appropriate contour length of the grafts to achieve small domains to which the grafts are effectively connected to, and (iv) a random grafting of the arms resulting in a multimodal network. In contrast, it was found that domain functionality (number of grafts connected to the domain) is less important to achieve improved mechanical properties. However, it is essential that these domains are highly deformable. Taking these molecular and morphological aspects into account, we can state further that while an increase of number of branch points mainly results in reduced hysteresis softening and increasing physical cross-link modulus, a random grafting additionally contributes to the chemical cross-link modulus.

## ■ AUTHOR INFORMATION

## Corresponding Author

\*E-mail: roland.weidisch@iwmmh.fraunhofer.de. Tel: (+49)3455589430.

## ■ ACKNOWLEDGMENT

The authors thank for financial support of this work within the framework of the German Science Foundation (DFG) and Fraunhofer IWM Halle. A portion of this research at Oak Ridge National Laboratory's Center for Nanophase Materials Sciences was sponsored by the Scientific User Facilities Division, Office of Basic Energy Sciences, U.S. Department of Energy (enabled through User Project # 2003-028), and supported in part by the Division of Materials Science and Engineering, Office of Basic Energy Sciences, U.S. Department of Energy (DE-ACOS-00OR22725). Y. X. Duan thanks the support from Shang dong Province Science Fund (ZR2009AL011). We thank DESY for beamtime within the project II-20060086.

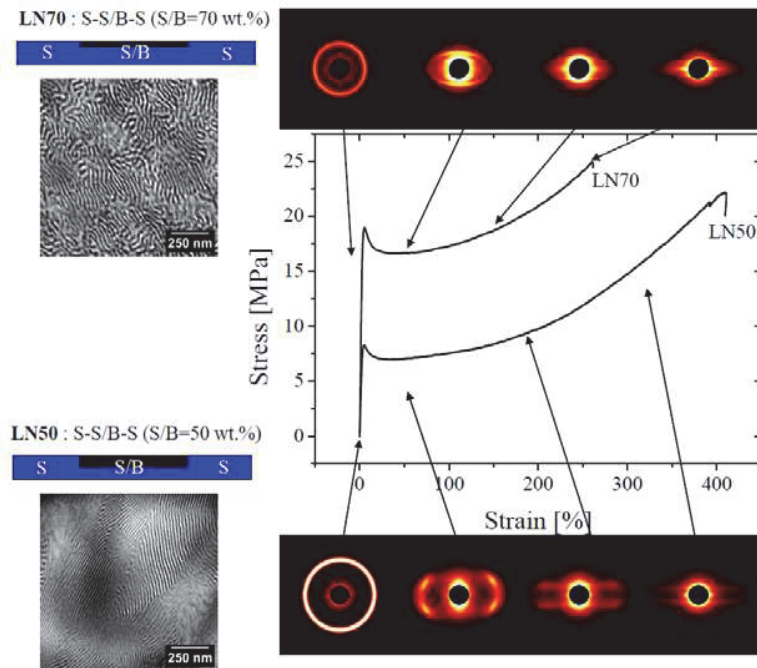
## ■ REFERENCES

- (1) Gido, S. P.; Lee, C.; Pochan, D. J.; Mays, J. W.; Hadjichristidis, N. *Macromolecules* **1996**, *29*, 7022–7028.
- (2) Xenidou, M.; Hadjichristidis, N. *Macromolecules* **1998**, *31*, 5690–5694.
- (3) Uhrig, D.; Mays, J. W. *Macromolecules* **2002**, *35*, 7182–7190.
- (4) Mays, J. W.; Uhrig, D.; Gido, S.; Zhu, Y.; Weidisch, R.; Iatrou, H.; Hadjichristidis, N.; Hong, K.; Beyer, F.; Lach, R.; Buschnakowski, M. *Macromol. Symp.* **2004**, *215*, 111–126. Uhrig, D.; Mays, J. *Polym. Chem.* **2011**, *2*, 69–76.
- (5) Roos, A.; Creton, C. *Macromolecules* **2005**, *38*, 7807–7818.
- (6) Staudinger, U.; Schlegel, R.; Weidisch, R.; Fritzsche, J.; Klüppel, M.; Heinrich, G.; Mays, J. W.; Uhrig, D.; Hadjichristidis, N. *Eur. Polym. J.* **2009**, *44*, 3790–3796.
- (7) Schlegel, R.; Wilkin, D.; Duan, Y.; Weidisch, R.; Heinrich, G.; Uhrig, D.; Mays, J. W.; Iatrou, H.; Hadjichristidis, N. *Polymer* **2009**, *50*, 6297–6304.
- (8) Duan, Y.; Rettler, E.; Schneider, K.; Schlegel, R.; Thunga, M.; Weidisch, R.; Siesler, H. W.; Stamm, M.; Mays, J. W.; Hadjichristidis, N. *Macromolecules* **2008**, *41*, 4565–4568.
- (9) Duan, Y.; Thunga, M.; Schlegel, R.; Schneider, K.; Rettler, E.; Weidisch, R.; Siesler, H. W.; Stamm, M.; Mays, J. W.; Hadjichristidis, N. *Macromolecules* **2009**, *4*, 4155–4164.
- (10) Sumpter, B. G.; Mays, J. W.; Noid, D. W.; Gido, S. P.; Weidisch, R. *Polym. News* **2004**, *29*, 302–310.
- (11) Zhu, Y.; Burgaz, E.; Gido, S. P.; Staudinger, U.; Weidisch, R.; Uhrig, D.; Mays, J. W. *Macromolecules* **2006**, *3*, 4428–4436.
- (12) Schneider, K.; Trabelski, S.; Zafeiropoulos, N. E.; Davies, R.; Riekkel, C.; Stamm, M. *Macromol. Symp.* **2006**, *236*, 241–248.
- (13) Rubinstein, M.; Panyukov, S. *Macromolecules* **2002**, *35*, 6670–6686.
- (14) Klüppel, M. *Adv. Polym. Sci.* **2003**, *164*, 1–84.
- (15) Langley, N. R.; Polmanteer, K. E. *J. Polym. Sci., Polym. Phys.* **1974**, *12*, 1023–1034.
- (16) Klüppel, M.; Schramm, J. *Macromol. Theory Simul.* **2000**, *9*, 742–754.
- (17) Kaliske, M.; Heinrich, G. *Rubber Chem. Technol.* **1999**, *72*, 602–632.
- (18) Elías-Zúñiga, A. *Polymer* **2005**, *46*, 3496–3506.
- (19) Zhu, Y.; Weidisch, R.; Gido, S. P.; Velis, G.; Hadjichristidis, N. *Macromolecules* **2002**, *35*, 5903–5909.
- (20) Huang, Y.-Y.; Chen, H.-L.; Hashimoto, T. *Macromolecules* **2003**, *36*, 764–770.
- (21) Milner, S. T. *Macromolecules* **1994**, *27*, 2333–2335.
- (22) Beyer, F.; Gido, S. P.; Büschl, C.; Iatrou, H.; Uhrig, D.; Mays, J. W.; Chang, M. Y.; Garetz, B. A.; Balsara, N. P.; Tan, N. B.; Hadjichristidis, N. *Macromolecules* **2000**, *33*, 2039–2048.
- (23) Mijović, J.; Sun, M.; Pejanović, S.; Mays, J. W. *Macromolecules* **2003**, *36*, 7640–7651.
- (24) Thunga, M.; Schlegel, R.; Staudinger, U.; Duan, Y.; Weidisch, R.; Heinrich, G.; Mays, J. W.; Hadjichristidis, N. *Kautsch. Gummi Kunstst.* **2008**, *11*, 597–605.
- (25) Matsen, M. W.; Tomsen, R. B. *J. Chem. Phys.* **1999**, *111*, 7139–7145.
- (26) Ding, Y.; Kisiuk, A.; Sokolov, A. P. *Macromolecules* **2004**, *37*, 161–166.
- (27) Morrison, F. A.; Winter, H. H. *Macromolecules* **1989**, *22*, 3533–3540.
- (28) Schlegel, R.; Staudinger, U.; Thunga, M.; Weidisch, R.; Heinrich, G.; Uhrig, D.; Mays, J. W.; Iatrou, H.; Hadjichristidis, N. *Eur. Polym. J.* **2008**, *45*, 2902–2912.
- (29) Mark, J. E. *Rubber Chem. Technol.* **1999**, *72*, 465–480.
- (30) Stribeck, N. *X-ray Scattering of Soft Matter*; Springer: Berlin, 2007.
- (31) Göritz, D. *Colloid Polym. Sci.* **1982**, *260*, 1993–197.
- (32) Dlubek, G. Positron Annihilation Spectroscopy. In *Encyclopedia of Polymer Science and Technology*; Seidel, A., Hoboken, N. J., Eds.; John Wiley & Sons: New York, 2008.

## Publication [P2]

### Deformation mechanisms in lamellar S-S/B-S triblock copolymers

Stefan Hölzer, Martin Ganß, Konrad Schneider, Konrad Knoll, Roland Weidisch



*European Polymer Journal* **2013**, *49*, 261–269





## Deformation mechanisms in lamellar S–S/B–S triblock copolymers

Stefan Hölzer<sup>a,1</sup>, Martin Ganß<sup>a,b</sup>, Konrad Schneider<sup>c</sup>, Konrad Knoll<sup>d</sup>, Roland Weidisch<sup>a,b,\*</sup>

<sup>a</sup>Fraunhofer Institute for Mechanics of Materials IWM, Walter-Hülse-Str. 1, D-06120 Halle/S., Germany

<sup>b</sup>Institute of Chemistry, Martin-Luther-University Halle-Wittenberg, Heinrich-Damerow-Str. 4, D-06099 Halle/S., Germany

<sup>c</sup>Leibniz Institute of Polymer Research Dresden, Hohe Strasse 6, D-01069 Dresden, Germany

<sup>d</sup>BASF SE, Research Thermoplastics, GKT/S - B001, D-67056 Ludwigshafen, Germany

### ARTICLE INFO

#### Article history:

Received 16 January 2012

Received in revised form 25 April 2012

Accepted 3 June 2012

Available online 14 June 2012

#### Keywords:

Deformation mechanism

Triblock copolymers

Styrene

Butadiene

SAXS

Online-deformation

### ABSTRACT

The deformation behaviour of two lamellar polystyrene-*block*-poly(styrene-*co*-butadiene)-*block*-polystyrene (S–S/B–S) triblock copolymers was investigated by small-angle X-ray scattering (2D-SAXS) during uniaxial stretching. The samples differed by the styrene content in the statistical S/B middle block, being 50 and 70 wt.% for LN50 and LN70 respectively. The positions of the SAXS reflections were estimated in order to relate the microscopic deformation behaviour with the macroscopic strain. The samples show different deformation mechanisms. A four-point SAXS pattern was found in LN50, which is typical for lamellae undulation and tilting. At higher strains, the contribution of lamellae tilting is decreasing until it is negligible at strains above 200%. During strain hardening, the deformation was affine, indicating triaxial deformation of the domains. In contrast, LN70 shows affine deformation in the whole investigated range. Thus, triaxial deformation is expected to dominate in LN70. The remarkable differences of the deformation mechanisms are expected to result from the different styrene contents in the S/B middle block. This leads to (i) a lower stiffness contrasts between the soft and hard phase and (ii) a reduced long-range order of the lamellae. Both factors may hinder lamellae tilting in LN70, which results in the absence of the four-point SAXS-pattern.

© 2012 Elsevier Ltd. All rights reserved.

### 1. Introduction

Polystyrene-*block*-polybutadiene-*block*-polystyrene (SBS) triblock copolymers are known to microphase separate into soft and hard domains, such as spherical, cylindrical, gyroid or lamellar morphologies. Controlling the molecular architecture and the morphology of SBS block copolymers offers the possibility to tailor the mechanical property profile, which could reach from that of thermo-plastic elastomers to that of tough thermoplastics [1,2]. This requires a detailed understanding of the interrelation

between the macromolecular architecture, the microphase separated morphology, the thermal and mechanical history and the resulting mechanical behaviour.

A novel pathway to tailor the mechanical behaviour of styrene-butadiene based block copolymers is to substitute the polybutadiene block by a statistical poly(styrene-*co*-butadiene) copolymer block (S/B) [3,4]. Hence the segregation strength, the morphology and the mechanical behaviour can be controlled by a well-directed adjusting of the S/B-ratio and the segregation strength  $\chi_{\text{eff}}N$  [5–7]. Thereby,  $\chi_{\text{eff}}N$  is a product of the overall degree of polymerisation  $N$  and the effective interaction parameter  $\chi_{\text{eff}}$ , which represents the interactions between the statistical copolymer block (S/B-phase) and the styrene block (PS-phase).

In the present contribution, the influence of the S/B-middle block ratio on the deformation mechanism of lamellar S–S/B–S triblock copolymers having high styrene contents in the S/B-middle block will be investigated by small-angle

\* Corresponding author at: Institute of Chemistry, Martin-Luther-University Halle-Wittenberg, Heinrich-Damerow-Str. 4, D-06099 Halle/S., Germany.

E-mail address: [roland.weidisch@chemie.uni-halle.de](mailto:roland.weidisch@chemie.uni-halle.de) (R. Weidisch).

<sup>1</sup> Laboratory of Organic and Macromolecular Chemistry (IOMC, Lehrstuhl II/Schubert) Friedrich-Schiller-Universität Jena, Humboldtstr. 10, 07743 Jena, Germany.

X-ray scattering during online deformation. This method is ideal to study the morphology development over a large area during stretching of block copolymers. SAXS studies on isotropic [8,9] and highly oriented [2,10] lamellar SBS block copolymers showed that the deformation mechanism strongly depends on the lamellae alignment. Lamellae that are initially parallel oriented to the stretching direction show a continuous fragmentation [10] or yielding [3] of the glassy PS-domains. In contrast, the deformation mechanism of perpendicular oriented lamellae is dominated by undulation, folding and tilting, which results in a chevron-like arrangement of the lamellae. The chevron structure is indicated by a characteristic four-point pattern in 2D-SAXS-investigations [10,11]. Upon further deformation, these undulated lamellae tilt towards the stretching direction. Thereby, the inclination angle between the undulated lamellae ( $\alpha$ ) increases with higher macroscopic strains  $\varepsilon_{M,x}$ . The microstrain from lamellae tilting ( $1/\cos\alpha$ ) and the macrostrain  $\varepsilon_{M,x}$  are related by [10]

$$1/\cos\alpha = a \cdot (1 + \varepsilon_{M,x}) \quad (1)$$

The parameter  $a$  describes the impact of the initial inclination angle  $\alpha_0$ . If tilting is the only deformation mechanism (affine tilting), then  $a = 1/\cos(\alpha_0)$  [10]. Affine tilting clearly differs from affine deformation, where the macroscopic deformation of the sample is similar to the microscopic deformation of the domains in every direction ( $\varepsilon_{\mu,i} = \varepsilon_{M,i}$ ). Here,  $\varepsilon_{\mu,i}$  is the microscopic strain, which is calculated from the shift of the first reflex  $q^*$  and the subscript “ $i$ ” is an arbitrary direction ( $x, y, z$ ). In other words, affine deformation represents triaxial deformation of the domains, where the elongations measured on different length scales (micro and macro) are the same. A first indication of an affine deformation process is the transformation of the initially circular rings into ellipses in the 2D-SAXS-patterns upon stretching [12].

The aim of this work is to analyse the deformation mechanisms of lamellar S–S/B–S triblock copolymers in order to better understand their outstanding mechanical behaviour, which combines high stiffness, strength and toughness. The deformation mechanism of these high styrene containing block copolymers is relatively unknown. Differences to classical SBS-triblock copolymers are expected, due to the decreased stiffness contrast between the hard PS and the soft S/B phase via incorporation of styrene segments in the statistical copolymer S/B-middle block. This assumption is affirmed by a theoretical study of Castañeda and co-workers [13]. They predict a change in the deformation mode from a high-energy triaxial deformation mode to a lower-energy rotation and shear-along-the-layers mode (lamellae tilting) for lamellar microstructures depending on the stiffness contrast between the soft and hard phase.

## 2. Experimental

### 2.1. Materials

The materials used in this study are symmetric polystyrene-*block*-poly(styrene-*co*-butadiene)-*block*-polystyrene

triblock copolymers (S–S/B–S), which were synthesised in the lab of the BASF SE [14]. The triblock copolymers consist of two PS-outer blocks, each having a weight fraction of 20 wt.% (20–60–20 architecture). The middle block is based on a statistical styrene–butadiene copolymer (S/B), which contains different amounts of styrene; 50 wt.% for LN50 and 70 wt.% for LN70. The index of polydispersity is less than 1.3. Molecular characteristics of the triblock copolymers are discussed elsewhere [4,7] and summarized in Table 1.

Due to the higher styrene-content in the S/B middle block in LN70, the glass transition temperature of the soft  $T_{g-S/B}$  is higher and the effective Flory–Huggins parameter  $\chi_{\text{eff}}$  is lower compared to LN50 [7]. The temperature dependence of  $\chi_{\text{eff}}$  for LN50 is given in Ref. [15] and was calculated for LN70 according to the procedure of Leibler et al. [16]. Similar segregation strengths  $\chi_{\text{eff}}N$  were achieved by increasing the degree of polymerization  $N$  of LN70. This leads to a significantly higher overall molecular weight ( $M_w = 288$  kg/mol) and a higher long-period  $d_0 = 43 \pm 3.5$  nm of LN70 (LN50:  $M_w = 110$  kg/mol,  $d_0 = 32 \pm 1$  nm). The long periods were calculated from the SAXS pattern of undeformed samples and the deviations of were estimated by FWHM method after subtraction of a linear baseline.

The materials were cast from 2 wt.-%-solutions with toluene, which is a non-preferable solvent for styrene and butadiene. The solution cast films have a thickness of approximately 0.5 mm and were annealed under vacuum at 120 °C for 48 h.

### 2.2. Methods

#### 2.2.1. Transmission electron microscopy (TEM)

Transmission electron microscopy studies were carried out on ultrathin sections (<100 nm) using a JEOL JEM-3010 (100–300 kV). Sections were cut with a diamond knife on a ultramicrotome at –100 °C and stained with osmium tetroxide vapour ( $\text{OsO}_4$ ) for 24 h.  $\text{OsO}_4$  reacts with the double bond of butadiene and enhances the contrast in TEM between the different the phases. The S/B domains appear dark and the styrene domains appear white in the TEM images.

#### 2.2.2. Mechanical behaviour

Tensile tests were performed on a Zwick/Roell Z010 universal testing machine on waisted specimen, having a similar geometry as those used for the online SAXS measurements. The tests were carried out at room temperature and a crosshead speed of 50 mm/min. The strain was measured optically by image correlation.

#### 2.2.3. Small-angle X-ray scattering (SAXS) during online deformation

SAXS measurements were carried out at the synchrotron beamline BW4 at HASYLAB (DESY, Hamburg) with a wavelength  $\lambda = 0.138$  nm, an exposure time of 120 s and a sample-to-detector distance of 4024 mm. Online deformation was realised with a home-made stretching apparatus. In order to ensure that the beam exposes the actually deformed volume, we used waisted tensile bars, having a



**Table 1**  
Composition and molecular characteristics of the studied block copolymers.

	S/B-middle block composition	$M_n$ (kg/mol)	$\chi_{\text{eff}}N$ (120 °C)	$T_{\text{g-soft}}$ (°C)	$d_0$ (nm)
LN50	50 wt.% styrene	110	30	−25	$32 \pm 1.0$
LN70	70 wt.% styrene	288	28	−7	$43 \pm 3.5$

width of initially 3 mm in the waist. The specimens were patterned with black dots next to the area, which is exposed to the beam. A setup as in Ref. [17] was used, so that the macroscopical strain could be estimated from digital images. During the beam exposition, the stretching machine was stopped.

Image processing was carried out with ImageJ [18], a Java-based open source image processing software. The raw SAXS data were corrected from background scattering and aligned, so that (i) the centre of the image equals the centre of the pattern and (ii) the stretching direction lies on the meridian. The beamstop has been erased and the four quadrants of the pattern were averaged. The pixel dimensions were converted into  $q$ -space ( $q = 4\pi/\lambda \cdot \sin \theta$ , with the scattering angle  $\theta$  [12]). In order to relate the macroscopic strain with the microscopic deformation, different methods of digital image processing were applied.

- (i) The inclination angle  $\alpha$  of undulated lamellae was determined by firstly applying a threshold on the image, so that the intensity maxima of the four-point pattern could be clearly assigned. From these maxima and the centre of the pattern, we determined the inclination angle  $\alpha$ .
- (ii) The microstrain  $\varepsilon_\mu$  was estimated with aid of the “Radial Profile Extended PlugIn” from Philippe Carl. Sections parallel and perpendicular the stretching direction were integrated with an angular range of  $\pm 10$ . From these sections, the long periods were calculated from the first reflex  $q^*$  according to Bragg’s law ( $d = 2\pi/q^*$ ). With the estimated long periods of the unstretched ( $d_0$ ) and the stretched ( $d_i$ ) samples, we determined the microstrain  $\varepsilon_\mu = (d_i - d_0)/d_0$ . However, at large deformations,  $\varepsilon_\mu$  cannot be estimated directly because  $q^*$  shifts towards very small angles and the beamstop hides the meridional reflexes. Hence, reasonable extrapolation methods are necessary to determine the meridional reflex. We used the elliptical overall shape of the SAXS pattern to interpolate the reflections by fitting ellipses at high strains. The long period  $q^*$  in stretching direction was then calculated from length of the minor semi-axis  $l_{\text{min}}$  ( $q^* = l_{\text{min}}/2$ ).

### 3. Results and discussion

#### 3.1. Morphology in the initial state

The SAXS and TEM-results of the initial morphologies of the triblock copolymers LN50 and LN70 are shown in Fig. 1. The 2D-SAXS images in the initial state exhibits circular rings for both samples. Azimuthal integration of the 2D-SAXS patterns reveals three significant reflexes for LN50

( $q^*$ ,  $2q^*$ ,  $3q^*$ ) and two for LN70 ( $q^*$ ,  $2q^*$ ), which indicates a random distribution of grains with lamellar structure. The SAXS-results are confirmed by the TEM-micrographs, showing grains with lamellar morphologies. The morphologies are in accordance with the theoretical phase diagram of symmetric triblock copolymers [19]. The long range order of LN70 is reduced, as shown by the smaller grain sizes in TEM-images and only two reflexes in the scattering curve of LN70. The higher styrene-content in the middle block of LN70 reduces the enthalpic force for microphase separation [4,20] and decreases the scattering power of LN70, due to the lower electron density difference between the phases.

The average long periods from SAXS are  $32 \pm 1$  nm for LN50 and  $43 \pm 3.5$  nm for LN70. The higher deviations of LN70 are expected to result from the reduced long-range order and a higher miscibility at the interface, due to the higher styrene-content in the middle block.

#### 3.2. Tensile response

Engineering stress–strain curves of LN50 and LN70 under uniaxial tensile deformation are shown in Fig. 2. Both curves exhibit a pronounced yield point, *cold drawing* (slope  $\approx 0$ ) and *strain hardening* at large deformations (slope  $\approx \text{const}$ ). Between these regimes, there is a *transition zone*, where the slope of the curve is continuously increasing. Compared to LN50, the curve of LN70 is shifted to much higher stresses (more than a factor of 2). The modulus of elasticity and the yield stress increase significantly with higher styrene-contents in the middle block, as shown in the inset of Fig. 2. The strain at break is decreasing from  $\approx 400\%$  to  $\approx 250\%$  with increasing styrene-content and the tensile strength remains almost the same for LN50 and LN70.

The stiffening of the soft phase, due to the higher styrene-content in the S/B-block is expected to enhance the ability of the material to carry a higher stress during deformation. Additionally, the S/B ratio in the middle block and the thereof resulting morphology may also directly influence the deformation mechanism of the triblock copolymer. The effect of the higher styrene content in the S/B middle block and the consequence of the morphological characteristics on the deformation behaviour were therefore investigated by SAXS during stretching.

#### 3.3. Morphology development under tensile deformation

##### 3.3.1. LN50 – 50 wt.% styrene in the S/B middle block

Based on the stress–strain diagram in Fig. 2, we divided the deformation process of LN50 into four regimes. The regime below the yield point ( $\varepsilon_M < 10\%$ ) is the *low deformation regime* and above the yield point, the material is the

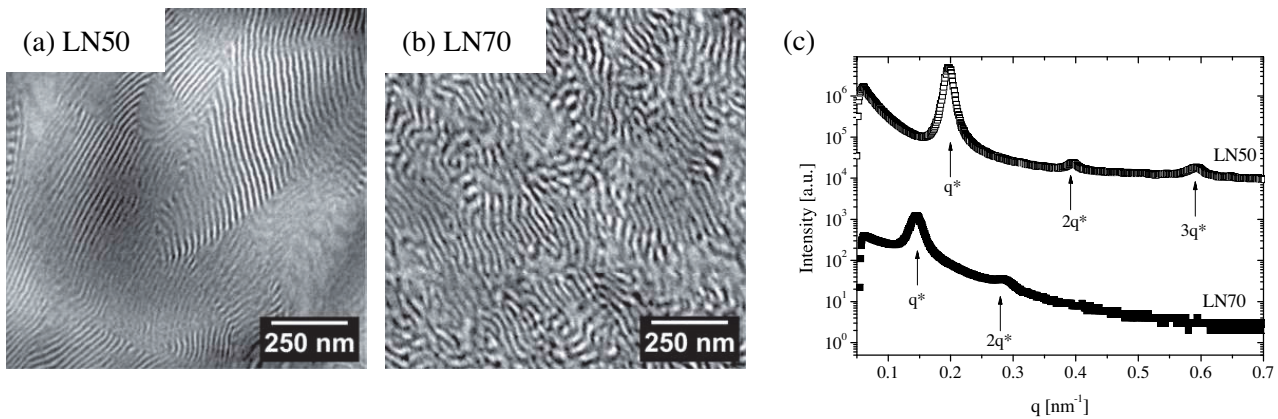


**Fig. 1.** Morphological investigations of LN50 and LN70 in the initial state. TEM micrographs of (a) LN50 and (b) LN70. (c) SAXS curves of LN50 and LN70, showing reflexes at integer ratios of  $q^*$ . The SAXS curves are vertically shifted. TEM and SAXS indicate lamellar morphologies with different degrees of long-range order.

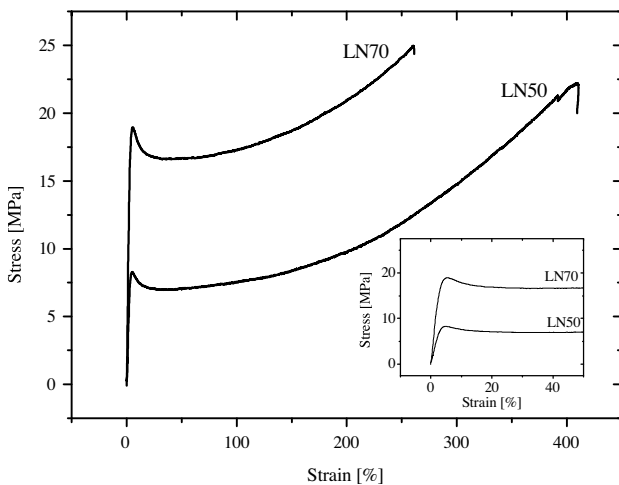


**Fig. 2.** Stress–strain behaviour of the investigated samples LN50 and LN70. The inset displays a magnification at low strains. With higher styrene-content in the middle block, the yield stress and E-modulus are increasing and the strain at break is decreasing.

*cold drawing regime*. Here, no additional stress is necessary to elongate the sample ( $10\% < \varepsilon_{M,x} < 80\%$ ), which is characterised by plateau in the stress–strain diagram. After cold drawing, the stress increases until the material breaks. We divided this last part of the curve in a *transition zone* ( $100\% < \varepsilon_{M,x} < 180\%$ ) and a *strain hardening regime* ( $\varepsilon_{M,x} > 180\%$ ). The slope of the curve is continuously increasing in the transition zone and whereas it is approximately constant during strain hardening.

The 2D-SAXS patterns of LN50 for different strains  $\varepsilon_{M,x}$  are shown in Fig. 3. The initially circular rings (Fig. 3a) transform into elliptical reflexes (Fig. 3b) in the low-deformation regime ( $\varepsilon_{M,x} = 5\%$ ). The minor axis of the ellipse is thereby parallel and the major axis perpendicular to the stretching direction. This indicates that the average domain spacing in stretching direction is increasing, whereas it is decreasing perpendicular to the stretching direction. The microscopical strain in Fig. 3b and the macroscopical strain were similar. Thus, we observed a triaxial deformation of the material at low strains, which is in accordance with

the literature [13]. Upon further deformation, the PS-lamellae start to break and hence the soft phase can deform more easily. The break down is discussed as a fragmentation [10] or yielding mechanism [3], which is indicated by a drop of the stress in the stress–strain-diagram in Fig. 2 at  $\varepsilon_{M,x} = 10\%$  (yield point). Fig. 3c depicts the 2D-SAXS pattern of the stretched LN50 above the yield point. A dramatic decrease of the intensity is found along the meridian and the development of a four-point pattern, which is characteristic for undulated and tilted lamellae, (“chevrons”) [3,10,11]. Thereby, perpendicular oriented lamellae, which normals are initially oriented in stretching direction, undulate to a specific inclination angle  $\alpha$ . Thus, scatter entities, formerly located on the meridian, shifted towards the azimuthal angle  $\alpha \approx 44^\circ$ , which leads to the four-point pattern. A scheme of the undulated lamellae or chevron structure and the corresponding 2D-SAXS pattern is shown in Fig. 4. The chevron formation has been studied in the group of Thomas on roll-casted and thus initially highly oriented lamellar SBS block copolymer samples [10,11]. They demonstrated that the deformation mechanism strongly depends on the lamellae orientation relative to the stretching direction [10]. Further, it was shown that perpendicular oriented lamellae deform at lower stress values compared to those, which are aligned in stretching direction. The deformation of parallel aligned lamellae necessitates a much higher stress due to the absence of chevron formation and lamellae tilting. Our results confirm this behaviour for initially isotropic samples. The intensity on the meridian is strongly decreasing at  $\varepsilon_{M,x} = 30\%$  that points to the disappearance of perpendicular oriented lamellae. Thus, most of the initially perpendicular oriented lamellae are tilted, whereas the parallel aligned lamellae still persist, as indicated by the high intensity reflections along the equator. This implies that the contribution to the deformation process at low strains of perpendicular aligned lamellae is significantly higher than the contribution of those aligned parallel to the stretching direction. A weak meridional reflex is found very close to the beam stop, which corresponds to long periods of  $d \approx 100$  nm. This is far beyond the value for affine deformation, which should be around  $d \approx 42$  nm at macrostrains of 30%. Such meridional reflexes

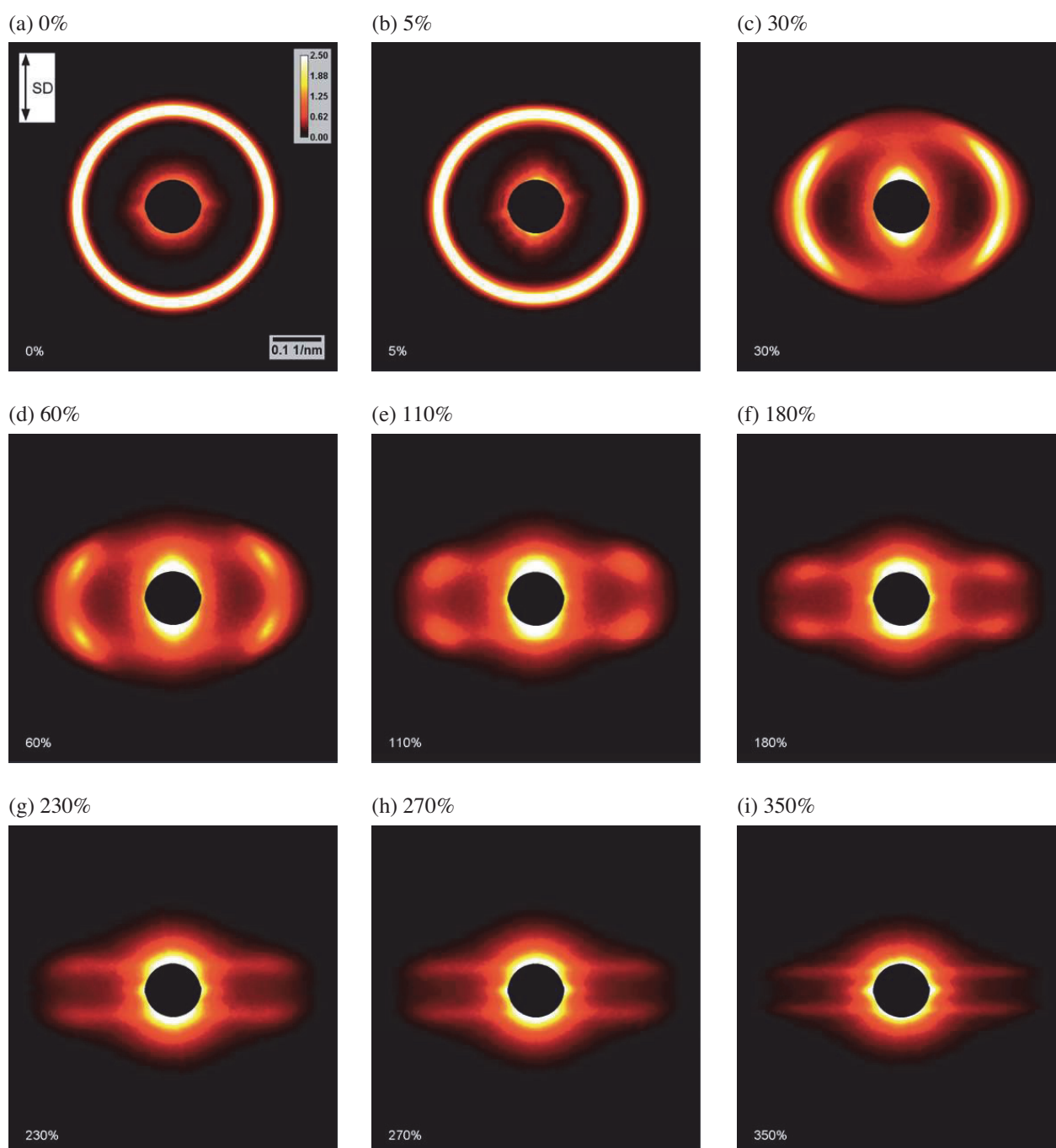


**Fig. 3.** 2D-SAXS patterns of LN50 at different deformation stages ( $\varepsilon_{M,x} = 0\%$ , 5%, 30%, 60%, 110%, 180%, 230%, 270% and 350%). The scale bar represents  $q$ , with a width of  $0.1 \text{ nm}^{-1}$ . The intensities are displayed in linear scale and are represented by the calibration bar from 0 to 2.5 (in arbitrary units). Scale and calibration bar count for all SAXS pattern in this Figure. The stretching direction SD is vertical, as marked by an arrow. The initial ring transforms upon deformation into a four-point pattern, which is characteristic for the formation of chevrons. In the strain hardening regime, broad meridional reflexes and small equatorial streaks are observable.

were reported in chevron morphologies and they were attributed to the hinge points of the undulated lamellae [10]. However, it may also be possible that the S/B soft phase of several perpendicular oriented lamellae are deformed without tilting and thus lead to high microstrains in stretching direction.

After lamellae undulation, the deformation is known to be controlled by a further tilting of the rigid PS-lamellae accompanied by a significant shearing of the soft phase

[8]. Thereby, the average long period of the undulated lamellae remains almost constant and the evolution of the microstrain is predominantly controlled by lamellae tilting [10]. Thus, the inclination angle  $\alpha$  is increasing during cold drawing and in the transition zone (Fig. 3d–f). Further, it is found that the intensity of the four-point pattern is continuously decreasing with increasing strain. Other features of the 2D-SAXS pattern at high deformations (Fig. 3e–i) are streaks parallel to the equator, which

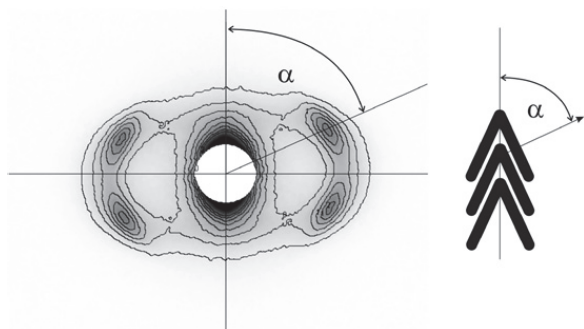


**Fig. 4.** Inclination angle  $\alpha$  of LN50 at  $\varepsilon_{M,x} = 60\%$  with a schema of the corresponding angle in the chevron morphology.

shift to smaller  $q^*$  with increasing strain. The streaks are suggested to be strong shoulders from a meridional reflex and they are interpreted as scattering from PS-fragments in the soft matrix. Different fragment orientations are represented in the 2D-SAXS pattern at different azimuthal angles, resulting in an overall elliptical shape. In the strain hardening regime (Fig. 3g–i), the four-point reflexes are vanishing, which may be attributed to a further yielding and fragmentation of the folded PS-lamellae. The inclination angle  $\alpha$  for the remaining weak reflection is constant at  $\approx 57^\circ$ . However, at strains above 210%, the four-point maxima cannot be distinguished from the underlying streaks anymore.

The presence of the four-point pattern indicates that LN50 exhibits lamellae undulation and tilting. However, lamella tilting is not necessarily the dominating deformation mechanism. Whether the lamella tilting is affine, was to be proven by the procedure of Thomas et al. (Eq. (1) in this text) [10]. The average inclination angle  $\alpha$  of the chevron structure was determined from the maxima in the four-point pattern. At its first appearance ( $\varepsilon_{M,x} \approx 30\%$ ), the inclination angle is  $\alpha \approx 44^\circ$ . The angle  $\alpha$  is subsequently increasing with further deformation, being  $\alpha \approx 52^\circ$  at  $\varepsilon_{M,x} \approx 100\%$  and  $\alpha \approx 57^\circ$  at  $\varepsilon_{M,x} \approx 200\%$ . In Eq. (1), the inclination angle of the lamellae in the unstretched state  $\alpha_0$  is represented by the parameter  $a = 1/\cos\alpha_0$ . Under the assumption of randomly distributed lamellae with orientations between  $0^\circ$  and  $90^\circ$ , the initial angle  $\alpha_0$  was replaced by an averaged initial angle  $\langle\alpha_0\rangle = 45^\circ$ . This rough simplification leads to  $a = \sqrt{2}$  for affine tilting and hence Eq. (1) turns into

$$1/\cos(\alpha) = \sqrt{2}(1 + \varepsilon_{M,x}), \quad \text{for } \langle\alpha_0\rangle = 45^\circ \quad (2)$$

In order to get more information on the dominating deformation mechanism in the different deformation regimes,  $1/\cos(\alpha)$  was plotted versus the macrostrain in Fig. 5. Thereby,  $1/\cos(\alpha)$  can be interpreted as microstrain, which only accounts on the contribution of lamellae tilting [10]. At strains below the yield point ( $\varepsilon_{M,x} < 10\%$ ), no four-point pattern was found and thus no inclination angle could be determined. Here, the deformation mechanism is dominated by the stretching of the domains. At  $\varepsilon_{M,x} \approx 30\%$  the first data point  $1/\cos(\alpha_1)$  was found at  $\approx 1.4$ . This value is continuously increasing with the macrostrain. As a first approximation, the dependence of microstrain from lamellae tilting  $\varepsilon_{\mu,\text{tilt}}$  as function of the macrostrain  $\varepsilon_{M,x}$  can be

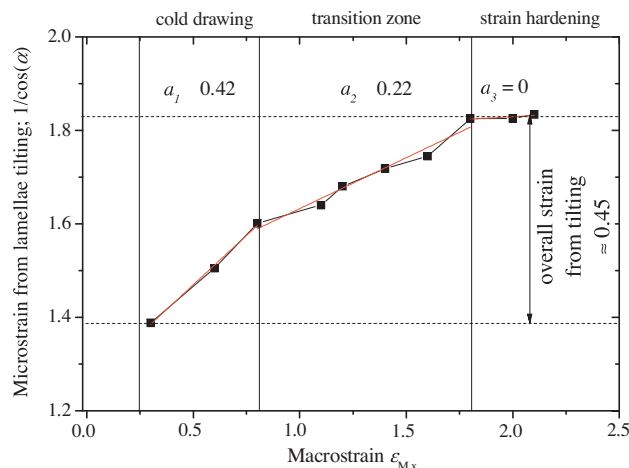


**Fig. 5.** Influence of lamellae tilting on the deformation of LN50. The inclination angle of the undulated lamellae from the four-point SAXS pattern ( $\alpha$ ) is plotted versus the macroscopic strain in order to determine the contribution of lamellae tilting. The curve has been divided into three regimes, according to the stress strain diagram – cold drawing, transition zone and strain hardening.

easily estimated by subtracting  $1/\cos(\alpha_1)$  from the ordinate value at the relative macrostrain in Fig. 5. Anyway, during our discussion, we focus on the slopes of the curves  $a$ , which could also be interpreted by the quotient  $\varepsilon_{\mu,\text{tilt}}/\varepsilon_{M,x}$ . During cold drawing ( $10\% < \varepsilon_{M,x} < 80\%$ ), the highest influence of lamellae tilting on the deformation process can be observed, which is decreasing at macrostrains higher than 80% (transition zone). The inclination angle  $\alpha$  does not change during strain hardening ( $\varepsilon_{M,x} < 180\%$ ) and the slope  $a$  in Fig. 5 is approximately zero in that deformation range.

It is found that even during cold drawing,  $a$  is far away from  $\sqrt{2}$ , which was expected for affine tilting. Although there are significant contributions of lamellae tilting; this model is improper to describe the overall macroscopic deformation of LN50. This is not surprising, since it is shown from Cohen et al. that mainly perpendicular oriented grains exhibit an affine lamellae tilting deformation mechanism [10]. In diagonal and parallel direction, they found no affine tilting. The parameter  $a$  is continuously decreasing non-linearly with increasing strain. In order to quantify this strain dependence, we divided the curve in Fig. 5 into three parts, with respect to the stress–strain behaviour of LN50. Thereby, the slopes  $a_1 = 0.42$ ,  $a_2 = 0.22$  and  $a_3 = 0$  describe the data points during cold drawing (1), in the transition zone (2) and in the strain hardening regime (3) respectively. The overall strain from lamellae tilting, measured between  $30\% < \varepsilon_{M,x} < 200\%$  was 0.45 as shown in Fig. 5.

In Fig. 6, the microstrain  $\varepsilon_{\mu,x}$  along the meridian of LN50 for perpendicular oriented lamellae is plotted versus the measured macrostrain  $\varepsilon_{M,x}$ . It can be found that the microstrain in stretching direction is higher than the macrostrain. Multiple facts account on a connection between the contribution of lamellae tilting on the deformation mechanism (Fig. 5, estimated from tilting angles  $\alpha$ ) and the microstrain behaviour in stretching direction (Fig. 6, estimated from elliptical fits of the SAXS pattern). A closer look at the Figures reveals that,

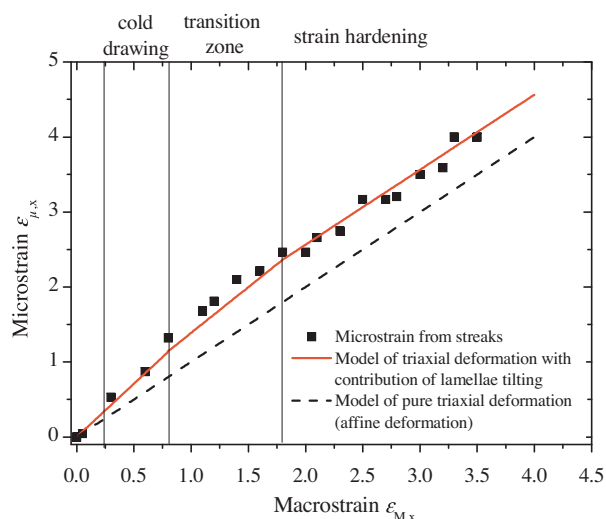


**Fig. 6.** Microstrain, calculated from SAXS-measurements along the stretching direction, is plotted versus the macrostrain. In the yielding regime, an above-average microstrain is measurable, which occurs from the preferential deformation of lamellae perpendicular to the stretching direction. In the strain hardening regime the slope is unity, indicating affine deformation behaviour. The black dashed line represents pure affine deformation and the red solid line stands for affine deformation with the additional impact of tilted lamellae.

- (i) In the cold drawing regime,  $\varepsilon_{\mu,x}$  is increasing significantly higher than  $\varepsilon_{M,x}$  (Fig. 6) and simultaneously, the contribution of lamellae tilting in this regime relatively high (Fig. 5).
- (ii) The contribution of lamellae tilting is decreasing at higher strains (Fig. 5) and at the same time, the slope in Fig. 6 is decreasing, which denotes that the contribution of triaxial deformation is increasing.
- (iii) At strains above 180%, no lamellae tilting could be observed (Fig. 5) and the slope in Fig. 6 is unity, implying affine triaxial deformation behaviour.
- (iv) The offset between the data points in Fig. 6 and the curve for pure affine deformation is approximately 0.5, which is very close to the overall contribution of lamellae tilting (0.45) in Fig. 5.

The connection between Figs. 5 and 6 is expected to result from meridional reflexes of the chevron SAXS-pattern, which are discussed as the hinge points between the undulated lamellae [10]. We proved, whether the obtained microstrain behaviour in stretching direction can be described by an additional contribution of lamellae tilting. Therefore, the prefactor of  $\varepsilon_{M,x}$ , which is 1 for affine deformation, was modified by adding  $a_1 = 0.42$ ,  $a_2 = 0.22$  and  $a_3 = 0$  in the relating deformation regime, which describes the additional contribution of lamellae tilting. Further, a microstrain-offset was appended, being  $\varepsilon_{\mu,x}(80\%)$  in the transition zone and  $\varepsilon_{\mu,x}(180\%)$  in the strain hardening regime. The resulting curve consists of three lines with different slopes and can be written as

$$\varepsilon_{\mu,x}(\varepsilon_{M,x}) = \begin{cases} (1 + a_1) \cdot \varepsilon_{M,x} & \text{for } 0\% \leq \varepsilon_{M,x} \leq 80\% \\ (1 + a_2) \cdot \varepsilon_{M,x} + \varepsilon_{\mu,x}(80\%) & \text{for } 80\% \leq \varepsilon_{M,x} \leq 180\% \\ (1 + a_3) \cdot \varepsilon_{M,x} + \varepsilon_{\mu,x}(180\%) & \text{for } 180\% \leq \varepsilon_{M,x} \end{cases} \quad (3)$$

The function describes the data points of Fig. 6 in a very good manner. Hence, we conclude that the preferential deformation of initially perpendicular oriented lamellae is responsible for higher micro- than macrostrains in stretching direction.

Thus, the deformation behaviour of LN50 is expected to be a combination of different deformation mechanism, which depends on the lamellae alignment relative to the stretching direction. Initially perpendicular aligned lamellae are able to undulate and tilt. Tilting is thereby expected to be the preferred deformation mechanism, because it necessitates lower deformation energies [10]. However, lamellae undulation and tilting is constrained by the deformability of adjacent grains, which might need higher stresses to deform. Lamellae aligned parallel to the stretching direction are unable to tilt. Rather, a fragmentation process [10] or thin-layer yielding mechanism [3,21] is proposed for such lamellae orientations. Depending on the initial lamellae alignment, the deformation mechanism is either tilting-dominated (particularly in perpendicular oriented lamellae) or yielding and fragmentation-dominated (particularly in parallel oriented lamellae). Further, it depends on the previous mechanical history of the sample. With increasing deformation, the contribution of lamellae tilting decreases whereas that of triaxial deformation increases. At strains above 200%, the impact of lamellae tilting is vanished and the sample shows affine deformation.

### 3.3.2. LN70 – 70 wt.% styrene in the S/B middle block

The stress–strain curve of LN70 offers similar features as that of LN50, although running at higher stress values. Accordingly, the curve was divided into the same four regimes – (i) low-deformation regime ( $\varepsilon_{M,x} < 30\%$ ), (ii) cold drawing ( $30\% < \varepsilon_{M,x} < 80\%$ ), (iii) transition zone ( $80\% < \varepsilon_{M,x} < 150\%$ ) and (iv) strain hardening regime ( $\varepsilon_{M,x} > 150\%$ ).

The 2D-SAXS patterns of LN70 at different deformation stages are shown in Fig. 7. The initial state shows a circular ring, which indicates an isotropic lamellae distribution with a long period of  $d = 43$  nm. Upon stretching, the ring transforms into an ellipse, whereas the minor axis is located on the meridian (in stretching direction) and the major axis lies on the equator. The long period of perpendicular oriented lamellae strongly increased from  $d = 43$  nm to  $d = 52$  nm at  $\varepsilon_{M,x} \approx 20\%$ , whereas the domain spacing of parallel oriented lamellae decreased. The elliptical shape of the 2D-SAXS pattern remains till the break, which points to affine deformation behaviour [12]. Elliptical fits of the pattern reveal a decreasing minor semi-axis and an increasing major semi-axis with higher strains. This indicates increasing domain spacings along the stretching direction and decreasing domain spacings perpendicular to the stretching direction. Based on the estimated long periods, we calculated the microstrain parallel ( $\varepsilon_{\mu,x}$ ) and perpendicular ( $\varepsilon_{\mu,y}$ ) to the stretching direction. The results are shown in Fig. 8, where both are plotted versus the macrostrain. The microstrain in stretching direction  $\varepsilon_{\mu,x}$  is almost similar to the macroscopic strain  $\varepsilon_{M,x}$ , indicating affine deformation behaviour. Under the assumption of incompressibility ( $(\varepsilon_{M,x} + 1)(\varepsilon_{M,y} + 1)(\varepsilon_{M,z} + 1) = 1$ ), similar strain dependence perpendicular to the stretching

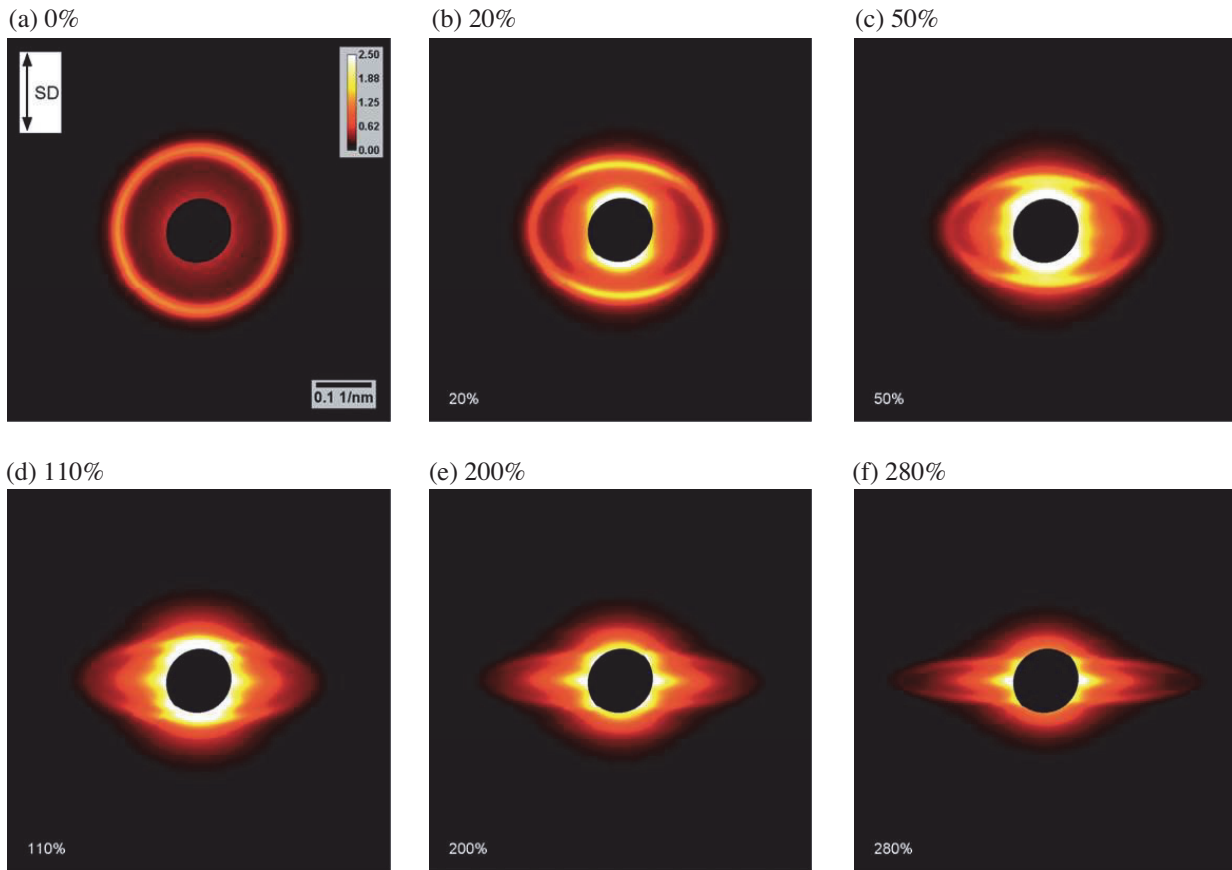


**Fig. 7.** 2D-SAXS patterns of LN70 at different deformation stages ( $\epsilon_{M,x} = 0\%$ , 20%, 50%, 110%, 200% and 280%). The scale bar represents  $q$ , with a width of  $0.1 \text{ nm}^{-1}$ . The intensities are displayed in linear scale and represented by the calibration bar, reaching from 0 to 2.5 (in arbitrary units). Scale and calibration bar count for all SAXS patterns in this figure. The stretching direction is vertical, as marked by an arrow. The initial ring transforms upon stretching into an ellipse. The minor axis of the ellipse becomes smaller with increasing strain, whereas the major axis decreases. Small equatorial streaks are observed at high strains.

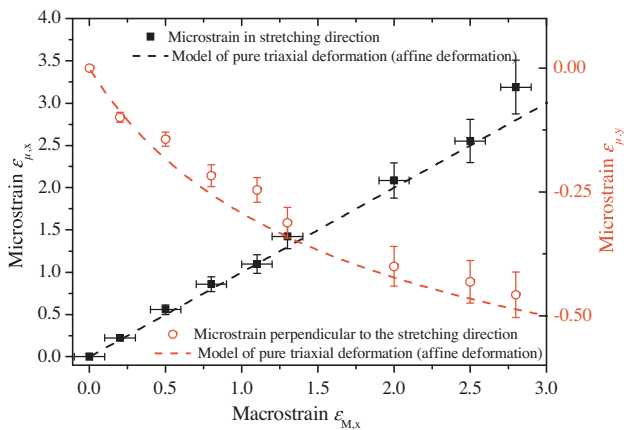


**Fig. 8.** Microstrain as function of the macrostrain. The microstrain was calculated from the major and minor axis of elliptical fits from the 2D-SAXS patterns of LN70.

direction ( $\epsilon_{M,y} = \epsilon_{M,z}$ ) and affine deformation behaviour ( $\epsilon_{\mu,y} = \epsilon_{M,y}$ ), it is possible to describe the macrostrain  $\epsilon_{M,x}$  as a function of the microstrain perpendicular to the stretching direction  $\epsilon_{M,y}$  by

$$\epsilon_{\mu,y} = \sqrt{\frac{1}{(\epsilon_{M,x} + 1)}} - 1 \quad (4)$$

The related curves for affine behaviour are plotted as dashed lines in Fig. 8 and describe the data points in a good manner. Thus, the deformation mechanism of LN70 is dominated by a triaxial deformation of the domains, which turns out to be affine. The four-point pattern, which was found in LN50 and which is typical for lamellar block copolymers was absent. This indicates that the cooperative tilting of lamellae and the therewith connected formation of chevrons is hindered.

#### 4. Conclusions

Different deformation mechanisms were found in the studied S-S/B-S triblock copolymers with similar block architectures and segregation strengths. The deformation mechanism depends on the styrene content in the S/B-middle block and the previous mechanical history. LN50, having a lower styrene-content in the S/B-middle block (50 wt.%), shows lamellae undulation and tilting above the yield point, which is comparable to the behaviour of classical SBS triblock copolymers. The contribution of lamellae tilting is decreasing with deformation and is suggested to be constraint by the deformation of adjacent grains with different lamellae orientations. At strains

above 180%, no further contribution of lamellae tilting was found. Instead, the deformation was affine. The higher styrene content in the S/B-middle block of 70 wt.% in LN70 results in a different deformation mechanism, as indicated by the absence of the distinct four-point SAXS-pattern. Micro- and macro-strain of LN70 were found to be similar over the whole investigated deformation range, which points to affine deformation. Three possible explanations for the different deformation behaviours shall be noted, which directly result from the different middle block composition.

- (i) The stiffness contrast between the soft and the hard phase is decreasing in LN70. Theoretical work of Castañeda et al. predicts a transition from lamellae tilting (shear along-the layers) to triaxial deformation by reducing the stiffness contrasts between the hard and the soft phase in block copolymers [13].
- (ii) The reduced long-range order (small grain size) of LN70 hinders a cooperative lamellae undulation. The formation of a chevron structure requires a highly cooperative lamellae undulation process [10]. Thus, large grain sizes favour the formation of chevrons.
- (iii) Both, the stiffness contrast and the reduced long-range order, hinder lamellae undulation and tilting.

However, it cannot be concluded yet, which of these effects dominates or if additional parameters have to be taken into account. Further experimental investigations are necessary to clearly understand the deformation mechanism on different length scales in order to improve the mechanical performance of these materials.

### Acknowledgement

The author's gratefully acknowledge the HASYLAB and DESY staff for providing beamtime within the project II-20060086 and particularly thank Andreas Timmann for his support during the experiments. M. Ganß thanks I. Thiele and J. Hempel from the Institute of Material Research and Technology at the Friedrich-Schiller-University of Jena for their support in cryo-ultramicrotomy and TEM-investigations. For the financial support of this work we thank the Deutsche Forschungsgemeinschaft (DFG, WE 2272/9-3).

### References

- [1] Holden G, Legge NR. *Thermoplastic Elastomers*, chapter Styrenic Thermoplastic Elastomers. München Wien: Carl Hanser Verlag München Wien; 1996. p. 47–70.
- [2] Honeker CC, Thomas EL. Impact of morphological orientation in determining mechanical properties in triblock copolymer systems. *Chem Mater* 1996;8(8):1702–14.
- [3] Adhikari R, Michler GH. Influence of molecular architecture on morphology and micromechanical behavior of styrene/butadiene block copolymer systems. *Prog Polym Sci* 2004;29(9):949–86.
- [4] Lach R, Weidisch R, Knoll K. Morphology and mechanical properties of binary triblock copolymer blends. *J Polym Sci, Part B: Polym Phys* 2005;43(4):429–38.
- [5] Ganß M, Satapathy BK, Thunga M, Weidisch R, Knoll K. Molecular-weight-controlled brittle-to-semiductile-to-ductile transition in s-(s/b)-s triblock copolymers. *Macromol Mater Eng* 2010;295(2):178–88.
- [6] Staudinger U, Satapathy BK, Thunga M, Lach R, Weidisch R, Knoll K. Influence of phase miscibility and morphology on crack resistance behaviour and kinetics of crack propagation of nanostructured binary styrene-(styrene/butadiene)-styrene triblock copolymer blends. *Acta Mater* 2007;55(17):5844–58.
- [7] Ganß M, Staudinger U, Thunga M, Knoll K, Schneider K, Stamm M, et al. Influence of S/B middle block composition on the morphology and the mechanical response of polystyrene-block-poly(styrene-co-butadiene)-block-polystyrene triblock copolymers. *Polymer* 2012;53(10):2085–98.
- [8] Seguela R, Prud'homme J. Deformation mechanism of thermoplastic two-phase elastomers of lamellar morphology having a high volume fraction of rubbery microphase. *Macromolecules* 1981;14(1):197–202.
- [9] Polizzi S, Bösecke P, Stribeck N, Zachmann HG, Zietz R, Bordeianu R. Small-angle x-ray scattering investigations of styrene-butadiene-styrene block copolymers during stretching. *Polymer* 1990;31:638–45.
- [10] Cohen Y, Albalak RJ, Dair BJ, Capel MS, Thomas EL. Deformation of oriented lamellar block copolymer films. *Macromolecules* 2000;33(17):6502–16.
- [11] Cohen Y, Brinkmann M, Thomas EL. Undulation, dilation, and folding of a layered block copolymer. *J Chem Phys* 2001;114(2):984–92.
- [12] Stribeck N. *X-Ray Scattering of Soft Matter*. Springer; 2007.
- [13] Racherla V, Lopez-Pamies O, Castañeda PP. Macroscopic response and stability in lamellar nanostructured elastomers with oriented and unoriented polydomain microstructures. *Mech Mater* 2010;42(4):451–68.
- [14] Knoll K, Niessner N. Styrolux(+) and styroflex(+) – from transparent high impact polystyrene to new thermoplastic elastomers – syntheses, applications and blends with other styrene based polymers. *Macromol Symp* 1998;132:231–43.
- [15] Thunga M, Satapathy BK, Weidisch R, Stamm M, Sommer JU, Knoll K. Influence of chain architecture on phase behaviour of styrene-(styrene/butadiene)-styrene triblock copolymers and their binary blends. *Eur Polymer J* 2009;45(2):537–49.
- [16] Jouenne S, Gonzalez-Leon JA, Ruzette AV, Lodefier P, Leibler L. Styrene-butadiene gradient block copolymers for transparent impact polystyrene. *Macromolecules* 2007;41(24):9823–30.
- [17] Schneider K, Schöne A, Jun TS, Korsunsky AM. Investigation of changes in crystalline and amorphous structure during deformation of nano-reinforced semi-crystalline polymers by space-resolved synchrotron SAXS and WAXS. *Proc Eng* 2009;1(1):159–62.
- [18] Abramoff MD, Magalhaes PJ, Ram SJ. Image processing with imagej. *Biophoton Int* 2004;11:36–42.
- [19] Matsen MW. Equilibrium behavior of asymmetric aba triblock copolymer melts. *J Chem Phys* 2000;113(13):5539–44.
- [20] Staudinger U, Satapathy BK, Weidisch R. Influence of block composition on crack toughness behaviour of styrene-b-(styrene-random-butadiene)-b-styrene triblock copolymers. *Eur Polymer J* 2008;44(6):1822–33.
- [21] Michler GH, Adhikari R, Lebek W, Goerlitz S, Weidisch R, Knoll K. Morphology and micromechanical deformation behavior of styrene butadiene-block copolymers. i. toughening mechanisms in asymmetric star block copolymers. *J Appl Polym Sci* 2002;85:683–700.

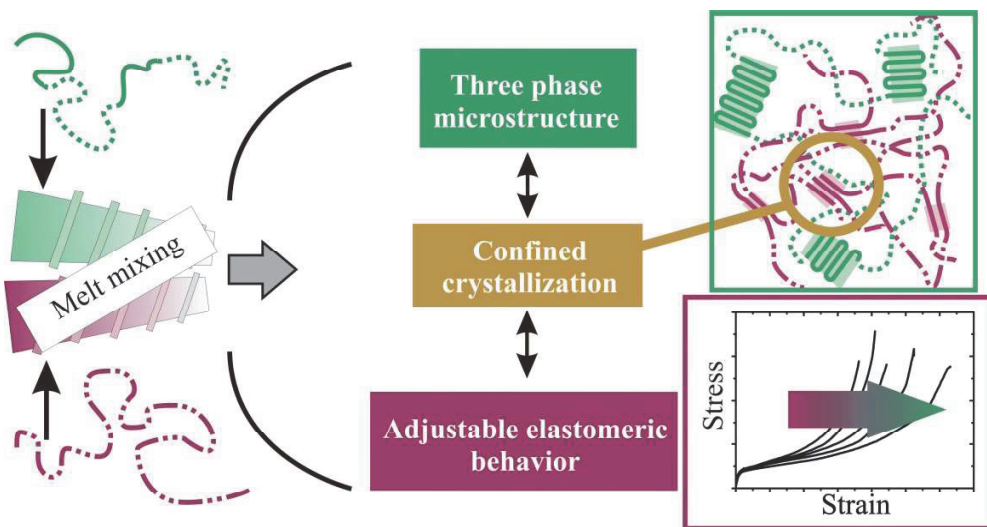




## Publication [P3]

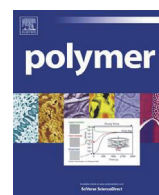
# Blends of ethylene–octene copolymers with different chain architectures – Morphology, thermal and mechanical behavior

Stefan Hölzer, Matthias Menzel, Qamer Zia, Ulrich S. Schubert, Mario Beiner, Roland Weidisch



*Polymer* **2013**, *54*, 5207–5213





# Blends of ethylene–octene copolymers with different chain architectures – Morphology, thermal and mechanical behavior

Stefan Hölzer<sup>a,b</sup>, Matthias Menzel<sup>a</sup>, Qamer Zia<sup>a,1</sup>, Ulrich Sigmar Schubert<sup>b</sup>,  
Mario Beiner<sup>a,c,\*</sup>, Roland Weidisch<sup>a,c,2</sup>

<sup>a</sup> Fraunhofer-Institut für Werkstoffmechanik IWM, Walter-Hülse-Str. 1, 06120 Halle (Saale), Germany

<sup>b</sup> Laboratory of Organic and Macromolecular Chemistry (IOMC), and Jena Center for Soft Matter (JCSM), Friedrich-Schiller-Universität Jena, 07743 Jena, Germany

<sup>c</sup> Institut für Chemie, Martin-Luther-Universität Halle-Wittenberg, 06099 Halle (Saale), Germany

## ARTICLE INFO

### Article history:

Received 22 May 2013

Received in revised form

14 July 2013

Accepted 17 July 2013

Available online 26 July 2013

### Keywords:

Olefin copolymers

Thermoplastic elastomer

Mechanical behavior

## ABSTRACT

Blends of two elastomeric ethylene–octene copolymers with similar octene contents having a random (ORC) and a blocky architecture (OBC) are prepared by melt mixing. The thermal and mechanical properties of ORC, OBC and their blends are investigated by DSC, dynamic mechanical analysis and tensile tests. The morphology of the semi-crystalline samples is studied by AFM and WAXS. Two types of crystals have been observed: (i) Orthorhombic crystals forming lamellae with an estimated thickness of about 13 nm composed mainly of long polyethylene-like sequences of OBC that melt a temperature of about 120 °C and (ii) fringed micellar crystals with a thickness of 2–4 nm formed basically by short polyethylene-like sequences of ORC that have melting temperatures between 30 and 80 °C. The amorphous phase contains a relatively homogeneous mixture of segments of both components indicated by the relatively uniform shape of the loss modulus peaks from dynamic-mechanical measurements for all investigated copolymers and blends. ORC crystallization is hindered in blends as indicated by lower melting enthalpies. This might be related to the high octene content of the amorphous phase at the relevant crystallization temperature as well as geometrical constraints since ORC crystallization occurs in an already semi-crystalline polymer. The results of tensile tests show that the mechanical behavior can be tailored via blend composition and morphology of the semi-crystalline material. The findings clearly indicate that blending is a powerful strategy to optimize the properties of polyolefin-based copolymers.

© 2013 Elsevier Ltd. All rights reserved.

## 1. Introduction

Statistical copolymerization with  $\alpha$ -olefins such as hexene or octene is a well known strategy to manipulate the crystallization behavior of polyethylene (PE). This effect is used in case of linear low density polyethylene (LLDPE) to optimize the mechanical and optical properties of these semi-crystalline materials. The influence of  $\alpha$ -olefin type and content on these properties has been studied in great detail [1–3]. At crystallinities of 10–20%, which are typical for

ethylene–octene (EO) elastomers, LLDPEs crystallize in form of fringed micelles, often accompanied by the occurrence of a hexagonal crystal structure [3,4]. At higher crystallinities ( $X_c \geq 40\%$ ) orthorhombic crystals forming lamellae and a conventional spherulitic superstructure are observed.

In the past, the production of olefin copolymers on an industrial scale has been basically limited to olefin random copolymers (ORC). Just recently, the new chain shuttling synthesis method of The DOW Chemical Company allowed the production of olefin block copolymers (OBCs) [5]. In this case, EO copolymers are synthesized by using two catalysts with a different octene-selectivity resulting either in (i) chain sequences with a very low octene-content, high crystallinity and high melting temperature ( $T_m \approx 120$  °C) or (ii) sequences with a high octene content and almost no crystallinity. A chain shuttling agent allows to change from one catalyst to the other and vice versa during chain growth, leading to a multiblock architecture in one-pot synthesis. Accordingly, the macroscopic properties of olefin block copolymers can be controlled by the chain

\* Corresponding author. Fraunhofer-Institut für Werkstoffmechanik IWM, Walter-Hülse-Str. 1, 06120 Halle (Saale), Germany.

E-mail addresses: [mario.beiner@iwmm.fraunhofer.de](mailto:mario.beiner@iwmm.fraunhofer.de), [beiner@physik.uni-halle.de](mailto:beiner@physik.uni-halle.de) (M. Beiner).

URL: <http://www.iwmm.fraunhofer.de> (M. Beiner)

<sup>1</sup> Present address: Ticona GmbH, 65926 Frankfurt (Main), Germany.

<sup>2</sup> In memory of Prof. Dr.-Ing. Roland Weidisch, who died in November 2012 at the age of only 47 years. We miss him as mentor, colleague and friend.

shuttling level, the overall octene-content and the hard-soft block ratio [5,6].

At octene contents of about 10 mol%, olefin block copolymers behave like thermoplastic elastomers, whereas crystalline segments act as physical cross-links in the amorphous matrix. Long and flexible chain segments between the crystals, which can stretch easily, lead to higher strain at break and better strain recovery at room temperature compared to random EO copolymers [7]. Hsiao and co-workers found a strong dependence of the chain shuttling level on the tensile properties, especially at elevated temperatures. High chain shuttling levels and more blocks per chain lead to better elastomeric properties, which was attributed to a more efficient molecular bridging between the physical cross-links [8,9].

Blending represents an effective method to tailor the properties of polyolefins such as processability or mechanical behavior. This is related to the fact that mixing or phase separation can occur in the crystalline phase as well as in the amorphous phase of the blend components. What happens is strongly depending on (i) molecular parameters, such as comonomer type and the chain architecture as well as (ii) the processing conditions. Coexistence of crystals with different sizes was commonly found in blends of different random EO copolymers, whereas cocrystallization has been gained by rapid cooling (quenching) [3,10–12]. The situation in the amorphous phase in blends of two different ORC copolymers depends on the comonomer content of both components [13]. Significant differences in their octene contents ( $\geq 10\%$ ) lead to phase separation [10,13,14]. Interestingly, the thermal and mechanical behavior of OBC:ORC blends have not yet been investigated in detail. This is rather surprising since blending offers an easy way to tune the mechanical properties which are of great importance for various applications. Further, synergistic effects can be expected since long (OBC) and short (ORC) flexible blocks are arranged in a non-crystalline matrix like in bimodal networks having advantageous elastomeric properties [15,16].

In this contribution, we report the thermal, mechanical and morphological properties of blends composed of two olefin copolymers with similar comonomer contents but either blocky or random chain architecture. Aim is to study the influence of chain architecture and composition of OBC:ORC blends on mechanical behavior, crystallization and morphology. The results show that application-relevant properties of innovative polyolefin copolymers can be systematically optimized by blending without changing the comonomer content.

## 2. Experimental

### 2.1. Materials and processing

Ethylene–octene copolymers with different molecular architectures were provided by The DOW Chemical Company (Horgen, Switzerland). ORC is a random copolymer, in which the octene units are randomly distributed along the polymer chain. OBC is a block copolymer synthesized by chain shuttling polymerization [5] consisting of nearly amorphous blocks with a high octene content and crystallizable blocks with a very low octene content. More detailed information on the ORC and OBC polymers is given in Table 1 and published elsewhere [7].

Blends of OBC and ORC have been compounded by melt mixing for at least 5 min in a minicomponenter (Minilab II, Thermo Scientific) at 190 °C with a screw speed of 100 min<sup>-1</sup>. The extruded stripes were cut into small pieces with dimensions of 5 × 5 × 1 mm<sup>3</sup>. Compression molded plates were obtained by (i) melting the blends at 190 °C for 5 min without pressure, (ii) pressing them at the same temperature for 30 s at a pressure of

**Table 1**  
Molecular structure of the used olefin copolymers [7].

Copolymers	$M_w$ [kg/mol]	PDI	Octene content [%]
Olefin block copolymer (OBC)	124	2.1	12
Olefin random copolymer (ORC)	111	2.1	12

30 N/cm<sup>2</sup> and (iii) subsequent cooling to 40 °C with a rate of 15 K/min while keeping the pressure constant. Before characterization, all samples were stored at room temperature for one week.

### 2.2. Methods

Calorimetric measurements were performed using a NETZSCH DSC 204 F1 Phoenix at temperatures between –50 and 150 °C with heating and cooling rates of 10 K/min. The crystallinity of the samples is estimated based on the ratio of the measured melting enthalpies to that of perfect PE crystals ( $\Delta H_{m,PE} = 290$  J/g) [7]. A DMA Q800 (TA Instruments) was used for dynamic mechanical analysis (DMA) in tension mode between –100 and 50 °C with a heating rate of 2 K/min, a strain amplitude of 0.5% and a measurement frequency of 1 Hz. Tensile tests were performed according to DIN EN ISO 527 on at least five specimens using a Zwick/Roell Z010. The initial gage length was 28 mm and the crosshead speed was held constant at 28 mm/min. For Atomic Force Microscopy (AFM), small areas of the compression molded plates were trimmed with a cryo-ultramicrotome (PT-PC Powertome with CR-X cryo unit, RMC products) at a temperature of –100 °C in order to minimize the irreversible deformation of the blend morphology. AFM images were obtained by a JPK Nanowizard II in tapping mode using super sharp silicon tips with tip radii  $\geq 2$  nm. Wide-angle X-ray scattering (WAXS) experiments were carried out on a Bruker Nanostar using X-ray radiation with a wavelength of  $\lambda = 1.54$  Å and a sample-to-detector distance of 124 mm. A silver behenate standard was used for scattering angle calibration.

## 3. Results

### 3.1. Thermal properties

First heating scans from DSC measurements on the olefin random copolymer (ORC), the olefin block copolymer (OBC) and their blends are shown in Fig. 1. Pure OBC exhibits a pronounced

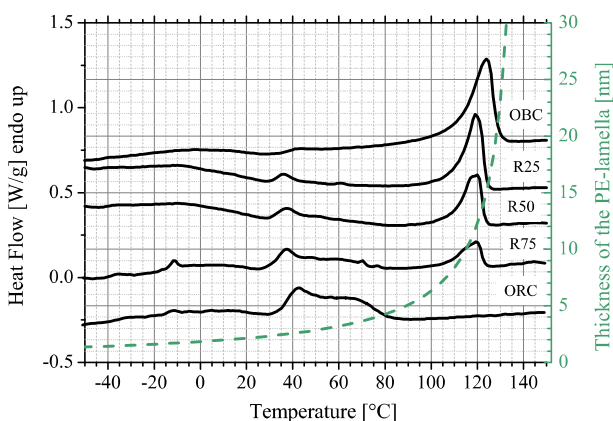


**Fig. 1.** DSC curves for copolymers and OBC:ORC blends obtained during the first heating. The curves are vertically shifted for better visualization. The dotted line represents the dependence of the crystal thickness on the melting temperature of an orthogonal PE crystal, based on the Broadhurst-equation (1) [17].

melting peak at  $T_m \approx 124$  °C, which is only 5–10 K lower than melting temperatures of classical, orthorhombic PE crystals. The melting enthalpy of OBC is found to be 38 J/g, which corresponds to an overall crystallinity of  $X_c = 13.1\%$ , estimated based on the melting enthalpy of perfect PE crystals ( $\Delta H_{m,PE} = 290$  J/g). The crystalline fraction of the random copolymer ORC is melting between 30 and 80 °C. The melting peak has a bimodal shape which could in principle originate either from different thicknesses of the crystalline lamellae (resulting in different melting temperatures according to the Gibbs–Thomson effect [17]) or from the coexistence of different crystalline forms (polymorphs) [18]. At low temperatures ( $-20 \leq T \leq 20$  °C), ORC shows additional small peaks which may be due to melting of extremely small crystals or structural relaxation phenomena in the (rigid) amorphous phase.

The DSC heating scans for blends exhibit similar features as found for pure OBC and ORC. In particular, all blends show two melting peaks. One melting peak occurs at temperatures between 30 and 80 °C (low-temperature peak, LTP) and the other one at about 120 °C (high temperature peak, HTP). A detailed analysis of the melting enthalpies (Fig. 2) confirms that the melting enthalpy of the high temperature peak,  $\Delta H_{m,1}$ , is increasing linearly with the OBC content while that of the low temperature peak,  $\Delta H_{m,2}$ , is decreasing non-linearly. The obtained melting temperatures,  $T_{m,1}$  and  $T_{m,2}$ , the melting enthalpies,  $\Delta H_{m,1}$  and  $\Delta H_{m,2}$ , and the estimated crystallinities,  $X_1$  and  $X_2$ , are given for both melting peaks in Table 2.

In order to approximate the crystal thickness and to estimate the number of methylene units  $n$  along the  $c$ -axis of the orthorhombic PE-like crystal, we used the Broadhurst equation [17]

$$T_m^n = T_m^\infty \frac{a+n}{b+n} \quad (1)$$

where  $T_m^\infty = 140.15$  °C is the melting point of an ideal PE crystal with infinite lamella thickness while  $a = 1.5$  and  $b = 5.0$  are fit parameters to describe the melting behavior of alkanes and PE crystals [17]. This function is plotted in the DSC diagram (Fig. 1) in order to compare the melting temperatures directly with the corresponding crystal thicknesses. Low-temperature peaks at 30–80 °C are related to ORC indicate crystal thickness between 2 and 4 nm or respectively 15 to 30 methylene units per crystalline stem. These results are in good accordance with the findings by Mauler et al., who found an average number of 16 successive ethylene units

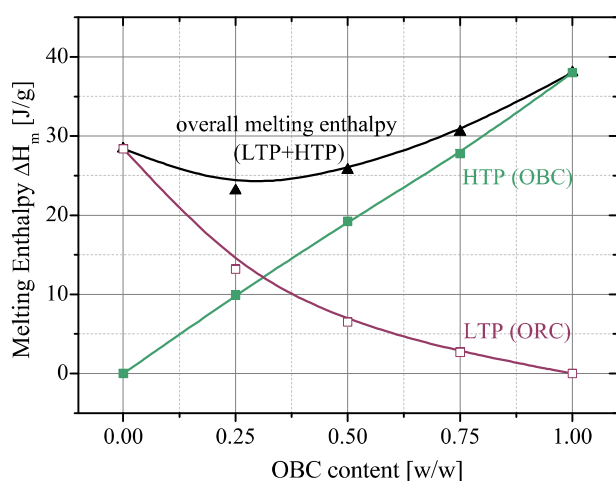


Fig. 2. Melting enthalpies of the high temperature OBC-peak (HTP, filled rectangles), the low temperature ORC-peak (LTP, open rectangles) and their sum (triangles) versus the fraction of OBC. The solid lines are guides to the eye and illustrate the overall trend.

Table 2

Parameters taken from DSC scans on olefin copolymer blends.

Sample	High temperature peak			Low temperature peak			
	$T_{m,1}$ [°C]	$\Delta H_{m,1}$ [J/g]	$X_1$ [%]	$T_{m,2}$ [°C]	$\Delta H_{m,2}$ [J/g]	$X_2$ [%]	$X_{total}$ [%]
OBC	123.9	38.0	13.1	—	—	—	13.1
R25	119.0	27.8	9.6	36.3	2.7	0.9	10.5
R50	120.0	19.2	6.6	37.9	6.5	2.3	8.9
R75	119.3	9.9	3.4	37.3	13.2	4.5	7.9
ORC	—	—	—	43.1	28.4	9.8	9.8

(i.e.  $n = 32$  methylene units) along the main chain in a similar ORC by  $^{13}\text{C}$  NMR [2]. Hence, one can conclude that the undisturbed PE-like sequences in ORC chains do crystallize partly in a fully stretched conformation which results in a fringed-micellar or bundle-like morphology, as described by Hiltner and co-workers [3]. The high melting temperature of OBC of  $T_m \approx 124$  °C corresponds to a crystal thickness of around 13 nm and about 100 methylene units per stem. Considering that the octene units are usually not incorporated in the crystals, one can conclude that the PE-like sequences in the investigated OBC have at least this average length. The coexistence of two distinct melting regions in the DSC heating scans of blends shows that independent crystalline phases exist related to OBC and ORC. The PE-like blocks of OBC with low octene-contents form obviously really thick crystals (13 nm). Additional melting peaks at temperatures  $\leq 20$  °C were not found for OBC indicating that the octene-rich OBC-block hardly crystallizes.

The linear increase of the melting enthalpy  $\Delta H_{m,1}$  of the high temperature peak (HTP) in DSC heating scans for blends with increasing OBC content evidences the weak influence of the ORC phase on the crystallization of OBC chains. The simultaneous non-linear decrease of the melting enthalpy  $\Delta H_{m,2}$  of the low temperature peak (LTP) with increasing OBC content indicates that the presence of OBC hinders the crystallization of relatively short PE-like sequences in ORC during cooling. This is somehow an expected finding since the crystallization in the random copolymer occurs at lower temperatures than that in the block copolymer. Consequently, crystallization of short PE-like sequences in ORC chains occurs in amorphous domains between already existing crystals formed by parts of the OBC chains. Crystallization under these conditions is surely more complicated than crystallization in pure ORC since the amorphous regions between OBC crystals (i) have nanoscopic dimensions, (ii) contain more entanglements and (iii) a significantly larger amount of octene units which are not incorporated in the OBC crystals. Hence, growth of ORC crystals in blends is kinetically hindered by geometrical constraints as well as the presence of non-crystallizable units. Moreover, nucleation is less efficient due to the limited size of the amorphous regions. These effects together should be responsible for the reduced crystallinity of the ORC chains in blends with OBC keeping all other conditions constant. Note that cocrystallization of PE-like sequences of ORC and OBC obviously does not occur, although they differ only in length.

### 3.2. Mechanical properties

**Dynamic-mechanical analysis.** Storage modulus  $E'$  and loss modulus  $E''$  taken from dynamic-mechanical measurements on OBC, R50 and ORC in the temperature range from  $-100$  to  $-30$  °C are presented in Fig. 3. All samples show a distinct relaxation process at temperatures between  $-60$  and  $-50$  °C which is indicated by a significant drop in  $E'(T)$  and a corresponding peak in  $E''(T)$ . The storage modulus decreases from 1 GPa at temperatures significantly below  $T_\alpha^{1\text{Hz}}$  to  $E' \approx 10$  MPa above. This feature reflects

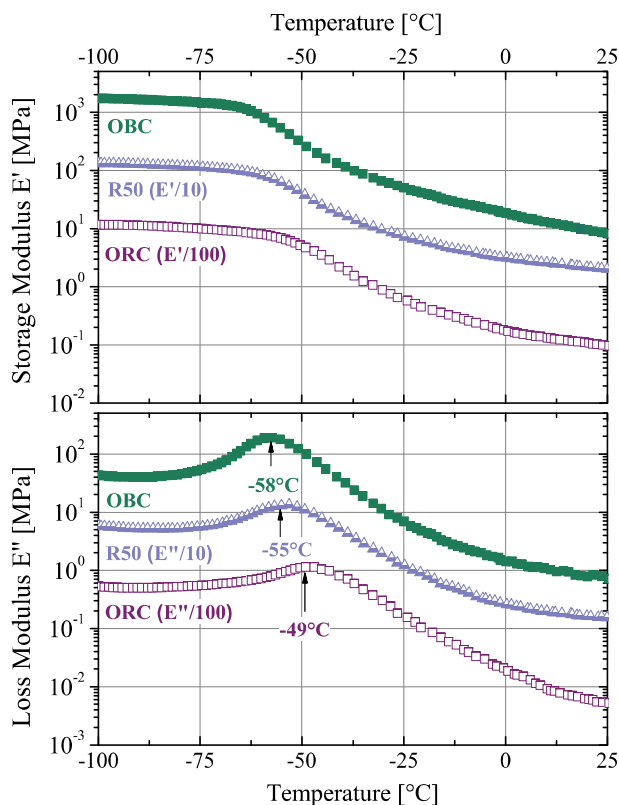


**Fig. 3.** Dynamic mechanical analysis data for OBC, R50 and ORC in the temperature range near the dynamic glass transition temperature  $T_{\alpha}^{1\text{Hz}}$ . The arrows indicate the estimated values of  $T_{\alpha}^{1\text{Hz}}$ .

the dynamic glass transition ( $\alpha$  relaxation) of the amorphous phase occurring in this temperature range at a frequency of 1 Hz. It should be noted that the dynamic glass transition temperature  $T_{\alpha}^{1\text{Hz}}$  of the amorphous phase in OBC is lower than that of ORC and that the transition in blends occurs at intermediate temperatures. Moreover, there is no significant difference in the  $E''$  peak width and no clear evidence for the existence of two superimposed  $E''$  peaks in case of blends. This points to a relatively homogeneous mixing of ORC and OBC segments in the amorphous phase. The lower  $T_{\alpha}^{1\text{Hz}}$  value for OBC indicates that a larger fraction of octene units in the amorphous domains is leading to a lower softening temperature compared to pure polyethylene ( $T_g \approx -36^\circ\text{C}$  [19]). This may be related to internal plasticization of main chains by alkyl side groups known from many other homologous series [20], probably accompanied by a decrease of the average density of the amorphous domains. Considering the concentration of octene units in the amorphous domains, this interpretation is in line with the discussion about trends in the DSC data.

**Tensile tests.** Representative stress–strain curves for the investigated olefin copolymers are depicted in Fig. 4. All samples show an elastomeric property profile. While the behavior at small strains ( $\leq 100\%$ ) is only weakly changing, the large strain behavior is significantly depending on blend composition. In particular, the onset of strain hardening and the strain at break are affected. Average values for important mechanical parameters are plotted versus OBC content in Fig. 5. Pure ORC samples show the highest values of the 300% secant modulus but the lowest strain at break. In blends, the strain at break is systematically increasing while the 300% modulus is decreasing with increasing OBC contents. The tensile strength, however, seems to be only slightly affected by blend composition (Fig. 5).

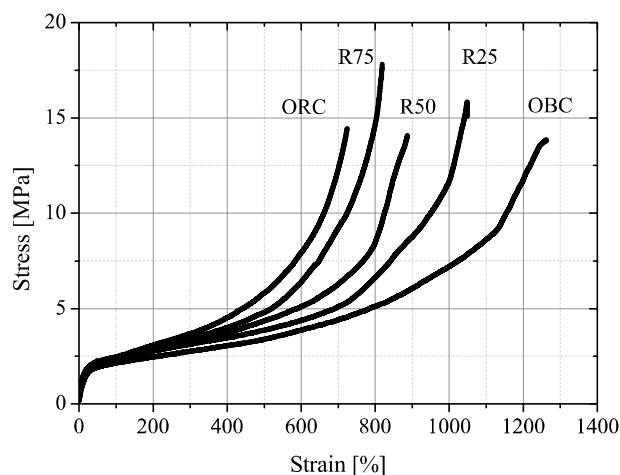


**Fig. 4.** Representative stress–strain curves of OBC, ORC and their blends.

In general, the results show that the mechanical properties can be easily tuned by changing the blend composition. Although the average octene content of all investigated copolymer systems is nearly identical, systematic trends are found in the mechanical behavior depending on the OBC:ORC ratio. This underlines a strong influence of crystallinity and morphology. Considering the dependence of mechanical properties on composition, one can conclude that the stress–strain behavior at large strains ( $\geq 100\%$ ) mainly depends on the average length of (flexible) chain segments between two adjacent crystallites acting as physical cross-links [21]. The blocky molecular architecture of OBC chains results in longer flexible chain segments between the relatively large, but rare crystals. In contrast, ORC contains much shorter non-crystallizable chain sequences where ethylene and octene units are truly randomly arranged. Hence, the flexible chain segments between numerous small ORC crystals (forming fringed micelles [3,7]) should be also much shorter. This leads to higher repulsive forces due to entropy elasticity and hence to higher stresses compared to OBC. This picture gives a consistent explanation for the systematic changes regarding 300% secant modulus and strain at break in OBC:ORC blends.

### 3.3. Structural properties

**Wide angle X-ray scattering (WAXS).** WAXS pattern for all investigated olefin copolymer samples are given in Fig. 6. Two

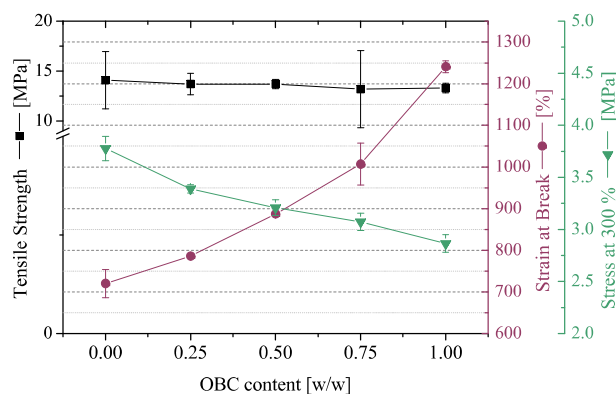


**Fig. 5.** Mechanical properties as a function of the OBC-content. The solid lines are guides to the eye highlighting trends.

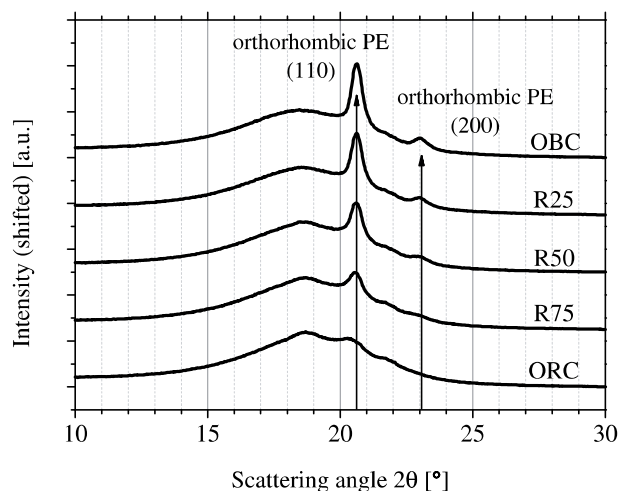


**Fig. 6.** WAXS pattern for the olefin copolymer blends. The patterns are vertically shifted for the sake of clarity.

Bragg peaks are found for OBC at about  $2\theta \approx 20.6^\circ$  and  $23^\circ$  which corresponds to spacings of 0.43 and 0.38 nm, respectively. These peaks are attributed to the (110) and (200) reflexes of an orthorhombic lattice, like known for PE. In pure ORC, the first peak is blurred and seems to be slightly shifted to smaller scattering angles while the second reflex is nearly absent. This finding is in agreement with the recent observation that hexagonal and orthorhombic crystals coexist in ORC systems with similar chain architectures [8]. In blends, the intensity of the sharp (110) peak as well as the (200) peak corresponding to orthorhombic OBC crystals are systematically increasing with increasing OBC content [22]. This points to a relatively independent crystallization of PE-like sequences in OBC chains supporting the DSC results reported above.

Compared to literature, there are obviously no dramatic changes in the crystallization behavior of the individual OBC [7] and ORC [8] chains in blends apart from a reduced crystallinity of the ORC component found by DSC. Hence, two polymorphic forms of polyolefin crystals are observed in blends – (i) large orthorhombic crystals originating from long PE-like blocks in OBC and (ii) small crystals mainly formed by short PE-like sequences in ORC, which is supposed to form fringed micelles. Based on the detected scattering pattern, it is hard to decide whether the ORC crystals are mainly orthorhombically or hexagonally packed.

**Atomic force microscopy.** Fig. 7 shows AFM phase contrast images of OBC (a), ORC (e) and their blends (b–d). For OBC, the crystals that are formed by the blocks with a very low octene content are seen as needle-like structures. Crystalline and amorphous phases have different hardness and can be detected relatively easily by AFM, in particular in phase contrast images. The average thickness of the crystals, estimated based on measurements of at least 50 representative crystals, is found to be  $14 \pm 4$  nm. In R25, the concentration of large crystals is reduced due to blending with ORC. This trend continues with increasing ORC content until large crystals cannot be observed anymore for pure ORC by AFM (Fig. 7e). The crystals formed by ORC chains cannot be fully resolved by this method, due to convolution effects of the small crystals (2–4 nm) and the AFM tip (radius  $\geq 2$  nm). What is seen in the images for ORC is only a certain network-like morphology, which indicates the existence of small crystals dispersed homogeneously in the material. In general, the AFM images for the different olefin copolymers and blends confirm that what has been concluded from other methods. The average OBC crystal thickness (14 nm) is in good agreement with the values estimated based on DSC melting temperatures (13 nm, cf. Fig. 1). The AFM images of the blends show big OBC crystals as well as a network-like structure attributed to small ORC crystals. Depending on composition, the features are differently pronounced. This finding is in accordance with the discussion about well distinguishable ORC and OBC crystals based on data from WAXS and DSC.

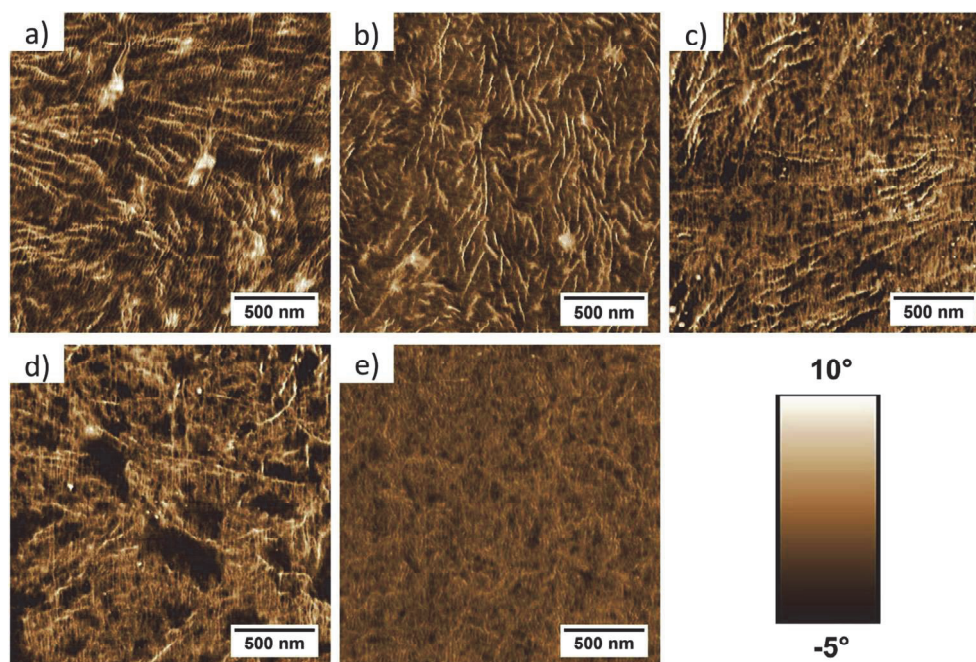


**Fig. 7.** AFM phase images showing  $2 \times 2 \mu\text{m}$  scans of (a) OBC, (e) ORC and (b–d) their blends R25, R50 and R75. The color bar is identical for all images and covers the range from  $-5^\circ$  to  $10^\circ$ .

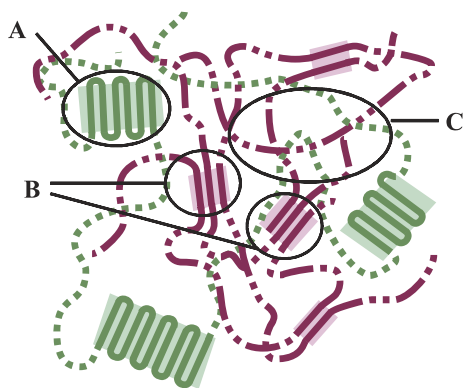


**Fig. 8.** Sketch of the proposed morphology of olefin copolymer blends. OBC and ORC chains are shown as green and red lines, respectively. Chain segments with high octene content are displayed as dotted lines while solid lines represent nearly undisturbed, crystallizable PE segments. A thick OBC crystals arranged as folded lamellae; B thin ORC crystals arranged in form of fringed micelles; C amorphous phase.

#### 4. Discussion and conclusions

Summarizing the results of our calorimetric, mechanical and morphological investigations on melt-mixed and extruded blends of ethylene–octene copolymers with random (ORC) and blocky (OBC) chain architecture one can conclude that these materials show a three phase structure as sketched in Fig. 8. The main phases, which have to be distinguished, are:

- A *OBC crystals* = orthorhombically packed PE-like crystals with a thickness of 10–15 nm along the crystallographic *c*-axis having a melting temperature of about 120 °C. These crystals are obviously formed by long methylene sequences in the OBC block with a very low octene content. The concentration of these crystals is nearly proportional to the OBC content in blends. In accordance with prior results from Hiltner et al., the formation of folded lamellae of OBC is expected [6].
- B *ORC crystals* = small PE-like crystals with a thickness of about 2–4 nm having melting temperatures in the range from 30 to 80 °C. These crystals should originate from the crystallization of short PE-like sequences in ORC chains to fringed micelles or bundles in accordance with literature [3,7]. Whether these crystals are mainly orthorhombic or hexagonal cannot be decided based on the experiments performed here. A mixture of hexagonal and orthorhombic crystals has been reported for similar ORC systems in the literature [8]. There are clear indications that the fraction of crystalline ORC sequences per chain is smaller in case of ORC:OBC blends compared to pure ORC. This might be due to geometrical constraints and an actually higher octene content in the amorphous phase of OBC:ORC blends containing already PE-like OBC crystals at the crystallization temperature of the relevant ORC sequences. This should hinder ORC crystal growth and reduce the nucleation efficiency.
- C *Amorphous phase* = quasi-homogeneous mixture of non-crystalline segments from both components of the investigated ORC:OBC blends. There is no clear evidence for a separation of chain segments from ORC and OBC in the amorphous phase. Bimodal loss modulus peaks or significant peak broadening which would be expected for well defined domains with typical dimensions larger than a very few nanometer are not observed. The observed relaxation temperatures of –60 to –50 °C are quite similar to those reported for other

ethylene–octene copolymers [3,6] and only 15–25 K lower than  $T_g$  values reported for fully amorphous PE [19].

It is interesting to find three phases in binary blends made of two polymeric components which contain two identical monomers. Although the mixed copolymers contain even the same average amount of ethylene and octene, the macroscopic properties of the blends vary strongly and systematically with chain architecture as well as blend composition. The results presented in this paper nicely demonstrate the importance of crystallinity and crystal morphology for the properties of macroscopic samples and show also how a systematic modification of the crystal size distribution can be used to tune the mechanical behavior. Blending of olefin blocky and random copolymers, OBC and ORC, is obviously a simple but efficient way to manipulate material properties. ORC rich blends have a higher secant modulus (300%) but lower strain at break while OBC rich blends have slightly lower secant moduli but significantly larger values for the strain at break. This underlines not only the large potential of innovative copolymerization techniques and olefin-based copolymers produced using such synthesis routes but shows also that blending can be a powerful strategy to control the morphology of the semi-crystalline polymers and to optimize their properties.

#### Acknowledgments

The authors kindly thank Dr. Olaf Henschke (The DOW Chemical Company, Horgen, Switzerland) for providing the polymers, support and fruitful discussions. Funding of the project ‘Triboelastomers’ by the Fraunhofer Gesellschaft as well as financial support by the Deutsche Forschungsgemeinschaft in the framework of projects B9 and A5 in the SFB TRR 102 is also greatly acknowledged.

#### References

- [1] Kim M, Phillips P. Nonisothermal melting and crystallization studies of homogeneous ethylene/alpha-olefin random copolymers. *Journal of Applied Polymer Science* 1998;70(10):1893–905.
- [2] Simanke AG, Galland GB, Freitas L, da Jornada JAH, Quijada R, Mauler RS. Influence of the comonomer content on the thermal and dynamic mechanical properties of metallocene ethylene/1-octene copolymers. *Polymer* 1999;40(20):5489–95.
- [3] Bensason S, Minick J, Moet A, Chum S, Hiltner A, Baer E. Classification of homogeneous ethylene-octene copolymers based on comonomer content. *Journal of Polymer Science Part B: Polymer Physics* 1996;34(7):1301–15.
- [4] Androsch R, Blackwell J, Chvalun SN, Wunderlich B. Wide- and small-angle x-ray analysis of poly(ethylene-co-octene). *Macromolecules* 1999;32(11):3735–40.
- [5] Arriola DJ, Carnahan EM, Hustad PD, Kuhlman RL, Wenzel TT. Catalytic production of olefin block copolymers via chain shuttling polymerization. *Science* 2006;312(5774):714–9.
- [6] Wang HP, Khariwala DU, Cheung W, Chum SP, Hiltner A, Baer E. Characterization of some new olefinic block copolymers. *Macromolecules* 2007;40(8):2852–62.
- [7] Wang HP, Chum SP, Hiltner A, Baer E. Comparing elastomeric behavior of block and random ethylene-octene copolymers. *Journal of Applied Polymer Science* 2009;113(5):3236–44.
- [8] Zuo F, Burger C, Chen X, Mao Y, Hsiao BS, Chen H, et al. An in situ X-ray structural study of olefin block and random copolymers under uniaxial deformation. *Macromolecules* 2010;43(4):1922–9.
- [9] Zuo F, Mao Y, Li X, Burger C, Hsiao BS, Chen H, et al. Effects of block architecture on structure and mechanical properties of olefin block copolymers under uniaxial deformation. *Macromolecules* 2011;44(9):3670–3.
- [10] Bensason S, Nazarenko S, Chum S, Hiltner A, Baer E. Elastomeric blends of homogeneous ethylene-octene copolymers. *Polymer* 1997;38(15):3913–9.
- [11] Morgan R, Hill M, Barham P. Morphology, melting behaviour and crystallization in polyethylene blends: the effect of cooling rate on two homogeneously mixed blends. *Polymer* 1999;40(2):337–48.
- [12] Frederix C, Lefebvre J, Rochas C, Séguéla R, Stoclet G. Binary blends of linear ethylene copolymers over a wide crystallinity range: rheology, crystallization, melting and structure properties. *Polymer* 2010;51(13):2903–17.
- [13] Bensason S, Nazarenko S, Chum S, Hiltner A, Baer E. Blends of homogeneous ethylene-octene copolymers. *Polymer* 1997;38(14):3513–20.



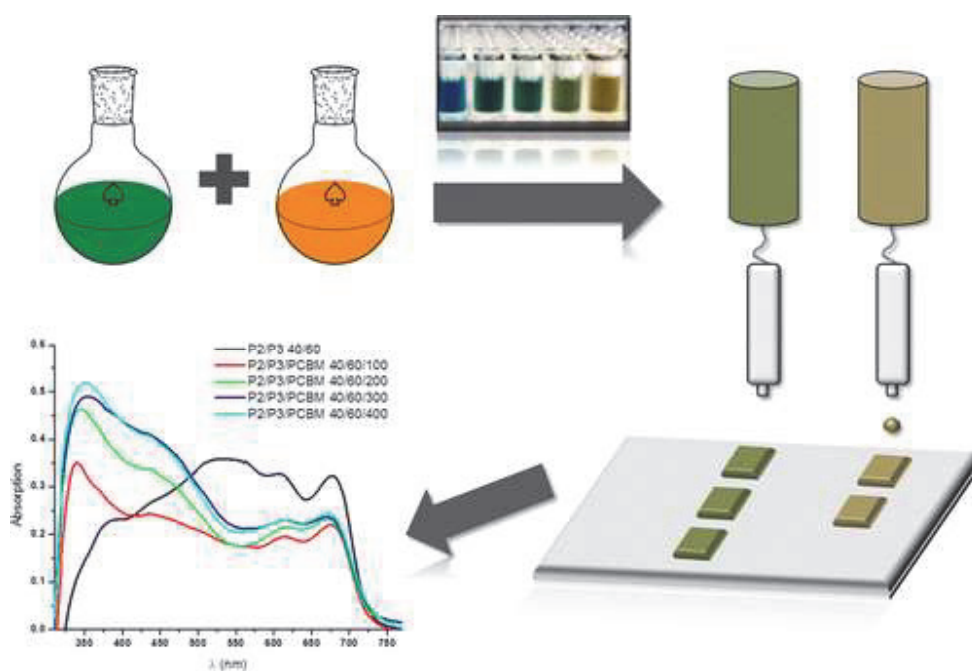
- [14] Kamdar AR, Wang HP, Khariwala DU, Taha A, Hiltner A, Baer E. Effect of chain blockiness on the phase behavior of ethylene-octene copolymer blends. *Journal of Polymer Science Part B: Polymer Physics* 2009;47(16):1554–72.
- [15] Mark JE, Tang M-Y. Dependence of the elastomeric properties of bimodal networks on the lengths and amounts of the short chains. *Journal of Polymer Science: Polymer Physics Edition* 1984;22(11):1849–55.
- [16] Termonia Y. Molecular model for the mechanical properties of elastomers. 2. Synergic effects in bimodal cross-linked networks. *Macromolecules* 1990;23(5):1481–3.
- [17] Höhne G. Another approach to the Gibbs–Thomson equation and the melting point of polymers and oligomers. *Polymer* 2002;43(17):4689–98.
- [18] Beiner M. Nanoconfinement as a tool to study early stages of polymer crystallization. *Journal of Polymer Science Part B: Polymer Physics* 2008;46(15):1556–61.
- [19] Gaur U, Wunderlich B. The glass transition temperature of polyethylene. *Macromolecules* 1980;13(2):445–6.
- [20] Beiner M, Huth H. Nanophase separation and hindered glass transition in side-chain polymers. *Nature Materials* 2003;2(9):595–9.
- [21] Sperling L. *Introduction to physical polymer science*. 4th ed. John Wiley & Sons, Inc; 2006.
- [22] The crystallinity of pure OBC estimated based on WAXS pattern is  $X_c = 13.2 \pm 1\%$ , which is comparable to values obtained from DSC ( $X_c = 13.1\%$ ). The crystallinities for pure ORC are seemingly significantly smaller but hard to detect from the measured WAXS pattern. This finding supports the results from DSC. A serious disadvantage of WAXS experiments compared to DSC is in the present case that different types of crystals (thin ORC and thick OBC crystals) cannot be discriminated in the WAXS pattern.



## Publication [P4]

# Combinatorial screening of inkjet printed ternary blends for organic photovoltaics: Absorption behavior and morphology

Anke Teichler, Stefan Hölzer, Jürgen Nowotny, Florian Kretschmer, Cornelia Bader, Jolke Perelaer, Martin D. Hager, Stephanie Hoepfener, Ulrich S. Schubert



*ACS Combinatorial Science* **2013**, *15*, 410–418



# Combinatorial Screening of Inkjet Printed Ternary Blends for Organic Photovoltaics: Absorption Behavior and Morphology

Anke Teichler,<sup>†,‡,§</sup> Stefan Hölzer,<sup>†,‡</sup> Jürgen Nowotny,<sup>†,‡</sup> Florian Kretschmer,<sup>†,‡</sup> Cornelia Bader,<sup>†,‡</sup> Jolke Perelaer,<sup>†,‡,§</sup> Martin D. Hager,<sup>†,‡,§</sup> Stephanie Hoeppeener,<sup>†,‡</sup> and Ulrich S. Schubert<sup>\*,†,‡,§</sup>

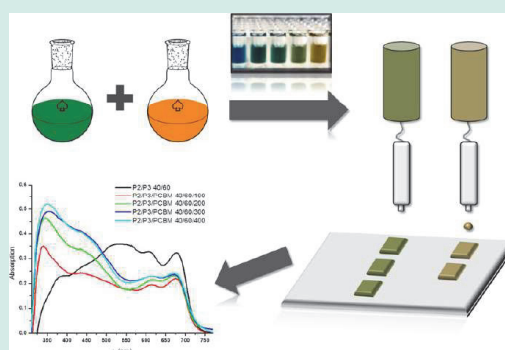
<sup>†</sup>Laboratory of Organic and Macromolecular Chemistry (IOMC), Friedrich Schiller University Jena, Humboldtstraße 10, 07743 Jena, Germany

<sup>‡</sup>Jena Center for Soft Matter (JCSM), Philosophenweg 7, 07743 Jena, Germany

<sup>§</sup>Dutch Polymer Institute (DPI), P.O. Box 513, 5600 MB Eindhoven, The Netherlands

**ABSTRACT:** Inkjet printing was used for the preparation of ternary polymer/polymer/fullerene layers for organic solar cell application, as part of a combinatorial setup for the preparation and characterization of thin-film libraries. Poly(phenylene-ethynylene)-*alt*-poly(phenylene-vinylene) (PPE-*alt*-PPV) and poly(diketopyrrolopyrrole-*alt*-fluorene) (P(DPP-*alt*-F)) were systematically blended with poly(3-octylthiophene) (P3OT) and investigated by UV-vis spectroscopy to improve the photon harvesting by extending the absorption range. The blends with the broadest absorption range (20 and 40 wt % of PPE-*alt*-PPV and P(DPP-*alt*-F), respectively) were mixed with mono(1-[3-(methoxycarbonyl)propyl]-1-phenyl)-[6,6]C<sub>61</sub> (PCBM). The blend with the low band gap polymer P(DPP-*alt*-F) revealed the most extended absorption, which ranges over the whole visible spectrum (350 to 750 nm). The mixing with PCBM (ratio 1/3) led to an optimal emission quenching and revealed a smooth film formation. In this contribution, we show that the combinatorial screening using inkjet printing represents an effective, time- and material-saving workflow for the investigation of polymer blend libraries, which is of high interest for the development of new materials for active layers in organic photovoltaics.

**KEYWORDS:** combinatorial screening, inkjet printing, ternary blends, absorption, morphology



## INTRODUCTION

The development of smaller, more flexible and cheaper optoelectronic devices, for example, organic light emitting diodes (OLEDs)<sup>1</sup> and organic photovoltaics (OPVs),<sup>2</sup> benefits from the tunable characteristics of conjugated polymers, in particular variable optical properties. Conjugated polymer structures in the field of OPVs include poly(phenylene-vinylene) (PPV),<sup>3,4</sup> poly(phenylene-ethynylene)-*alt*-poly(phenylene-vinylene) (PPE-*alt*-PPV),<sup>5,6</sup> poly(thiophene) (PT),<sup>7,8</sup> poly(fluorene) (PF),<sup>9,10</sup> and poly(diketopyrrolopyrrole) (PDPP).<sup>11,12</sup>

Thereby, a low polymer band gap<sup>2</sup> as well as a broad absorption range are required to improve quantum efficiencies of the final organic solar cell devices.<sup>13</sup> For instance, low band gap donor-acceptor copolymers were found to reveal improved photon harvesting properties.<sup>14,15</sup> In the past years, DPP moieties have gained an increased interest as a building unit for polymers used for organic solar cells because of their strong absorption in the visible region and their electron-withdrawing behavior.<sup>16</sup> For this reason, DPP represents a suitable building moiety for donor-acceptor polymers. Fluorene (F) moieties are rigid and planar building units that in contrast to DPP, act as an electron-donating unit.<sup>17</sup> As a

result, P(DPP-*alt*-F) is a donor-acceptor copolymer, which represents a low-band gap polymer.<sup>18</sup> Although fine-tuning of the optical properties can be enabled by attaching side chains to the polymer backbone, the polymer shows absorption only in a specific wavelength-range.

A straightforward approach to increase the absorption range is blending of two polymers with different absorption characteristics. Improved performances of organic solar cell devices have been reported in literature by using a ternary mixture of polymer/polymer/fullerene<sup>19,20</sup> or polymer/small molecule/fullerene.<sup>21</sup> Thereby, the fullerene derivatives act as electron acceptor in the active layer.

For the preparation of the active layer of an organic solar cell, inkjet printing as well as spin-coating can be used as solution deposition method.<sup>22,23</sup> In contrast to spin-coating, where more than 90% of the material is wasted, inkjet printing represents a highly material-efficient deposition method that requires only small amounts of functional materials and produces a minimal

Received: January 11, 2013

Revised: March 20, 2013

Published: April 26, 2013

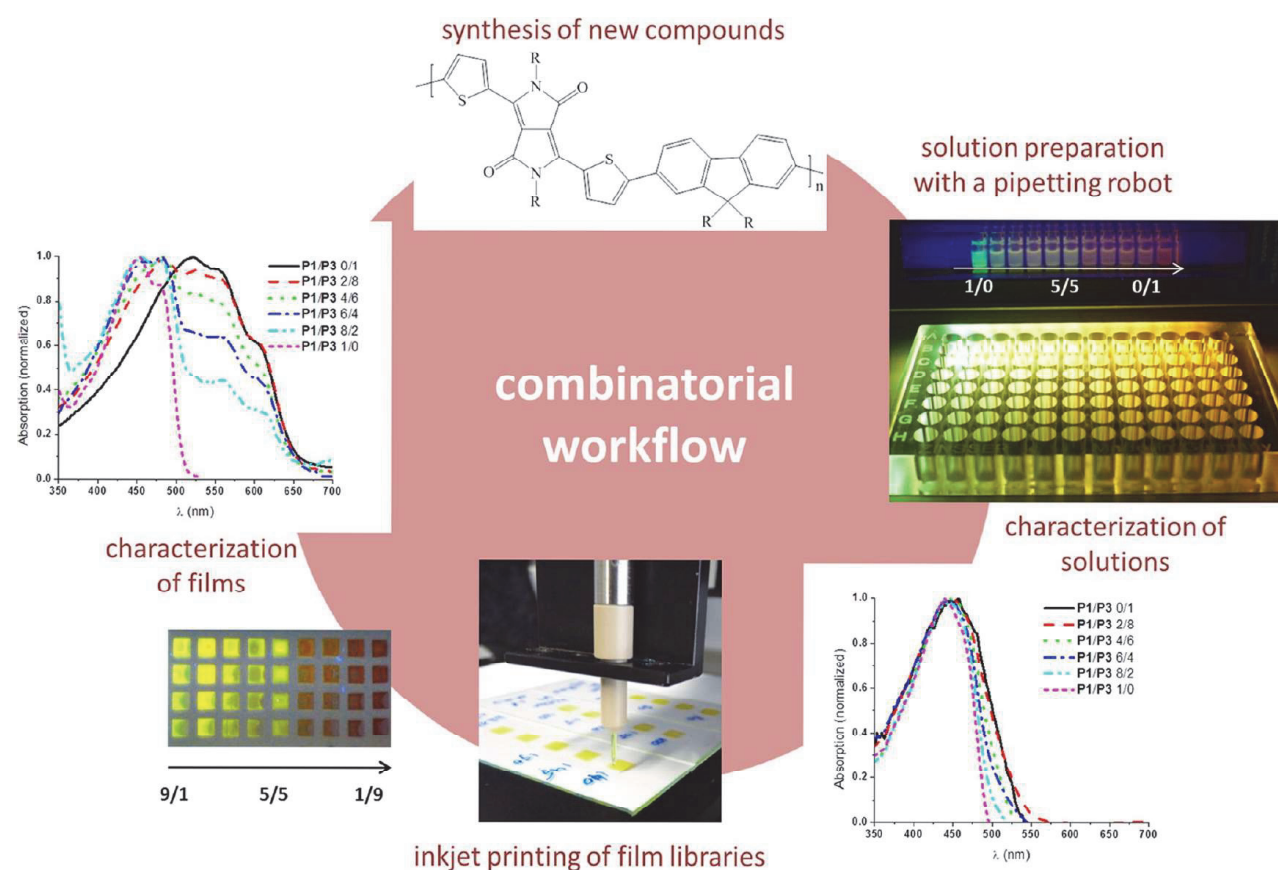


**Figure 1.** Experimental workflow for the combinatorial screening of binary polymer/polymer and ternary polymer/polymer/fullerene blends for the use in organic solar cells.

amount of waste, since the material is placed on-demand and where required.<sup>24,25</sup>

Many processing parameters influence the fabrication of the active layer and, as a consequence, the final device properties. Ink formulations, like the solvent, the concentration, and the polymer/fullerene ratio, as well as the process parameters, including film thickness, temperature, and, obviously, the processing technique itself, have a significant influence on the properties of the active layer. Furthermore, with the addition of more components to the mixture the number of combinations is exponentially increasing.

Therefore, a combinatorial screening approach is necessary to elucidate important structure–property relationships as well as to identify the most promising blends and blend ratios for the use as active bulk heterojunction solar cell layers. To reveal correlations between printing conditions and solar cell activities the investigation of the performance of the inkjet printed active layers in solar cells is the scope of future publications.

Inkjet printing is a precise and noncontact patterning technique, which can be used as a combinatorial screening tool to discover quantitative structure–property relationships, as described recently for the optimization of donor/acceptor materials for solar cells.<sup>26,27</sup> By using inkjet printing, synergies between ink properties and film characteristics can be found,<sup>28</sup> which significantly accelerates research and, subsequently, leads to a fast and simple handling of promising compounds for OPVs. Because of the continuous development of new polymers, many blend combinations might be promising as active layers. By using the presented workflow high perform-

ance materials and mixtures can be identified in a time- and material-efficient procedure.

In this contribution, we report the screening of two polymer/polymer blends, using a combinatorial experimental setup. To optimize the absorption of the active layer materials, two blend systems from poly(3-octylthiophene) (P3OT) with (i) PPE-*alt*-PPV and (ii) P(DPP-*alt*-F) were investigated according to their film formation and optical behavior.

## RESULTS AND DISCUSSION

**Combinatorial screening.** The experimental setup for the combinatorial screening of various binary polymer/polymer and ternary polymer/polymer/fullerene mixtures is depicted in Figure 1. The following combinatorial workflow was used:

(i) The mixtures with the desired compound ratios, solvent system, and concentration were prepared in a quartz 96-well microtiter plate. For each polymer a solvent mixture of chlorobenzene/*ortho*-dichlorobenzene (CB/*o*-DCB) in a ratio of 90/10 was used.

(ii) The filled microtiter plate was used for UV–vis absorption and emission measurements of the blend solutions with a UV–vis plate reader.

(iii) Individual wells of the plate were used as small solution reservoirs for the inkjet printing process.

(iv) Thin-film libraries were printed in a microtiter plate pattern according to the positions to the wells of a 96-well plate to screen the optical properties of the films using a high-throughput UV–vis plate reader.

**Single Polymers.** At first, the individual polymers poly(phenylene-ethynylene)-*alt*-poly(phenylene-vinylene) (PPE-*alt*-PPV) **P1** (Figure 2a), poly(diketopyrrolopyrrole-*alt*-fluorene) **P2** (Figure 2b), and poly(3-octylthiophene) **P3** (Figure 2c) were investigated concerning their printability, film formation, and absorption behavior in solution and film. The results are summarized in Table 1. The surface roughness  $R_a$  of **P1**, **P2**, and **P3**, as estimated by optical interferometry, was found to be 8, 15, and 30 nm, respectively (Table 1). Thus, the film formation via inkjet printing seems to be better for the polymers **P2** and **P3** under the given processing conditions.

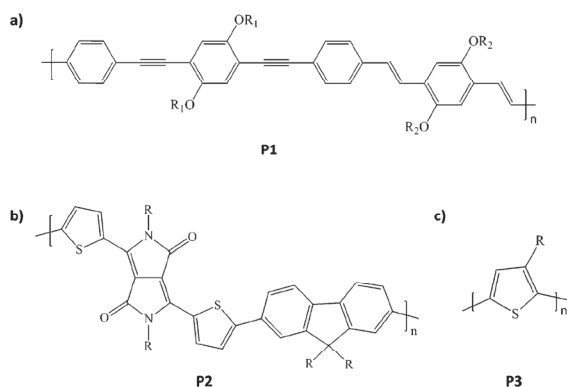


**Figure 2.** Schematic representation of the chemical structure of the investigated polymers. (a) Poly(phenylene-ethynylene)-*alt*-poly(phenylene-vinylene) **P1** ( $R_1$  = octyl,  $R_2$  = octadecyl), (b) poly(diketopyrrolopyrrole-*alt*-fluorene) **P2** ( $R$  = ethylhexyl on DPP, octyl on F) and (c) poly(3-octylthiophene) **P3** ( $R$  = octyl).

rene) P(DPP-*alt*-F) **P2** (Figure 2b), and poly(3-octylthiophene) (**P3OT**) **P3** (Figure 2c) were investigated concerning their printability, film formation, and absorption behavior in solution and film. The results are summarized in Table 1. The surface roughness  $R_a$  of **P1**, **P2**, and **P3**, as estimated by optical interferometry, was found to be 8, 15, and 30 nm, respectively (Table 1). Thus, the film formation via inkjet printing seems to be better for the polymers **P2** and **P3** under the given processing conditions.

To investigate the polymers as potential candidates for the use in ternary mixtures, the absorption of the single polymers in solution and as film needs to be measured. **P1** reveals in solution an absorption maximum at 443 nm (Figure 3a), whereas two absorption peaks are observed in the inkjet printed film at 451 and 480 nm (Figure 3c). A red-shift of the absorption peak in the solid state occurs because of an improved planarization of the polymer backbone.<sup>29</sup> According to literature, the revealed band-splitting in the film absorption spectra is correlated to the formation of aggregates.<sup>30</sup>

The absorption spectrum of the **P2** solution shows four peaks, which can be assigned to moieties of PDPP (417 nm, 609 nm, 661 nm) and PF (370 nm, Figure 3b). The absorption of **P2** of a printed film reveals only a small red-shift in comparison to the solution (Figure 3d). In contrast, polymer **P3** shows a more significant bathochromic shift between the solution (454 nm, Figure 3a) and the inkjet printed film ((522 nm, Figure 3c). Thereby, the three absorption peaks of

the inkjet printed film can be assigned to the  $\pi$ - $\pi^*$  transition (522 nm) and interchain interactions (550 nm, 610 nm). This behavior can be explained by an improved planarization and aggregation of the polymer in the solid state.<sup>29</sup>

The optical band gap of all three polymers was determined from the UV-vis spectra of the polymers in solution (Table 1).<sup>31</sup> The different optical properties of **P1**, **P2**, and **P3** can be explained by their chemical structures taking structural criteria for the design of conjugated polymers with reduced bandgaps into consideration.<sup>2</sup> **P1** has a relative high optical band gap of 2.4 eV, which is not favorable for their use in OPV as a single photon harvesting species. The high bandgap originates from a single bond rotation and therefore, from the hindered formation of the quinoid structure and delocalization of  $\pi$ -electrons. **P3** has a lower bandgap of 1.9 eV because of the high density of bulky side-chains, which cause a steric hindrance of the single bond rotation. Therefore, **P3** has a higher planarity of the aromatic backbone, which results in a higher degree of delocalization of  $\pi$ -electrons. Furthermore, the absorption spectrum of **P3** in the solid state is characterized by PT crystals that lead to a more ordered phase of the polymer and, hence, to a lower bandgap.<sup>18</sup> The copolymer of PDPP and PF, **P2**, reveals a band gap of 1.7 eV, which is classified as being a low bandgap polymer and which is favorable for solar cell applications.<sup>11</sup> Copolymer **P2** has a very rigid structure that does not undergo further planarization in the solid state and, as a consequence, no strong red-shift of the absorption in the solid state compared to the solution is observed.

**Polymer/Polymer Blends.** Since all individual polymers **P1**, **P2**, and **P3** show different absorption spectra in the solid state, a combination of the polymers is promising to improve the overall yield of photon harvesting.

The first investigated polymer/polymer blend consists of **P1**/**P3**. The polymers were mixed in different ratios ranging from 8/2 to 2/8 by weight. The absorption spectra of the blends in solution (Figure 3a) showed a single absorption peak at 439 nm for the ratio 8/2, which is compared to **P1** 4 nm blue-shifted. With increasing **P3**-content the maximum peak shifts to 445 nm for the ratio 2/8 and the absorption spectra become broader.

The spectra of the inkjet printed films of the blends **P1**/**P3** (Figure 3c) show a broad absorption from 350 to 650 nm; the observed absorption features can be assigned to **P1** (452 nm, 480 nm) and **P3** (557 nm, 610 nm, Table 1). Thereby, the intensity of the two absorption peaks at 557 and 610 nm increases systematically with the **P3**-content. However, even with a high **P3**-content in the blend, the **P1** absorption peaks show high intensities because of a high absorption coefficient of the **P1** material.<sup>32</sup> This implies that only a small addition of **P1** is required to increase the total absorption range of the polymer films significantly. Upon decreasing **P1**-content in the blend,

**Table 1.** Optical Properties in Solution and as Inkjet Printed Film As Well As Film Formation Characteristics of the Pristine Polymers **P1**, **P2**, and **P3** and the Binary Blends **P1**/**P3** 2/8 and **P2**/**P3** 4/6

	solution		inkjet printed film			
	$\lambda_{\max, \text{abs}}$ [nm]	$E_g^{\text{opt}}$ [eV]	$\lambda_{\max, \text{abs}}$ [nm]	film thickness [nm]	surface roughness $R_a$ [nm]	dot spacing [ $\mu\text{m}$ ]
<b>P1</b>	443	2.43	451	160	30	120
<b>P2</b>	661	1.70	660	190	8	100
<b>P3</b>	454	1.89	522	150	15	160
<b>P1</b> / <b>P3</b> (2/8)	445		482	140	30	100
<b>P2</b> / <b>P3</b> (4/6)	660		666	170	20	110

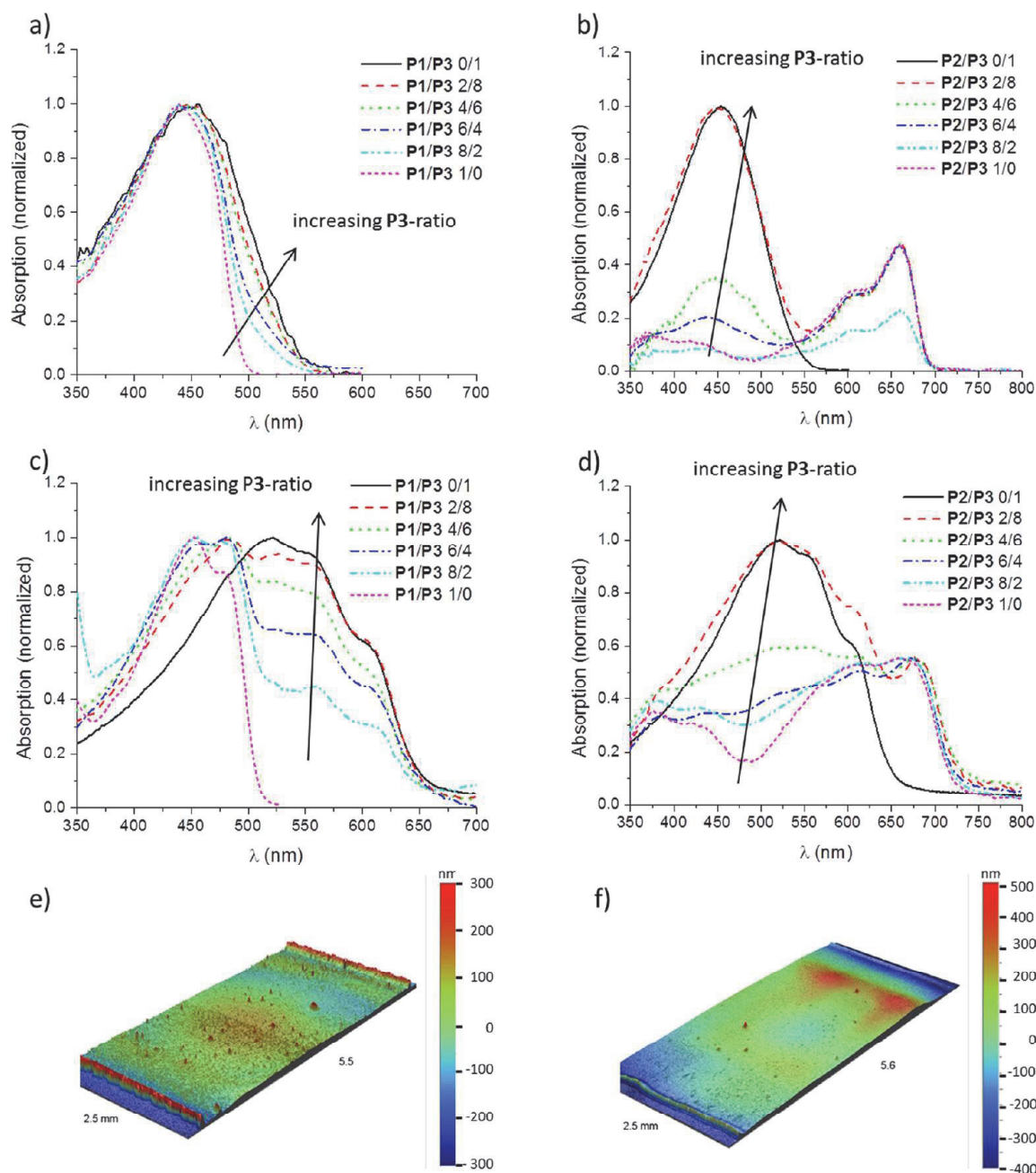


**Figure 3.** Absorption spectra of P1, P3, and P1/P3 blends (a) and P2, P3, and P2/P3 blends (b) in solution and inkjet printed films (c, d). Optical profiler images of the inkjet printed blend films P1/P3 2/8 (e) and P2/P3 4/6 (f).

the absorption peak of P1 (452 nm) shifts to 462 nm. Further decreasing of the P1-content leads to lower intensities. It can be assumed that the polymer P1 shows with increased P3-content a preferred formation of aggregates (as observed by the absorption at 480 nm) when inkjet printed from a P1/P3 mixture.<sup>30</sup> From Figure 3c it can be concluded that the blend ratio P1/P3 2/8 shows the best absorption performance, since the absorption range is the broadest when compared to the other ratios.

Figure 3e shows an optical profilometer image of the blend ratio P1/P3 2/8. Although inkjet printing of the films was performed directly after mixing the polymers and the mixtures are continuously stirred during printing, rough films with a

surface roughness  $R_a$  of 30 to 40 nm were formed. In contrast, a smooth surface with  $R_a$  of 15 nm was obtained when printing the single polymer P3 using the same solvent. The binary blends containing P1 and P3 reveal a similar roughness as the single polymer P1 (Table 1).

In summary, blending P3 with a small amount of P1 copolymer leads to an increased absorption range in the region from 350 to 630 nm. However, to improve the solar emission match, an absorption at higher wavelengths is required.<sup>13</sup>

Figure 3b shows the absorption spectra for the mixtures of P2 and P3 in solution. The peak at around 450 nm is assigned to P3 and the peaks at 376 nm, 430 nm, 608 nm, and 660 nm to P2. In the region between 430 and 450 nm, an overlay of



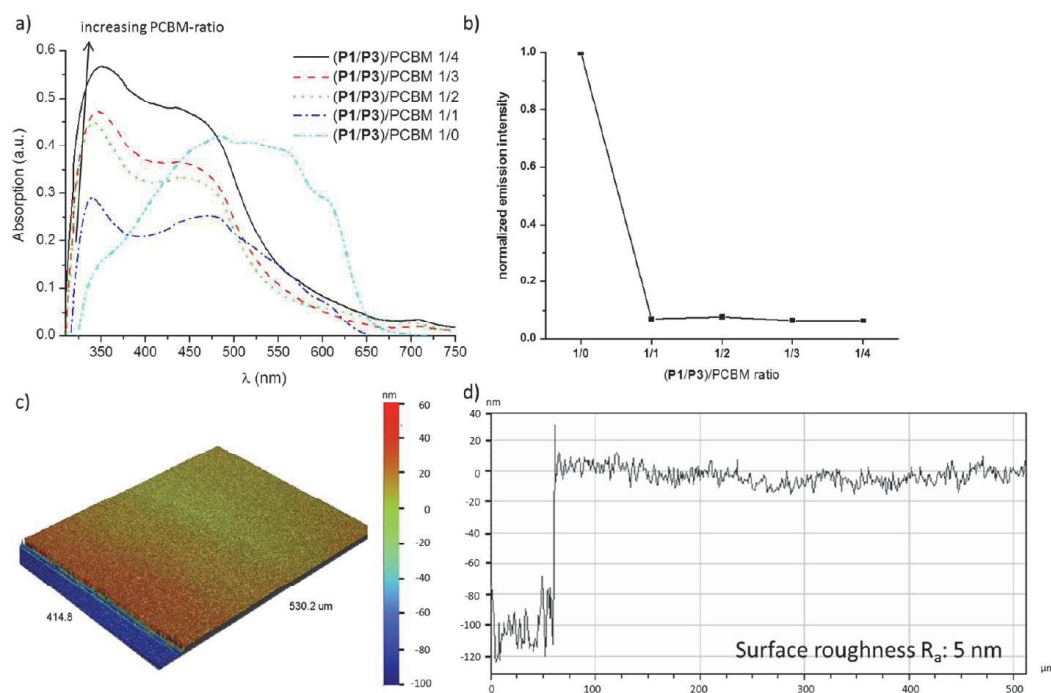


**Figure 4.** Absorption spectra (a) and normalized photoluminescence spectra (b) of inkjet printed films of **P1/P3** 2/8 in the mixture with PCBM with varied polymer/PCBM ratios. Optical profiler image (c) and corresponding cross-section (d) of an inkjet printed film of the polymer/PCBM ratio 1/1.

absorption from both polymers is observed. After printing, the UV–vis spectra show a significant broadening in the region of 650 to 750 nm, by adding a small fraction of **P2**, leading to an overall absorption range between 350 and 750 nm (Figure 3d). The absorption peaks of the printed samples are in comparison to the absorption in solution more structured as well as red-shifted; **P3** (520 nm, 550 nm, 610 nm) and **P2** (383 nm, 435 nm, 610 nm, 673 nm). From the absorption spectra in Figure 3d it was concluded that the blend ratio **P2/P3** 4/6 shows the broadest and most intense absorption of the investigated blends. Hence, this ratio was used for further investigations. In Figure 3f an optical profilometer image of an inkjet printed film of the blend ratio 4/6 is depicted. The image represents a 170 nm thick film with a surface roughness  $R_a$  of 20 nm (Table 1).

It is worth noting that the specific P3OT interchain interactions in the solid state (**P3**, 550 nm, 610 nm) is still observed when mixed with **P1** or **P2**, even at low **P3** contents. Thus, it can be assumed that the addition of **P1** or **P2** does not suppress the formation of highly ordered thiophene crystals.

**Polymer/Polymer/Fullerene Blends. Optical Properties.** As described in the previous sections the blend mixtures **P1/P3** 2/8 and **P2/P3** 4/6 were chosen from the combinatorial study of the binary blends for further investigations. Ternary blends were prepared from these mixtures by adding mono(1-[3-(methoxycarbonyl)propyl]-1-phenyl)-[6,6] $C_{60}$  (PCBM) as electron-accepting unit, which is commonly used in active layers of organic solar cells. The chosen polymer blend/PCBM ratios of 1/1, 1/2, 1/3, and 1/4 were inkjet printed and investigated according to their film formation behavior and optical properties.

Figure 4a shows the absorption spectra of inkjet printed films of the ternary blends that consist of **P1/P3** 2/8 and PCBM in the prescribed ratios. The absorption peak at 320 nm originates

from the fullerene derivative and increases in intensity with the PCBM content in the blend. The wavelength, at which the polymer **P3** absorbs in the ternary blend, differs from the binary polymer/polymer mixture. Whereas in the spectrum of the polymer/PCBM ratio 1/1 the absorption bands of **P3** (520 nm, 550 nm, 610 nm) are still visible, this band structure is not observed at higher PCBM contents. For the films with a higher fullerene content only a blue-shifted main absorption peak of the  $\pi-\pi^*$  transition is present. This is an indication for reduced interchain interactions of **P3** in the presence of PCBM in the blend. The polymer emission is quenched by a factor of 10 when PCBM was added in a ratio of polymer/PCBM 1/1, as can be seen in Figure 4b. Increasing the amount of PCBM did not lead to a further decrease of the polymer emission. The significant quenching is an indication for a good mixing of the components in the ternary blends, which lead to an efficient charge transfer from the electron-donor to the electron-acceptor.

The absorption spectra of the polymer blend **P2/P3** 4/6 in a mixture with different amounts of PCBM are shown in Figure 5a. Similar to the (**P1/P3**)/PCBM blend, the intensity of the absorption peak at 320 nm is increasing with higher PCBM contents. Figure 5b shows the emission measurements of the (**P2/P3**)/PCBM blends. A high quenching of the emission was observed for all investigated (**P2/P3**)/PCBM blends. The maximum quenching was found for a ratio of ((4/6)/30) (Figure 5b), indicating an appropriate charge transfer in the blend. A quick indication of effective mixing and charge separation could be obtained by measuring the photoluminescence quenching of the ternary blends. Combinatorial screening of different blend compositions yields the most promising mixtures, based on the optical and film formation behavior, being (**P1/P3**)/PCBM ((2/8)/10) and (**P2/P3**)/PCBM ((4/6)/30), respectively.

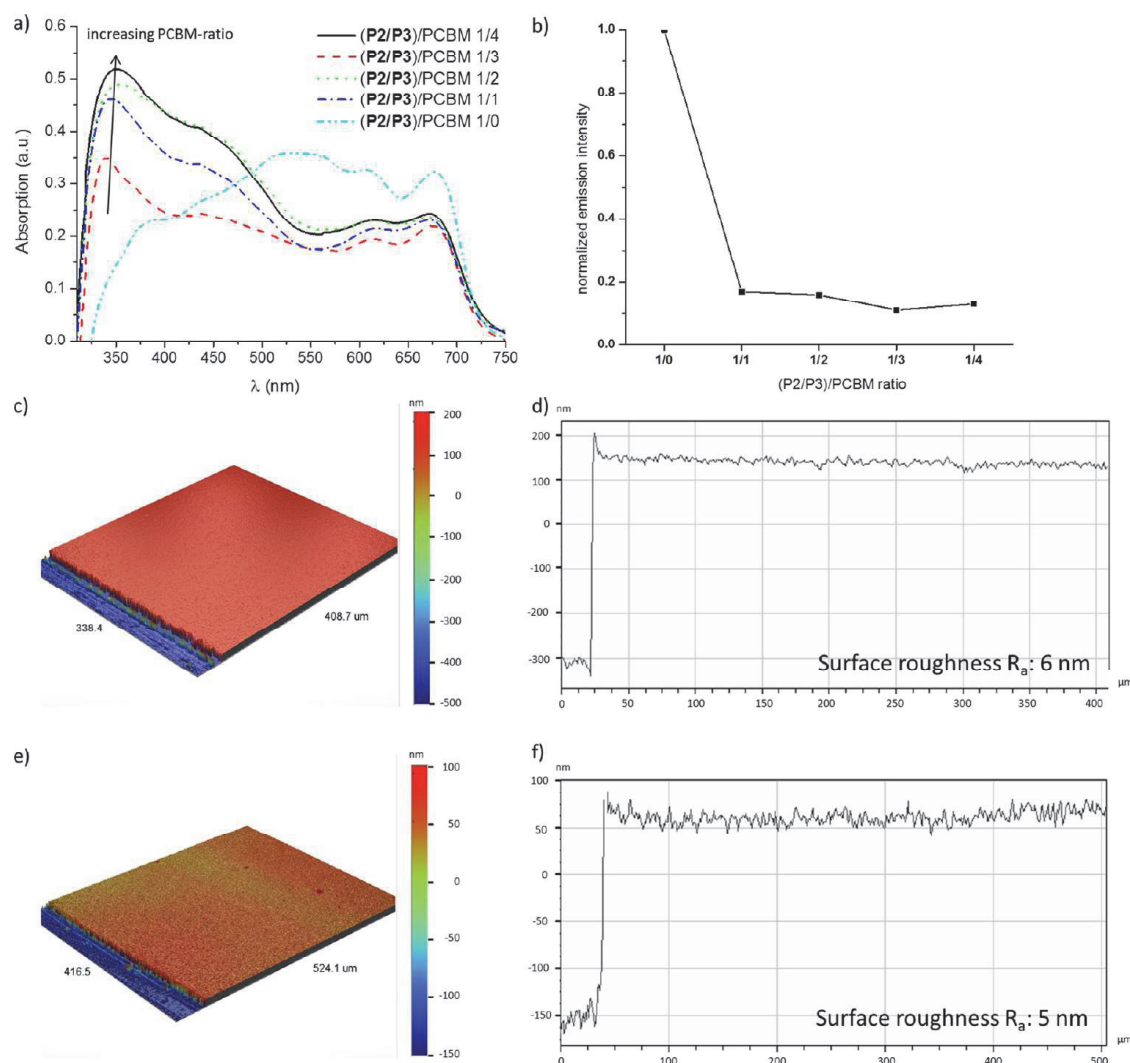


**Figure 5.** Absorption spectra (a) and normalized photoluminescence spectra at maximum (b) of inkjet printed films of P2/P3 4/6 in the mixture with PCBM with varied polymer/PCBM ratios. Optical profiler images (c, e) and corresponding cross sections (d, f) of inkjet printed films of the polymer/PCBM ratio 1/3 with a concentration of 0.8 wt % (c, d) and 0.5 wt % (e, f).

**Morphological Characterization.** The optical profilometer image of the inkjet printed film of the blend (P1/P3)/PCBM (2/8)/10 is depicted in Figure 4c, which shows a smooth film with a thickness of approximately 100 nm and a surface roughness  $R_a$  of 5 nm (Figure 4d). In Figure 5c an optical profiler image of an inkjet printed film of the blend (P2/P3)/PCBM (4/6)/30 is depicted, which demonstrates a smooth film formation ( $R_a = 6$  nm) with a thickness of approximately 450 nm (Figure 5d). To reveal the required optimal thickness for an active layer of solar cells, which is between 100 and 200 nm,<sup>13</sup> the concentration was reduced to 0.5 wt %, leading to a film thickness of approximately 200 nm with a low roughness ( $R_a = 5$  nm), as depicted in Figure 5e,f.

The active layer morphology affects the charge transport through the active layer and is crucial for an evaluation of applicable polymer/fullerene blends or active layer preparation conditions for OPVs.<sup>33</sup> Therefore, atomic force microscopy (AFM) measurements were performed on selected blends, although the required time for these measurements is far too long for a combinatorial screening method.

AFM images of the P1/PCBM 1/1 blend reveals a rough film with  $R_a$  of 17 nm (Figure 6a), which is also reflected in the results from the interferometric profiler. Inkjet printing of the PPE-*alt*-PPV polymer in the mixture with PCBM reveals an unfavorable morphology by the formation of PCBM clusters and a strong phase separation of the individual compounds. This observation is in good agreement with literature.<sup>6</sup>

For the binary polymer/fullerene blends P2/PCBM 1/3 (Figure 6b) and P3/PCBM 1/1 (Figure 6c) smooth film surfaces with  $R_a$  of 1 nm are obtained. The inkjet printed film of P2/PCBM reveals different phases in the range of 10 nm, which is reported to be suitable for active layer morphologies.<sup>34</sup>

P3/PCBM films prepared by inkjet printing from CB/*o*-DCB revealed fibrillar domains of P3OT that represent a highly ordered self-organization of the chains (Figure 6f). Note that the differences between the domain spacing in Figure 6f (being approximately 10 nm in the image) and the real distances between the thiophene crystals (of approximately 1 nm)<sup>35</sup> are screened by the convolution with dimensions of the AFM tip. The morphology observed for the as-printed film is comparable to the spin-coated films after annealing or additive addition.<sup>34,36</sup>

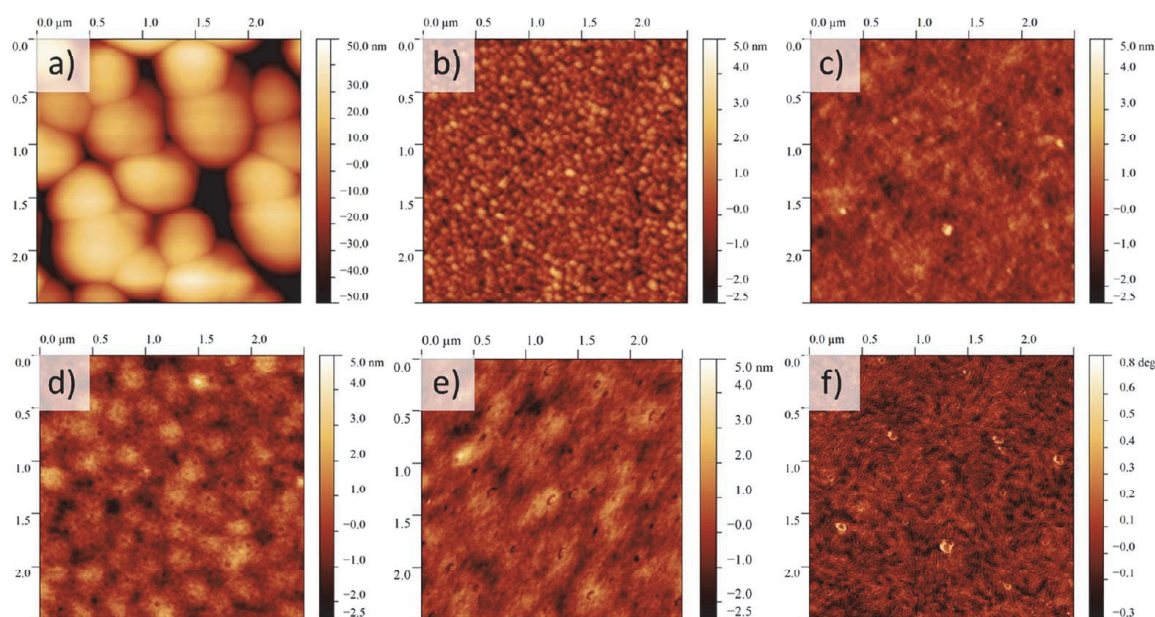


**Figure 6.** Atomic force microscopy height images of inkjet printed films of P1/PCBM 1/1 (a), P2/PCBM 1/3 (b), P3/PCBM 1/1 (c), (P1/P3)/PCBM (2/8)/10 (d), and (P2/P3)/PCBM 4/6/30 (e). Phase image of inkjet printed P3/PCBM 1/1 blend (f).

In the presence of PCBM, polythiophenes typically lose their chain alignment. As a result, postprocessing annealing methods, like thermal or solvent annealing, were developed to reorganize the polythiophene chains into the preferred fibrillar structure, which result in improved charge transport properties. As shown here, P3OT reveals self-organized domains in the blend with PCBM already in the as-inkjet printed films (Figure 6f). The reasons for the differences in film formation characteristics are explained by the use of the different film preparation techniques as well as processing solvents. When using conditions that cause a slow film drying, for example, by inkjet printing or by using the high boiling solvent chlorobenzene, the polythiophene chains may form highly ordered structures already during drying of the film. In contrast, when the drying proceeds too fast, for example, by using spin-coating or the low boiling solvent chloroform, the formation of the thermodynamically preferred crystalline polythiophene phases cannot take place.

AFM measurements of the ternary blends (P1/P3)/PCBM (2/8)/10 (Figure 6d) and (P2/P3)/PCBM (4/6)/30 (Figure 6e) revealed smooth (surface roughness  $R_a = 1$  nm) and well mixed layer morphologies. The typical main chain crystals of the P3OT, which are observed in the binary P3/PCBM blend, were not observed in the ternary blend films. This is in agreement with the findings of the absorption spectra of the (P2/P3)/PCBM blend, where only weak signals were found, which correspond to the P3OT interchain interactions. The band structure of P3 was observed in the absorption spectra of both binary blends, P1/P3 2/8 and P2/P3 4/6. Hence interchain interactions of P3 should also occur in polymer/P3 blends. As a result, the interruption of the self-organization of P3OT is only observed in the ternary blend film. Although improved absorption characteristics of the ternary blend films are observed, morphological investigations reveal an unpreferred P3OT morphology in comparison to the binary P3OT/PCBM mixture. To answer the question whether the successful mixing of two polymers with PCBM in a ternary blend reveals

an enhanced photon harvesting, solar cell characteristics need to be measured, which will be executed in the future.

Since not only optical film characteristics but also morphological properties are important for an evaluation of promising donor/acceptor blends for solar cells, the combinatorial screening workflow presented here can only reduce the amount of samples to be tested, but cannot provide a selection of one best donor/acceptor combination. Since morphological investigations represent a serious bottleneck for a fast and efficient screening procedure, the combinatorial screening workflow, which allows to identify promising formulations and reveals a reduction of the amount of samples, is of high importance.<sup>37</sup>

## CONCLUSIONS

We have demonstrated that the mixing of conjugated polymers represents a straightforward strategy for improving the absorption of the active layers for organic solar cells. An experimental setup for a combinatorial screening was presented here to investigate the absorption behavior of polymer/polymer blends in solution and films. The used polymers include poly(phenylene-ethynylene)-*alt*-poly(phenylene-vinylene) (PPE-*alt*-PPV), poly(diketopyrrolopyrrole-*alt*-fluorene) (P-(DPP-*alt*-F)), and poly(3-octylthiophene) (P3OT). An optimum absorption spectrum was found when mixing the compounds P(DPP-*alt*-F) and P3OT in a ratio of 4/6, while a quenching optimum was revealed when using a polymer/PCBM ratio of 1/3.

This ternary blend was found to cover a large absorption spectrum from 350 to 750 nm. Inkjet printing enabled a homogeneous film formation as well as a successful combinatorial screening of thin film properties of various compounds and blends for possible solar cell applications that lead to important structure–property-relationships. The next steps include the investigations of the inkjet printed active layers for their solar cell activity and the measurements of the resulting power conversion efficiencies.

## EXPERIMENTAL PROCEDURES

**Materials.** The polymers poly(phenylene-ethynylene)-*alt*-poly(phenylene-vinylene) (PPE-*alt*-PPV) **P1** ( $M_n = 10,200 \text{ g}\cdot\text{mol}^{-1}$ ,  $M_w = 39,400 \text{ g}\cdot\text{mol}^{-1}$ , PDI = 3.86) and poly(diketopyrrolopyrrole-*alt*-fluorene) (P(DPP-*alt*-F)) **P2** ( $M_n = 26,000 \text{ g}\cdot\text{mol}^{-1}$ ,  $M_w = 56,000 \text{ g}\cdot\text{mol}^{-1}$ , PDI = 2.15) were synthesized as described elsewhere.<sup>11,32</sup> Poly(3-octylthiophene) (P3OT) **P3** ( $M_n = 34,500 \text{ g}\cdot\text{mol}^{-1}$ ), mono(1-[3-(methoxycarbonyl)propyl]-1-phenyl)-[6,6]C<sub>61</sub> (PCBM), the used solvents chlorobenzene (CB) and *ortho*-dichlorobenzene (*o*-DCB) were purchased from Sigma-Aldrich (Steinheim, Germany) and were used without further purification. The polymers were dissolved in the required ratios in a solvent mixture of CB and *o*-DCB with a concentration of 0.8 wt % and 0.5 wt %, respectively, which is known to show a stable droplet formation and enables a homogeneous thin-film formation of such polymers.<sup>26,28</sup> For the ternary blends, the fullerene derivative was added to the polymer mixtures by using a constant polymer concentration. The solutions were filtered before printing (pore size 1  $\mu\text{m}$ ) to prevent nozzle clogging. Glass slides (3  $\times$  1 in.) were used as substrates and cleaned before printing by first rinsing with *iso*-propanol and subsequent drying with an air flow.

**Instrumentation.** UV-vis absorption and emission measurements of the blend solutions and films were carried out with a FLASHScan 530 (Analytik Jena, Jena, Germany) UV-vis plate reader. Inkjet printing was carried out with an Autodrop system from microdrop Technologies (Norderstedt, Germany). The printer was equipped with a piezo-based micropipette printhead with an inner diameter of 70  $\mu\text{m}$ . A voltage of 70 V and a pulse length of 35  $\mu\text{s}$  revealed a stable droplet formation for all inks in the solvent CB/*o*-DCB. The printing speed was set to 20  $\text{mm}\cdot\text{s}^{-1}$  for all experiments.

Surface topography and film thicknesses were measured with an optical interferometric profiler Wyko NT9100 (Veeco, Mannheim, Germany). Atomic force microscopy (AFM) measurements were performed in tapping mode with a NTegra Aura (NT-MDT, Moscow, Russia) on selected polymer/polymer/fullerene blends.

## AUTHOR INFORMATION

### Corresponding Author

\*E-mail: ulrich.schubert@uni-jena.de.

### Notes

The authors declare no competing financial interest.

## ACKNOWLEDGMENTS

For financial support the authors thank the Dutch Polymer Institute (DPI, technology area HTE, project #620) as well as the European Community's Seventh Framework Programme (FP7/2007-2013) under grant agreement no. 248816.

## REFERENCES

- (1) Grimsdale, A. C.; Chan, K. L.; Martin, R. E.; Jokisz, P. G.; Holmes, A. B. Synthesis of light-emitting conjugated polymers for applications in electroluminescent devices. *Chem. Rev.* **2009**, *109*, 897–1091.
- (2) Winder, C.; Sariciftci, N. S. Low bandgap polymers for photon harvesting in bulk heterojunction solar cells. *J. Mater. Chem.* **2004**, *14*, 1077–1086.
- (3) Shaheen, S. E.; Brabec, C. J.; Sariciftci, N. S.; Padinger, F.; Fromherz, T.; Hummelen, J. C. 2.5% efficient organic plastic solar cells. *Appl. Phys. Lett.* **2001**, *78*, 841–843.
- (4) van Duren, J. K. J.; Yang, X. N.; Loos, J.; Bulle-Lieuwma, C. W. T.; Sieval, A. B.; Hummelen, J. C.; Janssen, R. A. J. Relating the morphology of poly(*p*-phenylene vinylene)/methanofullerene blends to solar-cell performance. *Adv. Funct. Mater.* **2004**, *14*, 425–434.
- (5) Jadhav, R.; Türk, S.; Kühnlenz, F.; Cimrova, V.; Rathgeber, S.; Egbe, D. A. M.; Hoppe, H. Anthracene-containing PPE-PPV copolymers: Effect of side-chain nature and length on photophysical and photovoltaic properties. *Phys. Status Solidi A* **2009**, *206*, 2695–2699.
- (6) Hoppe, H.; Egbe, D. A. M.; Mühlbacher, D.; Sariciftci, N. S. Photovoltaic action of conjugated polymer/fullerene bulk heterojunction solar cells using novel PPE-PPV copolymers. *J. Mater. Chem.* **2004**, *14*, 3462–3467.
- (7) Li, G.; Shrotriya, V.; Yao, Y.; Huang, J. S.; Yang, Y. Manipulating regioregular poly(3-hexylthiophene): [6,6]-phenyl-C-61-butyl ester blends - route towards high efficiency polymer solar cells. *J. Mater. Chem.* **2007**, *17*, 3126–3140.
- (8) Schilinsky, P.; Asawapirom, U.; Scherf, U.; Biele, M.; Brabec, C. J. Influence of the molecular weight of poly(3-hexylthiophene) on the performance of bulk heterojunction solar cells. *Chem. Mater.* **2005**, *17*, 2175–2180.
- (9) Pacios, R.; Bradley, D. D. C.; Nelson, J.; Brabec, C. J. Efficient polyfluorene based solar cells. *Synth. Met.* **2003**, *137*, 1469–1470.
- (10) Mammo, W.; Admassie, S.; Gadisa, A.; Zhang, F. L.; Inganäs, O.; Andersson, M. R. New low band gap alternating polyfluorene copolymer-based photovoltaic cells. *Sol. Energy Mater. Sol. Cells* **2007**, *91*, 1010–1018.
- (11) Zoombelt, A. P.; Mathijssen, S. G. J.; Turbiez, M. G. R.; Wienk, M. M.; Janssen, R. A. J. Small band gap polymers based on diketopyrrolopyrrole. *J. Mater. Chem.* **2010**, *20*, 2240–2246.
- (12) Sonar, P.; Ng, G. M.; Lin, T. T.; Dodabalapur, A.; Chen, Z. K. Solution processable low bandgap diketopyrrolopyrrole (DPP) based derivatives: novel acceptors for organic solar cells. *J. Mater. Chem.* **2010**, *20*, 3626–3636.
- (13) Günes, S.; Neugebauer, H.; Sariciftci, N. S. Conjugated polymer-based organic solar cells. *Chem. Rev.* **2007**, *107*, 1324–1338.
- (14) Janietz, S.; Krueger, H.; Schleiermacher, H. F.; Würfel, U.; Niggemann, M. Tailoring of low bandgap polymer and its performance analysis in organic solar cells. *Macromol. Chem. Phys.* **2009**, *210*, 1493–1503.
- (15) Roncali, J. Molecular engineering of the band gap of  $\pi$ -conjugated systems: Facing technological applications. *Macromol. Rapid Commun.* **2007**, *28*, 1761–1775.
- (16) Huo, L. J.; Hou, J. H.; Chen, H. Y.; Zhang, S. Q.; Jiang, Y.; Chen, T. L.; Yang, Y. Bandgap and molecular level control of the low-bandgap polymers based on 3,6-dithiophen-2-yl-2,5-dihydropyrrolo-[3,4-*c*]pyrrole-1,4-dione toward highly efficient polymer solar cells. *Macromolecules* **2009**, *42*, 6564–6571.
- (17) Cheng, Y. J.; Yang, S. H.; Hsu, C. S. Synthesis of conjugated polymers for organic solar cell applications. *Chem. Rev.* **2009**, *109*, 5868–5923.
- (18) Bundgaard, E.; Krebs, F. C. Low band gap polymers for organic photovoltaics. *Sol. Energy Mater. Sol. Cells* **2007**, *91*, 954–985.
- (19) Kim, H.; Shin, M.; Kim, Y. Distinct annealing temperature in polymer:fullerene:polymer ternary blend solar cells. *J. Phys. Chem. C* **2009**, *113*, 1620–1623.
- (20) Kim, Y.; Shin, M.; Kim, H.; Ha, Y.; Ha, C. S. Influence of electron-donating polymer addition on the performance of polymer solar cells. *J. Phys. D: Appl. Phys.* **2008**, *41*, 225101.
- (21) Huang, J. H.; Velusamy, M.; Ho, K. C.; Lin, J. T.; Chu, C. W. A ternary cascade structure enhances the efficiency of polymer solar cells. *J. Mater. Chem.* **2010**, *20*, 2820–2825.
- (22) Hoth, C. N.; Choulis, S. A.; Schilinsky, P.; Brabec, C. J. On the effect of poly(3-hexylthiophene) regioregularity on inkjet printed organic solar cells. *J. Mater. Chem.* **2009**, *19*, 5398–5404.
- (23) Hoth, C. N.; Schilinsky, P.; Choulis, S. A.; Brabec, C. J. Printing highly efficient organic solar cells. *Nano Lett.* **2008**, *8*, 2806–2813.

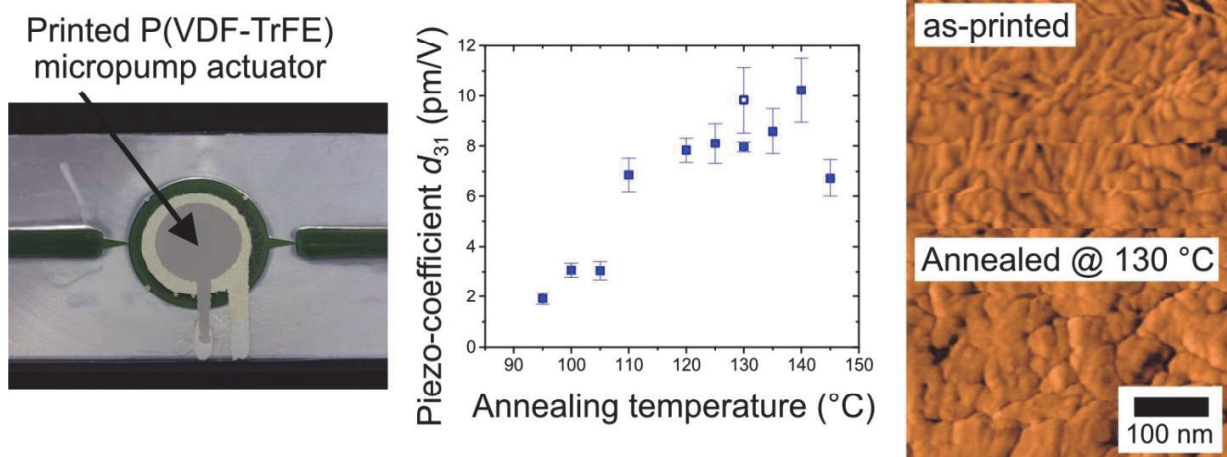
- (24) Tekin, E.; Smith, P. J.; Schubert, U. S. Inkjet printing as a deposition and patterning tool for polymers and inorganic particles. *Soft Matter* **2008**, *4*, 703–713.
- (25) Singh, M.; Haverinen, H. M.; Dhagat, P.; Jabbour, G. E. Inkjet Printing-Process and Its Applications. *Adv. Mater.* **2010**, *22*, 673–685.
- (26) Teichler, A.; Eckardt, R.; Hoepfener, S.; Friebe, C.; Perelaer, J.; Senes, A.; Morana, M.; Brabec, C. J.; Schubert, U. S. Combinatorial screening of polymer:fullerene blends for organic solar cells by inkjet printing. *Adv. Energy Mater.* **2011**, *1*, 105–114.
- (27) Marin, V.; Holder, E.; Wienk, M. M.; Tekin, E.; Kozodaev, D.; Schubert, U. S. Inkjet printing of electron donor/acceptor blends: Towards bulk heterojunction solar cells. *Macromol. Rapid Commun.* **2005**, *26*, 319–324.
- (28) Teichler, A.; Eckardt, R.; Friebe, C.; Perelaer, J.; Schubert, U. S. Film formation properties of inkjet printed poly(phenyleneethynylene)-poly(phenylene-vinylene)s. *Thin Solid Films* **2011**, *519*, 3695–3702.
- (29) Miteva, T.; Palmer, L.; Kloppenburg, L.; Neher, D.; Bunn, U. H. F. Interplay of thermochromicity and liquid crystalline behavior in poly(p-phenyleneethynylene)s:  $\pi$ - $\pi$  interactions or planarization of the conjugated backbone? *Macromolecules* **2000**, *33*, 652–654.
- (30) Tekin, E.; Wijlaars, H.; Holder, E.; Egbe, D. A. M.; Schubert, U. S. Film thickness dependency of the emission colors of PPE-PPVs in inkjet printed libraries. *J. Mater. Chem.* **2006**, *16*, 4294–4298.
- (31) Hellstrom, S.; Lindgren, L. J.; Zhou, Y.; Zhang, F. L.; Inganäs, O.; Andersson, M. R. Synthesis and characterization of three small band gap conjugated polymers for solar cell applications. *Polym. Chem.* **2010**, *1*, 1272–1280.
- (32) Egbe, D. A. M.; Tillmann, H.; Birckner, E.; Klemm, E. Synthesis and properties of novel well-defined alternating PPE/PPV copolymers. *Macromol. Chem. Phys.* **2001**, *202*, 2712–2726.
- (33) Kästner, C.; Susarova, D. K.; Jadhav, R.; Ulbricht, C.; Egbe, D. A. M.; Rathgeber, S.; Troshin, P. A.; Hoppe, H. Morphology evaluation of a polymer-fullerene bulk heterojunction ensemble generated by the fullerene derivatization. *J. Mater. Chem.* **2012**, *22*, 15987–15997.
- (34) Nguyen, L. H.; Hoppe, H.; Erb, T.; Gunes, S.; Gobsch, G.; Sariciftci, N. S. Effects of annealing on the nanomorphology and performance of poly(alkylthiophene): fullerene bulk-heterojunction solar cells. *Adv. Funct. Mater.* **2007**, *17*, 1071–1078.
- (35) Beiner, M.; Huth, H. Nanophase separation and hindered glass transition in side-chain polymers. *Nat. Mater.* **2003**, *2*, 595–599.
- (36) Yao, Y.; Hou, J.; Xu, Z.; Li, G.; Yang, Y. Effects of solvent mixtures on the nanoscale phase separation in polymer solar cells. *Adv. Funct. Mater.* **2008**, *18*, 1783–1789.
- (37) Neffati, R.; Alexeev, A.; Saunin, S.; Brokken-Zijp, J. C. M.; Wouters, D.; Schmatloch, S.; Schubert, U. S.; Loos, J. Automated scanning probe microscopy as a new tool for combinatorial polymer research: Conductive carbon black/poly(dimethylsiloxane) composites. *Macromol. Rapid Commun.* **2003**, *24*, 113–117.



## Publication [P5]

# Inkjet printed micropump actuator based on piezoelectric polymers: Device performance and morphology studies

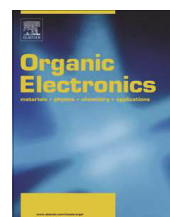
Oliver Pabst, Stefan Hölzer, Erik Beckert, Jolke Perelaer, Ulrich S. Schubert,  
Ramona Eberhardt, Andreas Tünnermann



*Organic Electronics* **2014**, 15, 3306–3315







# Inkjet printed micropump actuator based on piezoelectric polymers: Device performance and morphology studies



Oliver Pabst<sup>a,b,\*</sup>, Stefan Hölzer<sup>c,d</sup>, Erik Beckert<sup>b,\*</sup>, Jolke Perelaer<sup>c,d</sup>, Ulrich S. Schubert<sup>c,d</sup>, Ramona Eberhardt<sup>b</sup>, Andreas Tünnermann<sup>a,b</sup>

<sup>a</sup> Institute of Applied Physics, Abbe Center of Photonics (ACP), Friedrich Schiller University Jena, Max-Wien-Platz 1, D-07743 Jena, Germany

<sup>b</sup> Fraunhofer Institute for Applied Optics and Precision Engineering (IOF), Albert-Einstein-Str. 7, D-07745 Jena, Germany

<sup>c</sup> Laboratory of Organic and Macromolecular Chemistry (IOMC), Friedrich Schiller University Jena, Humboldtstr. 10, D-07743 Jena, Germany

<sup>d</sup> Jena Center for Soft Matter (JCSM), Friedrich Schiller University Jena, Philosophenweg 7, D-07743 Jena, Germany

## ARTICLE INFO

### Article history:

Received 8 July 2014

Received in revised form 8 September 2014

Accepted 9 September 2014

Available online 18 September 2014

### Keywords:

P(VDF-TrFE)

Printed electronics

Piezoelectric actuators

Inkjet printing

Micropump

Lab-on-a-chip systems

## ABSTRACT

All inkjet printed piezoelectric actuators based on poly(vinylidene fluoride-co-trifluoroethylene) (P(VDF-TrFE)) for applications as pump actuators in microfluidic lab-on-a-chip systems (LOC) are manufactured and investigated in terms of their morphology and actuator performance. Furthermore, a pump demonstrator with an all-printed P(VDF-TrFE) actuator is characterized here for the first time. The actuators are manufactured in a fully additive and flexible way by successive inkjet printing of a P(VDF-TrFE) film sandwiched between two silver electrodes on a polyethylene terephthalate (PET) substrate. Different from most current micropumps where actuator elements are fabricated separately, no additional joining step is required in the manufacturing approach employed here. Actuator performance is investigated by measurements of piezoelectric  $d_{31}$  coefficients as well as remanent polarization  $P_{\text{rem}}$  for different thermal treatments of the as-printed P(VDF-TrFE) films. A strong dependence of the device performance on the annealing temperature is found with maximum values for  $d_{31}$  and  $P_{\text{rem}}$  of approximately  $10 \text{ pm V}^{-1}$  and  $5.8 \text{ } \mu\text{C cm}^{-2}$ , respectively. Morphology investigations of the printed films by differential scanning calorimetry (DSC), X-ray diffraction (XRD) and Atomic Force Microscopy (AFM) indicate an increased degree of crystallinity of the piezoelectric  $\beta$ -phase for samples annealed at temperatures above  $110 \text{ }^\circ\text{C}$ , which coincides with improved device performance. A basic pumping function with pump rates of up to  $130 \text{ } \mu\text{L min}^{-1}$  is demonstrated, which is promising for future applications in LOC. Furthermore, the process chain and characterization presented here can be employed to design and manufacture also other P(VDF-TrFE)-based devices and allows the combination with additional printed on-chip functionalities in future LOC.

© 2014 Elsevier B.V. All rights reserved.

## 1. Introduction

The fields of organic and printed electronics have attracted increased research interest within the past 15 years due to their abilities of cost-effective manufacturing and

material deposition on large areas. Digital printing technologies, like drop-on-demand inkjet, do not require any masking and can realize fully additive, non-contact processing [1–3]. Manufacturing is compatible with low-cost flexible polymer substrates and can be performed either sheet-based or, in particular for large area printing also using roll-to-roll production lines [4,5]. Various functionalities have been realized using printing technologies, including radio-frequency

\* Corresponding author. Tel.: +49 3641 807 360.

E-mail addresses: [oliver.pabst@iof.fraunhofer.de](mailto:oliver.pabst@iof.fraunhofer.de) (O. Pabst), [erik.beckert@iof.fraunhofer.de](mailto:erik.beckert@iof.fraunhofer.de) (E. Beckert).

identification antennae, transistors, organic light-emitting diodes, organic photodiodes, organic photovoltaics and memory devices [6]. Furthermore, pyroelectric sensors [7] as well as piezoelectric pressure sensor networks [8] have been prepared using printing technologies.

Microfluidic lab-on-a-chip systems (LOC) are a promising field of application of organic and printed electronics. These systems are also termed miniaturized total analysis systems and integrate biological or chemical microreactions on compact chips [9]. Fluidic paths or channels are often structured into a glass or polymer substrate and sealed with a polymer cover foil. LOC are often designed as single-use, disposable chips to avoid contamination. Furthermore, the long-term stability requirements are relatively low in disposable LOC compared to systems that are designed for extended use. In order to keep the manufacturing costs low, the chips can be manufactured using polymer materials and cost-effective replication techniques [10]. When further on-chip functionalities are desired, low-cost manufacturing and low processing temperatures are essential, which hinders the use of conventional lithography-based electronics manufacturing techniques.

Defined fluid transport represents a key issue in LOC and is often realized using external pumps. To avoid separate equipment, various micropumps that are suitable for on-chip integration have been demonstrated [11,12]. They are frequently designed as reciprocating membrane pumps, in which a periodic membrane movement creates a volume change that leads to a fluid flow in combination with inlet and outlet valves. Membranes are often actuated by piezoceramic lead zirconate titanate (PZT) actuators [13], but also electroactive polymer actuators have been employed, e.g. ionic polymer–metal composites [14] or piezoelectric polymers [15]. The actuators are typically mounted on the pump membrane in a separate joining step, which results in increased manufacturing costs.

In this contribution, all inkjet printed polymer actuators based on piezoelectric poly(vinylidene fluoride-co-trifluoroethylene) (P(VDF-TrFE)) that are suitable for pump actuation in LOC are presented. The actuators are printed on a polyethylene terephthalate (PET) substrate and consist of a sandwich of two printed silver electrodes and a P(VDF-TrFE) film. After printing each layer, an annealing or sintering step is required. Compared to most current micropumps where an actuator is mounted on a pump membrane, this separate joining step is avoided in the all-printed manufacturing approach described here. In a previous publication we described the basic manufacturing process of the actuators and reported the piezoelectric  $d_{31}$  coefficient for inkjet printed P(VDF-TrFE) actuators for the first time. Moreover, studies of static and dynamic actuator deflection as well as the device stability were described [16]. However, a deeper insight into the underlying morphological changes within the P(VDF-TrFE) films during printing and subsequent annealing steps is crucial in order to control and improve the actuator behavior and, hence, the performance of the micropump.

It is well-known that an annealing step is required for solution-processed P(VDF-TrFE) films to reach a high

degree of crystallinity of the piezoelectric  $\beta$ -phase, which is necessary for significant piezoelectric behavior [17–19]. Moreover, the influence of annealing, polymer composition and mechanical stretching on morphology has been widely studied [17]. The first investigations of screen-printed piezo- and pyroelectric P(VDF-TrFE) sensors were published by Zirkel et al. [7,8]. The first direct correlations between annealing temperature, film morphology and remanent polarization of P(VDF-TrFE) films were reported by Mao et al. [20,21]. The authors observed a high degree of crystallinity of the piezoelectric  $\beta$ -phase and large  $P_{\text{rem}}$  values for films that were annealed above the Curie temperature of approximately 110 °C, but below the melting temperature of P(VDF-TrFE) of approximately 150 °C. Annealing above the melting temperature lead to a degraded  $\beta$ -phase and reduced polarization. However, it should be noted that the films investigated by Mao et al. were processed by spin-coating, which is known to yield different morphologies compared to inkjet printing, as known from other polymeric systems [22]. Up to now, a detailed study on the relationship between morphology and the piezoelectric behavior of inkjet printed P(VDF-TrFE) films has not been reported.

Therefore, the influence of the thermal annealing of printed P(VDF-TrFE) films on the morphology and the resulting device performance is investigated in this contribution. For that purpose, P(VDF-TrFE) actuators are subjected to different thermal treatments. The electromechanical as well as electrical device performance is studied by actuator deflection measurements and ferroelectric hysteresis measurements, respectively. The influence of the thermal annealing on the piezoelectric  $d_{31}$  coefficient as well as the remanent polarization  $P_{\text{rem}}$  is extracted from those measurements. Results are compared to morphology investigations of the P(VDF-TrFE) films by differential scanning calorimetry (DSC), X-ray diffraction (XRD) and Atomic Force Microscopy (AFM). Furthermore, a membrane pump with an inkjet printed P(VDF-TrFE) actuator is characterized here for the first time.

## 2. Experimental

### 2.1. Materials

The actuators were printed onto biaxially oriented PET substrates (Goodfellow GmbH, Germany, 125  $\mu\text{m}$  thickness, upper working temperature 140 °C). A P(VDF-TrFE) film sandwiched between two silver electrodes was subsequently inkjet printed, leading to a unimorph actuator setup with one active layer on a passive substrate. Inkjet printing was performed using a 2 wt% solution of P(VDF-TrFE) (VDF:TrFE ratio of 70:30 wt%, Solvay Specialty Polymers Italy S.p.A.) dissolved in cyclopentanone. Bottom and top electrodes were printed using two commercial silver nanoparticle dispersions in tetradecane (NPS-JL, Harima Chemicals, Inc., Japan, solid content 55 wt%) and in a mixture of ethanol and ethylene glycol (CCI-300, Cabot Corp., USA, solid content 20 wt%), respectively. A detailed process description is provided in Ref. [16].

Pump substrates were manufactured by milling in a polishable aluminum alloy (RSA 905). The cylindrical pump chamber had a diameter of 15 mm and a depth of 0.5 mm, while the channels had a width of 3 mm and a depth of 0.5 mm. After milling, the channel and pump chamber surface were polished manually in order to achieve a low surface roughness and, thus, good wetting behavior in the channels.

## 2.2. Inkjet printing and post-processing

Bottom and top electrodes were printed using a compact inkjet deposition system (Omnijet 100, Unijet Co., Ltd., South Korea) and 10 pL printing cartridges with 16 nozzles (DMC-11610, Dimatix Fujifilm Inc., USA). After printing, the electrode layers were dried and sintered using a thermal treatment in a convection oven (60 min, 100 °C) followed by a low-pressure argon plasma exposure (30 min, 240 W, 50 kHz generator). This procedure leads to successful sintering of the silver nanoparticles and is compatible with temperature-sensitive polymer substrates. The P(VDF-TrFE) films were printed using a custom inkjet deposition setup, 80 pL printheads with 256 nozzles (Dimatix Nova 256/80, controlled by Apollo II printhead support kit) and a six-axis robot as a positioning system (KR 5, Kuka Roboter GmbH, Germany). In total, 100 layers were printed to achieve a P(VDF-TrFE) film thickness of approximately 9 μm. The as-printed films were annealed in a convection oven for 24 h at different temperatures. In order to study the effect of the annealing step on actuator performance and morphology, ten temperature profiles with maximum temperatures between 95 °C and 145 °C were tested. Heating and cooling rates of 0.8 K min<sup>-1</sup> were employed. For all temperature profiles, the effect of the plasma sintering step applied to top electrodes on actuator performance was studied. For that purpose, also samples with exclusively thermally sintered top electrodes were characterized.

Measurements of actuator deflection were run with cantilever bending beam actuators with a designed active area of 4 × 15 mm<sup>2</sup>. Square test pads with an active area of 3 × 3 mm<sup>2</sup> were used for ferroelectric hysteresis measurements. For demonstration of a pumping function, circular membrane actuators with a membrane diameter of 15 mm were manufactured. Fig. 1 shows photographs of the bottom electrodes for ferroelectric test pads (a), cantilever bending beam actuators (b) as well as readily processed samples (c). In order to realize a cantilever beam fixed at one end, cantilever actuators were mounted on microscopic glass slides using cyanoacrylate adhesive. Fig. 1d–f shows membrane actuators after printing the bottom electrode (d), the P(VDF-TrFE) layer (e) and fully processed actuators (f).

The calorimetric and morphological investigations (DSC, XRD and AFM) were performed on P(VDF-TrFE) films that were printed on metallized microscopic glass slides (soda-lime glass, VWR International GmbH, metallized with sputtered Ti/Pt/Au) to ensure easy removal of the P(VDF-TrFE) films for DSC characterization and to avoid signals associated to residuals of the metal electrodes. These samples underwent similar thermal treatments that were applied for the top electrodes and were poled electrically by placing an aluminum-coated polypropylene film (PP, Goodfellow GmbH, thickness 8 μm) on top of the printed P(VDF-TrFE) as a top electrode.

A pump demonstrator was assembled by mounting a PET cover foil with a printed membrane actuator on top of a milled RSA 905 substrate using cyanoacrylate adhesive.

## 2.3. Characterization

The piezoelectric  $d_{31}$  coefficients of printed P(VDF-TrFE) films were derived from static deflection measurements of cantilever actuators. The deflection of the cantilever tip was measured using a laser triangulation sensor (LK-G10,

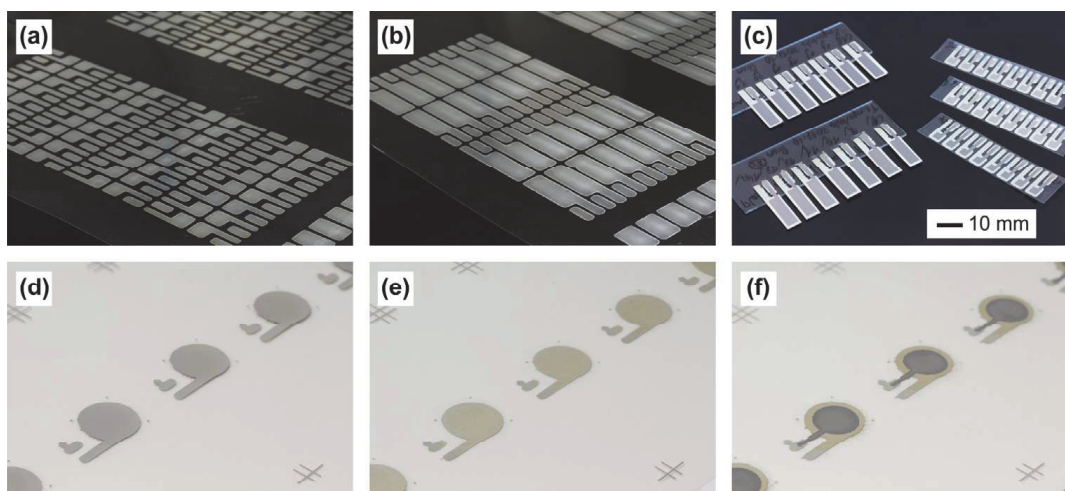


**Fig. 1.** Test structures for investigation of the performance of inkjet printed P(VDF-TrFE) actuators: (a) bottom electrodes for ferroelectric test pads, cantilever actuators (b) and (c) fully processed samples before characterization. Membrane actuators for micropump demonstrator after printing (d) the bottom electrode, (e) the P(VDF-TrFE) layer and (f) fully processed membrane actuators.

Keyence Corp., Japan), while defined voltages were applied by a high-voltage amplifier (2220CE, Trek Inc., USA). From the cantilever deflection at a driving voltage of 400 V, the piezoelectric  $d_{31}$  coefficient was calculated by an analytical model for voltage-dependent cantilever deflection. Details on poling, measurement procedure, material properties used and the analytical model can be found in reference [16]. Ferroelectric hysteresis measurements were performed using a commercial ferroelectric characterization setup (EasyCheck 300, Aixacct GmbH, Germany) and the same high-voltage amplifier that was used for deflection measurements. Maximum voltages of 600 V were applied at a frequency of 0.05 Hz and measurements were repeated five times. The values of remanent polarization  $P_{\text{rem}}$  were extracted from all measurements. An example of a measurement curve is provided in Supporting Information Fig. 1. For each temperature profile, at least five cantilever actuators and ferroelectric test pads were characterized.

XRD measurements were performed at room temperature using a Bruker D5005 (Bruker, Karlsruhe, Germany) diffractometer ( $\lambda = 0.154$  nm, step size  $0.03^\circ$ , integration time 2 s, geometry theta-2 theta).

Calorimetric measurements were carried out on a DSC 204 F1 Phoenix (Netzsch, Selb, Germany) in a temperature range between  $-20$  and  $200$  °C after carefully removing the polymer film from the metallized glass slide with a razor blade. The DSC heating and cooling rates were  $10$  K  $\text{min}^{-1}$  for all measurements. The morphology of the inkjet printed P(VDF-TrFE) films was investigated by Atomic Force Microscopy (AFM) on an NT-MDT Solver (NT-MDT, Moscow, Russia) in tapping-mode, using JPK NSC35 tips with a radius of  $>10$  nm. The denoted sizes were estimated from line scans of at least 30 objects.

Flow rate measurements of the pump demonstrator with an inkjet printed P(VDF-TrFE) membrane actuator were performed by video analysis. Videos were recorded during operation of the pump and the volume change per time was derived from selected still images and the corresponding time difference. During measurements, the pump demonstrator was mounted on a rotation stage. The back-pressure was calculated based on the fluid volume in the setup, angle-dependent normal force component and the cross-sectional channel area. As a pumping medium,

isopropanol was selected due to its good wetting behavior on the metallic pump substrate and the PET cover foil.

### 3. Results and discussion

#### 3.1. Electromechanical characterization

Fig. 2 shows the  $d_{31}$  coefficients that were derived from static deflection measurements for different annealing temperatures. Deflections in the range of  $12$ – $160$   $\mu\text{m}$  were observed, which corresponds to  $d_{31}$  coefficients between approximately  $0.8$   $\text{pm V}^{-1}$  and  $10$   $\text{pm V}^{-1}$ . Maximum values were obtained for samples annealed at  $140$  °C and are in good accordance with literature values for other P(VDF-TrFE) films [23]. A strong temperature-dependence of  $d_{31}$  with a critical temperature of approximately  $110$  °C is visible. Samples annealed below  $110$  °C exhibit very low electromechanical coupling with  $d_{31}$  coefficients between  $0.8$   $\text{pm V}^{-1}$  and  $3$   $\text{pm V}^{-1}$ . For samples annealed above  $110$  °C, significantly higher deflections and  $d_{31}$  coefficients between  $5$   $\text{pm V}^{-1}$  and  $10$   $\text{pm V}^{-1}$  were measured. This observation agrees with other investigations of temperature-dependence of the crystallinity of the piezoelectric  $\beta$ -phase [24]. For an annealing temperature of  $145$  °C, lower  $d_{31}$  coefficients were observed than for an annealing temperature of  $140$  °C. Possible reasons for this behavior are thermally induced deformations of the PET substrate at this annealing temperature, as  $145$  °C is slightly outside the recommended range of application temperatures of the PET substrate [25].

An argon plasma treatment of the top electrodes leads to higher  $d_{31}$  coefficients compared to samples that were solely heat-treated. An average increase of  $1.6$   $\text{pm V}^{-1}$  was measured. Furthermore, the influence of the temperature ramps applied during heating up and cooling down of the samples was studied very briefly for cantilever actuators annealed at  $130$  °C. Apart from the gradient of  $0.8$  K  $\text{min}^{-1}$  that was applied for all samples, also a lower gradient of  $0.3$  K  $\text{min}^{-1}$  was investigated and lead to an increase in  $d_{31}$  of approximately  $1.7$   $\text{pm V}^{-1}$  (plotted as unfilled squares in Fig. 2). Standard deviations in the range of  $3$ – $20\%$  were obtained during the measurements with an

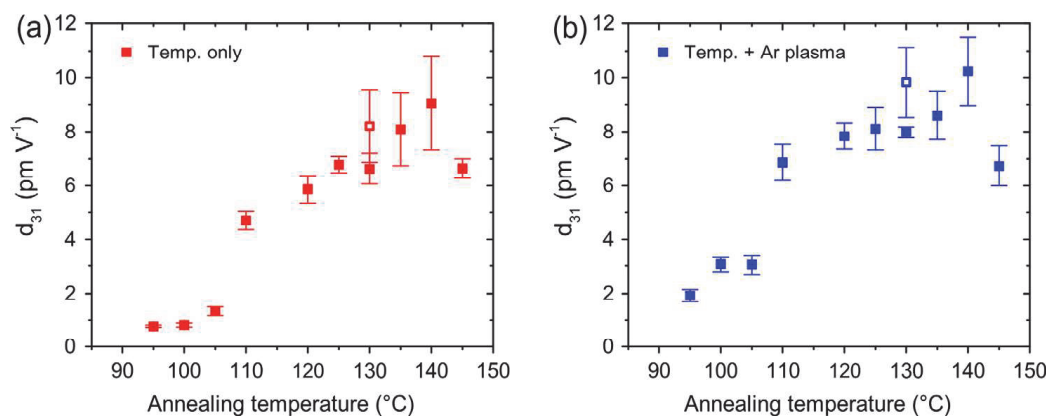


Fig. 2. Piezoelectric  $d_{31}$  coefficients for different thermal treatments of inkjet printed P(VDF-TrFE) films.  $d_{31}$  values were obtained from static cantilever deflection measurements using an analytical model. Films with pure thermal treatment (a) as well as a combined thermal and plasma sintering of the top electrodes (b) were investigated.

average value of 12%. These are assumed to be mainly due to the manual mounting process of the cantilever actuators on glass slides which can lead to varying clamping conditions as well as to the positioning of the measurement spot on the sample.

### 3.2. Ferroelectric hysteresis measurements

Fig. 3 plots the remanent polarization  $P_{\text{rem}}$  for different temperature profiles. Samples that were solely heat-treated (Fig. 3a) exhibit a clear dependency of  $P_{\text{rem}}$  on annealing temperature with low  $P_{\text{rem}}$  of less than  $1 \mu\text{C cm}^{-2}$  for samples annealed below  $110^\circ\text{C}$  and significantly higher values between  $4 \mu\text{C cm}^{-2}$  and  $5.2 \mu\text{C cm}^{-2}$  for samples annealed above  $110^\circ\text{C}$ . Similar to the investigations of the  $d_{31}$  coefficient, maximum values were measured on samples annealed at  $140^\circ\text{C}$ . Samples with argon plasma sintered top electrodes (see Fig. 3b) exhibit in average  $1.4 \mu\text{C cm}^{-2}$  higher  $P_{\text{rem}}$  values than solely heat-treated samples with maximum values of up to  $5.8 \mu\text{C cm}^{-2}$ . Standard deviations of the ferroelectric hysteresis measurements were small with average values of  $0.2 \mu\text{C cm}^{-2}$  for solely heat-treated samples and  $0.3 \mu\text{C cm}^{-2}$  for plasma-treated samples. In general, the  $P_{\text{rem}}$  values determined in this work compare well with literature values [21] and demonstrate the applicability of inkjet printing as a processing technique for P(VDF-TrFE) films. For further information, the corresponding values of the maximum polarization  $P_{\text{max}}$  are provided in Supporting Information Fig. 2.

From the measurements of the piezoelectric coupling coefficient  $d_{31}$  and the remanent polarization  $P_{\text{rem}}$  for different annealing temperatures it can be concluded that annealing of the as-printed P(VDF-TrFE) films should be performed at temperatures of at least  $110^\circ\text{C}$  to obtain a distinct piezoelectric behavior. This temperature range is

typical for obtaining a high degree of crystallinity in the P(VDF-TrFE) copolymers that were used [19,24].

### 3.3. Structure and morphology

In order to study the structure and morphology of the actual inkjet printed films in this contribution, three samples that were exposed to different thermal treatments were selected and investigated in detail by differential scanning calorimetry (DSC), X-ray diffraction (XRD) and Atomic Force Microscopy (AFM). Two solely heat-treated samples annealed at  $95^\circ\text{C}$  and  $145^\circ\text{C}$  were characterized. Furthermore, one sample was annealed at  $130^\circ\text{C}$  and subjected to argon plasma sintering of the top electrode. Table 1 lists the  $d_{31}$  coefficients, remanent polarization values  $P_{\text{rem}}$  and important morphological information that were obtained for those samples.

#### 3.3.1. Thermal behavior

Fig. 4 shows the first DSC heating runs of the as-printed and thermally annealed P(VDF-TrFE) films between  $80$  and  $160^\circ\text{C}$ . The as-printed film will be discussed as a reference sample in here. All curves show two distinct endothermic peaks with maxima at  $105$  and  $150^\circ\text{C}$ , respectively. It is generally accepted that the first peak at around  $105^\circ\text{C}$  corresponds to the phase transformation of the ferroelectric  $\beta$ -crystals into the paraelectric  $\alpha$ -modification, also known as the Curie transformation temperature [26,27]. Note that this peak is relatively broad in the as-printed reference sample. It becomes more distinct after an additional annealing step at  $95^\circ\text{C}$ , which is slightly below the peak phase transition temperature. A similar effect was observed by Barique and Ohigashi [28] in solvent-cast films and was explained by the transformation of chain segments in the crystalline parts of the polymer from

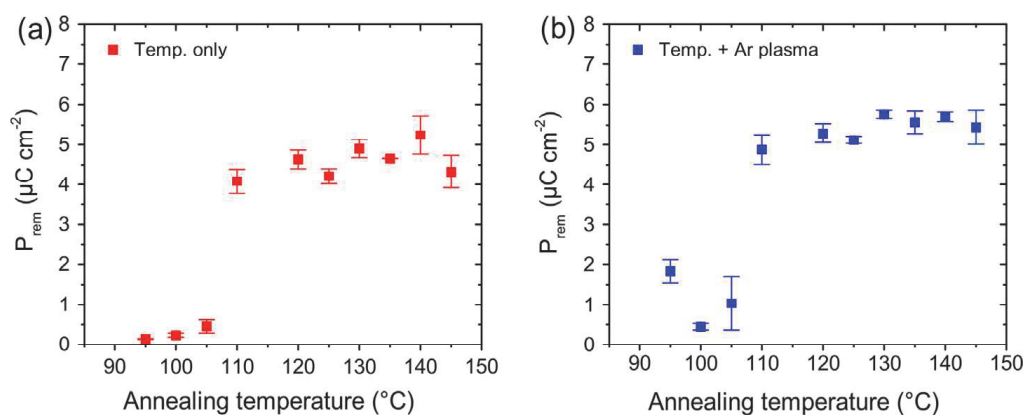
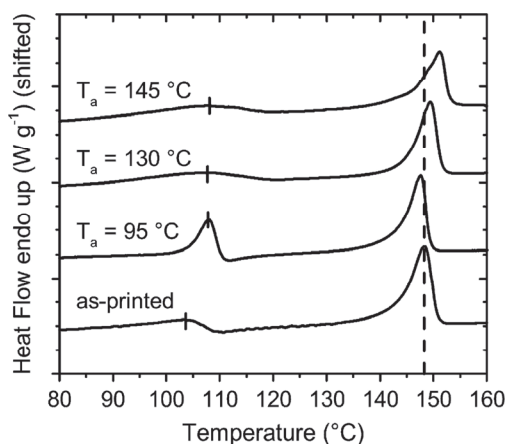


Fig. 3. Remanent polarization  $P_{\text{rem}}$  for different thermal treatments of inkjet printed P(VDF-TrFE) films.

Table 1

Overview of piezoelectric coupling coefficients  $d_{31}$ , remanent polarization values  $P_{\text{rem}}$  and important morphological information after different annealing conditions of the inkjet printed P(VDF-TrFE) films.

Sample	Treatment	$d_{31}$ ( $\text{pm V}^{-1}$ )	$P_{\text{rem}}$ ( $\mu\text{C cm}^{-2}$ )	Morphology from AFM	Domain size (nm)
A	$95^\circ\text{C}$	$0.8 \pm 0.04$	$0.1 \pm 0.01$	Rod-like	$21 \pm 7$
B	$130^\circ\text{C} + \text{Ar plasma}$	$8.0 \pm 0.2$	$5.8 \pm 0.1$	Globular	$63 \pm 24$
C	$145^\circ\text{C}$	$6.6 \pm 0.4$	$4.3 \pm 0.4$	Globular	$138 \pm 62$



**Fig. 4.** DSC plots of the inkjet printed P(VDF–TrFE) films for different thermal treatments after the first heating run. The dashed line represents the peak melting temperature of the as-printed reference sample and the ticks on the curves point to the maxima of the first endothermic peak. All curves are shifted for better visibility.

*gauche* defects into the all-*trans* configuration, which is present in  $\beta$ -crystals. Our results here denote an analogous behavior for the inkjet printed films.

At higher annealing temperatures of 130 and 145 °C, three main features can be deduced from the first DSC heating scans. (i) The Curie transition peak is much broader compared to the one obtained at an annealing temperature of 95 °C. This is a somewhat expected finding, since the annealing was performed in a temperature range where the  $\alpha$ -phase is stable, which is known to exhibit a *gauche–trans* chain configuration [29]. Thus, defect healing into an all-*trans* chain configuration, as observed in the case of the 95 °C-sample, is not favorable. (ii) The Curie transition temperature peaks, with their maxima at 108 °C, are shifted to slightly higher temperatures compared to the as-printed reference sample (104 °C). This effect might be explained by the different crystallization conditions of the samples. In case of the as-printed sample, the polymer crystallization is mainly determined by drying of the inkjet printed film (and, thus, depends on the ink formulation and the printing temperature). In case of the samples annealed at 130 and 145 °C, the crystallization and phase transformation processes are expected to depend strongly on the cooling rate after annealing. Since the cooling rate was kept comparable at 0.8 K min<sup>−1</sup> for all annealed samples, this also explains the similar Curie transition peak temperatures. (iii) The endothermic peak at around 150 °C, which is attributed to the melting of the P(VDF–TrFE) crystals, shifts to higher temperatures upon annealing between the Curie transition temperature and the peak melting temperature (148.3, 149.4 and 151.1 °C for the as-printed, 130 °C and 145 °C-sample, respectively).<sup>1</sup> The higher melting temperatures observed

<sup>1</sup> The results of the second DSC heating run, after deleting the thermal history of the sample, showed similar melting peak temperatures at 151.8 ± 0.2 °C for all of the investigated samples. As a consequence, we expect the shift of the endothermic peak that was observed during the first DSC heating run to be an effect from the thermal treatment and not a measurement error. The interested reader shall be referred to the corresponding DSC scans in Supporting Information Fig. 3.

in the first DSC heating runs indicate the formation of larger crystals during annealing at 130 and 145 °C (Gibbs–Thomson effect) [30]. The higher melting temperatures hint to a morphological rearrangement during the annealing at temperatures where the crystals are partly molten [31]. However, in order to approve this, additional results from XRD and AFM are necessary, which will be presented in the following.

### 3.3.2. X-ray diffraction

The results from XRD measurements of the three different samples are plotted in Fig. 5. A distinct Bragg peak at  $2\theta = 19.9^\circ$  (spacing of 0.45 nm) can be observed for all samples. This peak is attributed to the (110) and (200) reflexes of the ferroelectric  $\beta$ -phase (110/200) $_{\beta}$  [32]. The broad halo at  $2\theta = 17.1^\circ$  in the sample that was annealed at 95 °C is interpreted as scattering from amorphous regions within the polymer. However, it should be noted that its maximum is close to literature values of the (110/200) $_{\alpha}$  reflexes of the paraelectric  $\alpha$ -phase [27,32,33]. This may point to different polymorphic forms of the P(VDF–TrFE) copolymer crystals that can be found in these inkjet printed films after treating the sample at 95 °C for 24 h. At higher annealing temperatures of 130 °C, the intensity of the amorphous halo significantly decreases and the intensity of the (110/200) $_{\beta}$  reflex increases. This clearly points to a structural rearrangement induced during annealing at 130 °C, leading to the formation of  $\beta$ -crystals after cooling to room temperature. The small shoulder observed at  $2\theta = 18.3^\circ$  (spacings of 0.48 nm) might be interpreted as reflexes from other polymorphic crystals. However, this shoulder is not observed any more after annealing at 145 °C and the area under the reflex increases. Thus, we expect a higher degree of crystallinity after an annealing treatment at this temperature.

### 3.3.3. Atomic force microscopy

Fig. 6 displays AFM phase contrast images of the as-printed reference sample (a) and the films after a thermal treatment at 95 °C, 130 °C and 145 °C (b)–(d). Without

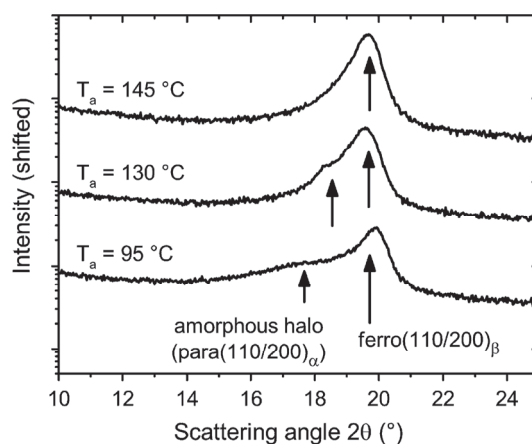


**Fig. 5.** XRD plots for different thermal treatments of the inkjet printed P(VDF–TrFE) films. For higher annealing temperatures, (110/200) $_{\beta}$  reflexes of the ferroelectric  $\beta$ -phase become more pronounced and the signals from the amorphous regions are decreasing. All curves are shifted for better visibility.

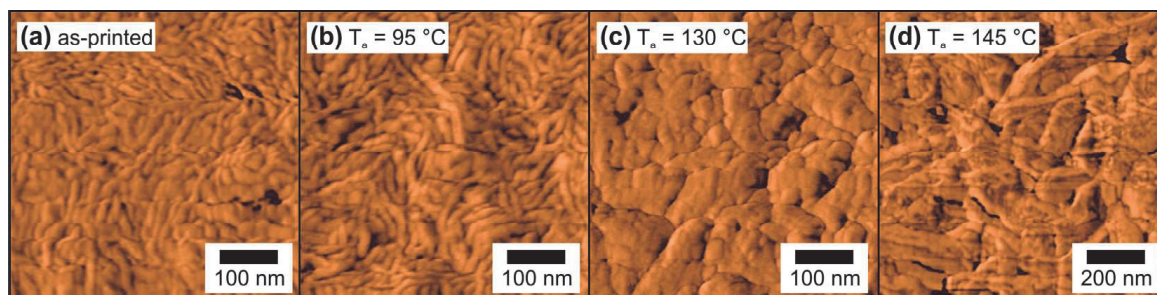


**Fig. 6.** AFM phase images for as-printed (a) and annealed P(VDF-TrFE) films (b)–(d). The scale bar represents 100 nm for all samples except (d)  $T_a = 145\text{ °C}$  (200 nm).

annealing, the surface exhibits rod-like structures with a diameter of  $21.0 \pm 6.9\text{ nm}$  which are typical for P(VDF-TrFE) crystals [21]. After annealing at low temperatures of  $95\text{ °C}$ , similar features were observed, with the crystalline domains having comparable diameters ( $21.2 \pm 6.9\text{ nm}$ ). The morphology significantly changes after annealing above the Curie transition temperature, as can be seen for the samples annealed at  $130\text{ °C}$  (Fig. 6c) and  $145\text{ °C}$  (Fig. 6d). Both samples exhibit distinct crystal thickening and the morphology changes from rod-like to globular structures. Thus, it is expected that these annealing conditions are not only providing sufficient thermal energy to transform the crystals into the  $\alpha$ -phase, but also to generate far-reaching changes in the overall morphology. The crystal thickening becomes even more prominent after annealing at  $145\text{ °C}$ , where the observed crystalline regions are much larger ( $>100\text{ nm}$ ) compared to the other investigated films. This effect might result from two circumstances. Firstly, higher temperatures increase the polymer chain mobility, which accelerates the defect healing process and thus leads to larger crystalline domains. Secondly, the polymer is partly molten at an annealing temperature of  $145\text{ °C}$  (cf. DSC data in Fig. 4). Smaller P(VDF-TrFE) crystals are not stable at  $145\text{ °C}$  and, hence, either melt and recrystallize upon cooling or the chains attach to the larger P(VDF-TrFE) crystals that obtain a higher melting temperature [31]. The presence of a partly molten state might further promote an accelerated defect healing.

The provided data from DSC, XRD and AFM give consistent information about the morphological development of the inkjet printed P(VDF-TrFE) films during annealing. At an annealing temperature of  $T_a = 95\text{ °C}$  (below the Curie temperature), the overall topological morphology remains similar to the as-printed reference; revealing rod-like crystalline domains that are typical for  $\beta$ -phase crystals [21]. Defect healing is thereby localized and limited to the transformation of *gauche*-defects in the  $\beta$ -phase crystal, leading to a slightly higher Curie temperature. This thermal treatment lead to samples that revealed only low piezoelectric  $d_{31}$  coefficients and remanent polarization  $P_{\text{rem}}$ . Annealing between the Curie transition temperature and the onset-melting temperature ( $T_a = 130\text{ °C}$ ) changes shape of the crystalline domains from rod-like to globular. Furthermore, the DSC peak and offset melting temperatures increase which indicates the existence of larger crystals that are formed during annealing and XRD measurements

point to a higher crystallinity compared to the sample annealed at  $95\text{ °C}$ . Higher annealing temperatures ( $T_a = 145\text{ °C}$ ) lead to further crystal thickening. These characteristic changes in morphology coincide with significantly higher piezoelectric  $d_{31}$  coefficients and remanent polarization  $P_{\text{rem}}$  compared to samples annealed at  $95\text{ °C}$ . Unfortunately, it is hard to estimate the absolute crystallinity of these samples by DSC and XRD. Due to the high polarity of the samples and the resulting electrostatic interactions with the DSC pan, we cannot assure complete thermal contact between sample and the measurement device and only interpret the temperature position of the endotherms. In case of the XRD, it is difficult to clearly separate the signals from the crystalline and amorphous phase from the scattering pattern in these samples. This might be the reason that, alternatively, the intensity of the (110)/(200) reflexes in the XRD patterns are discussed in terms of higher or lower crystallinities in literature [21].

For an actual application of the actuators, the annealing temperature has to be chosen considering both device performance as well as thermal stability of the substrate materials. The PET substrates used in this work exhibit an upper working temperature of approximately  $140\text{ °C}$  [25], which is relatively high compared to other technical polymer substrates like e.g. PMMA. If temperature-sensitive substrates are required for specific applications, a trade-off between high actuator performance and low processing temperatures has to be made.

### 3.4. Demonstration of pumping function

Based on the investigations on actuator performance, a basic pump demonstrator was manufactured. Fig. 7a and b shows photographs of the demonstrator. It consists of an aluminum alloy (RSA 905) as a substrate into which a pump chamber, an inlet and an outlet channel as well as passive nozzle/diffuser valves were milled. For a first pumping demonstration, a metallic substrate was chosen because it can be easily cleaned and used several times with different actuators. However, the design is compatible with polymer replication techniques like hot embossing or injection molding that are commonly used for microfluidic lab-on-a-chip systems [10]. On top of the substrates, an inkjet printed membrane actuator was mounted. The pump is setup as a reciprocating membrane pump, in which the volume change caused by cyclic driving of the actuated membrane leads to a net fluid flow due to the

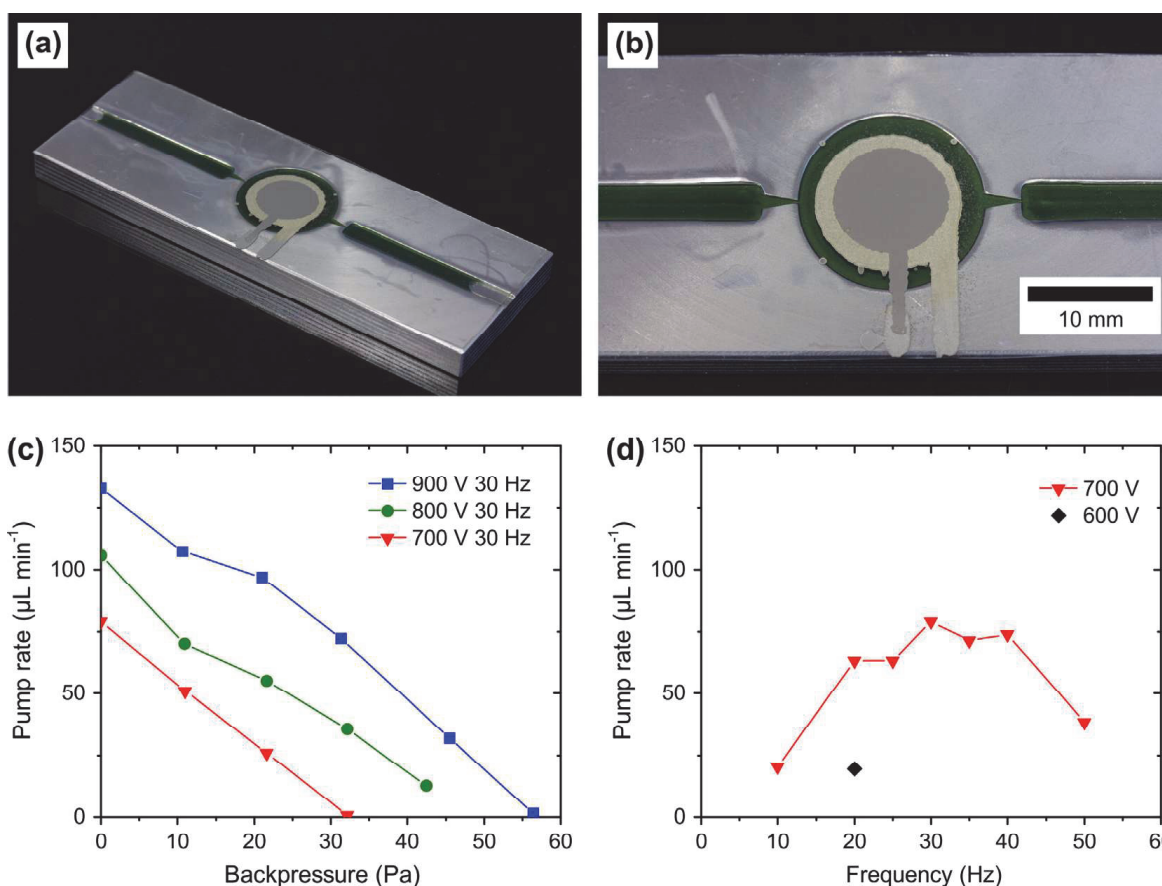


**Fig. 7.** Pump demonstrator with an inkjet printed P(VDF–TrFE) membrane actuator (a) and (b). Pump rate with respect to backpressure (c) and frequency-dependent pump rate (d). For quasi-static driving, pump rates of up to  $130 \mu\text{L min}^{-1}$  were obtained.

valves [13]. The characteristic dimensions of the valves were chosen based on typical values for passive nozzle/diffuser valves by Olsson [13]. As the goal of this study was the demonstration of a basic pump function, no elaborate optimization of the fluidic design was performed. In order to keep the annealing temperatures significantly below the recommended working temperatures of the PET substrates, annealing of the printed P(VDF–TrFE) films was performed at a temperature of  $130 \text{ }^\circ\text{C}$ . Top electrodes were sintered using a combined thermal and argon plasma treatment.

Fig. 7c plots the pump rate that was measured on the pump demonstrator with respect to backpressure. With large voltage amplitudes in the range of 700–900 V, pump rates of up to  $130 \mu\text{L min}^{-1}$  at zero backpressure and a driving frequency of 30 Hz were observed. Such pump rates are promising for applications in on-chip reactions [34], which demonstrates the applicability of inkjet printed P(VDF–TrFE) actuators for pumping applications in LOC. A linear decrease of pump rate with increasing backpressure was observed ( $R^2 = 0.98$ ). The maximum backpressure for a driving voltage of 900 V was 56 Pa. The dependencies of both maximum backpressure and pump rate on driving voltage were approximately linear for the voltage range that was investigated. A video file that shows the operation of the micropump demonstrator is provided as [Supplementary Material](#) along with the online version of this manuscript. Fig. 7d displays the dependency of pump rate

on driving frequency for a voltage amplitude of 700 V. The curve exhibits a parabolic shape with an optimum at a frequency of 30 Hz. For lower frequencies, the duration of one pumping cycle allows a relaxation of the fluid flow, as described by Woias [35]. The author also stated that for larger driving frequencies, insufficient relaxation and energy losses due to e.g. squeeze film damping can lead to a reduction in flow rate [35]. The optimum frequency range depends on the geometries of the valves, fluid channels as well as on the mechanical properties of the pump membrane.

For driving voltages below 600 V, however, no significant pump rate was observed. The reason for this is believed to be the function of the nozzle/diffuser valve design in this work. For low volume changes or flow gradients associated to lower driving voltages, the direction sensitivity of the passive valves is obviously too low to generate a directed fluid flow. Furthermore, larger backpressures than the ones realized so far would be beneficial. An optimization of the valve design is therefore necessary to generate significant pump rates also at reduced driving voltages, larger driving frequencies as well as larger backpressures, which is planned in future work.

#### 4. Summary and outlook

The actuator performance and morphology for different thermal treatments of all inkjet printed P(VDF–TrFE)



actuators were investigated here for the first time. The actuators consist of a printed P(VDF–TrFE) film sandwiched between two silver electrodes on a PET substrate. The device performance was characterized by deflection measurements of cantilever actuators and ferroelectric hysteresis measurements in order to estimate the piezoelectric  $d_{31}$  coefficient and the remanent polarization  $P_{\text{rem}}$ , respectively. A strong dependence of both  $d_{31}$  and  $P_{\text{rem}}$  on the annealing temperature used during the post-processing step for the as-printed P(VDF–TrFE) films was found. Enhanced piezoelectric behavior was observed for annealing temperatures above 110 °C, with maximum values for  $d_{31} = 10 \text{ pm V}^{-1}$  and  $P_{\text{rem}} = 5.8 \text{ } \mu\text{C cm}^{-2}$ . The structure and morphology of printed P(VDF–TrFE) films were investigated by DSC, XRD as well as AFM measurements. The results indicate an increased crystallinity as well as larger crystalline domain sizes for samples annealed at higher temperatures. Crystal thickening becomes pronounced at temperatures above 110 °C, which coincides with an improved actuator behavior. This underlines the strong impact of structure and morphology on the electromechanical behavior of P(VDF–TrFE). These findings can be used as a guideline for designing printed actuators based on P(VDF–TrFE) and for selecting appropriate combinations of processing temperatures and polymer substrate materials.

As a proof of concept, the first micropump with an inkjet printed P(VDF–TrFE) actuator was presented here. The pump is designed as a reciprocating membrane pump with passive nozzle/diffuser valves. Pump rates of up to  $130 \text{ } \mu\text{L min}^{-1}$  were realized, which is promising for applications in lab-on-a-chip systems. However, an optimization of the valve design is planned in order to achieve a pumping function at lower driving voltages and higher driving frequencies as well as higher backpressures. Apart from the application as a pump actuator, the results presented in this contribution demonstrate the suitability of the suggested manufacturing route for other P(VDF–TrFE) based devices like pressure sensors [8] or memory elements [20]. Knowledge about the parameters that were investigated here is also crucial for the design of such devices. Furthermore, the process chain that was established is compatible with the integration of further functionalities into lab-on-a-chip systems along with a pumping function. Possible further printed functionalities include resistive heaters, capacitive detectors or organic light sources or detectors, which can be used for example for fluorescent detection of on-chip reactions. The manufacturing approach introduced here therefore enables cost-efficient function integration for disposable, polymer-based lab-on-a-chip systems.

#### Author contributions

OP and SH contributed equally to this work. All other co-authors have provided input concerning either planning of the experiments or analysis of the results. All authors have given approval to the final version of the manuscript.

#### Acknowledgments

The work presented in this paper was funded by the German Federal Ministry of Education and Research (BMBF) within the joint research project “Komplexer Optofluidchip” (FKZ 03IPT609A) and by the German Research Foundation (DFG) within the priority program “Active Micro-optics” (SPP 1337). The authors thank R. Paulus (IOMC) for performing DSC measurements, S. Yulin and V. Nesterenko (both IOF) for XRD characterization as well as R. Schulze (Friedrich Schiller University Jena, Chair of Materials Science) for recommendations concerning morphology investigations.

#### Appendix A. Supplementary material

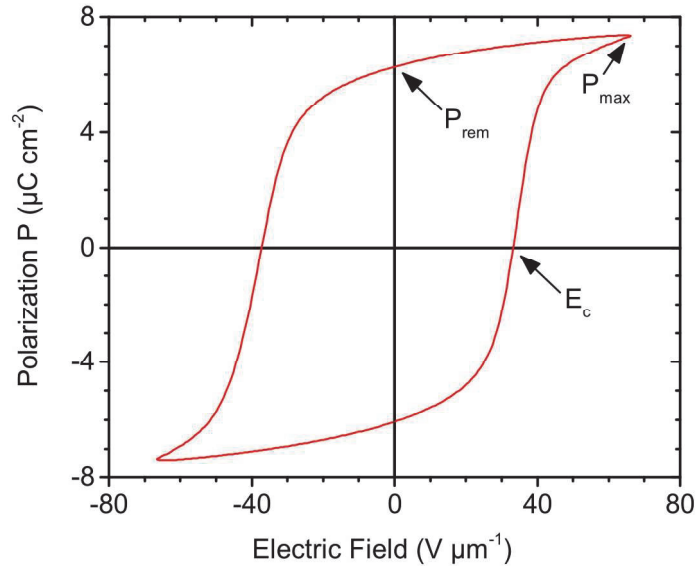
As supplementary information, an example of a ferroelectric hysteresis loop, measurement results for the maximum polarization as well as the DSC-scans from cooling and second heating are provided. Moreover, a video showing the operation of a micropump with an inkjet printed actuator can be found here. This material is available with the online version of the manuscript. Supplementary data associated with this article can be found, in the online version, at <http://dx.doi.org/10.1016/j.orgel.2014.09.007>.

#### References

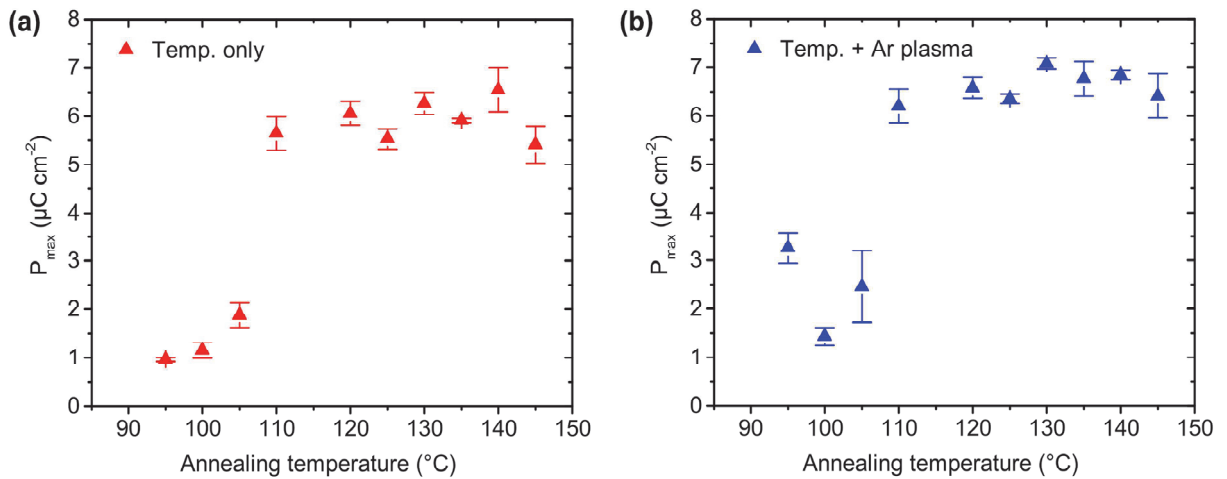
- [1] J.G. Korvink, P.J. Smith, D.-Y. Shin (Eds.), *Inkjet-Based Micromanufacturing*, Wiley-VCH Verlag GmbH & Co. KGaA, 2012.
- [2] J. Perelaer, U.S. Schubert, Novel approaches for low temperature sintering of inkjet-printed inorganic nanoparticles for roll-to-roll (R2R) applications, *J. Mater. Res.* 28 (4) (2013) 564–573.
- [3] S. Wünscher, R. Abbel, J. Perelaer, U.S. Schubert, Progress of alternative sintering approaches of inkjet-printed metal inks and their utilization for manufacturing of flexible electronics, *J. Mater. Chem. C* (accepted manuscript).
- [4] R.R. Søndergaard, M. Hösel, F.C. Krebs, Roll-to-roll fabrication of large area functional organic materials, *J. Polym. Sci., Part B: Polym. Phys.* 51 (1) (2013) 16–34.
- [5] J. Willmann, D. Stocker, E. Dörsam, Characteristics and evaluation criteria of substrate-based manufacturing. Is roll-to-roll the best solution for printed electronics?, *Org Electron.* 15 (7) (2014) 1631–1640.
- [6] M. Singh, H.M. Haverinen, P. Dhagat, G.E. Jabbour, Inkjet printing-process and its applications, *Adv. Mater.* 22 (6) (2010) 673–685.
- [7] M. Zirkel, A. Haase, A. Fian, H. Schön, C. Sommer, G. Jakopic, G. Leising, B. Stadlober, I. Graz, N. Gaar, R. Schwödiauer, S. Bauer-Gogonea, S. Bauer, Low-voltage organic thin-film transistors with high-k nanocomposite gate dielectrics for flexible electronics and optothermal sensors, *Adv. Mater.* 19 (17) (2007) 2241–2245.
- [8] M. Zirkel, A. Sawatdee, U. Helbig, M. Krause, G. Scheipl, E. Kraker, P.A. Ersman, D. Nilsson, D. Platt, P. Bodö, S. Bauer, G. Domann, B. Stadlober, An all-printed ferroelectric active matrix sensor network based on only five functional materials forming a touchless control interface, *Adv. Mater.* 23 (18) (2011) 1–6.
- [9] A. Manz, N. Graber, H. Widmer, Miniaturized total chemical analysis systems: a novel concept for chemical sensing, *Sens. Actuators, B* 1 (1990) 244–248.
- [10] H. Becker, C. Gärtner, Polymer microfabrication technologies for microfluidic systems, *Anal. Bioanal. Chem.* 390 (2008) 89–111.
- [11] D.J. Laser, J.G. Santiago, A review of micropumps, *J. Micromech. Microeng.* 14 (6) (2004) R35–R64.
- [12] F. Amirouche, Y. Zhou, T. Johnson, Current micropump technologies and their biomedical applications, *Microsyst. Technol.* 15 (5) (2009) 647–666.
- [13] A. Olsson, Valve-less diffuser micropumps, Ph.D. Thesis, Royal Institute of Technology Stockholm, Sweden, 1998.
- [14] S. Lee, K.J. Kim, Design of IPMC actuator-driven valve-less micropump and its flow rate estimation at low Reynolds numbers, *Smart Mater. Struct.* 15 (4) (2006) 1103–1109.

- [15] S. Zhang, B. Neese, K. Ren, B. Chu, F. Xia, T. Xu, S. Tadigadapa, Q. Wang, Q.M. Zhang, F. Bauer, Relaxor ferroelectric polymers, thin film devices, and ink-jet microprinting for thin film device fabrication, *Ferroelectrics* 342 (1) (2006) 43–56.
- [16] O. Pabst, J. Perelaer, E. Beekert, U.S. Schubert, R. Eberhardt, A. Tünnermann, All inkjet-printed piezoelectric polymer actuators: characterization and applications for micropumps in lab-on-a-chip systems, *Org. Electron.* 14 (12) (2013) 3423–3429.
- [17] Y. Tajitsu, H. Ogura, A. Chiba, T. Furukawa, Investigation of switching characteristics of vinylidene fluoride/trifluoroethylene copolymers in relation to their structures, *Jpn. J. Appl. Phys.* 26 (1987) 554–560.
- [18] J.F. Legrand, Structure and ferroelectric properties of P(VDF-TrFE) copolymers, *Ferroelectrics* 91 (1) (1989) 303–317.
- [19] F. Baltá-Calleja, A. González Arche, T.A. Ezquerra, C. Santa Cruz, F. Batallán, B. Frick, E. López Cabarcos, Structure in polymers with special properties, in: H.-G. Zachmann (Ed.), *Ch. Structure and Properties of Ferroelectric Copolymers of Poly(Vinylidene) Fluoride*, Springer-Verlag, 1993, pp. 1–48.
- [20] D. Mao, M. Quevedo-Lopez, H. Stiegler, B. Gnade, H. Alshareef, Optimization of poly(vinylidene fluoride-trifluoroethylene) films as non-volatile memory for flexible electronics, *Org. Electron.* 11 (5) (2010) 925–932.
- [21] D. Mao, B.E. Gnade, M.A. Quevedo-Lopez, *Ferroelectrics – physical effects*, in: M. Lallart (Ed.), *Ch. Ferroelectric Properties and Polarization Switching Kinetic of Poly(Vinylidene Fluoride-Trifluoroethylene) Copolymer*, InTech Europe, 2011, pp. 77–100.
- [22] A. Teichler, J. Perelaer, U.S. Schubert, Inkjet printing of organic electronics – comparison of deposition techniques and state-of-the-art developments, *J. Mater. Chem. C* 1 (2013) 1910–1925.
- [23] H. Wang, Q.M. Zhang, L.E. Cross, A.O. Sykes, Piezoelectric, dielectric, and elastic properties of poly(vinylidene fluoride/trifluoroethylene), *J. Appl. Phys.* 74 (5) (1993) 3394–3398.
- [24] D. Mao, I. Mejia, H. Stiegler, B.E. Gnade, M.A. Quevedo-Lopez, Polarization behavior of poly(vinylidene fluoride-trifluoroethylene) copolymer ferroelectric thin film capacitors for nonvolatile memory application in flexible electronics, *J. Appl. Phys.* 108 (9) (2010) 094102.
- [25] Goodfellow GmbH homepage, Material properties table. <www.goodfellow.com> (accessed 04.07.2014).
- [26] K.J. Kim, G.B. Kim, C.L. Vanlencia, J.F. Rabolt, Curie transition, ferroelectric crystal structure, and ferroelectricity of a VDF/TrFE(75/25) copolymer 1. The effect of the consecutive annealing in the ferroelectric state on Curie transition and ferroelectric crystal structure, *J. Polym. Sci. Polym. Phys.* 32 (15) (1994) 2435–2444.
- [27] N. Shingne, Morphology and crystal orientation of ferroelectric P(VDF-ran-TrFE) nanostructures in porous aluminium oxide, Ph.D. Thesis, University of Halle, Germany, 2011.
- [28] M. Barique, H. Ohigashi, Annealing effects on the Curie transition temperature and melting temperature of poly(vinylidene fluoride/trifluoroethylene) single crystalline films, *Polymer* 42 (11) (2001) 4981–4987.
- [29] A.J. Lovinger, Ferroelectric polymers, *Science* 220 (4602) (1983) 1115–1121.
- [30] G. Höhne, Another approach to the Gibbs–Thomson equation and the melting point of polymers and oligomers, *Polymer* 43 (17) (2002) 4689–4698.
- [31] B. Fillon, J.C. Wittmann, B. Lotz, A. Thierry, Self-nucleation and recrystallization of isotactic polypropylene ( $\alpha$  phase) investigated by differential scanning calorimetry, *J. Polym. Sci. Polym. Phys.* 31 (10) (1993) 1383–1393.
- [32] M.-C. Garcia-Gutierrez, A. Linares, I. Martin-Fabiani, J.J. Hernandez, M. Soccio, D.R. Rueda, T.A. Ezquerra, M. Reynolds, Understanding crystallization features of P(VDF-TrFE) copolymers under confinement to optimize ferroelectricity in nanostructures, *Nanoscale* 5 (2013) 6006–6012.
- [33] E. Bellet-Amalric, J. Legrand, Crystalline structures and phase transition of the ferroelectric P(VDF-TrFE) copolymers, a neutron diffraction study, *Eur. Phys. J. B* 3 (2) (1998) 225–236.
- [34] C. Zhang, D. Xing, Y. Li, Micropumps, microvalves, and micromixers within PCR microfluidic chips: advances and trends, *Biotechnol. Adv.* 25 (5) (2007) 483–514.
- [35] P. Woias, Micropumps – past, progress and future prospects, *Sens. Actuators, B* 105 (1) (2005) 28–38.

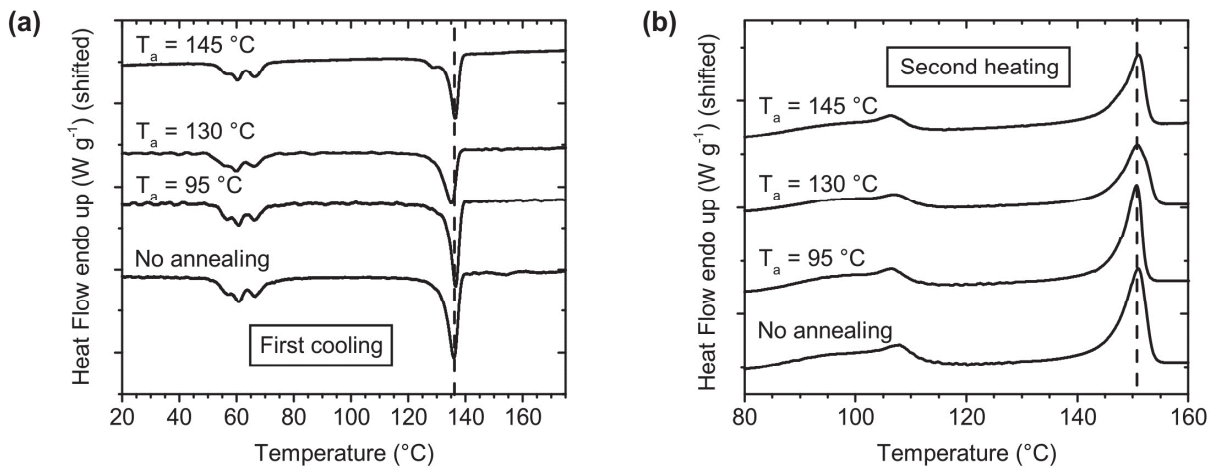
## Supplementary material



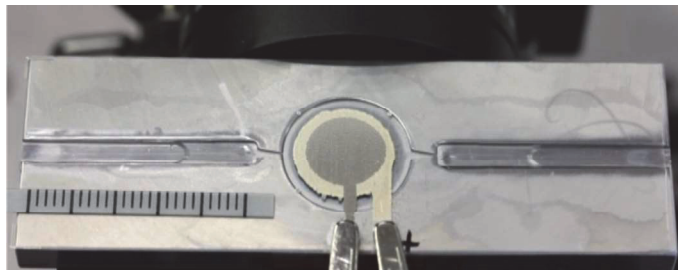
**Supporting Information Fig. 1.** Example of a ferroelectric hysteresis loop for one sample. As characteristic points, the remanent polarization  $P_{\text{rem}}$ , the maximum polarization  $P_{\text{max}}$  as well as the coercive field  $E_c$  are marked.



**Supporting Information Fig. 2.** Maximum polarization  $P_{\text{max}}$  for different thermal treatments (a) and combined thermal and plasma treatments (b) of inkjet printed P(VDF-TrFE) films. Similar trends as discussed for  $P_{\text{rem}}$  can be observed. The values of  $P_{\text{max}}$  are in the range of  $1 \mu\text{C cm}^{-2}$  to  $7 \mu\text{C cm}^{-2}$ .



**Supporting Information Fig. 3.** DSC plots of the first cooling (a) and the second heating run (b) for different thermal treatments of the inkjet printed P(VDF-TrFE) films. Since the samples were heated well above their melting temperature during the first heating run, their thermal history is erased and mostly similar DSC curves are obtained.

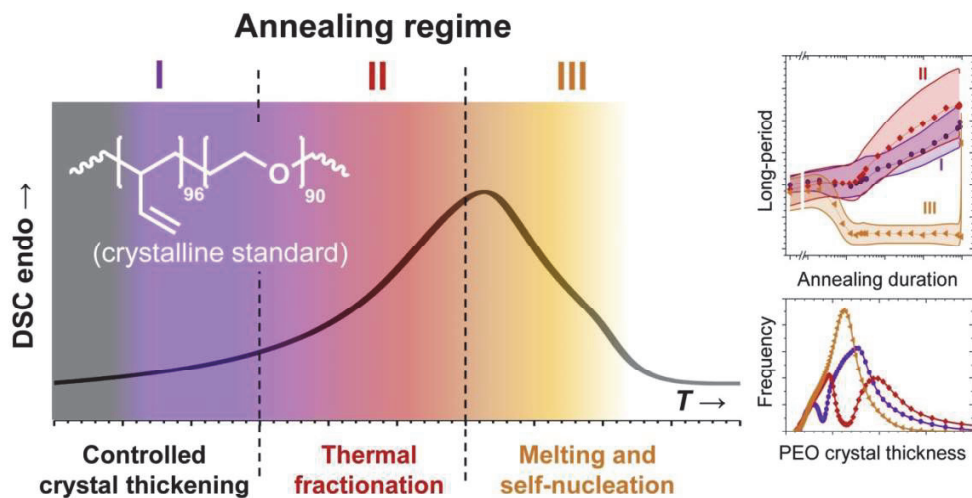


**Supporting Information Fig. 4.** Still image taken from a video that shows the pump demonstrator during operation. Pumping medium is isopropanol. The video file is available along with the online version of the manuscript.

## Publication [P6]

# Mechanisms and Kinetics of the Crystal Thickening of Poly(butadiene)-block-poly(ethylene oxide) during Annealing within the Melting Range

Stefan Hölzer, Tobias N. Büttner, Robert Schulze, Matthias M. L. Arras,  
Felix H. Schacher, Klaus D. Jandt, Ulrich S. Schubert



*Eur. Polym. J. in press.*

DOI: 10.1016/j.eurpolymj.2015.04.010



# Morphological Development of Poly(butadiene)-*block*-poly(ethylene oxide) during Annealing within the Melting Range: Mechanisms and Kinetics.

Stefan Hölzer,<sup>a</sup> Tobias N. Büttner,<sup>b</sup> Robert Schulze,<sup>b</sup> Matthias M. L. Arras,<sup>b</sup> Felix H. Schacher,<sup>a,c</sup> Klaus D. Jandt<sup>\*b,c</sup> and Ulrich S. Schubert<sup>\*a,c</sup>

<sup>a</sup> Laboratory of Organic and Macromolecular Chemistry (IOMC), Friedrich Schiller University Jena, Humboldtstraße 10, 07743 Jena, Germany.

<sup>b</sup> Chair of Materials Science (CMS), Otto Schott Institute of Materials Research (OSIM), Friedrich Schiller University Jena, Löbdergraben 32, 07743 Jena, Germany.

<sup>c</sup> Jena Center for Soft Matter (JCSM), Friedrich Schiller University Jena, Philosophenweg 7, 07743 Jena, Germany.

KEYWORDS: block copolymer; morphology; crystallization; self-nucleation; Gibbs-Thomson

**ABSTRACT:** The morphology of crystallizable block copolymers can be tuned by controlled crystal thickening. To understand the underlying mechanics and kinetics, we investigated the morphological development of a PB-*b*-PEO block copolymer during annealing near its melting point by time and temperature dependent SAXS, WAXS and DSC measurements. Thereby, DSC based PEO crystal thickness distributions yield qualitative information about the mechanisms during annealing. Conclusions on the kinetics and the absolute long-period growth due to crystal thickening can be drawn from the SAXS investigations, by calculating the average long-period and its deviations from the SAXS reflex position and shape, respectively. By this combined study, we identified three annealing regimes: (i) At low annealing temperatures  $T_a$ , steady lamellae-thickening was found, due to defect healing of the PEO crystals. (ii) Thermal fractionation was observed at intermediate  $T_a$ , due to the exclusion of shorter PEO chains from the crystals. (iii) Annealing close to and above the peak melting temperature, self-nucleation of the molten PEO fractions dominates. Long-periods up to 40% larger than the initial crystalline standard (22 nm) were observed in that regime. However, break-out crystallization impedes a regulated morphology development within regime (iii). Thus, the annealing regimes (i) and (ii) are more suitable to obtain controlled crystal thickening. The combination of the applied techniques provides deeper insights into the kinetics and ordering mechanisms of controlled long-period growth by crystal thickening under variable confinements, which allows us to tailor the morphology of the block copolymer within several nanometers, without changing the degree of polymerization.

## INTRODUCTION

The ever growing miniaturization of devices leads to an increasing demand of geometrically defined, highly-ordered nanostructures. Conventional top-down approaches, like lithographical techniques, are inherently limited by physical fundamentals and the high costs of the lithographical production tools.<sup>1</sup> Fortunately, highly ordered nanostructures can be formed by self-assembly of organic molecules such as block copolymers (BCPs).<sup>2-5</sup>

The chemical incompatibility of the different blocks in BCPs leads to microphase separation and the formation of nanostructured materials, which have different morphologies.<sup>6,7</sup> Size and shape of the BCP morphology are defined by the degree of polymerization, the volume fraction of the blocks as well as the interactions between the constituting segments.<sup>6,7</sup> Depending on the ability to crystallize, BCPs are categorized as amorphous or semi-crystalline.<sup>8</sup> The crystallization process can be interpreted as another influencing factor for the microphase separation. Understanding the mutual relation of the BCP morphology and the BCP crystallization is of great interest: On the one hand it provides new

insight into the general polymer crystallization process under soft- or hard-confinement.<sup>8,9</sup> On the other hand it represents an interesting tool to control the BCP morphology by defined isothermal crystallization from the melt or an annealing procedure of previously crystallized systems.<sup>10,11</sup>

Isothermal crystallization from the melt has been widely investigated for the amorphous-crystalline block copolymer polybutadiene-*block*-poly(ethylene oxide) (PB-*b*-PEO), where the PB phase imposes a soft confinement on the PEO crystallization.<sup>11-16</sup> Consequently, the formation of PEO crystals occurs either within the confined PEO domains or overwrites the pre-existing microphase separated domain structure (break-out crystallization).<sup>14</sup> Thickness and lateral dimensions of these PEO crystals depend on the crystallization process, *i.e.*, the crystallization temperature  $T_c$  and duration.<sup>11-14</sup> Reiter *et al.* observed larger spacings of the lamellar morphology with increasing  $T_c$  of a low molar mass PB-*b*-PEO. The different thickness values of the crystalline lamellae were explained by differently folded PEO chains.<sup>12</sup>

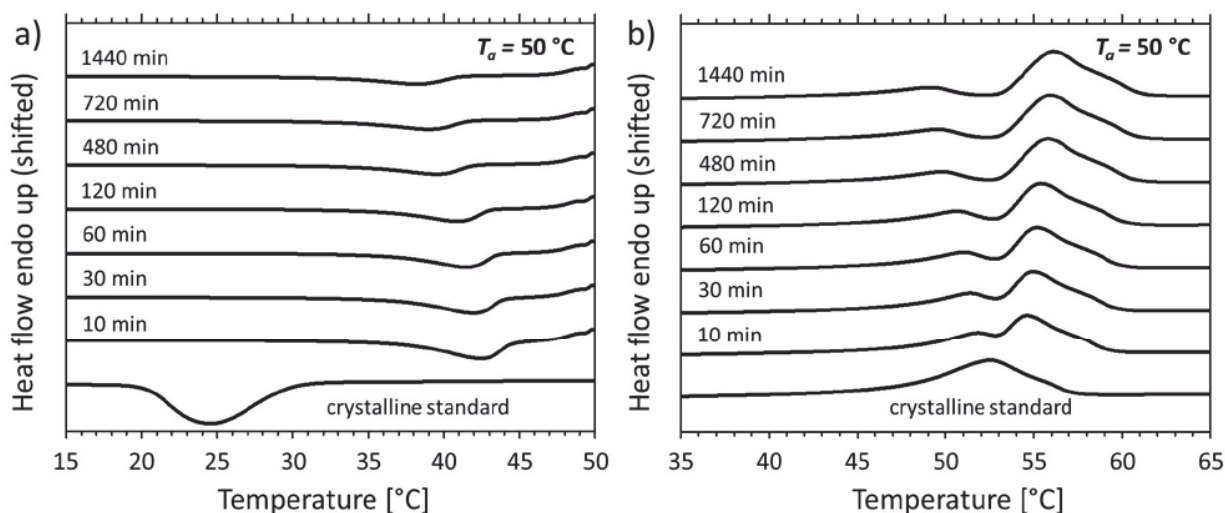


Figure 1. a) Cooling scans of  $B_{96}EO_{90}$  after annealing at an annealing temperature  $T_a = 50\text{ }^{\circ}\text{C}$  for different annealing periods  $t_a$ . b) Heating scans for different  $t_a$  after the subsequent cooling step. The curves are shifted for better visibility.

Another approach to control the morphology of PB-*b*-PEO is to anneal the sample within the melting range, after defining a crystalline standard state (CS).<sup>15-20</sup> Crystal thickening as well as partial and complete melting can be observed, depending on the respective annealing temperature.<sup>15-17</sup> It was shown that the spacing of a thin film surface morphology of a low molar mass PB-*b*-PEO can be systematically increased by this approach.<sup>11</sup>

For potential applications, understanding the mechanisms and kinetics of the crystal thickening in soft confined BCPs is mandatory. The underlying mechanisms have been intensively studied on low molar mass homopolymers, which have been isothermally crystallized from the melt or solution.<sup>21-24</sup> Moreover, crystal thickening was investigated for amorphous-crystalline BCPs in bulk and thin films.<sup>11-14, 25</sup> However, studies regarding lamellae thickening based on CS are rare and these investigations focus on the surface topology of the corresponding thin films.<sup>10, 11</sup>

Up to now, crystal thickening mechanisms and kinetics of amorphous-crystalline BCPs in the bulk are, to the best of our knowledge, not reported in the literature. Potential applications of tunable BCP nanostructures can be found in the fields of biomedicine, and -analytics, photonics or high density data storage. In particular in the fields of biomedicine and -analytics, these nanostructures are interesting for patterning purposes in order to investigate and control the protein adsorption on the surface of biomaterials, which is a key factor for the development of next generation implants and biosensors.

For our investigations, we used a combination of differential scanning calorimetry (DSC) as well as temperature and time dependent X-ray scattering experiments for PB-*b*-PEO to investigate the development of structure and morphology within this system. In order to analyze the DSC data, we applied a modified model of Crist and Mirabella<sup>26</sup> (CM-model), which has frequently been used to describe the crystal lamellae thickness of polyolefins.<sup>26-28</sup> Average long-periods and their deviations are estimated by small-angle X-ray scattering (SAXS) from the first reflex  $q^*$  at 100% and 90% of the reflex intensity, respectively. This is followed by a critical dis-

cussion about the applicability and comparability of these data representations. Our results contribute to the understanding of BCP crystallization and are focused on the controlled formation and manipulation of self-assembled BCP nanostructures where crystalline segments are involved.

## EXPERIMENTAL

### Materials

The investigated poly(butadiene)-*block*-poly(ethylene oxide) (PB-*b*-PEO) was purchased from Polymer Source Inc. (Dorval, Canada). The PB block has a molar mass of  $M_n = 5200\text{ g/mol}$  and a PDI value of 1.12, as given by the supplier. The molar mass of the PEO block was determined by <sup>1</sup>H-NMR measurements to be  $M_n = 3960\text{ g/mol}$ . The corresponding degrees of polymerization are 96 and 90 for the PB and the PEO block, respectively. Following the syntax of other investigations on this block copolymer system, this polymer will be named as  $B_{96}EO_{90}$ . The volume fraction of PEO in  $B_{96}EO_{90}$  is 35.4 vol.% at 20 °C.

### Differential scanning calorimetry

Differential scanning calorimetry (DSC) was carried out on a PerkinElmer Pyris 1 equipped with a thermal analysis controller 7/DX (PerkinElmer Inc., Waltham, MA). Heating and cooling rates were 10 °C/min for all measurements. The sample was kept for at least one minute at the final temperature after each heating/cooling step.

To create comparable sample conditions before each experiment,  $B_{96}EO_{90}$  was heated to 90 °C in the calorimeter, which is well above the peak melting temperature of the crystalline PEO block and erases the thermal history of the sample. Subsequently, the sample was cooled to 0 °C. This initial state is referred to as crystalline standard (CS) and has a peak crystallization temperature of  $T_c = 24.5\text{ }^{\circ}\text{C}$  and a peak melting temperature of  $T_m = 52.5\text{ }^{\circ}\text{C}$ . The degree of crystallinity of the PEO block for the CS was 66%, as determined by DSC.



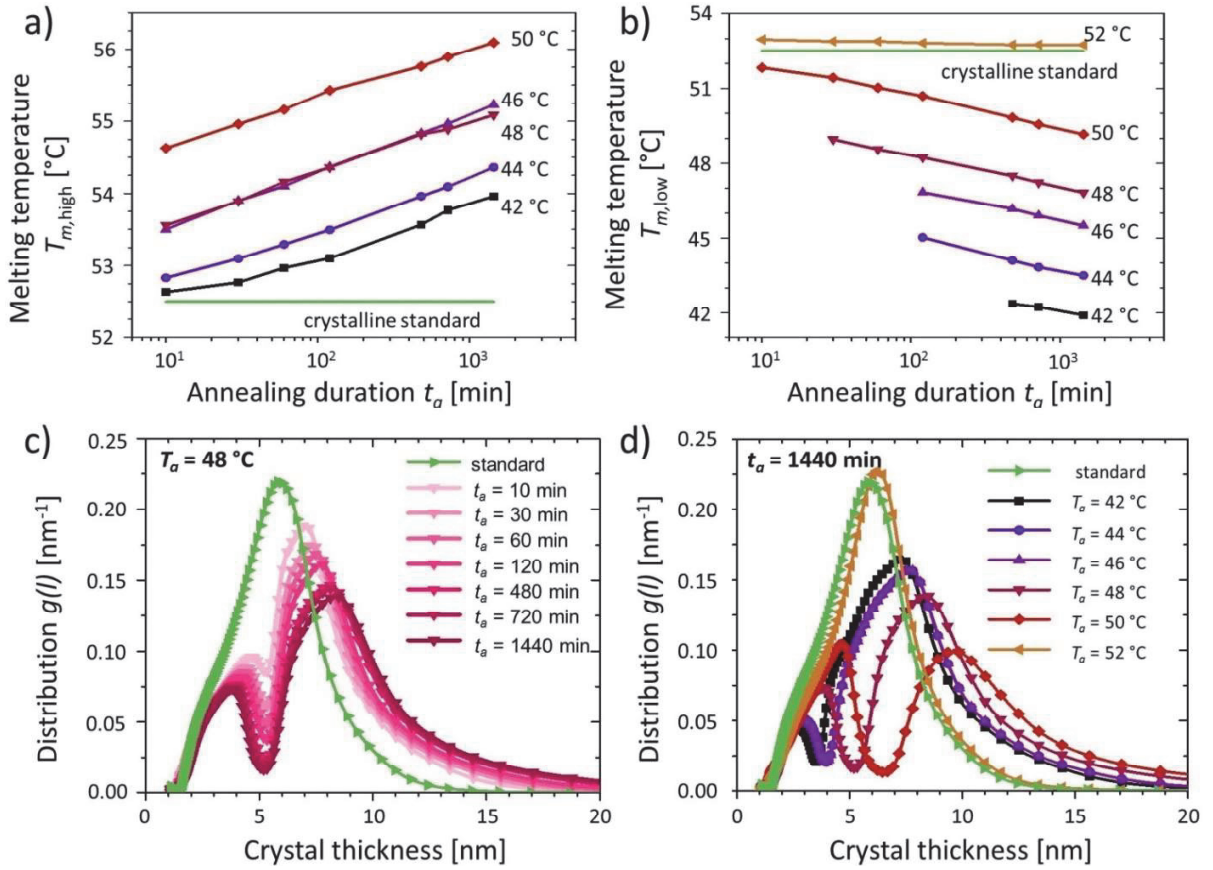


Figure 2. Peak melting temperatures for different  $t_a$  and distributions of the corresponding crystal thickness distributions according to the modified CM-model (equation 1).<sup>26</sup> a) higher peak melting temperature  $T_{m,high}$  and b) lower peak melting temperature  $T_{m,low}$ . c) Crystal thickness distributions at  $T_a = 48$  °C after different  $t_a$ . d) Crystal thickness distributions after annealing between 42 and 52 °C for 24 h.

After creating the CS, the sample was heated to the selected annealing temperature  $T_a$  between 42 and 52 °C, which is within the melting range of the PEO block. B<sub>96</sub>EO<sub>90</sub> was held for different annealing periods  $t_a$ , ranging from  $t_a = 10$  min to  $t_a = 24$  h and was subsequently cooled to 0 °C to crystallize the already molten parts of the polymer. Afterwards, the sample was heated again to 90 °C, which provides information about the thermal properties after the annealing procedure. A modified approach of Crist and Mirabella<sup>26</sup> (CM-model) was applied to correlate the DSC melting temperatures  $T_m$  with the thickness of the PEO crystals  $l_{PEO,c}$ . Its dependence can be calculated by:

$$g(l_{PEO,c}) = K \cdot P_c(T) \cdot (T_{m,corr}^0 - T)^2 \quad (1)$$

Here,  $g(l_{PEO,c})$  is the distribution function of the PEO crystal thickness,  $K$  is a normalizing factor and  $P_c(T)$  is the heat flow of the crystalline PEO fractions, which can be estimated from the DSC heating scans.  $T_{m,corr}^0$  originates from  $T_m^0$ , which is a material constant, known from the Gibbs-Thomson equation and describes the melting temperature of an infinitely thick PEO crystal. The correction of  $T_m^0$  for low molar mass PEO was carried out according to Buckley and Kovacs<sup>29</sup> for low molar mass PEO, which leads to  $T_{m,corr}^0 = 61.75$  °C. Details are given in the electronic supplementary information.

## X-ray Scattering

Small- and wide angle X-ray scattering experiments (SAXS and WAXS) were carried out on a Bruker AXS Nanostar (Karlsruhe, Germany), equipped with (i) a microfocus copper X-ray source (Incoatec I $\mu$ SCu E025, Incoatec, Geesthacht, Germany), at a wavelength of  $\lambda = 0.154$  nm, (ii) a two-dimensional Bruker AXS VANTEC-2000 gas detector (Karlsruhe, Germany) and (iii) a temperature controller unit. The distances between sample and detector were 107 and 12 cm for the SAXS- and WAXS-setup, respectively, using silver behenate for calibration. Exposure times were between 1 min and 9 min for each SAXS measurement and 60 min for WAXS. The samples were placed in the hole of a metal plate, which is used to mount the samples in the temperature controller unit of the SAXS/WAXS device. Prior to the morphological investigations, each sample was placed together with the metal plate in the calorimeter in order to establish the crystalline standard (CS).

For the temperature-dependent WAXS experiments, the CS was heated from room temperature to 42 °C. The temperature was held for 20 min to ensure that the sample was completely heated through. After measuring for one hour, the temperature was increased by 2 °C. This procedure was repeated until the signals of the crystalline PEO vanished completely.

The data acquisition of each SAXS annealing procedure was carried out by (i) collecting an initial pattern at 20 °C, (ii) heating the sample up to the desired annealing temperature  $T_a$  between 42 and 54 °C, (iii) collecting patterns after several annealing periods (1 min to  $\approx 10^4$  min) at  $T_a$  and (iv) collecting a final pattern after cooling to 20 °C. The heating and cooling rates in the experiments were set to 10 °C/min and the maximum temperature deviations that were measured during annealing were  $\pm 0.2$  °C.

The scattering patterns were post-processed using ImageJ, an open source image processing software.<sup>30</sup> SAXS and WAXS patterns were converted into  $q$ -space ( $q = (4\pi/\lambda) \cdot \sin \theta$ ) and  $2\theta$ -space, respectively. Here,  $q$  is the scattering vector and  $2\theta$  is the scattering angle. All patterns were corrected regarding background scattering, normalized to the exposure time and rotated so that preferential orientations of the CS-patterns of each temperature series are located on the meridian. After azimuthal integration of the 2D-SAXS patterns, the average long-period  $l_p$ , which is the sum of the PB and the PEO domain size, of each SAXS sample was calculated from the maximum of the reflex  $q^*$  by:

$$l_p = 2\pi/q^* \quad (2)$$

To estimate the long-period distributions, additional values at a height of 90% of the  $q^*$  reflex were extracted. The corresponding spacings are interpreted as deviations from  $l_p$ . The domain spacings of each phase  $l_i$  can be calculated from  $l_p$  and the volume fractions  $f_i$ , where the subscript  $i$  stands for PB or PEO:<sup>14</sup>

$$l_i = l_p \cdot f_i \quad (3)$$

## RESULTS

### Differential scanning calorimetry

Exemplary cooling curves after annealing at  $T_a = 50$  °C and the subsequent heating curves are given in Figures 1a and 1b, respectively. For comparison, the DSC data of the crystalline standard (CS) is also given in this plot. In the cooling scans after annealing, shown in Figure 1a, the crystallization temperature  $T_c$  is shifting to lower temperatures with increasing annealing duration ( $t_a$ ). Moreover, the area under the crystallization exotherm is systematically decreasing. This indicates that the degree of crystallinity of the sample is increasing during annealing with time, since less crystallizable PEO is available in the later cooling step. In the heating scans (Figure 1b), two melting endotherms were observed for the samples annealed at 50 °C: The melting endotherm at the higher temperature ( $T_{m,high}$ ) shifted with increasing  $t_a$  to higher peak temperatures of 54.6 °C (10 min), 55.4 °C (120 min) and 56.1 °C (24 h). The second melting endotherm features lower peak melting temperatures  $T_{m,low}$  which, in turn, systematically decrease with longer annealing durations. The observed melting enthalpies of these lower temperature melting peaks are close to the crystallization enthalpies, which are observed in the previous cooling scans. Thus, it is obvious that  $T_{m,low}$  originates from the PEO fractions, which crystallize upon cooling. The shift of the high-temperature melting endotherm is attributed to crystal thickening during annealing. Note that the small high-temperature shoulder near  $T_{m,high}$  is expected to be a measurement artefact that arises from crystals formed during heating in the DSC, as discussed elsewhere.<sup>14</sup> The effect of the annealing temperature  $T_a$  and duration  $t_a$  on the peak melting temperatures  $T_{m,high}$  and  $T_{m,low}$  is shown in Figure 2. The

trend, which was exemplarily presented for the 50 °C-sample, is in agreement with the observations at the other annealing temperatures. With longer annealing durations,  $T_{m,high}$  increased (Figure 2a), while  $T_{m,low}$  decreased (Figure 2b). Two distinct melting peaks were only observed at either higher temperatures ( $T_a \geq 48$  °C) or very long annealing periods. After annealing at  $T_a = 52$  °C, only one melting peak was observed in the heating scans. The slightly higher peak melting temperatures, compared to the CS, are expected to result from self-nucleation or self-seeding effects.<sup>31-33</sup>

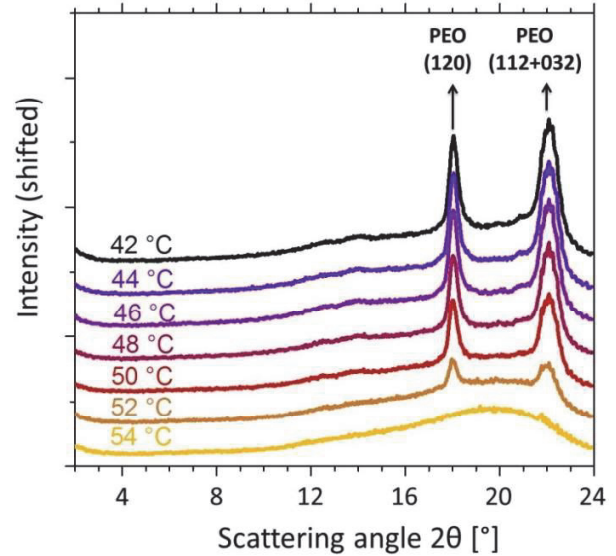


Figure 3. WAXS signals of B<sub>96</sub>EO<sub>90</sub> at temperatures between 42 and 54 °C. The PEO reflexes are systematically decreasing with increasing temperature. Complete melting of the PEO crystals is observed at temperatures of 54 °C and above.

Figure 2c shows the crystal thickness distributions of the CS and samples that were annealed between 10 min and 24 h, at  $T_a = 48$  °C. The results are based on Equation (1), applied to the DSC heating scans.<sup>26</sup> The crystal thickness distribution of the CS reveals a single maximum at 5.90 nm. Two distinct maxima were observed for the annealed samples. With increasing annealing periods, the maxima became more separated *i.e.* the thickness of the thinner crystals decreases, whereas it increases for the thicker crystals. The fractions of each species can be calculated from the integral of the corresponding peak in the distribution diagram. It was found that the fraction of the larger crystals is continuously increasing, being 75% after 10 min and 83% after 24 h at  $T_a = 48$  °C.

In Figure 2d, similar crystal thickness distributions are given for different  $T_a$ , after annealing for 24 h. A single maximum was observed for  $T_a = 52$  °C; two distinct distribution maxima can be found for  $42$  °C  $\leq T_a \leq 50$  °C. Both maxima shifted to larger crystal thicknesses with higher  $T_a$ . Further, the peak area is increasing for the lower crystal thickness peak and decreasing for larger crystal thicknesses. This indicates that larger crystal species are being formed with increasing  $T_a$ ; their respective fraction, however, is decreasing with  $T_a$ . The general thermal behavior of B<sub>96</sub>EO<sub>90</sub> points to a fractionation of the PEO chains during annealing within the melting range.<sup>34</sup>

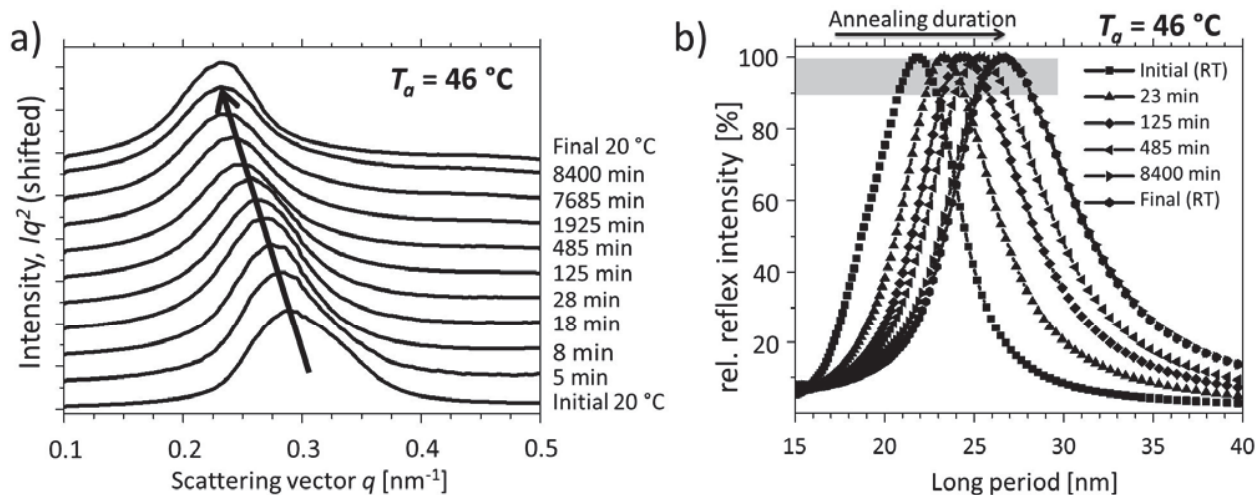


Figure 4. a) Exemplary presentation of SAXS curves at  $T_a = 46\text{ }^\circ\text{C}$  at different annealing durations  $t_a$ , which are provided on the right side of the graph. The curves are shifted for better visibility. b) Relative reflex intensity over the long-period at different  $t_a$ . The grey bar marks the region that is used to describe the long-period deviations.

### Wide-angle X-ray scattering

Figure 3 shows WAXS data at temperatures between 42 and 54 °C. Broad signals between 10 and 24° were observed in all samples investigated, which originate from diffuse scattering of amorphous regions.<sup>35</sup> Two distinct reflexes appeared for temperatures below 54 °C. The maxima of these reflexes were found at scattering angles of 18 and 22° and were attributed to the (120) and (112 + 032) reflections of the crystalline PEO, respectively.<sup>36</sup> The absolute value of the degree of crystallinity is generally calculated from the different scattering contributions of the crystalline and amorphous phases.<sup>37</sup> Unfortunately, it was difficult to accurately estimate the correct degree of crystallinity in this case, since the angular range of the scattered angles did not cover the whole range of the amorphous halo, which leads to an overestimation of the degree of crystallinity within the samples. Thus, only the change of the relative degree of crystallinity can be discussed, which is based on the peak areas of the different crystalline reflexes.

The degree of crystallinity of B<sub>96</sub>EO<sub>90</sub> annealed at 42 °C is similar to the one obtained at room temperature (data not shown). At 44 and 46 °C, the relative degree of crystallinity is slightly decreasing to 90% of its original value. Distinctly lower values were observed above 46 °C, being 80%, 67% and 22% for 48 °C, 50 °C and 52 °C, respectively. At 54 °C, the reflexes from the PEO crystals were absent. This is a clear indication that the PEO crystals were completely molten at this temperature.<sup>37</sup>

### Small-angle X-ray scattering

Results of the SAXS experiments are given in the Figures 4 to 6. The curves of the crystalline standard (CS) and selected curves after different annealing periods  $t_a$  at the annealing temperature  $T_a = 46\text{ }^\circ\text{C}$  are shown in Figure 4. The scattering curve of the CS shows a maximum at  $q^* = 0.29\text{ nm}^{-1}$  at room temperature, which corresponds to an average long-period of  $l_p = 21.9\text{ nm}$ . During annealing at  $T_a = 46\text{ }^\circ\text{C}$ , the reflex maximum decreased, which points to an increasing  $l_p$  for longer  $t_a$ . After cooling to room temperature, only minor changes in the SAXS pattern were observed. To describe the morphology development more appropriately, the long-

period distribution is plotted over the reflex intensity in Figure 4b.  $l_p$  increased from approximately 22 nm (CS) up to 27 nm (after  $\approx 140\text{ h}$ ). Although the Figures 4a and 4b contain in principle the same information, the data representation in Figure 4b is helpful to understand the subsequent analysis steps.

For the description of the morphological development during annealing it is not only necessary to provide information about the average long-period. The distribution of domain spacings in the system is important, too. In order to represent this distribution in dependence of  $T_a$ , additional values were extracted from the SAXS data at 90% of the relative reflex intensity. This is, firstly, depicted as a semi-transparent bar in Figure 4b for  $T_a = 46\text{ }^\circ\text{C}$ . Secondly, the deviation of the long-period is given as a deviation band around the average long-period for  $42\text{ }^\circ\text{C} \leq T_a \leq 54\text{ }^\circ\text{C}$  at different  $t_a$  in Figure 5.

The corresponding 2D-SAXS patterns are provided in Figure 6. At the start of each annealing experiment, all samples exhibited a CS morphology with  $l_p \approx 22\text{ nm}$ . Moreover, higher order reflexes were observed at  $2q^*$ ,  $3q^*$  and  $4q^*$ , which can also be found in Figure 6 (a, d, g and j) at  $q = 0.55\text{ nm}^{-1}$ ,  $0.85\text{ nm}^{-1}$  and  $1.05\text{ nm}^{-1}$ . Since all reflex positions are integer ratios of  $q^*$  (1:2:3), a lamellar morphology can be expected for this system in the CS state.<sup>38</sup>

The samples show a distinct orientation, as can be seen from the azimuthal dependence of the intensity in the 2D-SAXS data for selected samples in Figure 6 (left column). Calculating Herman's orientation parameter  $H$ ,<sup>39</sup> which is 0 for random orientation and 1 for perfect parallel orientation, yields values between  $0.1 \leq H \leq 0.4$  for the different initial states. Most probably, this depends on the sample position due to small differences in the local crystallization conditions during the establishment of the CS. Unfortunately, it is difficult to control the orientation of the CS morphology, which is formed in the cooling step during the creation of the crystalline standard. Therefore, we have to exclude the influence of the different initial orientations on the morphology development from our considerations.

After heating to  $T_a$ , larger long-periods were observed with increasing  $t_a$  for all  $T_a$  between 42 and 50 °C and decreasing long-periods were found at  $T_a = 52$  and 54 °C. From the characteristics

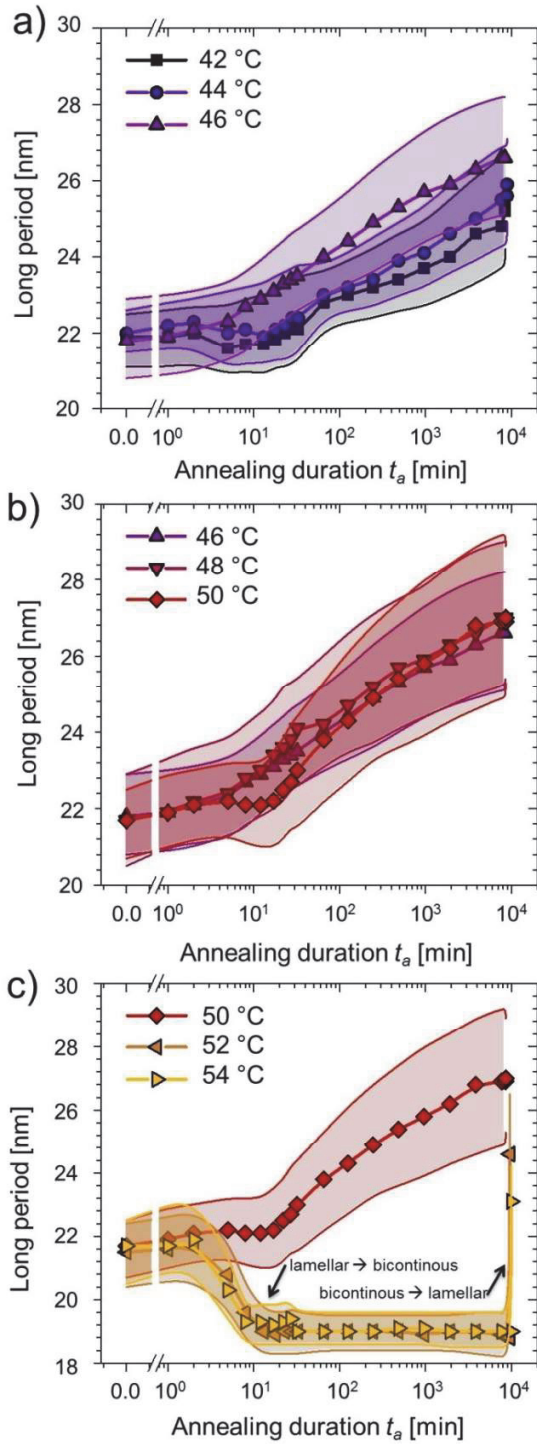


Figure 5. Average long-periods and deviation bands (90% of the reflex intensity) at different  $T_a$  and  $t_a$ . a) 42 to 46 °C, b) 46 to 50 °C and c) 50 to 54 °C.

in Figure 5, it is obvious that approximately 10 to 20 min are necessary to completely heat the sample through. This is expected to result from a non-ideal thermal contact and the low thermal conductivity of the sample. However, we expect only a minor influence of this warm-up period on the final morphology, since the samples were subjected to very long annealing times of up to 140 h. Between  $T_a = 42$  and 46 °C, the long-period growth is faster with in-

creasing  $T_a$ , as depicted in Figure 5a. Average long periods  $l_p$  of 25.2 nm, 25.6 nm and 26.6 nm were measured after  $8 \cdot 10^3$  min for 42, 44 and 46 °C, respectively.

The slightly different long-period growth rates may be explained by a higher chain flexibility and partly higher fraction of molten PEO chains that promote defect healing inside the PEO crystals. The long-period deviations were found to be relatively similar at  $\pm 1.4$  nm, which points to a uniform crystal thickening in this annealing region.

Figure 5b shows the long-period development for 46, 48 and 50 °C. In this annealing temperature region, almost similar long-period growth rates were observed, leading to average long-periods in the order of 27 nm after  $8 \cdot 10^3$  min (27.0 nm and 26.9 nm for 46, 48 and 50 °C, respectively). However, it is also found that the long-period deviations, as given by the 90% distribution band, significantly broaden from  $\pm 1.4$  nm, in the case of 46 °C, to  $\pm 2.0$  nm (48 °C) and  $\pm 2.3$  nm (50 °C) at higher  $T_a$ . These deviations indicate that the morphological development is less uniform compared to annealing between 42 and 46 °C.

At annealing temperatures  $T_a \geq 52$  °C (Figure 5c), the average long-period decreased already after the warm-up period of approximately 10 min. The observed long-period of 19 nm was constant until the sample was cooled to room temperature and the estimated deviations of  $\pm 0.6$  nm are significantly smaller compared to the other investigated  $T_a$ . Moreover, distinct higher-order reflexes were observed at  $T_a = 52$  and 54 °C, which are shown in the 2D-SAXS scattering pattern in the Figures 6h and 6k. Reflex positions are observed at  $q^* = 0.32 \text{ nm}^{-1}$ ,  $q = 0.67 \text{ nm}^{-1}$  and  $0.87 \text{ nm}^{-1}$ , having ratios of  $1 : \sqrt{4} : \sqrt{7}$ , which is typical for spherical, cylindrical as well as gyroid morphologies or hexagonal-perforated lamellae (HPL).<sup>38</sup> Obviously, the initially lamellar morphology transformed at temperatures  $\geq 52$  °C after sufficiently long  $t_a$ .

The volume fractions of PEO are in the order of 35 vol.% and, thus, close to the phase boundary between cylindrical and lamellar morphologies in diblock copolymers.<sup>40</sup> However, gyroid morphologies<sup>41, 42</sup> and HPL<sup>15, 43</sup> are also often observed in PEO containing BCPs. In Ref. 15, very similar scattering features compared to the obtained SAXS data were observed and these results were attributed to a HPL morphology. Therefore, we expect that  $B_{96}E_{90}$  transforms into a HPL morphology at  $T_a \geq 52$  °C. This phase transformation might also explain the decreasing long-periods during the experiment at  $T_a = 52$  and 54 °C. After cooling the samples back to room temperature, the integer higher-order reflexes indicate again the formation of a lamellar morphology, which points to a break-out crystallization of the PEO chains during cooling.<sup>44, 45</sup>

It is also interesting to note that a reflex at approximately  $q^* = 0.2 \text{ nm}^{-1}$  (long-periods of 31 nm) could be observed for the 52 °C-sample that emerges after approximately  $10^3$  min. This is highlighted in Figure 6h and indicates the co-existence of larger, thermodynamically stable PEO crystals with high melting points (Gibbs-Thomson effect).<sup>46</sup>

## DISCUSSION

Based on the DSC and SAXS investigations, three distinct annealing regimes were identified. (i) Between  $T_a = 42$  and 46 °C, a steady long-period growth of the CS long-period, reaching from 15%

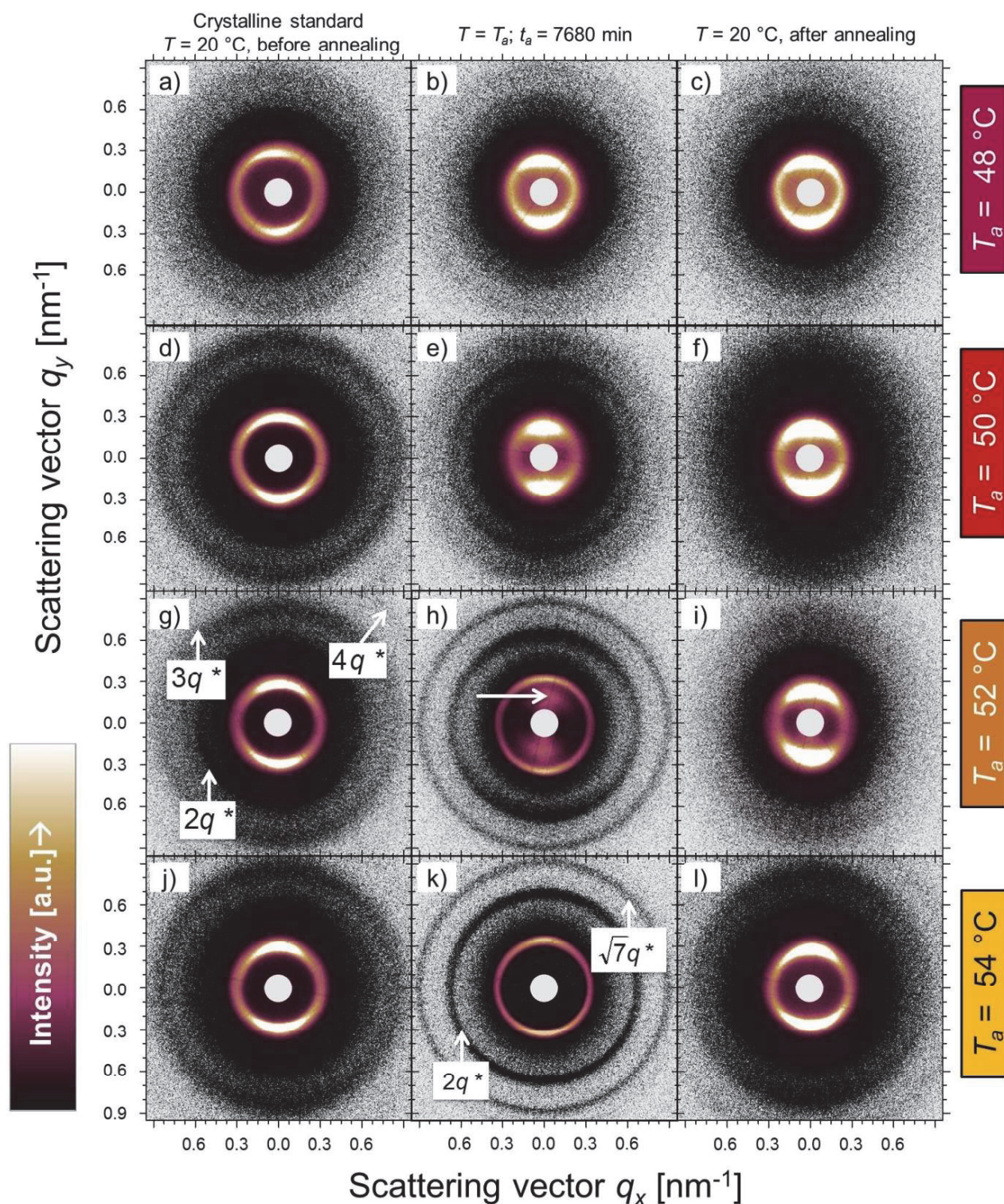


Figure 6. 2D-SAXS patterns of the initial morphology (left column), morphologies after  $t_a = 7680$  min at the annealing temperature  $T_a$  (center column) and after cooling to  $20\text{ }^\circ\text{C}$  (right column).  $T_a$  is denoted for each row on the right side. Samples annealed between  $42$  and  $46\text{ }^\circ\text{C}$  (not displayed) show similar features like the  $48\text{ }^\circ\text{C}$  measurement (a – c). The false color representation of the intensity is linearly scaled and similar for all images. Absent signals are displayed in light grey to enhance the visibility of the reflexes. The arrow in h) highlights the additional reflex at small scattering angles, as discussed in the text.

(42 °C) to 22% (46 °C) was observed. The deviation from the average long-period  $l_p$  was about  $\pm 1.4$  nm, as estimated by the deviation band. Within this regime, it is expected that different PEO crystal thicknesses and long-periods can be achieved in a defined manner. This is also supported by the DSC results, where only small fractions of  $B_{96}EO_{90}$  crystallized upon cooling, as indicated by the small shoulder at lower PEO thickness values in Figure 2d. Hence, it is assumed that the lamellae thickening in this temperature regime is dominated by defect healing of the PEO crystals, whereby the PEO chains become less folded, which increases  $l_p$ .<sup>12</sup>

(ii) Almost similar average long-periods of  $l_p \approx 27$  nm were found after annealing for approximately 140 h between 46 and 50 °C. This corresponds to an average increase of 22% compared to the CS. The deviations of  $l_p$  systematically increased with higher  $T_a$ . Further, a distinct second melting endotherm ( $T_{m,low}$ ) was observed after annealing at 50 °C (Figure 2b), which is particularly pronounced in annealing regime (ii). The observed area fractions of the high and low temperature melting peaks indicate that only 70% of the PEO chains form crystals with a higher thickness (Figure 2d). Thus, it can be concluded that, on the one hand, shorter chains will be excluded from the thicker PEO crystals and will crystallize independently during cooling. On the other hand, the thermal energy is high enough to form even higher PEO crystal thicknesses, which is revealed by the additional broadening of the SAXS reflex towards lower scattering angles as well as a broad crystal distribution of the higher melting species. This behavior can be described as thermal fractionation of the PEO chains, which prevails in this annealing regime.<sup>16</sup>

(iii) In the third regime, found above 52 °C for  $B_{96}EO_{90}$ , the initially crystalline fractions of the PEO block are almost completely molten, as indicated by WAXS measurements in Figure 3. Similar trends were observed in the DSC trace for the 52 °C sample, where only a single melting endotherm was observed, having an enthalpy of approximately 115 J/g, which is close to the value of the CS (124 J/g). Further, the melting enthalpy was independent of  $t_a$ . In this regime, the development of structure and morphology is expected to be determined by the crystallizing conditions and self-nucleation effects,<sup>31</sup> rather than the annealing duration, since the morphology is being re-written during the cooling step, due to break-out crystallization from the presumably HPL (melt) to a lamellar morphology (solid).

However, it should be emphasized that lamellae thickening at  $T_a = 52$  °C was observed, despite the low crystalline fractions. This is indicated by the formation of the reflex at very small scattering angles ( $l_p \approx 31$  nm, increase of 40%), as highlighted in Figure 6h. Three facts point to lamellae thickening in this case, rather than the formation of a second phase due to melting of the PEO crystallites. First, the HPL morphology exhibits a smaller  $l_p$  (19.0 nm) compared to the CS (21.9 nm, Figure 5c). Therefore, the chains either have to stretch to obtain a long-period of  $l_p \approx 31$  nm, which is thermodynamically unfavorable, or they are present in the crystalline state. Second, there are still some residual crystals at this annealing temperature, as shown by the temperature dependent WAXS-investigations (Figure 3). Hence, crystalline regions exist within  $B_{96}EO_{90}$  at this temperature. The third point can be derived from the orientation of the observed reflex (Figure 6h), which is similar to that of the CS (Figure 6g). Thus, the scattering entities of the

reflex at small angles are expected to originate from the already present crystals in the CS. Unfortunately, the used X-ray setup prevented the investigation of smaller scattering angles, which might give a hint of the existence of less folded or extended chain species within the annealed samples.

**Table 1. Comparison between PEO domain spacings (SAXS) and crystalline lamellae thickness (DSC) after 24 h annealing.**

$T_a$ [°C]	SAXS		DSC (CM-model)
	$l_0$ [nm] <sup>a)</sup>	$l_{PEO}$ [nm] <sup>b)</sup>	$l_{PEO,c}$ (avg.) [nm] <sup>c)</sup>
CS	21.9 ± 1.2	7.8	5.9
42	23.9 ± 1.4	8.5	7.0
44	24.4 ± 1.3	8.6	7.3
46	25.8 ± 1.7	9.1	7.2
48	26.1 ± 2.1	9.2	7.6
50	26.1 ± 2.2	9.2	8.0

a) Calculated from equation (2), error from 90% of reflex height.

b) Calculated from equation (3).

c) Estimated from crystal thickness distribution peak maxima, weighted by the respective area fractions.

Another important point is the estimation of the PEO domain size and the crystal thickness distribution. This can be calculated from the obtained long-periods in SAXS and volume fraction of the PEO. For the crystalline standard, this yields a PEO domain size ( $l_{PEO}$ ) of approximately 7.8 nm, which is in fair agreement to our observations in the AFM (data not shown). The calculation of the PEO crystal thickness ( $l_{PEO,c}$ ), which is based on the DSC measurements, yields average values of 5.9 nm for CS. The differences between the SAXS and DSC based results presumably originate from the presence of amorphous regions, which are included in the results from SAXS, but not in the DSC based crystal thickness distribution. An overview of the calculated long-periods  $l_p$  and domain spacings after annealing for 24 h at different  $T_a$  is provided in Table 1. There,  $l_{PEO}$  was estimated according to equation (3) and the crystalline lamellae thickness of PEO ( $l_{PEO,c}$ ) was calculated from the crystal thickness distributions, multiplied by the area fraction of respective peaks in Figure 2d. Although the results are quite plausible, there are some approximations carried out within the CM-model, which shall be briefly discussed in the following.

The CM-model is based on the approach of Gibbs-Thomson, which was originally developed for high molar mass homopolymers, rather than low molar mass diblock copolymers, as employed in this study. For the calculation, we used a modification of  $T_m^0$  for PEO, which has a similar molar mass compared to the PEO block in  $B_{96}EO_{90}$ , as proposed by Buckley and Kovacs<sup>29</sup> ( $T_{m,corr}^0$ ). Hence, the influence of the lower molar mass is considered in this model. However, contributions of the covalently attached PB block are not incorporated. It is generally accepted that the presence of a second block affects the surface energy of the PEO crystal. Further, Gido and co-workers discussed that the equilibrium chain configuration of the PEO differs from the extended chain in confined BCPs.<sup>14</sup> Both, the altered crystal surface energy and the modified chain

configuration would directly affect the relation between the melting temperature and the crystal thickness and, hence, shift the distribution curves in the Figures 2c and 2d. However, the (non)-existence of extended chain species in semi-crystalline block copolymers is still controversially debated. Other studies demonstrated the existence of extended (PEO chain defines the thickness of the PEO domain) and double-extended PEO chains (two consecutively arranged, extended PEO chains define the PEO domain size) in PB-*b*-PEO by AFM.<sup>10,11</sup> This more fundamental question cannot be answered within the scope of this contribution. From the presented results, however, it is obvious that the modified CM-model is suitable to describe the mechanism of crystalline lamellae thickening by defect healing or thermal fractionation of the PEO chains. Thus, the crystal thickness distribution provides a valuable tool to describe the mechanism of the PEO domain growth. However, great care should be taken with the absolute values of the calculated crystal thicknesses, due to approximations in the applied model and its sensibility on the employed  $T_{m,corr}^0$ . Hence, it is essential that complementary SAXS investigations are carried out to obtain information about the absolute spacings and the kinetics of their development during annealing, directly from the experiment.

## CONCLUSIONS AND OUTLOOK

The kinetics of the lamellae thickening during annealing in the melting region of B<sub>96</sub>EO<sub>90</sub>, which has a previously defined morphology, was investigated by time and temperature dependent DSC and SAXS measurements. The SAXS data provide information about the kinetics of the long-period growth of the system, whereas the melting endotherms of the DSC measurements were correlated to the thickness values of the crystalline PEO lamellae, by applying a modified Gibbs-Thomson approach (CM-model).<sup>26</sup> Three distinct annealing regimes were identified, which are either dominated by (i) defect healing, (ii) thermal fractionation or (iii) melting and self-nucleation.

The thickest species, having a long-period of approx. 31 nm, was observed at an annealing temperature of 52 °C, firstly visible after an annealing period of 24 h. This increased long-period corresponds to a relative long-period growth of 40% compared to the initial crystalline standard.

However, up to now, it is necessary to anneal such samples in regime (i) in order to have a controlled crystal thickening. Nevertheless, the long-period growth of up to 40% is promising for future applications, since it offers a wide scope of achievable spacings without increasing the block copolymers degree of polymerization. There is a strong demand to understand the underlying ordering kinetics, to perform the morphological development in a controlled manner. Future studies should, therefore, investigate the effect of the cooling rate after thermal treatment within the annealing regime (ii). Additional interesting issues are the chain dynamics and crystal thickening in highly oriented samples as well as studies on block copolymer systems with more than one crystallizable block. The presented time- and temperature-dependent SAXS and DSC investigations as well as the application of the modified CM-model and long-period deviation bands, to describe the respective data, offer suitable tools to study the morphological development and lamellae thickening mechanism of such crystallizable block copolymer systems.

## ASSOCIATED CONTENT

### SUPPORTING INFORMATION

Derivation of the applied model to describe the crystal thickness distributions from the DSC heating scans. This material is available free of charge via the Internet at <http://pubs.acs.org>.

### AUTHOR INFORMATION

#### Corresponding Authors

\* E-mail: [ulrich.schubert@uni-jena.de](mailto:ulrich.schubert@uni-jena.de); Phone: +49 3641 94 8201; Fax: +49 3641 948202 (U. S. S.).

\* E-mail: [kjandt@uni-jena.de](mailto:kjandt@uni-jena.de); Phone: +49 3641 94 7730; Fax +49 3641 94 77 32 (K. D. J.).

### ACKNOWLEDGMENT

F. H. S. and U. S. S. are grateful to the Thuringian Ministry for Education, Science, and Culture (TMBWK; #B515-11028, SWAXS-JCSM) for financial support. R. S., T. N. B. and K. D. J. gratefully acknowledge the financial support of the Carl-Zeiss Foundation for a postdoctoral stipend.

### REFERENCES

- (1) A. Biswas, I. S. Bayer, A. S. Biris, T. Wang, E. Dervishi, F. Faupel, *Adv. Colloid. Interfac.* **2012**, *170*, 2-27.
- (2) S. B. Darling, *Prog. Polym. Sci.* **2007**, *32*, 1152-1204.
- (3) A. Katsuhiko, P. H. Jonathan, V. L. Michael, V. Ajayan, C. Richard, A. Somobrata, *Sci. Tech. Adv. Mater.* **2008**, *9*, 014109.
- (4) B. Nandan, B. K. Kuila, M. Stamm, *Eur. Polym. J.* **2011**, *47*, 584-599.
- (5) J. N. L. Albert, T. H. Epps III, *Mater. Today* **2010**, *13*, 24-33.
- (6) F. S. Bates, G. H. Fredrickson, *Annu. Rev. Phys. Chem.* **1990**, *41*, 525-557.
- (7) I. W. Hamley, *Prog. Polym. Sci.* **2009**, *34*, 1161-1210.
- (8) W.-N. He, J.-T. Xu, *Prog. Polym. Sci.* **2012**, *37*, 1350-1400.
- (9) E. Ostas, K. Schröter, M. Beiner, T. Z. Yan, T. Thurn-Albrecht, W. H. Binder, *J. Polym. Sci. A Polym. Chem.* **2011**, *49*, 3404-3416.
- (10) R. Schulze, M. M. L. Arras, G. Li Destri, M. Gottschaldt, J. Bossert, U. S. Schubert, G. Marletta, K. D. Jandt, T. F. Keller, *Macromolecules* **2012**, *45*, 4740-4748.
- (11) R. Schulze, M. M. L. Arras, C. Helbing, S. Hölzer, U. S. Schubert, T. F. Keller, K. D. Jandt, *Macromolecules* **2014**, *47*, 1705-1714.
- (12) G. Reiter, G. Castelein, P. Hoerner, G. Riess, J. -U. Sommer, G. Floudas, *EPJE* **2000**, *2*, 319-334.
- (13) H.-L. Chen, J.-C. Wu, T.-L. Lin, J. S. Lin, *Macromolecules* **2001**, *34*, 6936-6944.
- (14) S. Hong, L. Yang, W. J. MacKnight, S. P. Gido, *Macromolecules* **2001**, *34*, 7009-7016.
- (15) D. M. Lambrea, R. Opitz, G. Reiter, P. M. Frederik, W. H. de Jeu, *Polymer* **2005**, *46*, 4868-4875.
- (16) R. V. Castillo, M. L. Arnal, A. J. Müller, I. W. Hamley, V. Castelletto, H. Schmalz, V. Abetz, *Macromolecules* **2008**, *41*, 879-889.
- (17) A. T. Lorenzo, M. L. Arnal, A. J. Müller, M.-C. Lin, H.-L. Chen, *Macromol. Chem. Phys.* **2011**, *212*, 2009-2016.
- (18) B. Fillon, J. C. Wittmann, B. Lotz, A. Thierry, *J. Polym. Sci. Part B Polym. Phys.* **1993**, *31*, 1383-1393.
- (19) A. J. Müller, V. Balsamo, M. L. Arnal, *Adv. Polym. Sci.* **2005**, *190*, 1-63.
- (20) A. J. Müller, A. T. Lorenzo, M. L. Arnal, A. B. de Fierro V. Abetz, *Macromol. Symp.* **2006**, *240*, 114-122.
- (21) G. Ungar and X.-b. Zeng, *Chem. Rev.* **2001**, *101*, 4157-4188.
- (22) S. Z. D. Cheng, B. Lotz, *Philos. Trans. R. Soc. London, Ser. A* **2003**, *361*, 517-537.

- (23) S. Z. D. Cheng, A. Zhang, J. Chen, D. P. Heberer, *J. Polym. Sci. Part B Polym. Phys.* **1991**, 29, 287-297.
- (24) S. Z. D. Cheng, J. Chen, *J. Polym. Sci. Part B Polym. Phys.* **1991**, 29, 311-327.
- (25) B. Lotz, A. J. Kovacs, G. A. Bassett, A. Keller, *Kolloid. Z. Z. Polym.* **1966**, 209, 115-128.
- (26) B. Crist, F. M. Mirabella, *J. Polym. Sci. Part B Polym. Phys.* **1999**, 37, 3131-3140.
- (27) B. Crist, P. R. Howard, *Macromolecules* **1999**, 32, 3057-3067.
- (28) F. Spieckermann, H. Wilhelm, M. Kerber, E. Schafler, G. Polt, S. Bernstorff, F. Addiego, M. Zehetbauer, *Polymer* **2010**, 51, 4195-4199.
- (29) C. P. Buckley, A. J. Kovacs, *Colloid. Polym. Sci.* **1976**, 254, 695-715.
- (30) C. A. Schneider, W. S. Rasband, K. W. Eliceiri, *Nat. Meth.* **2012**, 9, 671-675.
- (31) A. J. Müller, V. Balsamo, M. L. Arnal, T. Jakob, H. Schmalz, V. Abetz, *Macromolecules* **2002**, 35, 3048-3058.
- (32) L. Zhu, P. Huang, W. Y. Chen, Q. Ge, R. P. Quirk, S. Z. D. Cheng, E. L. Thomas, B. S. Hsiao, F. J. Yeh, L. Z. Liu, *Macromolecules* **2002**, 35, 3553-3562.
- (33) A. T. Lorenzo, M. L. Arnal, J. J. Sánchez A. J. Müller, *J. Polym. Sci. Part B Polym. Phys.* **2006**, 44, 1738-1750.
- (34) A. J. Müller and M. L. Arnal, *Prog. Polym. Sci.* **2005**, 30, 559-603.
- (35) N. Stribeck, *X-ray scattering of soft matter*, Springer, **2007**.
- (36) L. Zhu, S. Z. D. Cheng, B. H. Calhoun, Q. Ge, R. P. Quirk, E. L. Thomas, B. S. Hsiao, F. Yeh, B. Lotz, *J. Am. Chem. Soc.* **2000**, 122, 5957-5967.
- (37) C. Vonk, *J. Appl. Crystallogr.* **1973**, 6, 148-152.
- (38) N. Hadjichristidis, S. Pispas, G. Floudas, *Block Copolymers: Synthetic Strategies, Physical Properties, and Applications*, John Wiley & Sons Inc., **2003**.
- (39) U. Gedde, *Polymer Physics*, Springer, **1995**.
- (40) M. Matsen, F. S. Bates, *Macromolecules* **1996**, 29, 1091-1098.
- (41) M. W. Hamersky, M. A. Hillmyer, M. Tirrell, F. S. Bates, T. P. Lodge, E. D. von Meerwall, *Macromolecules* **1998**, 31, 5363-5370.
- (42) W. Cao, K. Tashiro, H. Masunaga, S. Sasaki, M. Takata, *J. Phys. Chem. B* **2009**, 113, 8495-8504.
- (43) L. Li, Y. Séréro, M. H. J. Koch, W. H. de Jeu, *Macromolecules* **2003**, 36, 529-532.
- (44) C. Vasilev, G. Reiter, S. Pispas, N. Hadjichristidis, *Polymer* **2006**, 47, 330-340.
- (45) A. M. Mihut, A. Chiche, M. Drechsler, H. Schmalz, E. Di Cola, G. Krausch, M. Ballauff, *Soft Matter* **2009**, 5, 208-213.
- (46) G. W. H. Höhne, *Polymer* **2002**, 43, 4689-4698.



## Supporting information

### Morphological Development of Poly(butadiene)-*block*-poly(ethylene oxide) during Annealing within the Melting Range: Mechanisms and Kinetics

Stefan Hölzer,<sup>a</sup> Tobias N. Büttner,<sup>b</sup> Robert Schulze,<sup>b</sup> Matthias M. L. Arras,<sup>b</sup> Felix H. Schacher,<sup>a,c</sup> Klaus D. Jandt<sup>\*b,c</sup> and  
Ulrich S. Schubert<sup>\*a,c</sup>

<sup>a</sup> Laboratory of Organic and Macromolecular Chemistry (IOMC),

Friedrich Schiller University Jena, Humboldtstraße 10, 07743 Jena, Germany

<sup>b</sup> Chair of Materials Science (CMS), Otto Schott Institute of Materials Research (OSIM),

Friedrich Schiller University Jena, Löbdergraben 32, 07743 Jena, Germany

<sup>c</sup> Jena Center for Soft Matter (JCSM), Friedrich Schiller University Jena, Philosophenweg 7, 07743 Jena, Germany

\* Corresponding authors:

E-mail [ulrich.schubert@uni-jena.de](mailto:ulrich.schubert@uni-jena.de); [k.jandt@uni-jena.de](mailto:k.jandt@uni-jena.de)

#### Derivation of the model to calculate the crystal thickness from the DSC heating scans

During a heating run in a DSC the heat flow  $P(T)$  into the sample that is necessary to maintain the same temperature in both, the reference and the sample pan, is measured. To melt (polymer) crystals requires enthalpy of fusion and, thus, the heat flow, which can be attributed to the crystalline part of the sample  $P_c(T)$  increases.  $P_c(T)$  can be calculated from the measured heat flow  $P(T)$  by subtraction of a baseline related to the heat capacity of the amorphous parts  $P_a(T)$ :<sup>S1</sup>

$$P_c(T) = P(T) - P_a(T) \quad (\text{S1})$$

In the following, a relation between the endothermic heat flow  $P(T)$  as measured by the DSC during a heating run and the thickness of the PEO crystals  $l_{\text{PEO},g}$  which melt during this procedure, is established. For simplicity, but deviating from the main manuscript, the thickness of the PEO crystals will be referred to as  $l \equiv l_{\text{PEO},c}$  throughout this derivation.

The weight fraction of PEO crystals with a thickness between  $l$  and  $(l + dl)$  is denoted by  $g(l)dl$ . During the heating run, these PEO crystals melt in the yet unknown temperature interval  $dT$ . This fraction of crystals that melt between  $T$  and  $(T + dT)$  is denoted by  $f(T)dT$ , thus:

$$f(T)dT = g(l)dl \quad (\text{S2})$$

It is the crystal thickness distribution  $g(l)$  which is of interest:

$$g(l) = f(T) \frac{dT}{dl} \quad (S3)$$

In a DSC experiment, our polymer of mass  $m$  was heated with a constant heating rate  $(dT/dt) = 10^\circ\text{C}/\text{min}$ . The fraction of PEO crystals, which melts between  $T$  and  $(T + dT)$  can be expressed by:<sup>S2</sup>

$$f(T)dT = \frac{P_c(T)}{\left(\frac{dT}{dt}\right)} \cdot \frac{1}{m\alpha_M\Delta h_m^0} dT \quad (S4)$$

Here,  $\alpha_M$  is the mass fraction crystallinity of the whole sample;  $\Delta h_m^0$  is the heat of fusion of the completely crystalline polymer. The term  $\frac{P_c(T)}{dT/dt}$  can be understood as the energy absorbed by the crystals per Kelvin. The second term in equation (S4) denotes how much energy is necessary to melt the crystals. Here,  $\alpha_M$  normalizes the distribution. Combining equation (S3) and (S4), the crystal thickness distribution  $g(l)$  can be re-written as:

$$g(l) = \frac{P_c(T)}{\left(\frac{dT}{dt}\right)} \cdot \frac{1}{m\alpha_M\Delta h_m^0} \cdot \frac{dT}{dl} \quad (S5)$$

Thus, the remaining unknown term is how  $T$  depends on the thickness  $l$  of the crystal. In the original model of Crist and Mirabella,<sup>S2</sup> the Gibbs-Thomson equation (S6) was applied to describe the  $(dT/dl)$ . Equation (S6) relates the melting temperature  $T = T_m$  of a lamellar high molar mass polymer crystal to its thickness  $l$ . It further depends on known polymer specific constants: The surface energy  $\sigma_e$  of the crystals folding plane, the enthalpy of fusion of the completely crystalline polymer  $\Delta h_m^0$ , the density of the PEO  $\rho_c$  crystal and the melting temperature of an infinitely thick lamellar crystal with an infinitely high molar mass  $T_m^0$ . Details of the used constants and variables are provided in Table S1.

$$T = T_m^0 \left( 1 - \frac{2\sigma_e}{\rho_c \cdot \Delta h_m^0 \cdot l} \right) \quad (S6)$$

Due to the fact that the Gibbs-Thomson equation is only valid for high molar mass polymers, this equation is not readily applicable to be used with B<sub>96</sub>EO<sub>90</sub>, since it is a very low molar mass polymer. Therefore, in the present case the refined model of Buckley and Kovacs<sup>S3</sup> was used to describe the relation of melting temperature  $T_m$  and crystal thickness  $l$  for low molar mass PEO under the following additional assumption: The surface energy  $\sigma_e$  is independent from the temperature and has a constant value, *i.e.*  $\sigma_e$  does not depend

**Table S1. Constants used in this supplementary information**

Symbol	Description	Value	Ref.
$\rho_c$	Density of the crystalline PEO phase	1.23 g/cm <sup>3</sup>	S4
$\Delta h_m^0$	Melting enthalpy of completely crystalline PEO	196.4 J/g	S3
$\sigma_e$	Surface energy of the crystals at the folding plane	22.43 mJ/m <sup>2</sup>	S3
$T_m^0$	Melting temperature of an infinitely thick lamellar PEO crystal	68.9 °C	S3
$T_{m,corr}^0$	$T_m^0$ , corrected for lower molar mass PEO	61.75 °C	here
$N$	Degree of polymerization of the PEO block (B <sub>96</sub> EO <sub>90</sub> )	90	here

on the chain folding condition of the lamellar crystal. Then, the PEO crystal thickness  $l$  can be related to its melting temperature  $T_m$  by:

$$T = \frac{T_m^0}{1 + \frac{\ln N}{N} \cdot \frac{RT_m^0}{\Delta h_m^0}} \left( 1 - \frac{2\sigma_e}{\rho_c \cdot \Delta h_m^0 \cdot l} \right) \quad (S7a)$$

The first term of equation (S7a) contains the degree of polymerization  $N = 90$  and the gas constant  $R$ . The denominator of this term serves as a scaling factor for  $T_m^0$ , which accounts for low molar mass polymers and will be renamed as  $T_{m,corr}^0$ :

$$T_{m,corr}^0 = \frac{T_m^0}{1 + \frac{\ln N}{N} \cdot \frac{RT_m^0}{\Delta h_m^0}} \quad (S7b)$$

The similarity of the equation according to Buckley and Kovacs<sup>S3</sup> (S7c) to the original Gibbs-Thomson equation (S6) becomes apparent:

$$T = T_{m,corr}^0 \left( 1 - \frac{2\sigma_e}{\rho_c \cdot \Delta h_m^0 \cdot l} \right) \quad (S7c)$$

This modified equation is used to determine the unknown term  $(dT/dl)$  in equation (S5) to describe the crystal thickness distribution  $g(l)$ :

$$\frac{dT}{dl} = \frac{d}{dl} \left( T_{m,corr}^0 \cdot \left( 1 - \frac{2\sigma_e}{\rho_c \cdot \Delta h_m^0 \cdot l} \right) \right) = \frac{T_{m,corr}^0 \cdot 2\sigma_e}{\Delta h_m^0 \cdot l^2} \quad (S8)$$

Inserting equation (S8) into equation (S5) leads to equation (S9), which describes the PEO crystal thickness distribution  $g(l)$ :

$$g(l) = \frac{P_c(T)}{\left(\frac{dT}{dt}\right)} \cdot \frac{T_{m,corr}^0 \cdot 2\sigma_e}{\rho_c \cdot m \cdot a_m (\Delta h_m^0)^2} \cdot \frac{1}{l^2} \quad (S9a)$$

Solving the modified Gibbs-Thomson equation (S7c) for  $l$ , the crystal thickness  $l$  can be described as a function of the respective melting temperature  $T_m$  which is observed in during DSC. Thus equation (S9a) can be re-written as:

$$g(l) = \frac{P_c(T)}{\left(\frac{dT}{dt}\right)} \cdot \frac{T_{m,corr}^0 \cdot 2\sigma_e}{\rho_c \cdot m \cdot a_m (\Delta h_m^0)^2} \cdot \left( \frac{\rho_c \cdot \Delta h_m^0 \cdot (T_{m,corr}^0 - T)}{2 \cdot T_{m,corr}^0 \cdot \sigma_e} \right)^2 \quad (S9b)$$

After reducing equation (S9b),  $g(l)$  can be denoted as

$$g(l) = K \cdot P_c(T) \cdot (T_{m,corr}^0 - T)^2 \quad (S10a)$$

with

$$K = \frac{\rho_c \cdot}{2\sigma_e \cdot T_{m,corr}^0 \cdot m \cdot a_m \cdot \left(\frac{dT}{dt}\right)} \quad (S10b)$$

Here, the factor  $K$  is a normalizing constant, which is calculated by numerical integration. By integration and transposing of equation (S9b) the factor  $K$  can be reduced to known constants:

$$K = \frac{1 \cdot \Delta h_m^0}{2\sigma_e \cdot T_{m,corr}^0 \cdot m \cdot \int_0^{T_{m,corr}^0} P_c(T) dT} \quad (S10c)$$

For the calculation of  $K$  the density of the crystalline PEO phase  $\rho_c = 1.23 \text{ g/cm}^3$ , the enthalpy of fusion of the completely crystalline PEO,  $\Delta h_m^0 = 196.4 \text{ J/g}$  and the surface energy of the crystals at the folding plane  $\sigma_e = 22.43 \text{ mJ/m}^2$  were used as PEO specific constants.<sup>S3</sup>

## References:

- S1 B. Wunderlich, *Thermal Analysis of Polymeric Materials*, Springer, **2005**.  
 S2 B. Crist and F. M. Mirabella, *J. Polym. Sci. Part B Polym. Phys.*, **1999**, 37, 3131-3140.  
 S3 C. P. Buckley and A. J. Kovacs, *Colloid. Polym. Sci.*, **1976**, 254, 695-715.

## Accepted Manuscript

Mechanisms and Kinetics of the Crystal Thickening of Poly(butadiene)-*block*-poly(ethylene oxide) during Annealing within the Melting Range

Stefan Hölzer, Tobias N. Büttner, Robert Schulze, Matthias M.L. Arras, Felix H. Schacher, Klaus D. Jandt, Ulrich S. Schubert

PII: S0014-3057(15)00226-8

DOI: <http://dx.doi.org/10.1016/j.eurpolymj.2015.04.010>

Reference: EPJ 6872

To appear in: *European Polymer Journal*

Received Date: 8 March 2015

Revised Date: 9 April 2015

Accepted Date: 10 April 2015

Please cite this article as: Hölzer, S., Büttner, T.N., Schulze, R., Arras, M.M.L., Schacher, F.H., Jandt, K.D., Schubert, U.S., Mechanisms and Kinetics of the Crystal Thickening of Poly(butadiene)-*block*-poly(ethylene oxide) during Annealing within the Melting Range, *European Polymer Journal* (2015), doi: <http://dx.doi.org/10.1016/j.eurpolymj.2015.04.010>

This is a PDF file of an unedited manuscript that has been accepted for publication. As a service to our customers we are providing this early version of the manuscript. The manuscript will undergo copyediting, typesetting, and review of the resulting proof before it is published in its final form. Please note that during the production process errors may be discovered which could affect the content, and all legal disclaimers that apply to the journal pertain.



# Mechanisms and Kinetics of the Crystal Thickening of Poly(butadiene)-*block*-poly(ethylene oxide) during Annealing within the Melting Range.

*Stefan Hölzer,<sup>a</sup> Tobias N. Büttner,<sup>b</sup> Robert Schulze,<sup>b</sup> Matthias M. L. Arras,<sup>b</sup> Felix H. Schacher,<sup>a,c</sup> Klaus D. Jandt<sup>\*b,c</sup> and Ulrich S. Schubert<sup>\*a,c</sup>*

<sup>a</sup> Laboratory of Organic and Macromolecular Chemistry (IOMC), Friedrich Schiller University Jena, Humboldtstraße 10, 07743 Jena, Germany.

<sup>b</sup> Chair of Materials Science (CMS), Otto Schott Institute of Materials Research (OSIM), Friedrich Schiller University Jena, Löbdergraben 32, 07743 Jena, Germany.

<sup>c</sup> Jena Center for Soft Matter (JCSM), Friedrich Schiller University Jena, Philosophenweg 7, 07743 Jena, Germany.

## Corresponding Authors

\* E-mail: [ulrich.schubert@uni-jena.de](mailto:ulrich.schubert@uni-jena.de); Phone: +49 3641 94 8201;  
Fax: +49 3641 948202 (U. S. S.).

\* E-mail: [k.jandt@uni-jena.de](mailto:k.jandt@uni-jena.de); Phone: +49 3641 94 7730;  
Fax +49 3641 94 77 32 (K. D. J.).

KEYWORDS: block copolymer; morphology; crystallization; self-nucleation; Gibbs-Thomson

Highlights:

- The long-period of PB-*b*-PEO can be tailored by controlled annealing.
- We studied the underlying mechanisms and kinetics by *t*-*T*-SAXS and DSC.
- Three different annealing regimes were identified.

### Abstract

Self-assembled nanostructures of crystallizable block copolymers can be tuned by controlled crystal thickening during annealing. In this contribution, we present a strategy, based on time- and temperature-dependent DSC, SAXS and WAXS measurements, which enables to study, both, the mechanisms and kinetics of crystal thickening and the respective morphological development, exemplarily discussed for the soft-confined PB-*b*-PEO block copolymer. Thereby, DSC based PEO crystal thickness distributions yield qualitative information about the mechanisms during annealing. Conclusions on the kinetics and the absolute long-period growth due to crystal thickening can be drawn from the time- and temperature dependent SAXS investigations, by calculating the average long-period and its deviations from the SAXS reflection position and shape, respectively. By this combined study, three annealing regimes were observed. (i) At low annealing temperatures  $T_a$ , steady lamellae-thickening was found, due to defect healing of the PEO crystals. (ii) Thermal fractionation was observed at intermediate  $T_a$ , due to the exclusion of shorter PEO chains from the crystals. (iii) Annealing close to and above the peak melting temperature, self-nucleation of the molten PEO fractions dominates. The combination of the applied techniques provides deeper insights into the kinetics and ordering mechanisms of the controlled long-period growth by crystal thickening under variable confinements, which enables to tailor the morphology of the block copolymer within several nanometers, without changing the degree of polymerization.

## INTRODUCTION

The ever growing miniaturization of devices leads to an increasing demand of geometrically defined, highly-ordered nanostructures. Conventional top-down approaches, like lithographical techniques, are inherently limited by physical fundamentals and the high costs of the lithographical production tools.[1] Fortunately, highly ordered nanostructures can be formed by self-assembly of organic molecules such as block copolymers (BCPs).[2-5]

The chemical incompatibility of the different blocks in BCPs leads to microphase separation and the formation of nanostructured materials, which have different morphologies.[6, 7] Size and shape of the BCP morphology are defined by the degree of polymerization, the volume fraction of the blocks as well as the interactions between the constituting segments.[6, 7] Depending on the ability to crystallize, BCPs are categorized as amorphous or semi-crystalline.[8] The crystallization process can be interpreted as another influencing factor for the microphase separation. Understanding the mutual relation of the BCP morphology and the BCP crystallization is of great interest: on the one hand it provides new insight into the general polymer crystallization process under soft- or hard-confinement.[8, 9] On the other hand it represents an interesting tool to control the BCP morphology by defined isothermal crystallization from the melt or an annealing procedure of previously crystallized systems.[10, 11]

It should be noted that the process of crystal thickening and polymer crystallization strongly depends on the mobility of the polymer chain segments. The interested reader to this more fundamental research work might be referred to the works of Strobl [12] and Beiner [13].

Isothermal crystallization from the melt has been widely investigated for the amorphous-crystalline block copolymer polybutadiene-*block*-poly(ethylene oxide) (PB-*b*-PEO), where the PB phase imposes a soft confinement on the PEO crystallization.[11, 14-18] Consequently, the formation of PEO crystals occurs either within the confined PEO domains or overwrites the pre-



existing microphase separated domain structure (break-out crystallization).[16] Thickness and lateral dimensions of these PEO crystals depend on the crystallization process, *i.e.* the crystallization temperature  $T_c$  and duration.[11, 14-16] Reiter *et al.* observed larger spacings of the lamellar morphology with increasing  $T_c$  of a low molar mass PB-*b*-PEO. The different thickness values of the crystalline lamellae were explained by differently folded PEO chains.[14]

Another approach to control the morphology of PB-*b*-PEO is to anneal the sample within the melting range, after defining a crystalline standard (CS).[17-22] In particular, the works of Fillon *et al.* must be mentioned here, who, to the best of our knowledge, invented the self-nucleation approach.[20] Crystal thickening as well as partial and complete melting can be observed, depending on the respective annealing temperature.[17-20] Moreover, it was shown that the spacing of a thin film surface morphology of a low molar mass PB-*b*-PEO can be systematically increased by this approach.[11]

For potential applications, understanding the mechanisms and kinetics of the crystal thickening in soft confined BCPs is mandatory. The underlying mechanisms have been intensively studied on low molar mass homopolymers, which have been isothermally crystallized from the melt or solution.[23-26] Moreover, crystal thickening was investigated for amorphous-crystalline BCPs in bulk and thin films. [11, 14-16, 27] However, studies regarding lamellae thickening based on CS are rare and these investigations focus on the surface topology of the corresponding thin films.[10, 11]

Up to now, crystal thickening mechanisms and kinetics of amorphous-crystalline BCPs in the bulk are, to the best of our knowledge, not reported in the literature. Potential applications of tunable BCP nanostructures can be found in the fields of biomedicine, and -analytics, photonics or high density data storage. In particular in the fields of biomedicine and -analytics, these nanostructures are interesting for patterning purposes in order to investigate and control the protein adsorption on

the surface of biomaterials, which is a key factor for the development of next generation implants and biosensors.

In order to investigate the underlying crystal thickening mechanisms and kinetics, we propose a combination of differential scanning calorimetry (DSC) as well as temperature and time dependent X-ray scattering experiments for PB-*b*-PEO to investigate the development of structure and morphology within this system. In order to analyze the DSC data, we applied a modified model of Crist and Mirabella[28] (CM-model), which has frequently been used to describe the crystal lamellae thickness of polyolefins.[28-30] Average long-periods and their deviations are estimated by small-angle X-ray scattering (SAXS) from the first reflection  $q^*$  at 100% and 90% of the reflection intensity, respectively. This is followed by a critical discussion about the applicability and comparability of this strategy. The presented results on PB-*b*-PEO contribute to the understanding of BCP crystallization and are focused on the controlled formation and manipulation of self-assembled BCP nanostructures where crystalline segments are involved. Moreover, we offer a tool that enables the investigation of the mechanism and kinetics of the morphological development of such systems.

## EXPERIMENTAL

### Materials

The investigated PB-*b*-PEO was purchased from Polymer Source Inc. (Dorval, Canada). The PB block has a molar mass of  $M_n = 5200$  g/mol and a PDI value of 1.12, as given by the supplier. The molar mass of the PEO block was determined by  $^1\text{H-NMR}$  measurements to be  $M_n = 3960$  g/mol. The corresponding degrees of polymerization are 96 and 90 for the PB and the PEO block, respectively. Following the syntax of other investigations on this block copolymer system, this polymer will be named as B<sub>96</sub>EO<sub>90</sub>. The volume fraction of PEO in B<sub>96</sub>EO<sub>90</sub> is 35.4 vol.% at 20 °C.

### Differential scanning calorimetry

Differential scanning calorimetry (DSC) was carried out on a PerkinElmer Pyris 1 equipped with a thermal analysis controller 7/DX (PerkinElmer Inc., Waltham, MA). Heating and cooling rates were 10 °C/min for all measurements. The sample was kept for at least one minute at the final temperature after each heating/cooling step.

To create comparable sample conditions before each experiment, B<sub>96</sub>EO<sub>90</sub> was heated to 90 °C in the calorimeter, which is well above the peak melting temperature of the crystalline PEO block and erases the thermal history of the sample. Subsequently, the sample was cooled to 0 °C. This initial state is referred to as crystalline standard (CS) and had a peak crystallization temperature of  $T_c = 24.5$  °C and a peak melting temperature of  $T_m = 52.5$  °C. The degree of crystallinity of the PEO block for the CS was 66%, as determined by DSC.

After creating the CS, the sample was heated to the selected annealing temperature  $T_a$  between 42 and 52 °C, which is within the melting range of the PEO block. B<sub>96</sub>EO<sub>90</sub> was held for different annealing periods  $t_a$ , ranging from  $t_a = 10$  min to  $t_a = 24$  h and was subsequently cooled to 0 °C to crystallize the already molten parts of the polymer. Afterwards, the sample was heated again to 90 °C, which provides information about the thermal properties after the annealing procedure. A modified approach of Crist and Mirabella[28] (CM-model) was applied to correlate the DSC melting temperatures  $T_m$  with the thickness of the PEO crystals  $l_{\text{PEO},c}$ . Its dependence can be calculated by:

$$g(l_{\text{PEO},c}) = K \cdot P_c(T) \cdot (T_{m,\text{corr}}^0 - T)^2 \quad (1)$$

Here,  $g(l_{\text{PEO},c})$  is the distribution function of the PEO crystal thickness,  $K$  is a normalizing factor and  $P_c(T)$  is the heat flow of the crystalline PEO fractions, which can be estimated from the DSC heating scans.  $T_{m,\text{corr}}^0$  originates from  $T_m^0$ , which is a material constant, known from the Gibbs-Thomson equation and describes the melting temperature of an infinitely thick PEO crystal. The

correction of  $T_m^0$  for low molar mass PEO was carried out according to Buckley and Kovacs[31] for low molar mass PEO, which leads to  $T_{m,corr}^0 = 61.75$  °C. Details are given in the electronic supporting information.

### X-ray Scattering

Small- and wide angle X-ray scattering experiments (SAXS and WAXS) were carried out on a Bruker AXS Nanostar (Karlsruhe, Germany), equipped with (i) a microfocus copper X-ray source (Incoatec I $\mu$ SCu E025, Incoatec, Geesthacht, Germany), at a wavelength of  $\lambda = 0.154$  nm, (ii) a two-dimensional Bruker AXS VANTEC-2000 gas detector (Karlsruhe, Germany) and (iii) a temperature controller. The distances between sample and detector were 107 and 12 cm for the SAXS- and WAXS-setup, respectively, using silver behenate for calibration. Exposure times were between 1 min and 9 min for each SAXS measurement and 60 min for WAXS. The samples were placed in the drill hole (diameter 3 mm) of a metal sheet (10 x 5 x 1 mm<sup>3</sup>), which is used to mount the samples in the temperature controller unit of the SAXS/WAXS device. Prior to the morphological investigations, each sample was placed together with the metal plate in the calorimeter in order to establish the CS.

For the temperature-dependent WAXS experiments, the CS was heated from room temperature (RT) to 42 °C. The temperature was held for 20 min to ensure that the sample was completely heated through. After measuring for one hour, the temperature was increased by 2 °C. This procedure was repeated until the signals of the crystalline PEO vanished completely.

The data acquisition of each SAXS annealing procedure was carried out by (i) collecting an initial pattern at 20 °C, (ii) heating the sample up to the desired annealing temperature  $T_a$  between 42 and 54 °C, (iii) collecting patterns after several annealing periods (1 min to  $\approx 10^4$  min) at  $T_a$  and (iv) collecting a final pattern after cooling to 20 °C. The heating and cooling rates in the experiments were set to 10 °C/min and the maximum temperature deviations that were measured during annealing were  $\pm 0.2$  °C.

The scattering patterns were post-processed using ImageJ, an open source image processing software.[32] SAXS and WAXS patterns were converted into  $q$ -space ( $q = (4\pi/\lambda)\cdot\sin \theta$ ) and  $2\theta$ -space, respectively. Here,  $q$  is the scattering vector and  $2\theta$  is the scattering angle. All patterns were corrected regarding background scattering, normalized to the exposure time and rotated so that preferential orientations of the CS-patterns of each temperature series are located on the meridian. After azimuthal integration of the 2D-SAXS patterns, the average long-period  $l_p$ , which is the sum of the PB and the PEO domain size, of each SAXS sample was calculated from the maximum of the reflection  $q^*$  by:

$$l_p = 2\pi/q^* \quad (2)$$

To estimate the long-period distributions, additional values at a height of 90% of the  $q^*$  reflection were extracted. The corresponding spacings are interpreted as deviations from  $l_p$ . The domain spacings of each phase  $l_i$  can be calculated from  $l_p$  and the volume fractions  $f_i$ , where the subscript  $i$  stands for PB or PEO:[16]

$$l_i = l_p \cdot f_i \quad (3)$$

## RESULTS

### Differential scanning calorimetry

Exemplary cooling curves after annealing at  $T_a = 50$  °C and the subsequent heating curves are given in Figures 1a and 1b, respectively. For comparison, the DSC data of the CS is also given in this plot. In the cooling scans after annealing, shown in Figure 1a, the crystallization temperature  $T_c$  is shifting to lower temperatures with increasing annealing duration ( $t_a$ ). Moreover, the area under the crystallization exotherm is systematically decreasing. This indicates that the degree of crystallinity of the sample is increasing during annealing with time, since less crystallizable PEO is available in the later cooling step. In the heating scans (Figure 1b), two melting endotherms were observed for the samples annealed at 50 °C. The melting endotherm at the higher temperature ( $T_{m,high}$ ) shifted with increasing  $t_a$  to higher peak temperatures of 54.6 °C (10 min),

55.4 °C (120 min) and 56.1 °C (24 h). The second melting endotherm features lower peak melting temperatures  $T_{m,low}$  which, in turn, systematically decrease with longer annealing durations. The observed melting enthalpies of these lower temperature melting peaks are close to the crystallization enthalpies, which are observed in the previous cooling scans. Thus, it is obvious that  $T_{m,low}$  originates from the PEO fractions, which crystallize upon cooling. The shift of the high-temperature melting endotherm is attributed to crystal thickening during annealing. Note that the small high-temperature shoulder near  $T_{m,high}$  is expected to be a measurement artefact that arises from crystals formed during heating in the DSC, as discussed elsewhere.[16] The effect of the annealing temperature  $T_a$  and duration  $t_a$  on the peak melting temperatures  $T_{m,high}$  and  $T_{m,low}$  is shown in Figure 2. The trend, which was exemplarily presented for the 50 °C-sample, is in agreement with the observations at the other annealing temperatures. With longer annealing durations,  $T_{m,high}$  increased (Figure 2a), while  $T_{m,low}$  decreased (Figure 2b). Two distinct melting peaks were only observed at either higher temperatures ( $T_a \geq 48$  °C) or very long annealing periods. A similar behavior was also observed by Fillon and co-workers during self-nucleation studies on polypropylene.[20] However, after annealing at  $T_a = 52$  °C, only one melting peak was observed in the heating scans. The slightly higher peak melting temperatures, compared to the CS, are expected to result from self-nucleation or self-seeding effects.[33-35]

Figure 2c shows the crystal thickness distributions of the CS and samples that were annealed between 10 min and 24 h, at  $T_a = 48$  °C. The results are based on Equation (1), applied to the DSC heating scans.<sup>26</sup> The crystal thickness distribution of the CS reveals a single maximum at 5.90 nm. Two distinct maxima were observed for the annealed samples. With increasing annealing periods, the maxima became more separated *i.e.* the thickness of the thinner crystals decreases, whereas it increases for the thicker crystals. The fractions of each species can be calculated from the integral of the corresponding peak in the distribution diagram. It was found that the fraction of the larger crystals is continuously increasing, being 75% after 10 min and 83% after 24 h at  $T_a = 48$  °C.

In Figure 2d, similar crystal thickness distributions are given for different  $T_a$ , after annealing for 24 h. A single maximum was observed for  $T_a = 52$  °C; two distinct distribution maxima can be found for  $42$  °C  $\leq T_a \leq 50$  °C. Both maxima shifted to larger crystal thicknesses with higher  $T_a$ . Further, the peak area was increasing for the lower crystal thicknesses and decreasing for larger crystal thicknesses. This indicates that larger crystal species are being formed with increasing  $T_a$ ; their respective fraction, however, is decreasing with  $T_a$ . The general thermal behavior of B<sub>96</sub>EO<sub>90</sub> points to a fractionation of the PEO chains during annealing within the melting range.[36]

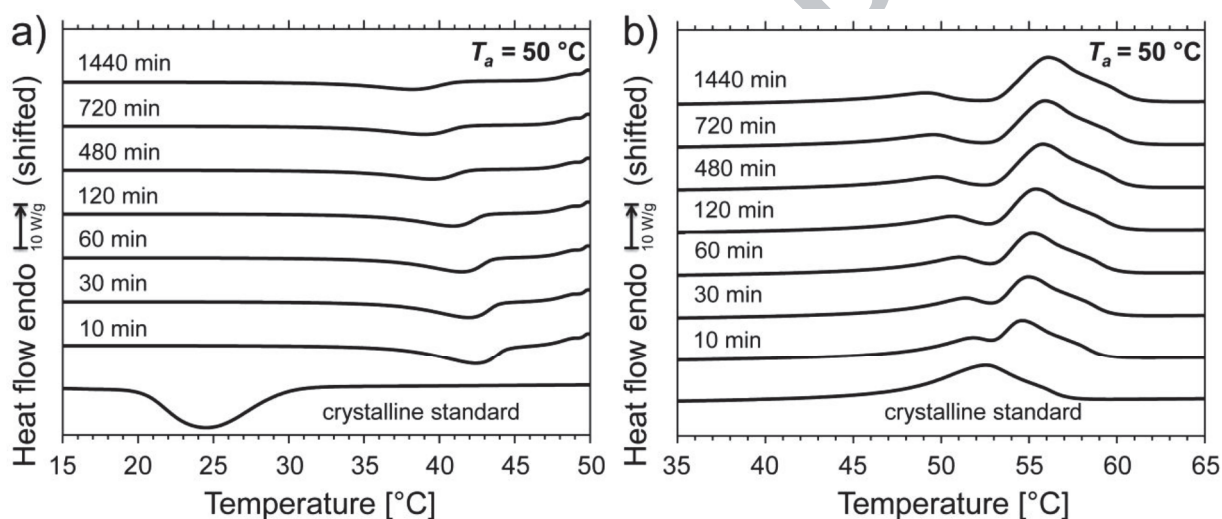


Figure 1. a) Cooling scans of B<sub>96</sub>EO<sub>90</sub> after annealing at an annealing temperature  $T_a = 50$  °C for different annealing periods  $t_a$ . b) Heating scans for different  $t_a$  after the subsequent cooling step. Each subsequent curve is shifted by 10 W/g with respect to the former for better visibility.

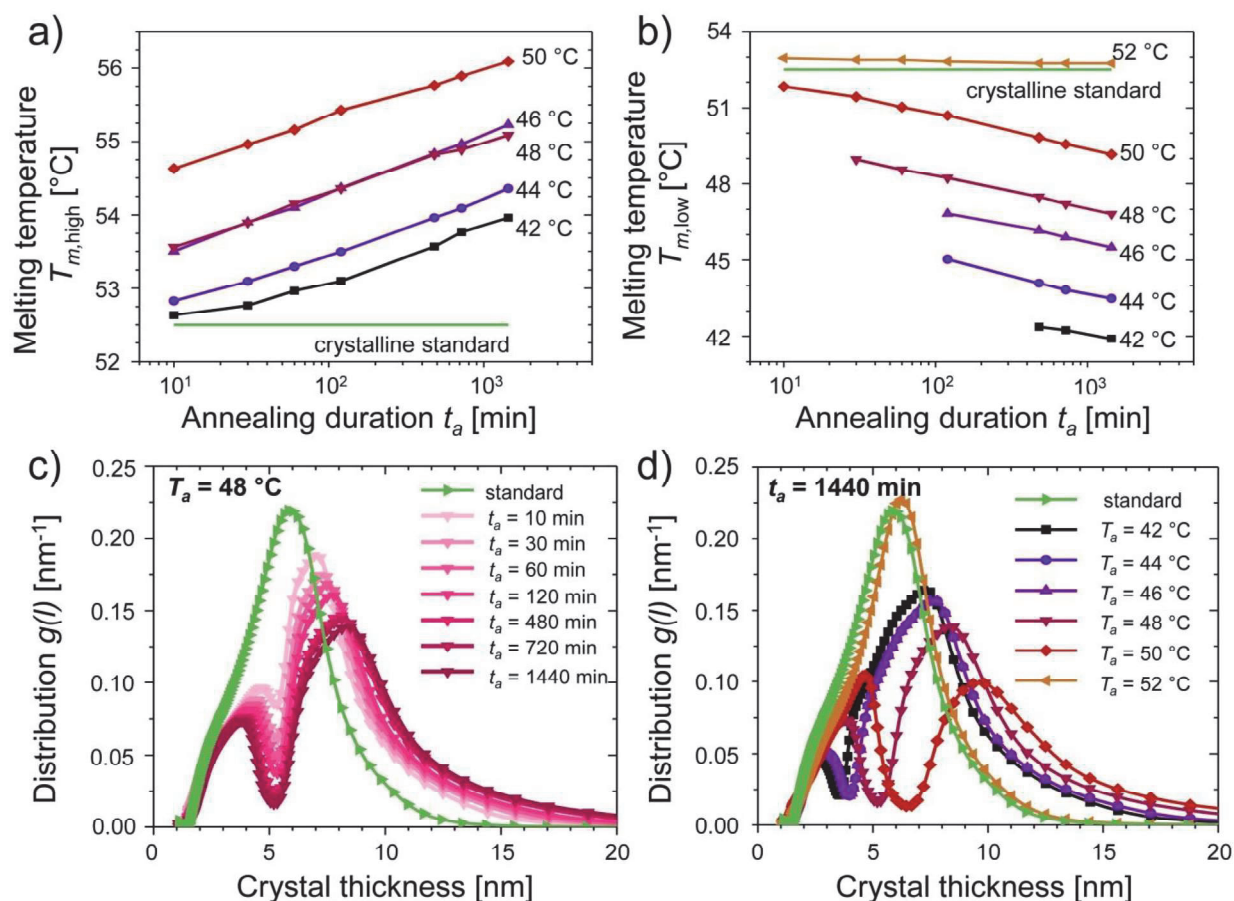


Figure 2. Peak melting temperatures for different  $t_a$  and distributions of the corresponding crystal thickness distributions according to the modified CM-model (equation 1).[28] a) higher peak melting temperature  $T_{m,high}$  and b) lower peak melting temperature  $T_{m,low}$ . c) Crystal thickness distributions at  $T_a = 48$  °C after different  $t_a$ . d) Crystal thickness distributions after annealing between 42 and 52 °C for 24 h.

### Wide-angle X-ray scattering

Figure 3a shows WAXS data at temperatures between 42 and 54 °C. Broad signals between 10 and 24° were observed in all samples investigated, which originated from diffuse scattering of amorphous regions.[37] Two distinct reflections appeared for temperatures below 54 °C. The maxima of these reflections were found at scattering angles of 18 and 22° and were attributed to the (120) and (112 + 032) reflections of the crystalline PEO, respectively.[38] The absolute value of the degree of crystallinity is generally calculated from the different scattering contributions of



the crystalline and amorphous phases.[39] Unfortunately, it was difficult to accurately estimate the correct degree of crystallinity in this case, since the angular range of the scattered angles did not cover the whole range of the amorphous halo, which leads to an overestimation of the degree of crystallinity within the samples. Thus, only the change of the relative degree of crystallinity can be discussed, which is based on the peak areas of the different crystalline reflections.

The degree of crystallinity of B<sub>96</sub>EO<sub>90</sub> annealed at 42 °C is similar to the one obtained at RT (data not shown). At 44 and 46 °C, the relative degree of crystallinity is slightly decreasing to 90% of its original value. Distinctly lower values were observed above 46 °C, being 80%, 67% and 22% for 48 °C, 50 °C and 52 °C, respectively. At 54 °C, the reflections from the PEO crystals were absent. This is a clear indication that the PEO crystals were completely molten at this temperature.[39]

The differences in the observed melting ranges of DSC and WAXS can be explained by the differences in the temporal course of the heating. During the DSC measurements, the sample was heated with 10 K·min<sup>-1</sup>. Thus, the melting temperature range was passed within two minutes, whereas during the WAXS measurements, the temperature was equilibrated for 20 min, followed by 60 min measurement time. We suggest that different holding times during the measurements were responsible for the changes in the observed PEO melting ranges between WAXS and DSC.

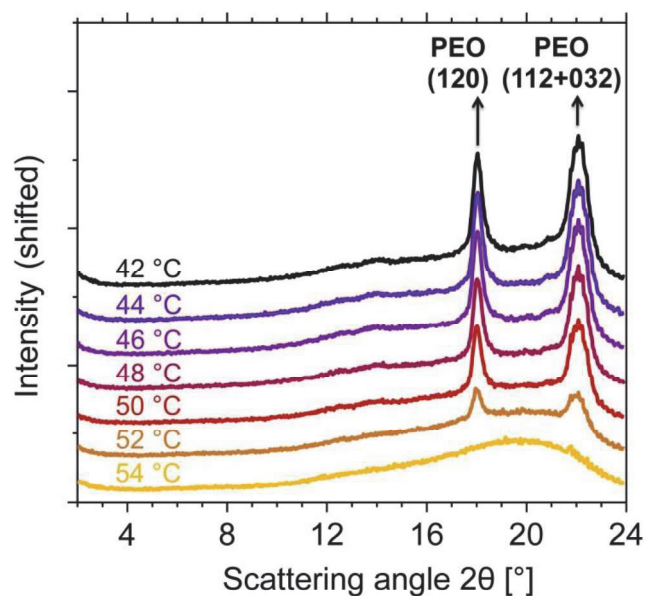


Figure 3. WAXS signals of B<sub>96</sub>EO<sub>90</sub> at temperatures between 42 and 54 °C. The PEO reflections are systematically decreasing with increasing temperature. Complete melting of the PEO crystals is observed at temperatures of 54 °C and above.

### Small-angle X-ray scattering

The results of the SAXS experiments are given in the Figures 4 to 6. The curves of the CS and selected curves after different annealing periods  $t_a$  at the annealing temperature  $T_a = 46\text{ }^\circ\text{C}$  are shown in Figure 4. The scattering curve of the CS shows a maximum at  $q^* = 0.29\text{ nm}^{-1}$  at RT, which corresponds to an average long-period of  $l_p = 21.9\text{ nm}$ . During annealing at  $T_a = 46\text{ }^\circ\text{C}$ , the reflections maximum decreased, which points to an increasing  $l_p$  for longer  $t_a$ . After cooling to RT, only minor changes in the SAXS pattern were observed. To describe the morphology development more appropriately, the long-period distribution is plotted over the reflections intensity in Figure 4b.  $l_p$  increased from approximately 22 nm (CS) up to 27 nm (after  $\approx 140\text{ h}$ ). Although the Figures 4a and 4b contain in principle the same information, the data representation in Figure 4b is helpful to understand the subsequent analysis steps.

For the description of the morphological development during annealing it is not only necessary to provide information about the average long-period. The distribution of domain spacings in the system is important, too. In order to represent this distribution in dependence of  $T_a$ , additional values were extracted from the SAXS data at 90% of the relative reflection intensity. This is, firstly, depicted as a semi-transparent bar in Figure 4b for  $T_a = 46\text{ }^\circ\text{C}$ . Secondly, the deviation of the long-period is given as a deviation band around the average long-period for  $42\text{ }^\circ\text{C} \leq T_a \leq 54\text{ }^\circ\text{C}$  at different  $t_a$  in Figure 6, which will be described later in the text.

One dimensional scattering curves of  $\text{B}_{96}\text{EO}_{90}$  before (a), during (b) and after annealing (c) at different  $T_a$  are given in Figure 5 (a-c). In Figure 5a, the scattering curves of the CS state prior to the annealing experiment are depicted. As expected, the scattering curves show similar features, such as a  $q^*$  at  $0.29\text{ nm}^{-1}$  and integer ratios of the first reflection  $q^*$ , indicating lamellar morphologies prior to the annealing step.[40] The similarity of the scattering curves verifies a successful creation of the CS at the respective temperatures. During annealing at  $T_a \leq 50\text{ }^\circ\text{C}$ ,  $q^*$

shifted to lower scattering vectors, which denotes increasing long-period due to annealing (Figure 5b). However, at  $T_a \geq 52$  °C we observed decreasing long-periods. Moreover, a  $\sqrt{7} q^*$  reflection appeared, which points to the formation of a bicontinuous morphology at such annealing temperatures. Figure 5c depicts the scattering curves of the annealed samples after cooling to RT. The reflection peaks of the samples annealed at 50 °C and below were found to be similar to the ones obtained at the end of the annealing step. For  $T_a \geq 52$  °C, we again observed integer ratios of  $q^*$ . Obviously, a lamellar morphology had formed during annealing, which indicates a break-out crystallization during the cooling step. The corresponding 2D SAXS patterns of Figure 5 are provided as supporting information.

It should be noted that the samples show a distinct orientation, as can be seen from the azimuthal dependence of the intensity in the 2D-SAXS data for selected samples in the supporting Figure S2 (left column). Calculating Herman's orientation parameter  $H$ , [41] which is 0 for random orientation and 1 for perfect parallel orientation, yields values between  $0.1 \leq H \leq 0.4$  for the different initial states. Most probably, this originates from a pre-orientation of the block copolymer melt or from small differences in the local crystallization conditions during the creation of CS. Unfortunately, it is difficult to control the orientation of the CS morphology, which is formed in the cooling step. Therefore, we have to exclude the influence of the different initial orientations on the morphology development from our considerations. However, it should be noted that the orientation factor  $H$  slightly increases during annealing between  $T_a = 42$  °C ( $H = 0.36 \rightarrow 0.42$ ) and 50 °C ( $H = 0.14 \rightarrow 0.19$ ). Decreasing orientation factors were observed for  $T_a = 52$  and 54 °C. The corresponding data is provided as supporting information.

The time-dependent, morphological development of B<sub>96</sub>EO<sub>90</sub> is depicted in Figure 6 for selected  $T_a$ . In order to enhance the visibility, the other results were moved to the supporting information. After heating to  $T_a$ , larger long-periods were observed with increasing  $t_a$  for all  $T_a$  between 42 and 50 °C and decreasing long-periods were found at  $T_a = 52$  and 54 °C. From the characteristics in

Figure 6, it is obvious that approximately 10 to 20 min are necessary to completely heat the sample through. This is expected to result from a non-ideal thermal contact and the low thermal conductivity of the sample. However, we expect only a minor influence of this warm-up period on the final morphology, since the samples were subjected to very long annealing times of up to 140 h. Between  $T_a = 42$  and  $46$  °C, the long-period growth is faster with increasing  $T_a$ , as depicted in Figure 6a, exemplarily for  $T_a = 42$  and  $46$  °C. Average long periods  $l_p$  of 25.2 nm and 26.6 nm were measured after 128 h for these  $T_a$ , respectively.

The slightly different long-period growth rates may be explained by a higher chain flexibility and partly higher fraction of molten PEO chains that promote defect healing inside the PEO crystals.[12] The long-period deviations were found to be relatively similar at  $\pm 1.4$  nm, which points to a uniform crystal thickening in this annealing region.

Figure 6b shows the long-period development between annealing temperatures of 46 and 50 °C, exemplarily for  $T_a = 50$  °C. In this annealing temperature region, almost similar long-period growth rates were observed, leading to average long-periods in the order of 27 nm after 128 h (27.0 nm and 26.9 nm for 46, 48 and 50 °C, respectively). However, it was also found that the long-period deviations, as given by the 90% distribution band, significantly broaden from  $\pm 1.4$  nm, in the case of 46 °C, to  $\pm 2.0$  nm (48 °C) and  $\pm 2.3$  nm (50 °C) at higher  $T_a$ . These deviations indicate that the morphological development is less uniform compared to annealing between 42 and 46 °C.

At annealing temperatures  $T_a \geq 52$  °C (Figure 6c), the average long-period decreased already after the warm-up period of approximately 1 min. The observed long-period of 19 nm was constant until the sample was cooled to RT and the estimated deviations of  $\pm 0.6$  nm were significantly smaller compared to the other investigated  $T_a$ . Moreover, distinct higher-order reflections were observed at  $T_a = 52$  and  $54$  °C, which are shown in the SAXS scattering curves in the Figure 5b. The scattering vectors of the reflection are observed at  $q^* = 0.32$  nm<sup>-1</sup>,  $q = 0.67$  nm<sup>-1</sup> and  $0.87$  nm<sup>-1</sup>.

<sup>1</sup>, having ratios of  $1:\sqrt{4}:\sqrt{7}$ , which is typical for spherical, cylindrical as well as gyroid morphologies or hexagonal-perforated lamellae (HPL).[40] Obviously, the initially lamellar morphology transformed at temperatures  $\geq 52$  °C after sufficiently long  $t_a$ .

The volume fractions of PEO are in the order of 35 vol.% and, thus, close to the phase boundary between cylindrical and lamellar morphologies in diblock copolymers.[42] However, gyroid morphologies[43, 44] and HPL[17, 45] are also often observed in PEO containing BCPs. In Ref. 15, very similar scattering features compared to the obtained SAXS data were observed and these results were attributed to a HPL morphology. Therefore, we suggest that B<sub>96</sub>E<sub>90</sub> transformed into a HPL morphology at  $T_a \geq 52$  °C. This phase transformation might also explain the decreasing long-periods during the experiment at  $T_a = 52$  and  $54$  °C. After cooling the samples back to RT, the integer higher-order reflections indicate again the formation of a lamellar morphology, which points to a break-out crystallization of the PEO chains during cooling.[46, 47]

It is also interesting to note that a reflections at approximately  $q^* = 0.2$  nm<sup>-1</sup> (long-periods of 31 nm) could be observed for the 52 °C-sample that emerges after approximately 1000 min. This is highlighted in Figure 5b and indicates the existence of larger, thermodynamically stable PEO crystals with high melting points (Gibbs-Thomson effect).[48]

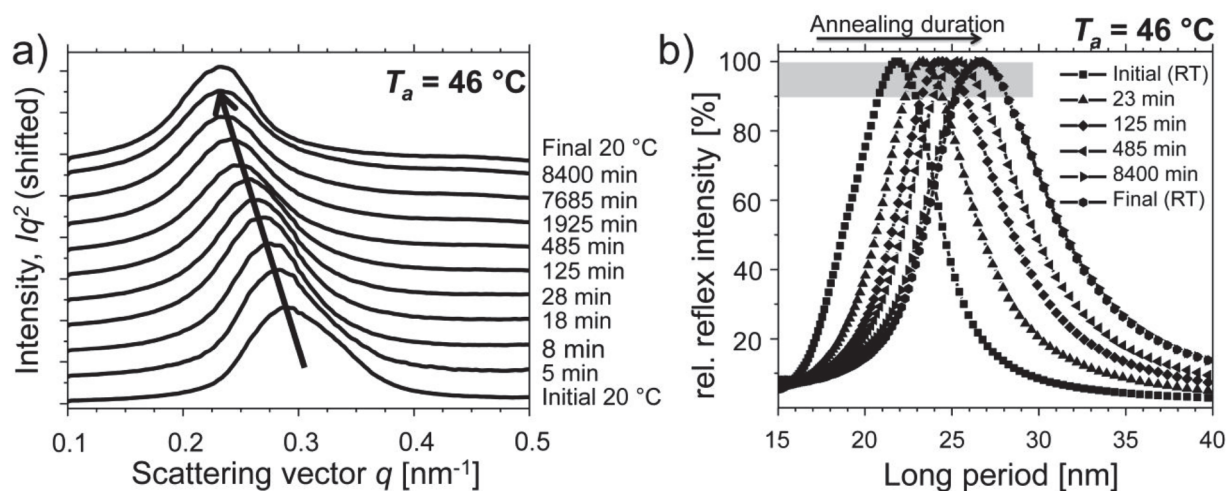


Figure 4. a) Exemplary presentation of SAXS curves at  $T_a = 46\text{ °C}$  at different annealing durations  $t_a$ , which are provided on the right side of the graph. The curves are shifted for better visibility. b) Relative reflection intensity over the long-period at different  $t_a$ . The grey bar marks the region that is used to describe the long-period deviations.

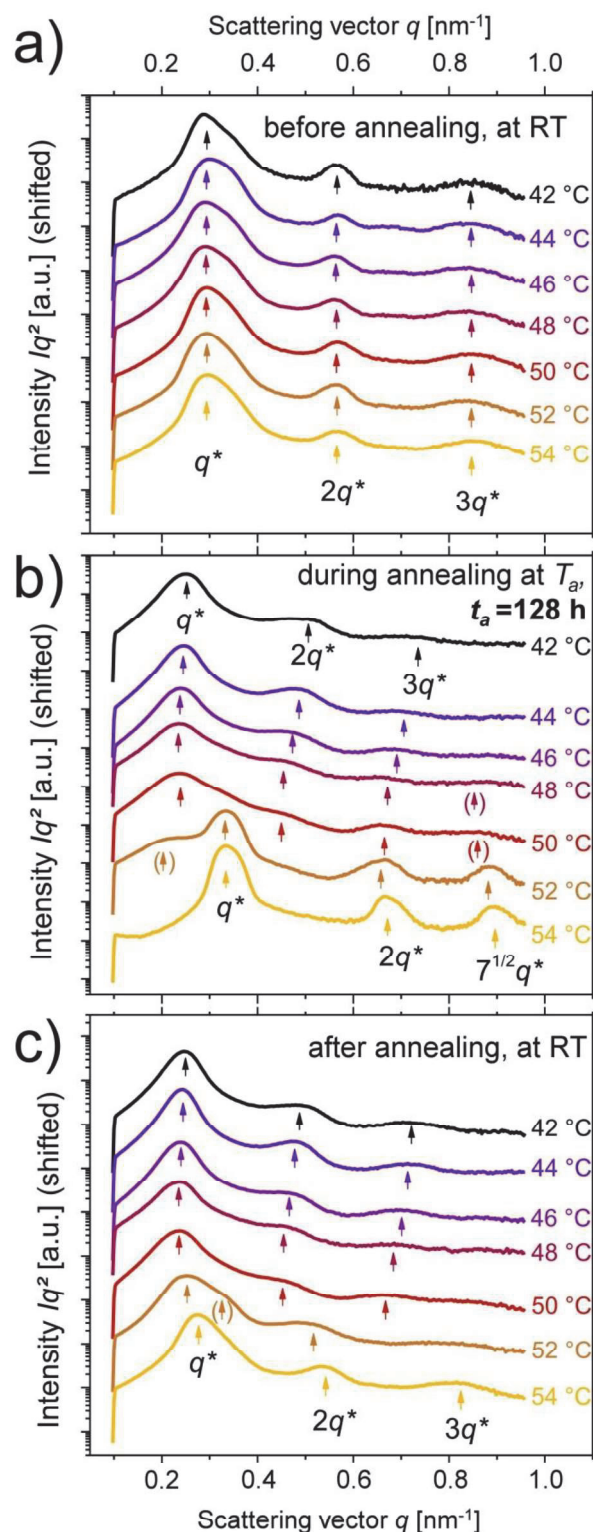


Figure 5. Scattering curves of B<sub>96</sub>EO<sub>90</sub> a) before annealing (CS at RT), b) during annealing after 128 h at different  $T_a$  and c) after annealing at different  $T_a$  and cooling to RT.  $T_a$  is given on the right side of the corresponding graph. All graphs are shifted for better visibility; the arrows



indicate different reflections. Corresponding 2D-SAXS patterns are provided in the supporting information.

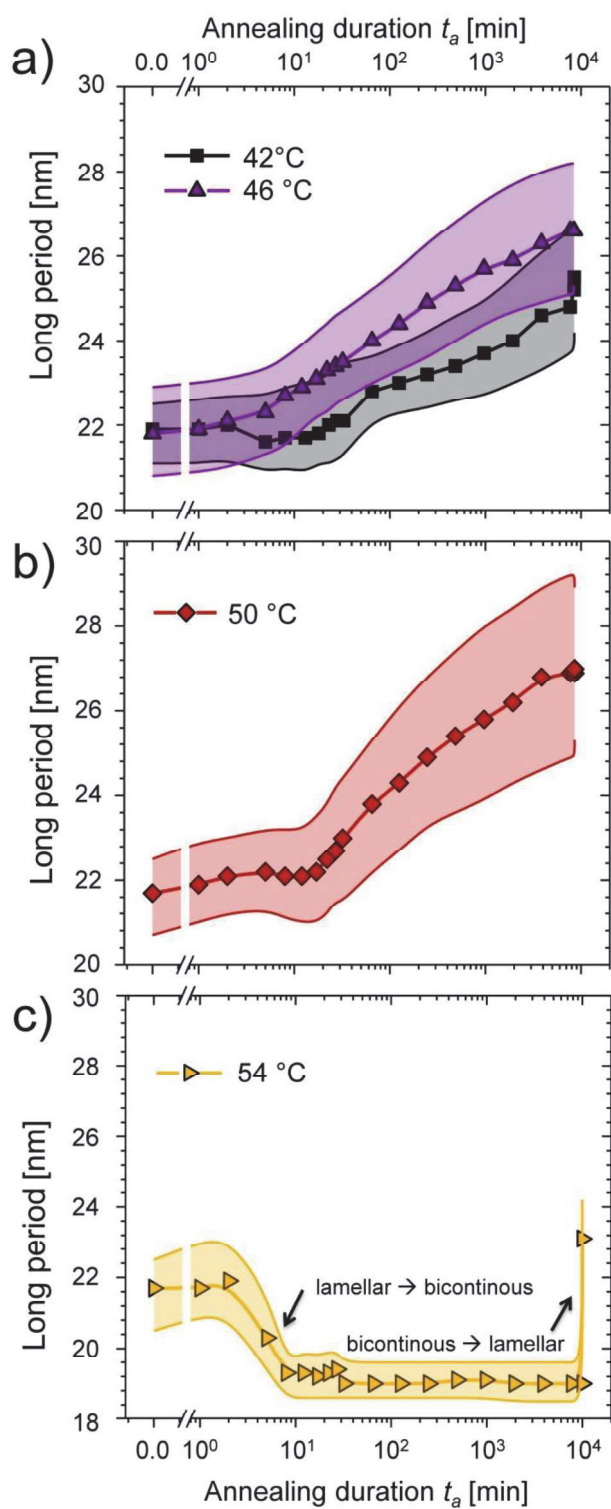


Figure 6. Average long-periods and deviation bands (90% of the reflection intensity) at selected  $T_a$ , a) 42 to 46 °C (regime of defect healing), b) 50 °C (regime of thermal fractionation) and c) 54 °C (melting and self-nucleation). The last data point in each curve represents the average long-period after cooling to RT.

ACCEPTED MANUSCRIPT

**DISCUSSION**

Based on the DSC and SAXS investigations, three distinct annealing regimes were identified. (i) Between  $T_a = 42$  and  $46^\circ\text{C}$ , a steady long-period growth of the CS long-period, reaching from 15% ( $42^\circ\text{C}$ ) to 22% ( $46^\circ\text{C}$ ) was observed. The deviation from the average long-period  $l_p$  was about  $\pm 1.4$  nm, as estimated by the deviation band. Within this regime, it is expected that different PEO crystal thicknesses and long-periods can be achieved in a defined manner. This is also supported by the DSC results, where only small fractions of  $\text{B}_{96}\text{EO}_{90}$  crystallized upon cooling, as indicated by the small shoulder at lower PEO thickness values in Figure 2d. Hence, it is assumed that the lamellae thickening in this temperature regime is dominated by defect healing of the PEO crystals, whereby the PEO chains become less folded, which increases  $l_p$ . [14]

(ii) Almost similar average long-periods of  $l_p \approx 27$  nm were found after annealing for approximately 140 h between  $46$  and  $50^\circ\text{C}$ . This corresponds to an average increase of 22% compared to the CS. The deviations of  $l_p$  systematically increased with higher  $T_a$ . Further, a distinct second melting endotherm ( $T_{m,\text{low}}$ ) was observed after annealing at  $50^\circ\text{C}$  (Figure 2b), which is particularly pronounced in annealing regime (ii). The observed area fractions of the high and low temperature melting peaks indicate that only 70% of the PEO chains formed crystals with a higher thickness (Figure 2d). Thus, it can be concluded that, on the one hand, shorter chains were excluded from the thicker PEO crystals and crystallized independently during cooling. On the other hand, the thermal energy is high enough to form even higher PEO crystal thicknesses, which was revealed by the additional broadening of the SAXS reflection towards lower scattering angles as well as a broad crystal distribution of the higher melting species. This behavior can be described as thermal fractionation of the PEO chains, which prevails in this annealing regime. [18]

(iii) In the third regime, found above  $52^\circ\text{C}$  for  $\text{B}_{96}\text{EO}_{90}$ , the initially crystalline fractions of the PEO block were almost completely molten, as indicated by WAXS measurements in Figure 3. Similar trends were observed in the DSC trace for the  $52^\circ\text{C}$  sample, where only a single melting

endotherm was observed, having an enthalpy of approximately 115 J/g, which is close to the value of the CS (124 J/g). Further, the melting enthalpy was independent of  $t_a$ . In this regime, the development of structure and morphology is expected to be determined by the crystallizing conditions and self-nucleation effects,[33] rather than the annealing duration, since the morphology is being over-written during the cooling step, due to break-out crystallization from the presumably HPL (melt) to a lamellar morphology (solid).

However, it should be emphasized that lamellae thickening at  $T_a = 52\text{ }^\circ\text{C}$  was observed, despite the low crystalline fractions. This is indicated by the formation of the reflection at very small scattering angles ( $l_p \approx 31\text{ nm}$ , increase of 40%), as shown in Figure 5b. Three facts point to lamellae thickening in this case, rather than the formation of a second phase due to melting of the PEO crystallites. First, the HPL morphology exhibited a smaller  $l_p$  (19.0 nm) compared to the CS (21.9 nm, Figure 6c). Therefore, the chains either had to stretch to obtain a long-period of  $l_p \approx 31\text{ nm}$ , which is thermodynamically unfavorable, or they were present in the crystalline state. Second, there were still some residual crystals at this annealing temperature, as shown by the temperature dependent WAXS-investigations (Figure 3). Hence, crystalline regions existed within B<sub>96</sub>EO<sub>90</sub> at this temperature. The third point can be derived from the orientation of the observed reflection (see supporting Figure S2h), which is similar to that of the CS (supporting Figure S2g). Thus, the scattering entities of the reflection at small angles are expected to originate from the already present crystals in the CS. Unfortunately, the used X-ray setup prevented the investigation of smaller scattering angles, which might give a hint of the existence of less folded or extended chain species within the annealed samples.

The observed three regimes are to some extent related to the “domains“ presented by Fillon and co-workers, who classified these “domains” according to the crystallization behavior during self-nucleation studies of polypropylene.[20] However, in crystallizable block copolymers, the morphological development due to crystal thickening is more complex than in homopolymers, due

to the confinement arising from the additional block(s) and the resulting microphase separation. Thus, it cannot be described solely by DSC self-nucleation experiments.

Subsequently, a brief basic discussion on the utilization of SAXS measurements within the melting range is given. The electron density of the PEO phase changes during its melting and crystallization, which directly influences the electron density contrast between the PB and the PEO phase and, thus, the scattering power of the system.[37] Since the electron density contrast between PB and PEO is very strong in both, the amorphous and the crystalline PEO, we do not expect a great influence on our experiments. However, there might be some smearing of the reflection peak  $q^*$  due to the presence of amorphous PEO between the PB phase and the PEO crystals (*e.g.* in the partial molten state) that would lead to an over-estimation of the deviations calculated from the reflex shape.

Another important point is the estimation of the PEO domain size and the crystal thickness distribution. This can be calculated from the obtained long-periods in SAXS and volume fraction of the PEO. For the CS, this yielded a PEO domain size ( $l_{\text{PEO}}$ ) of approximately 7.8 nm, which is in fair agreement to our observations in the AFM, given as supporting information. The calculation of the PEO crystal thickness ( $l_{\text{PEO},c}$ ), which is based on the DSC measurements, yielded average values of 5.9 nm for CS. The differences between the SAXS and DSC based results presumably originate from the presence of amorphous regions, which are included in the results from SAXS, but not in the DSC based crystal thickness distribution. An overview of the calculated long-periods  $l_p$  and domain spacings after annealing for 24 h at different  $T_a$  is provided in Table 1. There,  $l_{\text{PEO}}$  was estimated according to Equation (3) and the crystalline lamellae thickness of PEO ( $l_{\text{PEO},c}$ ) was calculated from the crystal thickness distributions, multiplied by the area fraction of the respective peaks in Figure 2d. Although the results are quite plausible, there are some approximations carried out within the CM-model, which shall be briefly discussed in the following.

The CM-model is based on the approach of Gibbs-Thomson, which was originally developed for high molar mass homopolymers, rather than low molar mass diblock copolymers, as employed in this study. For the calculation, we used a modification of  $T_m^0$  for PEO, which has a similar molar mass compared to the PEO block in B<sub>96</sub>EO<sub>90</sub>, as proposed by Buckley and Kovacs ( $T_{m,\text{corr}}^0$ ).[31] Hence, the influence of the lower molar mass is considered in this model. However, contributions of the covalently attached PB block are not incorporated. It is generally accepted that the presence of a second block affects the surface energy of the PEO crystal. Further, Gido and co-workers discussed that the equilibrium chain configuration of the PEO differs from the extended chain in confined BCPs.[16] Both, the altered crystal surface energy and the modified chain configuration would directly affect the relation between the melting temperature and the crystal thickness and, hence, shift the distribution curves in the Figures 2c and 2d. However, the (non)-existence of extended chain species in semi-crystalline block copolymers is still controversially debated. Other studies demonstrated the existence of extended (PEO chain defines the thickness of the PEO domain) and double-extended PEO chains (two consecutively arranged, extended PEO chains define the PEO domain size) in PB-*b*-PEO by AFM.[10, 11] This more fundamental question cannot be answered within the scope of this contribution. From the presented results, however, it is obvious that the modified CM-model is suitable to describe the mechanism of crystalline lamellae thickening by defect healing or thermal fractionation of the PEO chains. Thus, the crystal thickness distribution provides a valuable tool to describe the mechanism of the PEO domain growth. However, great care should be taken with the absolute values of the calculated crystal thicknesses, due to approximations in the applied model and its sensibility on the employed  $T_{m,\text{corr}}^0$ . Hence, it is essential that complementary SAXS investigations are carried out to obtain information about the absolute spacings and the kinetics of their development during annealing, directly from the experiment.

**Table 1. Comparison between PEO domain spacings (SAXS) and crystalline lamellae thickness (DSC) after 24 h annealing.**

$T_a$ [°C]	SAXS		DSC (CM- model)
	$l_0$ [nm] <sup>a)</sup>	$l_{\text{PEO}}$ [nm] <sup>b)</sup>	$l_{\text{PEO,c}}$ (avg.) [nm] <sup>c)</sup>
CS	21.9 ± 1.2	7.8	5.9
42	23.9 ± 1.4	8.5	7.0
44	24.4 ± 1.3	8.6	7.3
46	25.8 ± 1.7	9.1	7.2
48	26.1 ± 2.1	9.2	7.6
50	26.1 ± 2.2	9.2	8.0

<sup>a)</sup> Calculated from equation (2), error from 90% of reflection maximum intensity.

<sup>b)</sup> Calculated from equation (3).

<sup>c)</sup> Estimated from crystal thickness distribution peak maxima, weighted by the respective area fractions.

**CONCLUSIONS AND OUTLOOK**

Time- and temperature-dependent SAXS, WAXS and DSC investigations provide a powerful combination to study the mechanisms and kinetics of crystal thickening in crystallizable block copolymer systems, as exemplarily presented for a PB-*b*-PEO block copolymer. The SAXS data provide information about the kinetics of the long-period growth of the system, whereas the melting endotherms of the DSC measurements were correlated to the thickness values of the crystalline PEO lamellae, by applying a modified Gibbs-Thomson approach (CM-model).[28] Three distinct annealing regimes were identified, which are either dominated by (i) defect healing, (ii) thermal fractionation or (iii) melting and self-nucleation.

The thickest species, having a long-period of approx. 31 nm, was observed at an annealing temperature of 52 °C, firstly visible after an annealing period of 24 h. This increased long-period corresponds to a relative long-period growth of 40% compared to the initial CS.

However, up to now, it is necessary to anneal such samples in regime (i) in order to have a controlled crystal thickening. Nevertheless, the long-period growth of up to 40% is promising for future applications, since it offers a wide scope of achievable spacings without increasing the block copolymers degree of polymerization. There is a strong demand to understand the underlying ordering kinetics, to perform the morphological development in a controlled manner. Future studies should, therefore, investigate the effect of the cooling rate after thermal treatment within the annealing regime (ii). Additional interesting issues are the chain dynamics and crystal thickening in highly oriented samples as well as studies on block copolymer systems with more than one crystallizable block. The presented time- and temperature-dependent SAXS and DSC investigations as well as the application of the modified CM-model and long-period deviation bands, to describe the respective data, offer suitable tools to study the morphological development and lamellae thickening mechanism of such crystallizable block copolymer systems.



**SUPPORTING INFORMATION**

The following supporting information is provided online: (i) The derivation of the applied model to describe the crystal thickness distributions from the DSC heating scans. (ii) Additional data derived from the SAXS measurements. a) The long-period development at different annealing temperatures and durations. b) 2D-SAXS pattern of prior, during and after annealing between  $48\text{ }^{\circ}\text{C} \leq T_a \leq 54\text{ }^{\circ}\text{C}$ . c) Development of the orientation factor during annealing. (iii) AFM phase images of B<sub>96</sub>EO<sub>90</sub> before and after annealing.

**ACKNOWLEDGMENT**

F. H. S. and U. S. S. are grateful to the Thuringian Ministry for Education, Science, and Culture (TMBWK; #B515-11028, SWAXS-JCSM) for financial support. R. S., T. N. B. and K. D. J. gratefully acknowledge the financial support of the Carl-Zeiss Foundation for a postdoctoral stipend.

**REFERENCES**

- [1] Biswas A, Bayer IS, Biris AS, Wang T, Dervishi E, Faupel F. Advances in top-down and bottom-up surface nanofabrication: Techniques, applications & future prospects. *Adv Colloid Interfac.* 2012;170(1-2):2-27.
- [2] Darling SB. Directing the self-assembly of block copolymers. *Prog Polym Sci.* 2007;32(10):1152-1204.
- [3] Katsuhiko A, Jonathan PH, Michael VL, Ajayan V, Richard C, Somobrata A. Challenges and breakthroughs in recent research on self-assembly. *Sci Tech Adv Mater.* 2008;9(1):014109.
- [4] Nandan B, Kuila BK, Stamm M. Supramolecular assemblies of block copolymers as templates for fabrication of nanomaterials. *Eur Polym J.* 2011;47(4):584-599.
- [5] Albert JNL, Epps III TH. Self-assembly of block copolymer thin films. *Mater Today.* 2010;13(6):24-33.

- [6] Bates FS, Fredrickson GH. Block Copolymer Thermodynamics: Theory and Experiment. *Annu Rev Phys Chem.* 1990;41(1):525-557.
- [7] Hamley IW. Ordering in thin films of block copolymers: Fundamentals to potential applications. *Prog Polym Sci.* 2009;34(11):1161-1210.
- [8] He W-N, Xu J-T. Crystallization assisted self-assembly of semicrystalline block copolymers. *Prog Polym Sci.* 2012;37(10):1350-1400.
- [9] Ostas E, Schröter K, Beiner M, Yan TZ, Thurn-Albrecht T, Binder WH. Poly(epsilon-caprolactone)-Poly(isobutylene): A Crystallizing, Hydrogen-Bonded Pseudo-Block Copolymer. *J Polym Sci Pol Chem.* 2011;49(15):3404-3416.
- [10] Schulze R, Arras MML, Li Destri G, Gottschaldt M, Bossert J, Schubert US, et al. Extended-Chain Induced Bulk Morphologies Occur at Surfaces of Thin Co-Oligomer Films. *Macromolecules.* 2012;45(11):4740-4748.
- [11] Schulze R, Arras MML, Helbing C, Hölzer S, Schubert US, Keller TF, et al. How the Calorimetric Properties of a Crystalline Copolymer Correlate to Its Surface Nanostructures. *Macromolecules.* 2014;47(5):1705-1714.
- [12] Strobl G. Crystallization and melting of bulk polymers: New observations, conclusions and a thermodynamic scheme. *Prog Polym Sci.* 2006;31(4):398-442.
- [13] Beiner M. Nanoconfinement as a tool to study early stages of polymer crystallization. *J Polym Sci, Part B: Polym Phys.* 2008;46(15):1556-1561.
- [14] Reiter G, Castelein G, Hoerner P, Riess G, Sommer JU, Floudas G. Morphologies of diblock copolymer thin films before and after crystallization. *Eur Phys J E.* 2000;2(4):319-334.
- [15] Chen H-L, Hsiao S-C, Lin T-L, Yamauchi K, Hasegawa H, Hashimoto T. Microdomain-Tailored Crystallization Kinetics of Block Copolymers. *Macromolecules.* 2001;34(4):671-674.
- [16] Hong S, Yang L, MacKnight WJ, Gido SP. Morphology of a Crystalline/Amorphous Diblock Copolymer: Poly((ethylene oxide)-b-butadiene). *Macromolecules.* 2001;34(20):7009-7016.

- [17] Lambreva DM, Opitz R, Reiter G, Frederik PM, de Jeu WH. Morphology of an asymmetric ethyleneoxide-butadiene di-block copolymer in bulk and thin films. *Polymer*. 2005;46(13):4868-4875.
- [18] Castillo RV, Arnal ML, Müller AJ, Hamley IW, Castelletto V, Schmalz H, et al. Fractionated crystallization and fractionated melting of confined PEO microdomains in PB-b-PEO and PE-b-PEO diblock copolymers. *Macromolecules*. 2008;41(3):879-889.
- [19] Lorenzo AT, Arnal ML, Müller AJ, Lin M-C, Chen H-L. SAXS/DSC Analysis of the Lamellar Thickness Distribution on a SSA Thermally Fractionated Model Polyethylene. *Macromol Chem Phys*. 2011;212(18):2009-2016.
- [20] Fillon B, Wittmann JC, Lotz B, Thierry A. Self-nucleation and recrystallization of isotactic polypropylene ( $\alpha$  phase) investigated by differential scanning calorimetry. *J Polym Sci Part B Polym Phys*. 1993;31(10):1383-1393.
- [21] Müller AJ, Lorenzo AT, Arnal ML, de Fierro AB, Abetz V. Self-Nucleation Behavior of the Polyethylene Block as Function of the Confinement Degree in Polyethylene-Block-Polystyrene Diblock Copolymers. *Macromol Symp*. 2006;240(1):114-122.
- [22] Müller AJ, Balsamo V, Arnal ML. Nucleation and Crystallization in Diblock and Triblock Copolymers. In: Abetz V, editor. *Block Copolymers II*: Springer Berlin Heidelberg; 2005. p. 1-63.
- [23] Ungar G, Zeng X-b. Learning Polymer Crystallization with the Aid of Linear, Branched and Cyclic Model Compounds. *Chem Rev*. 2001;101(12):4157-4188.
- [24] Cheng SZD, Lotz B. Nucleation control in polymer crystallization: structural and morphological probes in different length- and time-scales for selection processes. *Philos Trans R Soc London, Ser A*. 2003;361(1804):517-537.
- [25] Cheng SZD, Chen J. Nonintegral and integral folding crystal growth in low-molecular mass poly (ethylene oxide) fractions. III. Linear crystal growth rates and crystal morphology. *J Polym Sci Part B Polym Phys*. 1991;29(3):311-327.

- [26] Cheng SZD, Zhang A, Chen J, Heberer DP. Nonintegral and integral folding crystal growth in low-molecular mass poly(ethylene oxide) fractions. I. Isothermal lamellar thickening and thinning. *J Polym Sci Part B Polym Phys*. 1991;29(3):287-297.
- [27] Lotz B, Kovacs AJ, Bassett GA, Keller A. Properties of copolymers composed of one polyethylene-oxide and one polystyrene block. *Kolloid Z Z Polym*. 1966;209(2):115-128.
- [28] Crist B, Mirabella FM. Crystal thickness distributions from melting homopolymers or random copolymers. *J Polym Sci Part B Polym Phys*. 1999;37(21):3131-3140.
- [29] Crist B, Howard PR. Crystallization and Melting of Model Ethylene-Butene Copolymers. *Macromolecules*. 1999;32(9):3057-3067.
- [30] Spieckermann F, Wilhelm H, Kerber M, Schafner E, Polt G, Bernstorff S, et al. Determination of lamella thickness distributions in isotactic polypropylene by X-ray line profile analysis. *Polymer*. 2010;51(18):4195-4199.
- [31] Buckley CP, Kovacs AJ. Melting behaviour of low molecular weight poly (ethylene-oxide) fractions. *Colloid Polym Sci*. 1976;254(8):695-715.
- [32] Schneider CA, Rasband WS, Eliceiri KW. NIH Image to ImageJ: 25 years of image analysis. *Nat Meth*. 2012;9(7):671-675.
- [33] Müller AJ, Balsamo V, Arnal ML, Jakob T, Schmalz H, Abetz V. Homogeneous nucleation and fractionated crystallization in block copolymers. *Macromolecules*. 2002;35(8):3048-3058.
- [34] Zhu L, Huang P, Chen WY, Ge Q, Quirk RP, Cheng SZD, et al. Nanotailored crystalline morphology in hexagonally perforated layers of a self-assembled PS-b-PEO diblock copolymer. *Macromolecules*. 2002;35(9):3553-3562.
- [35] Lorenzo AT, Arnal ML, Sánchez JJ, Müller AJ. Effect of annealing time on the self-nucleation behavior of semicrystalline polymers. *J Polym Sci Part B Polym Phys*. 2006;44(12):1738-1750.
- [36] Müller AJ, Arnal ML. Thermal fractionation of polymers. *Prog Polym Sci*. 2005;30(5):559-603.

- [37] Stribeck N. X-ray scattering of soft matter: Springer; 2007.
- [38] Zhu L, Cheng SZD, Calhoun BH, Ge Q, Quirk RP, Thomas EL, et al. Crystallization Temperature-Dependent Crystal Orientations within Nanoscale Confined Lamellae of a Self-Assembled Crystalline–Amorphous Diblock Copolymer. *J Am Chem Soc.* 2000;122(25):5957-5967.
- [39] Vonk C. Computerization of Ruland's X-ray method for determination of the crystallinity in polymers. *J Appl Crystallogr.* 1973;6(2):148-152.
- [40] Hadjichristidis N, Pispas S, Floudas G. *Block Copolymers: Synthetic Strategies, Physical Properties, and Applications.*: John Wiley & Sons, Inc.; 2003.
- [41] Gedde U. *Polymer Physics*: Springer; 1995.
- [42] Matsen M, Bates FS. Unifying weak-and strong-segregation block copolymer theories. *Macromolecules.* 1996;29(4):1091-1098.
- [43] Hamersky MW, Hillmyer MA, Tirrell M, Bates FS, Lodge TP, von Meerwall ED. Block Copolymer Self-Diffusion in the Gyroid and Cylinder Morphologies. *Macromolecules.* 1998;31(16):5363-5370.
- [44] Cao W, Tashiro K, Masunaga H, Sasaki S, Takata M. Relationship between Morphological Change and Crystalline Phase Transitions of Polyethylene–Poly(ethylene oxide) Diblock Copolymers. 3. Dependence of Morphological Transition Phenomena on the PE/PEO Segmental Lengths and Its Possible Origins. *J Phys Chem B.* 2009;113(25):8495-8504.
- [45] Li L, Séréro Y, Koch MHJ, de Jeu WH. Microphase Separation and Crystallization in an Asymmetric Diblock Copolymer: Coupling and Competition. *Macromolecules.* 2003;36(3):529-532.
- [46] Vasilev C, Heinzlmann H, Reiter G. Controlled melting of individual, nano-meter-sized, polymer crystals confined in a block copolymer mesostructure. *J Polym Sci Part B Polym Phys.* 2004;42(7):1312-1320.

[47] Mihut AM, Chiche A, Drechsler M, Schmalz H, Di Cola E, Krausch G, et al. Crystallization-induced switching of the morphology of poly(ethylene oxide)-block-polybutadiene micelles. *Soft Matter*. 2009;5(1):208-213.

[48] Höhne GWH. Another approach to the Gibbs–Thomson equation and the melting point of polymers and oligomers. *Polymer*. 2002;43(17):4689-4698.

ACCEPTED MANUSCRIPT



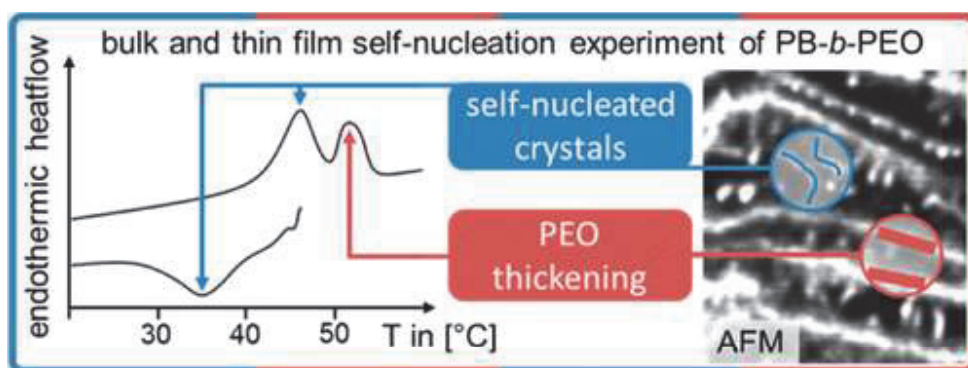




## Publication [P7]

How the calorimetric properties of a crystalline copolymer correlate to its surface nanostructures

Robert Schulze, Matthias M. L. Arras, Christian Helbing, Stefan Hölzer,  
Ulrich S. Schubert, Thomas F. Keller, Klaus D. Jandt



*Macromolecules* **2014**, *47*, 1705–1714



## How the Calorimetric Properties of a Crystalline Copolymer Correlate to Its Surface Nanostructures

Robert Schulze,<sup>†</sup> Matthias M. L. Arras,<sup>†</sup> Christian Helbing,<sup>†</sup> Stefan Hölzer,<sup>‡</sup> Ulrich S. Schubert,<sup>‡,§</sup> Thomas F. Keller,<sup>†,§</sup> and Klaus D. Jandt<sup>\*,†,§</sup>

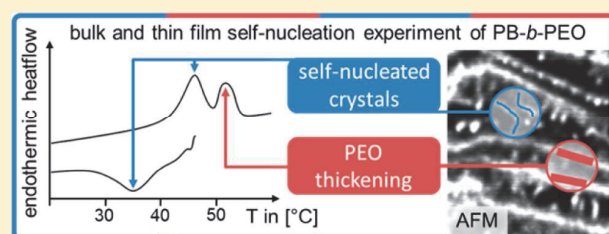
<sup>†</sup>Chair of Materials Science (CMS), Otto Schott Institute of Materials Research, Faculty of Physics and Astronomy, Friedrich Schiller University Jena, Löbdergraben 32, 07743 Jena, Germany

<sup>‡</sup>Laboratory of Organic Chemistry and Macromolecular Chemistry (IOMC), Friedrich Schiller University Jena, Humboldtstraße 10, 07743 Jena, Germany

<sup>§</sup>Jena Center for Soft Matter (JCSM), Friedrich Schiller University Jena, Philosophenweg 7, 07743 Jena, Germany

### Supporting Information

**ABSTRACT:** Thin film surface nanostructures of semicrystalline diblock copolymer are promising for the fabrication of photonic crystals and bioanalytical devices because they might be tailorable by controlled crystallization. One approach to systematically control polymer crystallization is a self-nucleation experiment. The self-nucleation experiment for block copolymers has only been reported for the bulk and so far not for thin films. Considering the versatility of a tailorable surface nanostructure, it is promising to apply the controlled crystallization of a bulk self-nucleation experiment to thin films of a diblock copolymer. In the current study we tested the hypothesis that within two self-nucleation experiments, i.e., in the bulk and thin film, the calorimetric bulk properties of a polybutadiene-*block*-poly(ethylene oxide) can be correlated to the resulting thin film surface nanostructures and to understand as well as predict their formation. The calorimetric bulk properties measured by differential scanning calorimetry in the bulk self-nucleation experiment were correlated to surface nanostructures measured by atomic force microscopy of the thin film self-nucleation experiment samples. In analogy to the bulk self-nucleation experiment, we introduced a crystalline standard for the thin film self-nucleation experiment where the crystalline lamellae consisted of once-folded chains. Annealing the thin film crystalline standard promoted the thickening of crystalline lamellae on the film surface which is explained by the formation of less folded chain crystals that obtain higher melting temperatures. The crystalline lamellae thickness was steplessly variable within the range of 8–16 nm. In analogy to the Hoffman–Weeks and Gibbs–Thomson plots, we derived a function which can be used to predict the lamellae thickness as a function of the annealing temperature. Bulk and thin film self-nucleation experiments were successfully related, since thin film surface nanostructures were consistently correlated to calorimetric results. We established the dual self-nucleation experiment as a powerful tool to predictably tailor thin film nanostructures in the range of several nanometers.



### INTRODUCTION

The microphase separation of diblock copolymers provides a bottom-up approach for the creation of self-assembled surface nanostructures.<sup>1,2</sup> These nanostructures are promising for nanopatterning applications, with emphasis especially in the fields of photonic crystals<sup>3</sup> and bioanalytics.<sup>2,4</sup>

In the diblock copolymer bulk, the shape and size of its nanostructures depend on the composition, the degree of polymerization, the block interactions, and their ability to crystallize. Diblock copolymer nanostructures can form in the bulk as well as at the surface of thin diblock copolymer films.<sup>2,5</sup>

In semicrystalline diblock copolymers, the microphase separation of the blocks competes with their crystallization.<sup>6–9</sup>

This enables the tailorability of lamellar nanostructures by crystallization without changing the macromolecular architecture.<sup>6–9</sup> For strongly segregated semicrystalline diblock

copolymers with a high order–disorder transition temperature ( $T_{ODT}$ ), the crystallization starts within the confinement of microphase-separated domains<sup>6,7</sup> and may induce the formation of crystalline lamellae.<sup>10</sup> If the glass transition temperature  $T_g$  of the amorphous block is lower than the crystallization temperature  $T_c$  of the crystallizable block, the amorphous phase imposes a soft confinement on the crystallization; i.e., chain diffusion processes are possible.<sup>11</sup> In dependence of the  $T_c$  and the crystallization kinetics which regulate thickness and lateral dimensions of the resulting crystallites,<sup>12,13</sup> crystallization can occur within the micro-

Received: September 25, 2013

Revised: January 15, 2014

Published: February 18, 2014

domain confinement or it overwrites the microdomain structure, which is called breakout crystallization.<sup>6,12</sup>

One approach for the controlled crystallization of polymers, e.g., to crystallize lamellae with a specific thickness, is the self-nucleation experiment (SNE).<sup>13–16</sup> In the SNE, a polymer with a crystalline standard (CS) is annealed at a self-nucleation temperature  $T_s$  within the melting range of the CS. The CS is prepared by heating the polymer sufficiently above the melting temperature  $T_m$  which erases the polymer's temperature history and by cooling it to a low  $T_c$  (high undercooling) in a controlled manner subsequently. Depending on the choice of the  $T_s$  either crystal thickening, self-nucleation, partial melting, or complete melting occurs.<sup>13</sup>

Crystal thickening is known for decades and most studied on homo- or copolymer single crystals.<sup>17,18</sup> Also, the self-nucleation mechanism is fairly well understood for homopolymers.<sup>13–15</sup> To our best knowledge, however, only two studies deal with the self-nucleation of copolymers with one crystalline block.<sup>16,19</sup> These studies suggest that the SNE is ideally suited to study the crystallization in a confinement imposed by the microphase separation. Nevertheless, both studies were restricted to the diblock copolymer bulk.

In semicrystalline diblock copolymer thin films, the controlled annealing of a CS within a SNE can potentially tailor surface nanostructures by a defined thickening of the crystalline lamellae. Large area tailored surface nanostructures have promising applications, e.g., in the bioanalytical field to align or to control the conformation and assembly of adsorbed biomolecules,<sup>20–22</sup> where previously investigated systems like single crystals or bulk polymer cannot be applied. Therefore, the aim of this current study was to create and understand the lamellar thickening on the surface of an amphiphilic polybutadiene-*block*-poly(ethylene oxide) (PB-*b*-PEO) based on a thin film SNE.

We tested the hypothesis that, within two self-nucleation experiments, i.e., bulk and thin film, the calorimetric bulk properties of a PB-*b*-PEO can be correlated with the resulting thin film surface nanostructures to understand and predict their formation. This study was carried out to address the growing need for a reliable, reproducible, and feasible pathway to obtain surface nanostructures with predefined dimensions.

## EXPERIMENTAL SECTION

**Materials.** For the purposes of this study, we chose the semicrystalline PB-*b*-PEO because PEO is a widely characterized linear, crystallizable polymer<sup>18</sup> and PB has a  $T_g < T_c$  of PEO.<sup>23,24</sup> The latter is a requirement for crystalline lamellae thickening in a soft confinement of the second block. The PB-*b*-PEO was purchased from Polymer Source Inc. (Dorval, Canada). According to the manufacturer, PB has a molar mass of 5000 g/mol ( $M_{n,PB}$ ), i.e., a degree of polymerization of 93, with a polydispersity index (PDI) of 1.06. We recorded <sup>1</sup>H NMR spectra on a Bruker Avance 300 MHz spectrometer (Billerica, MA) in deuterated chloroform to obtain the PEO block's degree of polymerization which was calculated to be 57 (molar mass of the PEO block 2500 g/mol).

The thiol methyl 3-mercaptopropionate (M3M, purity 95%, Sigma-Aldrich Corporation, St. Louis, MO) was used for surface modification as received. All solvents (VWR, Darmstadt, Germany) were distilled before use.

**Bulk SNE: Differential Scanning Calorimetry.** Differential scanning calorimetry (DSC) of the bulk PB-*b*-PEO was carried out with a PerkinElmer Pyris 1 equipped with a thermal analysis controller 7/DX (PerkinElmer Inc., Waltham, MA) to study the crystallization, melting, and self-nucleation behavior.

The temperature cycle of the bulk SNE, performed in the DSC, is schematically depicted in Figure 1. In a first step, the CS was prepared.

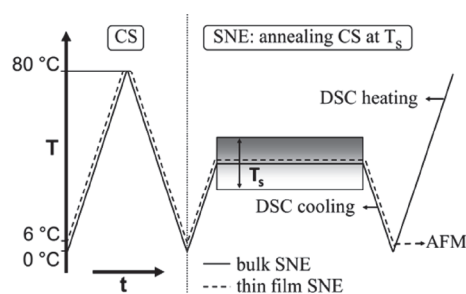


**Figure 1.** Schematic sketch illustrating the time–temperature  $t$ – $T$  profile of the bulk differential scanning calorimetry (DSC) based self-nucleation experiment (SNE) and the thin film SNE. The SNE can be divided into two steps: (i) the generation of a crystalline standard (CS) and (ii) annealing at the self-nucleation temperature  $T_s$  within the melting range of the CS. Subsequently, depending on the particular experiment, the annealed CS is characterized either by DSC or by atomic force microscopy (AFM). Note that the specific  $t$ – $T$  profiles may deviate from this schematic sketch.

In a second step, the CS samples were heated to a predefined  $T_s$  and annealed at that temperature for 10 min.  $T_s$  was varied from 36 to 52 °C.

Afterward, the samples were cooled to 0 °C and subsequently heated to 80 °C to analyze the resulting crystals (see Supporting Information for further details).

The  $T_c$  and  $T_m$  were defined by the corresponding peak values in the DSC scans. In all heating/cooling steps, the heating rate was 10 °C/min.

**Thin Film SNE: Sample Preparation.** Pieces of a gold-coated silicon wafer were used as substrates for the PB-*b*-PEO thin films because we aimed to modify them with the M3M thiol to increase the hydrophilicity (for details on the gold deposition and thiolation, see Supporting Information). In our experience, PB-*b*-PEO thin films on M3M modified substrates show considerably less dewetting than on pure gold or silicon surfaces.

Thin films were prepared by spin-coating 20  $\mu$ L of a 0.5 wt % copolymer/chloroform solution onto the M3M-modified gold surfaces at 4,000 rpm. The samples were heated in an oven at 80 °C for 1 h to erase the thermal history and were rapidly cooled by transferring them into a refrigerator set to a temperature of 6 °C afterward to create the thin film CS. The cooling rate in the refrigerator was not precisely determined, but within the crystallization range it was virtually comparable to the 10 °C/min used for the DSC measurements.

The thin film SNE was performed to investigate the influence of the chosen annealing temperature,  $T_s$ , on the thin film surface nanostructure. Therefore, thin film CS samples were held at selected  $T_s$  (36, 40, 44, 46, and 48 °C) in accordance with the bulk SNE. The annealing was performed for 96 h. All annealed film samples were immediately cooled in the refrigerator to 6 °C afterward. The entire thin film SNE temperature profile is schematically presented in Figure 1.

**Thin Film SNE: Atomic Force Microscopy.** The polymer films were characterized by atomic force microscopy (AFM) with a Dimension 3100 equipped with a Nanoscope Controller IV (Veeco Metrology, Santa Barbara, CA). The cantilevers were purchased from Olympus (model OMCL-AC160TS-W, Tokyo, Japan) and featured a resonance frequency of approximately 300 kHz, a spring constant of around 42 N/m, and a typical tip radius of less than 10 nm (typical 7 nm). AFM height and phase images were measured with a ratio of set-point  $A_{sp}$  to driving amplitude  $A_0$  of approximately  $A_{sp}/A_0 = 0.75$ . The polymer films' thickness was determined by AFM height measurements performed at carefully introduced scratches.

For the determination of the long-period  $l_0$ , i.e., the PB and PEO lamellae size, a two-dimensional fast Fourier transformation (FFT) was applied to the AFM phase images. The spatial frequency with the maximum intensity in the 2D FFT spectra was retransformed to the spatial domain and considered to be the long period. The results were compared with lamellae sizes, manually determined by studying ten line plots of the phase values perpendicularly to the lamellae direction. The half-height method was applied to calculate the individual thickness of the crystalline  $l_{\text{PEO}}$  and the adjacent amorphous lamellae  $l_{\text{PB}}$ .<sup>25</sup>

## RESULTS

First, the crystallization, melting, and self-nucleation behavior of the bulk polymer were studied in the framework of a bulk SNE by DSC. In a second step, the SNE was repeated with PB-*b*-PEO thin films, and the thin film surface structure was investigated with AFM, i.e., the thin film SNE.

**Bulk SNE: Differential Scanning Calorimetry.** Prior to the bulk SNE, the CS was calorimetrically characterized (Figure 2, bottom curves), and a  $T_c = 19.5$  °C (Figure 2A) and  $T_m =$

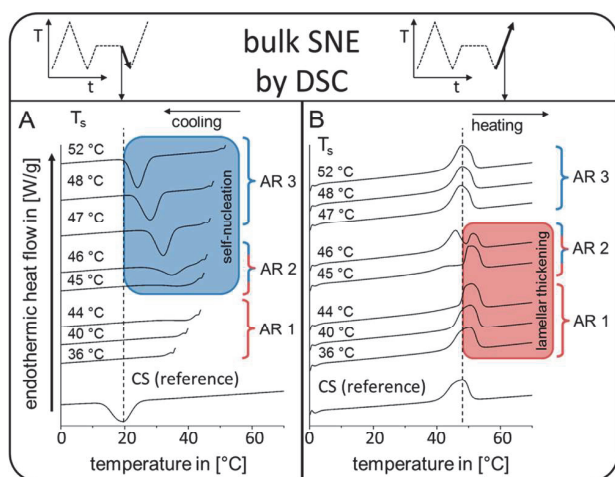


**Figure 2.** Calorimetric characterization of the PB-*b*-PEO in the bulk SNE. Plot A shows the cooling scans after annealing at indicated  $T_s$ . Plot B displays the corresponding heating scans. The distinct annealing regimes (ARs) are marked. The cooling and heating scan of the CS reference is shown at the bottom. Corresponding crystallization and melting peak temperatures as well as enthalpies are presented in Table 1.

47.9 °C (Figure 2B) were obtained. In addition, the melting range of the CS between the beginning of the melting peak at 36.0 °C and melting peak offset at 51.3 °C determined the  $T_s$  interval in which the SNE was performed (Figure 2B, bottom curve).

In dependence of the  $T_s$ , three different annealing regimes (AR) can be distinguished in the following bulk SNE, which are shown in Figure 2, split into the cooling (Figure 2A) and heating curves (Figure 2B):

**AR 1:** For a  $T_s$  between 36 and 44 °C, no crystallization peak was observed during cooling, but during heating the  $T_m$  increased monotonously from 50.3 to 50.9 °C.

**AR 2:** For a  $T_s$  of 45 and 46 °C, small crystallization peaks were observed during cooling, and two distinct melting peaks were observed during heating.

**AR 3:** For a  $T_s$  between 47 and 52 °C, broad crystallization peaks were observed during cooling, whereby  $T_c$  decreased

from 32.2 to 24.0 °C and the  $T_m = 48.0$  °C stayed constant, except for  $T_s = 47$  °C, where  $T_m = 47.6$  °C during heating.

Table 1 summarizes the  $T_c$  and  $T_m$  as well as the enthalpies of crystallization and fusion of the bulk SNE.

**Table 1. Summary of the Calorimetric Properties of the Bulk SNE for Selected  $T_s$ <sup>a</sup>**

$T_s$ (°C)	$T_c$ (°C)	$T_{m1}/T_{m2}$	$\Delta H_c$ (J/g)	$\Delta H_f$ (J/g)	annealing regime (AR)
—	19.5	47.9/—	38.9	38.7	CS (not annealed)
36	—	50.3/—	0	40.8	1
40	—	50.5/—	0	40.9	1
44	—	50.9/—	0	40.6	1
45	36.4	43.3/51.0	10.3	40.3	2
46	34.7	45.9/51.5	24.1	40.2	2
47	32.2	47.6/—	39.9	39.8	3
48	28.0	48.0/—	39.6	39.0	3
52	24.0	48.0/—	39.3	38.8	3

<sup>a</sup>The table lists the crystallization temperatures  $T_c$ , melting temperatures  $T_m$ , enthalpies of crystallization  $\Delta H_c$  and enthalpies of fusion  $\Delta H_f$  as determined from the data in Figure 2.  $T_{m2}$  applies in cases where the DSC heating scan featured two melting peaks and designates the one at higher temperatures.

**Thin Film SNE: Thin Film CS Nanostructure.** Figure 3A displays the AFM phase image of the thin film CS surface. The

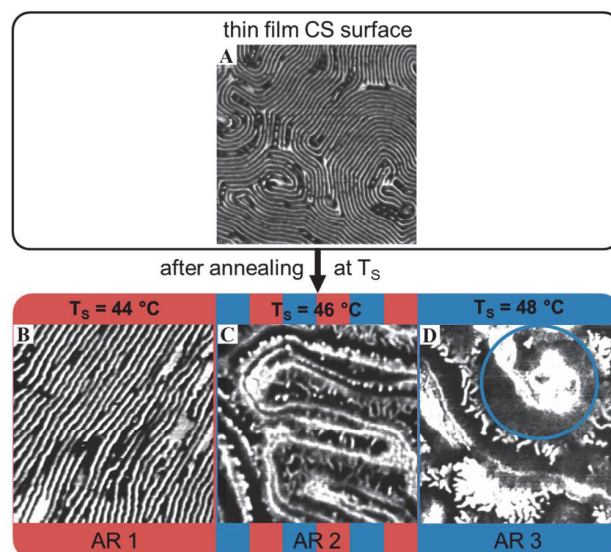


**Figure 3.** AFM phase images (image size  $1 \mu\text{m} \times 1 \mu\text{m}$ , maximum phase value range  $10^\circ$ ) of the PB-*b*-PEO thin films. The thin film CS surface is shown in (A). Film surfaces after annealing in the different annealing regimes at  $T_s$  of 44, 46, and 48 °C are displayed in (B), (C), and (D), respectively. The spherulite in (D) is highlighted in blue. The displayed nanostructures are representative for the respective AR. The crystalline PEO and amorphous PB appear bright and dark, respectively.

image shows two distinct phases that represent the PEO (bright) and PB (dark) phase which were arranged as meandering lamellae and were observed throughout the entire sample.

The observed phase contrast arises from stiffness differences at the film surface. Stiffer crystalline phases appear brighter than softer amorphous phases under the applied tapping mode

conditions with an amplitude ratio within the interval of  $0.3 < A_{sp}/A_0 < 0.8$ .<sup>26</sup> The long-period  $l_0$  ( $l_{PB} + l_{PEO}$ ) of the thin film CS surface's lamellar nanostructure was determined to be 21.7 nm by the 2D FFT spectrum and  $21.0 \pm 3.1$  nm by the line plot method. Furthermore, by analyzing the line plots with the half-height method, we determined the thickness of the amorphous PB and the crystalline PEO phase to be  $l_{PB} = 12.8 \pm 1.8$  nm and  $l_{PEO} = 8.2 \pm 1.3$  nm, respectively.

The CS thin films had a film thickness of approximately 60 nm, which was determined from AFM height images at carefully introduced scratches (data not shown).

**Thin Film SNE: Surfaces after Annealing.** To characterize the effect of the different annealing regions found in the bulk SNE (Figure 2) on the evolution of the thin film CS surfaces, they were annealed at similar  $T_s$  of 44, 46, and 48 °C located in AR 1, AR 2, and AR 3, respectively. The samples were characterized at room temperature by AFM phase imaging, shown in Figure 3B–D.

**AR 1:** Figure 3B illustrates the surface nanostructure of a PB-*b*-PEO film annealed at  $T_s = 44$  °C. The lamellar surface of the thin film CS after annealing was maintained but compared to the unannealed thin film CS the lamellar long-period  $l_0$  increased. The detailed values for the increased  $l_0$  are given in the next subsection in which the tailoring of lamellar nanostructures by AR 1 annealing is presented in detail.

**AR 2:** After annealing the thin film CS at  $T_s = 46$  °C, the film surface featured thick meandering crystalline lamellae and small crystallites in between (Figure 3C).

**AR 3:** Figure 3D displays the thin film CS surface after annealing at  $T_s = 48$  °C. The lamellar surface nanostructure disappeared, and spherulites with individual concentric lamellar crystals at their rim appeared.

**Thin Film SNE in AR 1: Tailoring Lamellae Thickness by the Choice of  $T_s$ .** Since we found a lamellar thickening effect in AR 1, we explored it in more detail by varying  $T_s$  in AR 1 using smaller temperature steps. Thin film CSs were annealed at a  $T_s$  of 36, 40, and 44 °C in AR 1, respectively. Figure 4 shows AFM phase images of the thin film CS after annealing and the corresponding AFM line plots.

Lamellar surface structures were observed for every  $T_s$  in AR 1. The  $l_0$  of these lamellar surface nanostructures as well as the thickness of the respective PEO and PB phase,  $l_{PEO}$  and  $l_{PB}$ , are shown in Table 2. In addition, the  $l_{PEO}$  values are displayed in relation to the PEO extended chain length  $l_{ext} = 15.9$  nm. The latter value is obtained by multiplying the PEO contour length of 0.2783 nm by the degree of polymerization (of 57).  $l_{PEO}/l_{ext}$  yields the basis for the chain fold models presented later.<sup>27</sup> It is obvious that the microdomain spacing increased with increasing  $T_s$  in AR 1 compared to the thin film CS.

## DISCUSSION

In this study, we identified three annealing regimes with specific calorimetric bulk properties of the PB-*b*-PEO in a bulk SNE. The analogue thin film SNE led to three thin film surface nanostructure types for these three ARs. Thus, each AR in the DSC SNE corresponds to a distinct surface nanostructure and hence strongly suggests a correlation between bulk and thin film SNE. As a key finding of this study, this correlation allows us to systematically tailor the surface nanostructure of a diblock copolymer thin film in AR 1.

This section is divided as follows: First, we establish the correlation between bulk and thin film SNE. Afterward, we discuss the lamellae thickening effect observed in the thin film

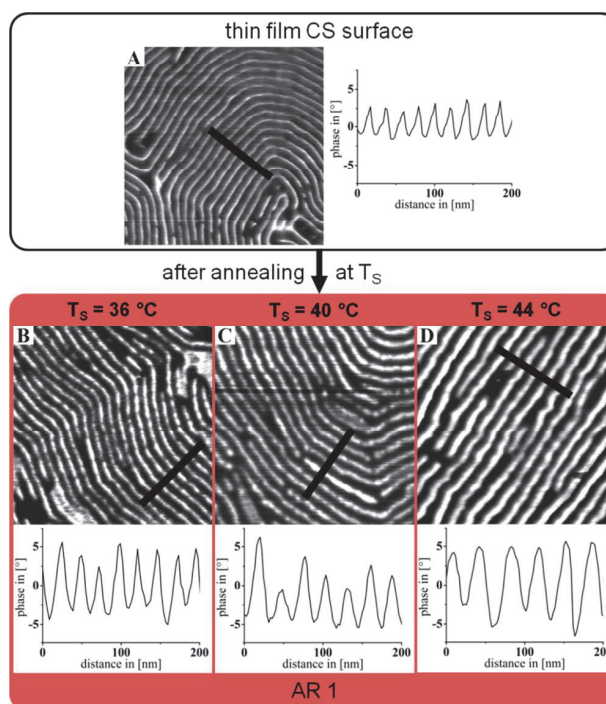


**Figure 4.** AFM phase images (image size 500 nm  $\times$  500 nm, maximum phase value range 10°) of PB-*b*-PEO thin films and the corresponding line plots. The thin film CS surface is shown in (A). The lamellar film surfaces after annealing at  $T_s$  of 36, 40, and 44 °C are displayed in (B), (C), and (D), respectively. The crystalline PEO is bright and the amorphous PB is dark. The corresponding line plots were derived from the corresponding lines in the phase images.

**Table 2. Quantification of Nanostructures in AR 1<sup>a</sup>**

annealing	$l_{PEO}$ (nm)	$l_{PEO}/l_{ext}$	$l_{PB}$ (nm)	$l_0$ (nm)
CS (none)	$8.2 \pm 1.3$	0.51	$12.8 \pm 1.8$	$21.0 \pm 3.1$ (21.7)
$T_s = 36$ °C	$10.8 \pm 1.6$	0.67	$13.5 \pm 2.0$	$24.3 \pm 3.6$ (25.2)
$T_s = 40$ °C	$12.4 \pm 1.8$	0.78	$15.4 \pm 2.4$	$27.8 \pm 4.2$ (27.6)
$T_s = 44$ °C	$16.1 \pm 2.2$	1.01	$18.1 \pm 2.0$	$34.2 \pm 4.3$ (33.7)

<sup>a</sup>The thickness of the PEO phase,  $l_{PEO}$ , its relative value to the extended PEO chain length  $l_{ext}$ , the thickness of the PB phase,  $l_{PB}$ , and the long period  $l_0$  are listed in dependence of the  $T_s$ . The length values were determined by line plots; the values obtained by the 2D FFT are given in parentheses.

SNE in AR 1. Finally, a brief theoretical discussion of the results in analogy to the Hoffman–Weeks and Gibbs–Thomson plots enables us to predict the self-nucleation temperature to obtain a specific PEO lamellae thickness.

**Bulk SNE: Differential Scanning Calorimetry.** The calorimetric properties of the PB-*b*-PEO were studied in the framework of the bulk SNE. Three different annealing regimes, i.e., AR 1, AR 2, and AR 3, were found in the bulk SNE (Figure 2).

The characteristics of the AR 1 are no crystallization peaks during cooling and increased melting temperatures, compared to the CS, during the subsequent heating. Both characteristics are explained by the annealing of the crystalline PEO block which induced thicker crystals with less crystal defects compared to the CS, yet no PEO was molten during annealing.<sup>13–16</sup> The annealing is evidenced by the increase of

the enthalpy of fusion from 38.7 J/g for the CS to  $40.7 \pm 0.2$  J/g in AR 1 (Table 1).

For AR 2, we observed small crystallization peaks during cooling and two distinct melting peaks, i.e.,  $T_{m,1}$  and  $T_{m,2}$  during heating. The crystallization occurred at increased temperatures compared to the CS which indicates self-nucleation during cooling.<sup>13–16</sup> In comparison to the CS, one of the melting peaks ( $T_{m,2}$ ) was shifted to higher temperatures, caused by a crystal thickening during annealing. The twofold observation, crystal thickening during the annealing and the self-nucleated crystallization during subsequent cooling, indicates a partial melting during annealing.<sup>13–16</sup> Therefore, the second melting peak ( $T_{m,1}$ ) can be assigned to the melting of self-nucleated crystals. In comparison to AR 1, the enthalpy of fusion for AR 2 slightly decreased to  $40.2 \pm 0.1$  J/g, which indicates less crystal perfection, in turn a potential result of the impediment of the crystal growth during cooling by the thickened, remaining crystals.

In AR 3, a broad crystallization peak during cooling and a single melting peak during subsequent heating were found. Here, the crystallization occurred at increased temperatures compared to the CS, too, which indicates self-nucleation during cooling.<sup>13–16</sup> The effect that  $T_c$  decreased with increasing  $T_s$  is explained by a decreased short-range order present in the melt during cooling.<sup>14–16</sup>  $T_m$  remained nearly constant compared to the CS at about 48 °C, which led to the conclusion that no crystal thickening occurred, and in turn, this suggests that all crystals were molten during annealing in AR 3. This agrees well with the enthalpies of fusion in AR 3 of  $39.0 \pm 0.2$  J/g, which approach the values of the CS, 38.7 J/g, again.

To the best of our knowledge, only two bulk SNE of semicrystalline diblock copolymers (polyethylene-*block*-polystyrene)<sup>16,19</sup> and one double crystalline diblock copolymer (poly(*p*-dioxanone)-*block*-poly( $\epsilon$ -caprolactone))<sup>28</sup> have been reported so far. Similar calorimetric characteristics for PEO crystallization and self-nucleation were found for the annealing of miscible blends of poly(ethylene oxide)/poly(3-hydroxybutyrate).<sup>29</sup> Nevertheless, our study is the first report of a bulk SNE on an amphiphilic diblock copolymer. Amphiphilic diblock copolymers are potentially useful for new applications of nanostructured polymers in the life sciences.<sup>2,4,30</sup>

**Thin Film SNE: Thin Film CS Nanostructure.** The thin film CS (Figure 3A) showed a meandering lamellar surface nanostructure, a sign that microphase separation occurred before crystallization,<sup>23,24</sup> which was prepared by complete melting and subsequent fast cooling of the PB-*b*-PEO thin films. In this subsection we explain the formation of the thin film CS nanostructure.

In our thin film CS (Figure 3A), the lamellar surface structure was homogeneously observable over the entire film surface. This is the result of the rapid cooling applied to obtain the thin film CS since in case of slow cooling lateral breakout crystallization occurred.<sup>31</sup> The rapid cooling probably promoted a high rate of nucleation and impeded the lateral crystal growth due to limited diffusion. The relaxation time of the PB phase is increased for lower temperatures which may have led to a stronger confinement.

The  $l_0$  as well as  $l_{PEO}$  and  $l_{PB}$  value of the thin film CS meandering lamellae were determined to be 21, 8, and 13 nm (Table 1), respectively. Assuming the lamellar structure of the PB-*b*-PEO thin film extends from the thin film surface to the substrate, a PEO volume fraction of  $21 \text{ nm}/8 \text{ nm} = 0.39$  can be calculated. However, this disagrees with the crystalline PEO

volume fraction  $f^{PEO,c}$  based on the molecular weight of the blocks of approximately 0.26 (see Supporting Information for details). Thus, we propose that the observed surface lamellar structure consisted of PEO cylinders oriented parallel to the surface, confined in a PB matrix. For this to occur, the PEO crystallization must have been confined to cylinders by the soft PB block. This agrees with previous reports on thin films of cylinder-forming low molar mass poly(ethylene-*co*-butylene)-*block*-poly(ethylene oxide) and PB-*b*-PEO diblock copolymers.<sup>32</sup>

For low molar mass crystalline homopolymers and diblock copolymers it has previously been observed that the crystalline lamellae thickness depends on the chain folding state and, thus, directly on the chain length.<sup>17,18,33–36</sup> For the polymer used here the theoretical length of the extended crystallized PEO block  $l_{ext}$  is 15.9 nm. Crystalline PEO lamellae consisting of once-folded chains, correspondingly, have a thickness of approximately 7.9 nm. Based on the double-layer crystal model of Lotz and Kovacs,<sup>17</sup> the theoretical, thickest conceivable PEO crystal for the PB-*b*-PEO consist of noninterdigitated extended PEO chains,<sup>34</sup> called the double extended conformation with a theoretical thickness of  $l_{de} = 31.8$  nm. The constancy of the enthalpies of fusion (Table 1), and thus the degree of crystallization, allows the interpretation of varying lamellae thicknesses as measured by AFM as a change in the chain conformation. The thickness of the thin film CS PEO phase of  $l_{PEO} = 8$  nm (Table 1) matches the once-folded PEO chain length, i.e., 7.9 nm, well. This can be explained if both nucleation and growth were restricted by the soft PB confinement to a cylinder with a smaller diameter than the PEO extended chain length. Once-folded chain crystals have previously been found for low molar mass crystallizable homopolymers, amorphous–crystalline and double crystalline diblock copolymers in the bulk and in the thin film.<sup>17,18,33–35</sup>

A model for the thin film CS nanostructure is presented in a following subsection and combined with corresponding models for emerging nanostructures (Figure 5).

**Thin Film SNE: Nanostructures after Annealing.** In the thin film SNE we observed three distinct types of thin film surface structures in dependence of the AR:

**AR 1:** After annealing the thin film CS at  $T_s = 44$  °C, the surface structure was still lamellar (Figure 3B), but the lamellar long-period  $l_0$  increased compared to the unannealed thin film CS. This observation is explained by the thickening of PEO crystals during the annealing because an increased  $T_m$ , a hallmark of thicker crystals, was measured in the corresponding bulk SNE heating scan (Figure 2B). Furthermore, no crystallization peaks were found in the bulk SNE cooling scan (Figure 2A), which means that the crystalline PEO just rearranged on a local scale but did not melt. Temperature-dependent lamellar thickening of PEO in AR 1 is discussed in more detail in the next subsection.

**AR 2:** After annealing the thin film CS at  $T_s = 46$  °C, the film surface nanostructure consisted of two crystal species: (i) thick, meandering crystalline lamellae and (ii) small crystallites in between (Figure 3C). Accordingly, the corresponding bulk SNE heating scan (Figure 2B) featured two melting peaks with  $T_{m,1} = 45.9$  °C and  $T_{m,2} = 51.5$  °C. In addition, compared to the CS, we observed a crystallization peak with an increased  $T_c = 36.4$  °C in the bulk SNE cooling scan (Figure 2A) that unveils self-nucleation during cooling. The residual, thick, meandering crystalline lamellae (Figure 3C) are correlated with the  $T_{m,2}$  and the small crystallites in between with  $T_c$  and  $T_{m,1}$ :

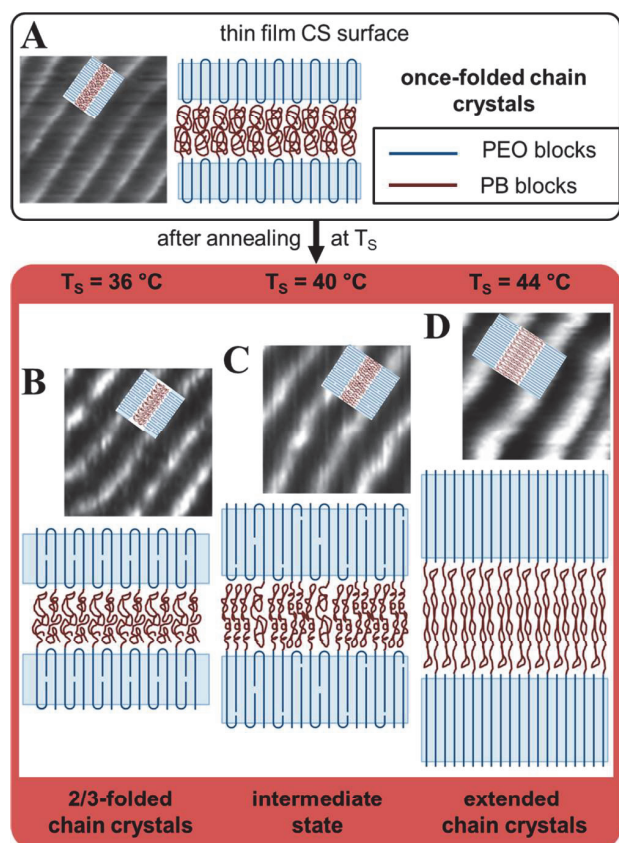


**Figure 5.** Schematic PEO thickening model. AFM phase images (image size 100 nm  $\times$  100 nm, maximum phase value range 10 $^\circ$ ) are magnifications of the AFM phase images in Figure 4. The corresponding models (not to scale) show two crystalline PEO lamellae and part of the PB matrix phase. (A) The initial once-folded crystals in the thin film CS. (B, C, D) PEO chain conformation after annealing in AR 1 at  $T_s = 36, 40,$  and  $44$   $^\circ\text{C}$ , respectively. Note that the polydispersity of chains, i.e. PEO chains with different length, is only shown in (C) and omitted in (A, B, D) for clarity.

The meandering of the thick crystalline lamellae (Figure 3C) indicates that they had originally been formed in the thin film CS and thickened afterward. We suppose that these thick crystalline lamellae were built by the longer PEO chains of the polymer weight distribution (PDI = 1.06) and, thus, exhibit the highest melting temperatures, i.e.,  $T_{m,2}$ . In fact, it is suggested by a theoretical analysis in the next subsection that the PEO crystals associated with  $T_{m,2}$  in AR 2 were comprised of double extended chains. Shorter PEO chains formed no crystallites because their  $T_m$  was too low to persist at  $T_s$ .

In the melt of the shorter PEO blocks a high degree of short-range order remained. This short-range order enabled self-nucleated recrystallization of the shorter PEO blocks during cooling, which is evident from the increased  $T_c$  in the corresponding bulk SNE (Figure 2A). The self-nucleated shorter PEO blocks formed small crystallites, which partially overwrote the original thin film CS structure (Figure 3C). This is a form of breakout crystallization because the higher crystallization temperatures lead to a softening of the PB phase.

In conclusion, the two crystalline species on the annealed film surface resulted from a partial melting of the thin film CS lamellae that included lamellar thickening and self-nucleated crystallization during cooling.

AR 3: After annealing at  $T_s = 48$   $^\circ\text{C}$ , the original lamellar thin film CS surface structure disappeared and spherulites with individual concentric lamellar crystals at their rim appeared (Figure 3D). In the corresponding bulk SNE cooling scan (Figure 2A), self-nucleation was detected because the  $T_c$  increased compared to the CS. In addition, the bulk SNE heating scan (Figure 2B) showed only one melting peak with a  $T_m = 48$   $^\circ\text{C}$ , similar to the CS. Thus, the obtained thin film surface nanostructure is explained by a melting of all thin film CS lamellae during annealing and a self-nucleated crystallization during subsequent cooling. The spherulitic shape is a result of the weaker PB block confinement, i.e., breakout crystallization, at elevated temperatures and the increased time the PEO crystal is given to grow parallel to the substrate in comparison to the thin film CS.

In previous studies, surface parallel crystallization, i.e., a type of breakout crystallization, has already been observed on the surface of cylindrical thin films for a hydrogenated PB-*b*-PEO after isothermal crystallization at 40  $^\circ\text{C}$  and after long-term storage of poly(isoprene-*block*-ethylene oxide) thin films at room temperature.<sup>31</sup>

In conclusion, the changes of the thin film CS surface structure in the thin film SNE (Figure 3) are explained by different events, interpreted on the basis of the bulk SNE data (Figure 2): (i) no melting and lamellar thickening for AR 1, (ii) partial melting including lamellar thickening and self-nucleated breakout crystallization during cooling in AR 2, and (iii) melting of all crystalline lamellae and self-nucleated breakout crystallization during cooling in AR 3.

None of the three previous studies which applied the SNE to diblock copolymers correlated the calorimetric properties with resulting surface micro- and nanostructures.<sup>16,19,28</sup> Yet, in this study good correlations were found between calorimetric bulk properties as measured by DSC ( $T_m$  ( $T_s$ ),  $T_c$  ( $T_s$ ),  $\Delta H_f$  ( $T_s$ )) and their changes relative to the CS values) and distinct thin film surface structures (crystalline lamellae, spherulites, and lamellar thickness as well as orientation) as measured by AFM. The knowledge of the systematic relation between calorimetric properties and surface nanostructure is essential to predictably tailor copolymer thin film nanostructures by crystal thickening.

At first glance, it surprises that the bulk polymer DSC data correlates so well with thin film polymer nanostructures. DSC, however, measures melting, crystallization, and microphase separation behavior of polymer nanostructures.<sup>37</sup> It is this nanostructure that we also observed in AFM measurements of thin diblock copolymer films.

One can at least expect two deviations of structure and/or properties between bulk polymers and thin film: (i) differences in  $T_g$  due to a change from bulk diffusion to surface diffusion and (ii) limited crystal orientation possibilities due to the confinement of the thin film. The former effect (i) will lead to an increased  $T_g$  value,<sup>38</sup> which can increase the rigidity of the PB soft confinement and might be relevant for our thin films with a thickness <60 nm. However, it has no effect on the crystalline properties of our film, as we used prolonged annealing times of 96 h for the thin film SNEs. Differences in crystal orientation between polymer bulk and thin film, i.e., effect (ii), will not have an effect on DSC results. In general, it has already been stated by Hoffman et al. that there is little difference between nanometer sized single crystals and bulk polymer crystals when the melting point is concerned.<sup>39</sup>

**Thin Film SNE in AR 1: Tailoring Lamellae Thickness by the Choice of  $T_s$ .** We have shown that a lamellar



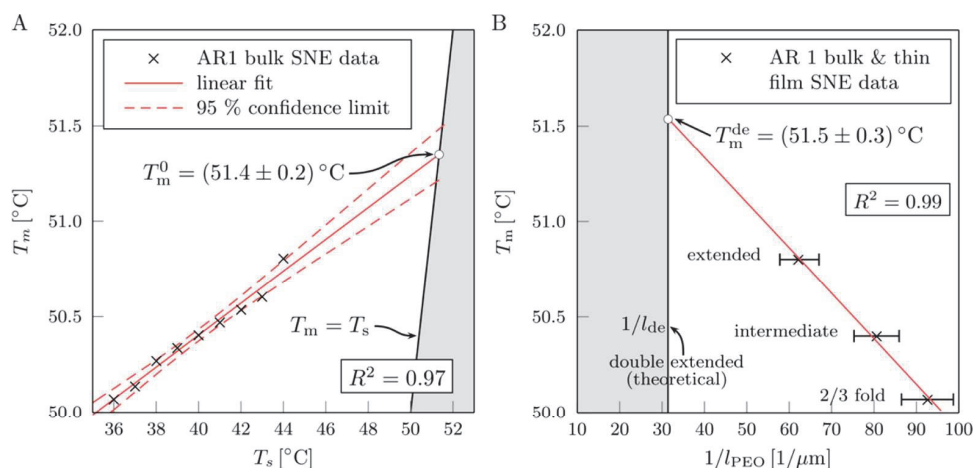


**Figure 6.** Theoretical analysis of bulk and thin film SNE data in AR 1. (A) is a Hoffman–Weeks analogous plot fitted according to eq 1. (B) is the Gibbs–Thomson plot fitted according to eq 2. The gray regions are experimentally “inaccessible” areas:  $T_m \geq T_s$  and  $l_{PEO} \leq l_{de}$  at all times.

thickening can be accomplished in PB-*b*-PEO thin films by increasing the  $T_s$  in the range of 36–44 °C (Figure 4). In this subsection, we develop a model of the  $T_s$  depending lamellar thickening (Figure 5) by comparing the  $l_{PEO}$  values measured by AFM to dimensions of a theoretical chain conformation. Afterward, on the basis of an analogy to the Hoffman–Weeks and Gibbs–Thomson plots for semicrystalline homopolymers, we establish a functional relationship between the lamellar thickness  $l_{PEO}$  and  $T_s$  which will allow us to predict the  $T_s$  for a desired  $l_{PEO}$ . Finally, we discuss the effect of the PEO lamellae thickening on the amorphous PB phase.

The following PEO lamellar thickening model is based on two established assumptions: First, we suggest that the *c*-axis of the PEO crystals and, thus, the PEO chains themselves were oriented parallel to the substrate surface. If this *c*-axis orientation had not been present, one would have observed crystal growth parallel to the film plane, which was not the case. The *c*-axis orientation effect has previously been investigated in polyethylene-*block*-poly(ethylene oxide) co-oligomer thin films by grazing incidence X-ray scattering experiments.<sup>40</sup> Second, PEO lamellae thinner than the extended PEO chain length consist of a single interdigitated crystal (zipper principle) where the PEO chains of the PB-*b*-PEO enter from both sides of the crystal.<sup>34</sup> A PEO lamellae thicker than the extended PEO chain length consists of noninterdigitated PEO crystals; thus, the thickest possible PEO crystalline lamellae consist of double extended PEO chains.<sup>17,34,41</sup>

On the basis of the obtained  $l_{PEO}/l_{ext}$  values (Table 2) we identify the following PEO chain conformations: The thin film CS consists of once folded chains (Figure 5A). The  $T_s = 36$  °C and  $T_s = 40$  °C samples fit the noninteger folded PEO chain (Figure 5B,C), while the  $T_s = 44$  °C sample comprises of extended PEO chains (Figure 5D).

According to the literature, the noninteger folded crystals are not stable for homopolymers and, thus, cannot be precisely assembled.<sup>42</sup> For semicrystalline diblock copolymers thin films, Reiter et al. observed that the lamellae were formed by stable integer folded as well as the noninteger folded chains.<sup>34</sup> In addition, they predicted extended chain lamellae but did not observe them. We think this is due to the fact that Reiter et al. crystallized the thin films from the melt. This has one great disadvantage: The formation of thicker crystals, e.g., consisting of extended chains, requires low undercoolings, where in turn

the nucleation rate is very low and the secondary nucleation rate (lateral crystal growth) is high. Because of the thin film geometry, lateral crystal growth occurs parallel to the film surface and, thus, inhibits the formation of surface perpendicular lamellar nanostructures, which are required for applications.

In contrast, in this study we avoided lateral crystal growth by thickening the CS, which contains a high nuclei density. Therefore, integer and noninteger folded as well as extended chain crystals can be individually observed in the surface lamellar nanostructures, depending on the subsequent annealing temperature. This extends the length range of tunable surface lamellae nanostructures by at least a factor of 1.5.

Then again, the observation of noninteger folded intermediate states at  $T_s = 36$  and 40 °C suggests that the crystalline lamellae thickness can be adjusted continuously between the integer folded and the extended state. This can only be explained by the block length distribution because for a monodisperse PB-*b*-PEO, discrete chain conformations similar to homopolymers are expected.

The intermediate thickness can, thus, be realized if PEO chains with different lengths form the crystalline PEO lamellae. Short PEO blocks, therefore, may be integrated as extended chains into the crystalline lamellae while long PEO blocks are integrated in the same crystal in a folded conformation.

Crystalline lamellae consisting of chains with different length were first observed for binary mixtures of *n*-alkanes.<sup>33</sup> We assume that the observed intermediate state will enable us to design nanostructures with continuously tunable lamellae widths.

**Thin Film SNE in AR 1: Prediction of  $l_{PEO}$  as a Function of  $T_s$ .** We will now establish a functional relation between  $l_{PEO}$  and  $T_s$  by applying an analogy to the Hoffman–Weeks and Gibbs–Thomson equations for homopolymers,<sup>39</sup> which predict a linear relationship between  $T_m$  and  $T_c$  and a linear relationship between  $T_m$  and  $l^{-1}$ , respectively:

$$T_m = T_m^\infty \left( 1 - \frac{1}{\gamma} \right) + \frac{T_c^i}{\gamma} \quad (1)$$

and

$$T_m = T_m^\infty \left( 1 - \frac{2\sigma}{\Delta H_f^0 l} \right) \quad (2)$$

In these equations  $T_m^\infty$  is the melting point of a perfect crystal composed of infinite long polymer chains (for PEO  $T_m^\infty = 68.9$  °C),<sup>18</sup>  $\gamma$  is the folding parameter,  $T_c^i$  is an isothermal crystallization temperature,  $\sigma$  is the surface free energy of the crystal forming in the melt (for extended PEO chains  $\sigma = 25.5$  erg/cm<sup>2</sup>),<sup>18</sup> and  $\Delta H_f^0$  the enthalpy of fusion for a completely crystalline polymer (for PEO  $\Delta H_f = 196.4$  J/g).<sup>18</sup> Ashman and Booth extended the theory to diblock copolymers, and their result is that essentially that the Gibbs–Thomson equation is preserved but the meaning of  $\sigma$  changes.<sup>43</sup>

Therefore, by equating eqs 1 and 2, we find

$$l = \left( \frac{2\sigma}{\Delta H_f^0} \right) \frac{\gamma T_m^\infty}{T_m^\infty - T_c} \quad (3)$$

Equations 1–3 have been questioned in the literature, and they do not apply here without severe limitations (see Supporting Information for details).<sup>18,44,45</sup> Nevertheless, we will use this simple model (eqs 1–3) and apply it as a first-order approximation due to its simplicity (for a more rigorous treatment the application of the theory of Buckley and Kovacs is suggested which accounts for low molecular weight effects).<sup>18</sup>

A second assumption we made is that the Hoffman–Weeks equation, which describes the thickening during the crystallization can be used to describe the thickening of already existing crystals (we equate  $T_c^i$  with  $T_s$ ). According to the derivation of the Hoffman–Weeks equation,<sup>39</sup> this modifies the meaning of the folding parameter  $\gamma$ . Therefore, we cannot extract thermodynamic properties from the first-order approximation, like the folding parameter or the surface free energy of the crystal in a physically meaningful way.

We used the  $T_m$  and  $T_s$  data of the bulk SNE in AR 1 (partly presented in Table 1) to generate the Hoffman–Weeks plot (Figure 6A). By extrapolating the data to  $T_m = T_s$ , the most stable crystalline species in the PB-*b*-PEO was found to melt at  $T_s = T_m = (51.4 \pm 0.2)$  °C =  $T_m^0$ . This fits the second melting peak  $T_{m,2} = 51.5$  °C (Table 2 and Figure 2) measured during the bulk SNE in AR 2, which, in turn, is linked to the thick meandering lamellae in the thin film SNE (Figure 3C).

We can further use the  $T_m$  and  $l_{\text{PEO}}$  data (bulk SNE and thin film SNE) in AR 1 (Tables 1 and 2) to display the Gibbs–Thomson plot (Figure 6B). By linearly extrapolating the Gibbs–Thomson plot, the melting point of the double extended chain PEO crystal with a length of  $l_{\text{de}} = 31.8$  nm is predicted to be  $T_m^{\text{de}} = 51.5 \pm 0.3$  °C. This value matches  $T_m^0$  fairly well (Figure 6). With  $T_m^0$ , we have the case that a DSC derived property can also predict structure because for the PB-*b*-PEO the hypothetically most stable crystal has a defined shape, i.e., double extended chain.<sup>17</sup> The agreement of the individually obtained  $T_m^0$  and  $T_m^{\text{de}}$  values lead to two findings. First, the assumption of the existence of the double extended PEO crystals in AR 2 (see above) is valid. Second, but even more important, it indicates that the relation between the bulk SNE and thin film SNE is viable and correct because here we combine data from both bulk SNE and thin film SNE, and they predict the same melting temperature for the most stable crystal, i.e.,  $T_m^0 = T_m^{\text{de}}$ . Thus, we conclude that all possible uncertainties and differences that may have occurred in the sample preparation between bulk and thin film SNE do not affect the crystallization of the PEO phase, at least not to an

extent that invalidates the relation between bulk and thin film SNE.

Thus, with the linear fitting parameters of the Hoffman–Weeks and Gibbs–Thomson plots (Figure 6), we obtain, in a first order approximation, the relation between  $l_{\text{PEO}}$  and  $T_s$  (in Kelvin):

$$l_{\text{PEO}} = \frac{\alpha}{\beta - T_s}, \quad \text{for } T_s \leq T_m^0 = T_m^{\text{de}} \quad (\text{in units of K}) \quad (4)$$

with  $\alpha = (2.4 \pm 0.3) \times 10^{-7}$  m K and  $\beta = 332.1 \pm 2.0$  K. The errors of the parameters are calculated by a propagation of uncertainties where for the fit of the Gibbs–Thomson plot (Figure 6B);  $T_m^0 = T_m^{\text{de}}$  and  $l_{\text{de}}$  were used as a fourth pair of values.

It would be desirable to increase the number of data-points for the Gibbs–Thomson plot or reduce the error of the length measurement by replacing the AFM measurements with grating incidence small-angle X-ray data measurements. The maximum achievable lamellae thickness predicted by eq 4 is  $l_{\text{PEO}} = l_{\text{de}} = 31.8$  nm. However, lamellae as thick as  $l_{\text{de}}$  with a  $T_m^{\text{de}}$  were only present in AR 2, but the corresponding thin film surface featured an inhomogeneous coverage of thick lamellae (Figure 3C) which precluded its direct measurement. Also from an application's point of view where a homogeneous surface coverage is desired, the predictable crystal thickness is limited to the thickness of the extended PEO chain length (AR 1). Nevertheless, it can be concluded that based on a dual SNE, it is possible to predict the PEO lamellae thickness  $l_{\text{PEO}}$  in thin block copolymer films obtained at a specific annealing temperature  $T_s$  which is a key result of the current study.

Concurrently to the thickening of the crystalline PEO phase, we observed an increase of the amorphous PB phase width (Table 2) with increasing  $T_s$ . The thickening of the PB phase is explained by an increased chain stretching as a result of the higher junction point density within the interface between the PB and PEO due to the formation of less folded chain crystals.

In general, the formation of polymer crystals with different thicknesses has been intensively studied for homopolymers by crystallization from the melt or solution and by lamellar thickening.<sup>18,33,39</sup> It has also been studied for semicrystalline diblock copolymers in the bulk or at their single crystals by crystallization from the melt or solution.<sup>9,17,34</sup> But, from an application's point of view, it is especially important to achieve heterogeneous lamellar structures *at the surface*, ideally with a (thermally) tunable lamellae size. In previous studies the tunable lamellae size was limited by decreased nucleation and increased lateral crystal growth at low undercoolings. In contrast, our approach, i.e. thickening of crystalline lamellae by annealing a CS, inhibits lateral crystal growth and, thus, enables the fabrication of defined predictable tunable lamellar surface nanostructures over the entire range of folded and extended crystal lamellae.

## CONCLUSION

In the current study, we introduce a relation between film surface structures and calorimetric bulk properties of a crystalline diblock copolymer within a dual self-nucleation experiment.

Starting from a thin film crystalline standard, a defined initial state, it is possible to explain changes in the thin film surface nanostructure after annealing by different calorimetric properties observed in the calorimetric bulk self-nucleation experiment: In annealing region 1, the lamellae were solely thickened

because no melting occurred. In annealing region 2, lamellae were thickened and self-nucleated breakout crystals formed during cooling, due to a partial melting. Finally, in annealing region 3, spherulites formed by the self-nucleated breakout crystallization, during cooling, because all original crystalline lamellae of the thin film crystalline standard were molten.

Furthermore, the thickening of crystalline lamellae of the low molar mass polybutadiene-*block*-poly(ethylene oxide) in annealing region 1 provides the possibility to tune the crystalline lamellae thickness within the range of 8–16 nm where the end points correspond to once-folded and nonfolded (extended) poly(ethylene oxide) chains, respectively. On the basis of the Hoffman–Weeks analogous and Gibbs–Thomson plots, we showed that the bulk and thin film self-nucleation experiments can be correlated consistently.

The dual self-nucleation experiment was demonstrated to be a systematic and precise approach to induce and tailor surface nanostructures of diblock copolymers. It will be an invaluable tool for upcoming studies on crystalline diblock copolymer thin films because it is now feasible to predict thin film surface nanostructure dimensions.

In contrast to previous studies, the crystalline lamellae width was continuously tunable in this range which can potentially be used to adapt the obtained nanostructures to the specific needs of the respective application. Crystallization-based tunable amphiphilic nanopatterns are interesting for materials science applications requiring surface structures with different sizes, as e.g., in photonics or the biomedical field.

## ■ ASSOCIATED CONTENT

### Supporting Information

Details on the temperature profile for the bulk SNE; gold substrate preparation and M3M thiolation; prediction of the bulk PB-*b*-PEO phase and calculation of  $f^{PEO,c}$ ; limitations of the Gibbs–Thomson equation for low molecular weight PB-*b*-PEO. This material is available free of charge via the Internet at <http://pubs.acs.org>.

## ■ AUTHOR INFORMATION

### Corresponding Author

\*E-mail [kjandtd@uni-jena.de](mailto:kjandtd@uni-jena.de); Tel +49 (0) 3641 94 77 30; Fax +49 (0) 3641 94 77 32 (K.D.J.).

### Present Address

T.F.K.: Deutsches Elektronen Synchrotron (DESY), Notkestr. 85, 22607 Hamburg, Germany.

### Author Contributions

R.S. and M.M.L.A. contributed equally to this work.

### Notes

The authors declare no competing financial interest.

## ■ ACKNOWLEDGMENTS

R. Schulze and K. D. Jandt gratefully acknowledge the partial financial support of the Carl-Zeiss Foundation via a postdoctoral stipend.

## ■ REFERENCES

- (1) Bates, F. S.; Fredrickson, G. H. *Annu. Rev. Phys. Chem.* **1990**, *41*, 525–557.
- (2) Hamley, I. W. *Prog. Polym. Sci.* **2009**, *34*, 1161–1210.
- (3) Kang, Y.; Walsh, J. J.; Gorishnyy, T.; Thomas, E. L. *Nat. Mater.* **2007**, *6*, 957–960.
- (4) Ekblad, T.; Liedberg, B. *Curr. Opin. Colloid Interface Sci.* **2010**, *15*, 499–509.
- (5) Fasolka, M. J.; Banerjee, P.; Mayes, A. M.; Pickett, G.; Balazs, A. C. *Macromolecules* **2000**, *33*, 5702–5712.
- (6) He, W.-N.; Xu, J.-T. *Prog. Polym. Sci.* **2012**, *37*, 1350–1400.
- (7) Zhu, L.; Chen, Y.; Zhang, A.; Calhoun, B. H.; Chun, M.; Quirk, R. P.; Cheng, S. Z. D.; Hsiao, B. S.; Yeh, F.; Hashimoto, T. *Phys. Rev. B: Condens. Matter Mater. Phys.* **1999**, *60*, 10022–10031.
- (8) Mueller, A.; Balsamo, V.; Arnal, M. Nucleation and Crystallization in Diblock and Triblock Copolymers Block Copolymers II. In *Block Copolymers II*; Abetz, V., Ed.; Springer: Berlin, 2005; Vol. 190.
- (9) Castillo, R. V.; Arnal, M. L.; Mueller, A. J.; Hamley, I. W.; Castelletto, V.; Schmalz, H.; Abetz, V. *Macromolecules* **2008**, *41*, 879–889.
- (10) Strobl, G. *The Physics of Polymers. Concepts for Understanding Their Structure and Behavior*, 3rd ed.; Springer: Berlin, 2007; DOI 10.1007/978-3-540-68411-4.
- (11) Quiram, D. J.; Register, R. A.; Marchand, G. R.; Adamson, D. H. *Macromolecules* **1998**, *31*, 4891–4898.
- (12) Loo, Y.-L.; Register, R. A.; Ryan, A. J. *Macromolecules* **2002**, *35*, 2365–2374.
- (13) Lorenzo, A. T.; Arnal, M. L.; Mueller, A. J.; Lin, M.-C.; Chen, H.-L. *Macromol. Chem. Phys.* **2011**, *212*, 2009–2016.
- (14) Fillon, B.; Wittmann, J. C.; Lotz, B.; Thierry, A. J. *Polym. Sci., Part B: Polym. Phys.* **1993**, *31*, 1383–1393.
- (15) Mueller, A. J.; Arnal, M. A. *Prog. Polym. Sci.* **2005**, *30*, 559–603.
- (16) Müller, A. J.; Lorenzo, A. T.; Arnal, M. A.; Boschetti de Fierro, A.; Abetz, V. *Macromol. Symp.* **2006**, *240*, 114–122.
- (17) Lotz, B.; Kovacs, A. J. *Kolloid Z. Z. Polym.* **1966**, *209*, 97–114.
- (18) Buckley, C. P.; Kovacs, A. J. *Colloid Polym. Sci.* **1976**, *254*, 695–715.
- (19) Müller, A. J.; Balsamo, V.; Arnal, M. A.; Jakob, T.; Schmalz, H.; Abetz, V. *Macromolecules* **2002**, *35*, 3048–3058.
- (20) Keller, T. F.; Müller, M.; Ouyang, W.; Zhang, J.-T.; Jandt, K. D. *Langmuir* **2010**, *26*, 18893–18901.
- (21) Omichi, M.; Kadowaki, K.; Kim, B. H.; Kim, S. O.; Maruyama, I.; Akashi, M. *Chem. Commun.* **2010**, *46*, 1911–1913.
- (22) Keller, T. F.; Schönfelder, J.; Reichert, J.; Tuccitto, N.; Licciardello, A.; Messina, G. M. L.; Marletta, G.; Jandt, K. D. *ACS Nano* **2011**, *5*, 3120–3131.
- (23) Chen, H.-L.; Wu, J.-C.; Lin, T.-L.; Lin, J. S. *Macromolecules* **2001**, *34*, 6936–6944.
- (24) Hong, S.; Yang, L.; MacKnight, W. J.; Gido, S. P. *Macromolecules* **2001**, *34*, 7009–7016.
- (25) Coulon, G.; Castelein, G.; G'Sell, C. *Polymer* **1998**, *40*, 95–110.
- (26) Magonov, S. N.; Reneker, D. H. *Annu. Rev. Mater. Sci.* **1997**, *27*, 175–222.
- (27) Takahashi, Y.; Tadokoro, H. *Macromolecules* **1973**, *6*, 672–675.
- (28) Müller, A. J.; Albuerna, J.; Marquez, L.; Raquez, J.-M.; Degée, P.; Dubois, P.; Hobbs, J.; Hamley, I. W. *Faraday Discuss. Chem. Soc.* **2005**, *128*, 231–252.
- (29) Pan, P.; Zhao, L.; Zhu, B.; He, Y.; Inoue, Y. *J. Appl. Polym. Sci.* **2010**, *117*, 3013–3022.
- (30) Holmberg, K. Applications of Block Copolymers. In *Amphiphilic Block Copolymers: Self-Assembly and Applications*, 1st ed.; Alexandridis, P., Lindman, B., Eds.; Elsevier Science: Amsterdam, 2000; pp 305–318.
- (31) Papadakis, C. M.; Darko, C.; Di, Z.; Troll, K.; Metwalli, E.; Timmann, A.; Reiter, G.; Förster, S. *Eur. Phys. J. E: Soft Matter* **2011**, *34*, 1–8.
- (32) Vasilev, C.; Reiter, G.; Pispas, S.; Hadjichristidis, N. *Polymer* **2006**, *47*, 330–340.
- (33) Ungar, G.; Zeng, X. *Chem. Rev.* **2001**, *12*, 4157–4188.
- (34) Reiter, G.; Castelein, G.; Hoerner, P.; Riess, G.; Sommer, J. U.; Floudas, G. *Eur. Phys. J. E: Soft Matter* **2000**, *2*, 319–334.
- (35) Cao, W.; Tashiro, K.; Masunaga, H.; Sasaki, S.; Takata, M. J. *Phys. Chem. B* **2009**, *113*, 8495–8504.

- (36) Sun, L.; Liu, Y.; Zhu, L.; Hsiao, B. S.; Avila-Orta, C. A. *Polymer* **2004**, *45*, 8181–8193.
- (37) Kim, J. K.; Lee, H. H.; Gu, Q.-J.; Chang, T.; Jeong, Y. H. *Macromolecules* **1998**, *31*, 4045–4048.
- (38) Schönherr, H.; Frank, C. W. *Macromolecules* **2003**, *36*, 1199–1208.
- (39) Hoffman, J. D.; Davis, G. T.; Lauritzen, Jr., J. I. The Rate of Crystallization of Linear Polymers with Chain Folding. In *Treatise on Solid State Chemistry: Crystalline and Noncrystalline Solids*; Hannay, N. B., Ed.; Plenum Press: New York, 1976; Vol. 3, p 531.
- (40) Schulze, R.; Arras, M. M. L.; Li Destri, G.; Gottschaldt, M.; Bossert, J.; Schubert, U. S.; Marletta, G.; Jandt, K. D.; Keller, T. F. *Macromolecules* **2012**, *45*, 4740–4748.
- (41) Gervais, M.; Gallot, B. *Polymer* **1981**, *22*, 1129–1133.
- (42) Dong, X.-H.; Van Horn, R.; Chen, Z.; Ni, B.; Yu, X.; Wurm, A.; Schick, C.; Lotz, B.; Zhang, W.-B.; Cheng, S. Z. D. *J. Phys. Chem. Lett.* **2013**, *4*, 2356–2360.
- (43) Ashman, P. C.; Booth, C. *Polymer* **1975**, *16*, 889–896.
- (44) Marand, H.; Xu, J.; Srinivas, S. *Macromolecules* **1998**, *31*, 8219–8229.
- (45) Alamo, R. G.; Viers, B. D.; Mandelkern, L. *Macromolecules* **1995**, *28*, 3205–3213.

# Supporting information for: How the Calorimetric Properties of a Crystalline Copolymer Correlate to its Surface Nanostructures

Robert Schulze,<sup>†,§</sup> Matthias M. L. Arras,<sup>†,§</sup> Christian Helbing,<sup>†</sup> Stefan Hölzer,<sup>‡</sup>  
Ulrich S. Schubert,<sup>‡,¶</sup> Thomas F. Keller,<sup>†,¶,||</sup> and Klaus D. Jandt<sup>\*,†,¶</sup>

*Chair of Materials Science (CMS), Otto Schott Institute of Materials Research,  
Department of Materials Science and Technology, Faculty of Physics and Astronomy,  
Friedrich-Schiller-University Jena, Löbdergraben 32, 07743 Jena, Germany, Institute of  
Organic Chemistry and Macromolecular Chemistry (IOMC), Friedrich-Schiller-University  
Jena, Humboldtstraße 10, 07743 Jena, Germany, and Jena Center for Soft Matter  
(JCSM), Friedrich-Schiller-University Jena, Humboldtstraße 10, 07743 Jena, Germany*

E-mail: K.Jandt@uni-jena.de

Phone: +49 (0)3641 94 77 30. Fax: +49 (0) 3641 94 77 32

## Materials & Methods

### Temperature profile for the bulk SNE – Details

In a first step, the crystalline standard was prepared. The samples were heated up to 80 °C to completely melt the polymer and to delete the thermal history. Subsequently, the samples were cooled from 80 °C to 0 °C to crystallize the polymer under uniform conditions. This procedure was repeated twice to characterize the CS in the DSC. The corresponding DSC cooling and heating scans provide information about the calorimetric properties of the CS, i.e., crystallization and melting. Based thereon, we chose the  $T_s$  range for the bulk SNE to sample

the interval within the range of the CS melting peak. In a second step, the CS samples were heated to a predefined  $T_s$  and annealed at that temperature for 10 min.  $T_s$  was varied from 36 to 52 °C, i.e., in the pre-determined melting range of the CS. Subsequently, the samples were cooled in the DSC scan from  $T_s$  to 0 °C to crystallize all molten material. These bulk SNE cooling scans provide information about the crystallization behavior of the crystallizable copolymer block after annealing at  $T_s$ . Afterwards, the samples were heated to 80 °C to completely melt the resulting crystals. The corresponding bulk SNE heating scans provide information about the melting behavior of the crystals generated by the aforementioned annealing and crystallization procedure.

\*To whom correspondence should be addressed

<sup>†</sup>Otto Schott Institute of Materials Research

<sup>‡</sup>Institute of Organic Chemistry and Macromolecular Chemistry

<sup>¶</sup>Jena Center for Soft Matter

<sup>§</sup>These authors contributed equally to this work.

<sup>||</sup>Present address: Deutsches Elektronen Synchrotron (DESY), Notkestr. 85, 22607 Hamburg, Germany

### Gold substrate preparation and M3M thiolation

The gold substrates were prepared by physical vapor deposition (Leybold Vakuum GmbH). 200 nm thick gold films were deposited on silicon wafers via electron-beam deposition, us-

ing a deposition rate of 0.4 nm/s. The gold coated substrates were ultrasonicated for 5 min in ethanol and subsequently cleaned in argon plasma for 5 min. Thereafter, the gold surfaces were modified with a self-assembled monolayer (SAM) by immersing the gold substrates for 2 h into a 5 mmol/L ethanol solution of the M3M followed by rinsing with ethanol and drying in a stream of compressed air. Finally, the M3M modified gold substrates were annealed for 1 h at 80 °C.

## Discussion

### Prediction of the bulk PB-*b*-PEO Phase - calculation of $f^{\text{PEO}}$

For PB-*b*-PEO, the  $T_g$  of the soft PB block is much lower than usual  $T_c$  of the PEO block.<sup>S1-S3</sup> This implies that the microphase separation of the PB-*b*-PEO imposed a soft confinement on the crystallization of the PEO block.<sup>S4</sup> The structure of the microphase separated PB-*b*-PEO before and after confined crystallization can be predicted by its composition. The composition can be described by the volume fractions of the PEO and PB block,  $f^{\text{PEO},j}$  and  $f^{\text{PB}}$ , respectively, whereby  $f^{\text{PEO},j} + f^{\text{PB}} = 1$  and ( $j = a, c$ ) for the amorphous (*a*) or crystalline (*c*) polymer. We determined  $f^{\text{PEO},j}$  by the blocks' molar masses  $M_n^{\text{PB}}$  and  $M_n^{\text{PEO}}$ , the density  $\rho$  of the components and the Avogadro constant  $N_A$ .  $M_n^{\text{PB}}$  and  $M_n^{\text{PEO}}$  were calculated by the degrees of polymerization obtained from the <sup>1</sup>H – NMR measurement. An either completely amorphous (*a*) or completely crystalline (*c*) PEO block ( $j = a, c$ ) is assumed for this calculation while the PB block can only be amorphous.  $f^{\text{PEO},a}$  and  $f^{\text{PEO},c}$  were determined by using the following equations:<sup>S5</sup>

$$f^{\text{PEO},j} = \frac{V_{\text{mol}}^{\text{PEO},j}}{V_{\text{mol}}^{\text{PEO},j} + V_{\text{mol}}^{\text{PB}}}, \text{ with } j = a, c \quad (1)$$

$$V_{\text{mol}}^{\text{PEO},j} = \frac{M_n^{\text{PEO}}}{\rho^{\text{PEO},j} N_A}, \text{ with } j = a, c \quad (2)$$

$$V_{\text{mol}}^{\text{PB}} = \frac{M_n^{\text{PB}}}{\rho^{\text{PB}} N_A}, \quad (3)$$

where  $V_{\text{mol}}^{\text{PEO},a}$  and  $V_{\text{mol}}^{\text{PEO},c}$  are the molecular volumes of the amorphous and crystalline PEO, respectively, and  $V_{\text{mol}}^{\text{PB}}$  is the molecular volume of the PB block. The densities of the amorphous PB, the amorphous PEO and the crystalline PEO are  $\rho^{\text{PB}} = 0.86 \text{ g/cm}^3$ ,  $\rho^{\text{PEO},a} = 1.13 \text{ g/cm}^3$  and  $\rho^{\text{PEO},c} = 1.23 \text{ g/cm}^3$ , respectively.<sup>S5</sup> Using equation (1),  $f^{\text{PEO},a}$  and  $f^{\text{PEO},c}$  were computed to be 0.28 and 0.26, respectively. Thus, in accordance with the theoretical diblock copolymer phase diagram,<sup>S6</sup> a cylindrical, microphase separated structure of the PB-*b*-PEO is expected at a temperature  $T_{ODT} > T > T_m$ , where both blocks are amorphous.<sup>S6,S7</sup> Cooling the PB-*b*-PEO below  $T_m$  induces nucleation of the PEO within the cylinders confined by the soft PB matrix phase.<sup>S1-S3</sup> Depending on the temperature profile, PEO can crystallize within the confinement of the microphase separation or break-out crystallization can occur.<sup>S4,S8-S10</sup>

## Theroretical interpretation

### Limitations of the Gibbs-Thomson equation for low molecular weight PB-*b*-PEO

To rigorously apply the Gibbs-Thomson and derived equations (4-5, main text) for low molecular weight polymers is complex because the surface free energy  $\sigma$  varies with the folding state (until folding becomes a smooth rather than a stepwise transition with respect to  $l$ ). Indeed, Buckley and Kovacs<sup>S11</sup> showed that for low molecular weight PEO the surface free energy  $\sigma$  depends on the folding state, e.g., extended versus once-folded. In fact, it *increases* from extended to once-folded. This would invalidate a linear fit for the case of a low molecular weight PEO homopolymer. But Ashman and Booth<sup>S12</sup> showed that in the case of a PEO containing diblock copolymer two additional surface free energy terms  $\sigma_1$  and  $\sigma_2$  arise ( $\sigma = \sigma_{\text{homopolymer}} + \sigma_1 + \sigma_2$ ).  $\sigma_1$  accounts for the enthalpy change in the amorphous block and is independent of the folding state but  $\sigma_2$  which accounts for the entropy change in the

amorphous block, *decreases* when the extended chain crystal changes to once-folded. Thus the dependencies of the surface free energy on the folding state cancel each other out partially. Yet, when we apply the more refined theory described by Buckley and Kovacs<sup>S13</sup> to extract the overall surface free energy for the 2/3 folded and the extended case, which yield 40 erg/cm<sup>2</sup> and 55 erg/cm<sup>2</sup>, respectively, it is obvious that the surface free energy is affected by the different folding of the chains.

- (S10) Quiram, D. J.; Register, R. A.; Marchand, G. R.; Ryan, A. J. *Macromolecules* **1997**, *30*, 8338–8343.
- (S11) Buckley, C. P.; Kovacs, A. J. *Colloid and Polymer Science* **1976**, *254*, 695–715.
- (S12) Ashman, P. C.; Booth, C. *Polymer* **1975**, *16*, 889–896.
- (S13) Ref. S11, equations 19 and 22.

## Notes and References

- (S1) Kim, S.; Briber, R. M.; Karim, A.; Jones, R. L.; Kim, H. *Macromolecules* **2007**, *40*, 4102–4105.
- (S2) Zhu, L.; Chen, Y.; Zhang, A.; Calhoun, B.; Chun, M.; Quirk, R.; Cheng, S.; Hsiao, B.; Yeh, F.; Hashimoto, T. *Physical Review B* **1999**, *60*, 10022–10031.
- (S3) Reiter, G.; Castelein, G.; Hoerner, P.; Riess, G.; Sommer, J. U.; Floudas, G. *The European Physical Journal E: Soft Matter and Biological Physics* **2000**, *2*, 319–334.
- (S4) Hong, S.; Yang, L.; MacKnight, W. J.; Gido, S. P. *Macromolecules* **2001**, *34*, 7009–7016.
- (S5) Lambreva, D. M.; Opitz, R.; Reiter, G.; Frederik, P. M.; de Jeu, W. H. *Polymer* **2005**, *46*, 4868–4875.
- (S6) Bates, F. S.; Fredrickson, G. H. *Annual Review of Physical Chemistry* **1990**, *41*, 525–557.
- (S7) Darling, S. B. *Progress in Polymer Science* **2007**, *32*, 1152–1204.
- (S8) He, W.-N.; Xu, J.-T. *Progress in Polymer Science* **2012**, *37*, 1350–1400.
- (S9) Strobl, G. R. *The Physics of Polymers: Concepts for Understanding Their Structures and Behavior*, 3rd ed.; Springer, 2007.